UNIVERSITY OF MINNESOTA
ST. ANTHONY FALLS HYDRAULIC LABORATORY

Project Report No. 315

INTEGRAL JET MODEL FOR FLOW FROM AN OPEN CHANNEL INTO A SHALLOW LAKE OR RESERVOIR

by

Xing Fang

and

Heinz G. Stefan

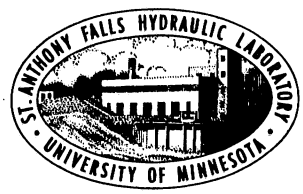

May, 1991

Minneapolis, Minnesota

ABSTRACT

Jet–like flows in sudden channel expansions with horizontal or sloping bottoms are investigated. These flows occur at inflows to lakes and reservoirs or at wastewater discharge sites. An integral analysis approach has been used. The main objective of the study has been to develop a method by which the dilution of inflows to lakes or reservoirs can be predicted if the geometry (simplified) and inflow conditions are known. If the diffuser angle ($\delta°$), the sloping angle of the bottom ($\beta°$), inflow channel aspect ratio (AR_o) and inflow densimetric Froude number (F_o) are given, the equations which will be presented can be used to estimate the dilution of plunging or non–plunging inflows. This information is needed in one–dimensional water quality models of stratified lakes or reservoirs. The integral jet flow analysis used herein includes a similarity hypothesis for velocity profiles, application of the entrainment principle and consideration of bottom friction effects on momentum. A general theoretical model is developed to predict jet centerline velocity, width and dilution of non–buoyant turbulent jet flows over horizontal or sloping bottoms in abruptly expanding channels. Wall effects in gradually expanding channels are also investigated for half jets. Predictions obtained with the theoretical model are compared with some experimental data of jet dimensions and dilution. The model is applied to geometrically simplified field conditions to illustrate effects of inflow channel aspect ratio, friction and bottom slope. All of these effects are found to be significant.

As a side product a Gauss fitting method has been developed to analyze a finite number of laboratory measurements in horizontal diffuser flows with finite water depth.

In an Appendix purely empirical equations for the dilution of horizontal jet–like flows through diffusers are also developed. Experimental results of density induced plunging flows into reservoirs (negatively buoyant) and of non–buoyant jet flows have been used.

ACKNOWLEDGEMENTS

This report is based on an M.S. thesis submitted to the University of Minnesota Graduate School in partial fulfillment of the requirements for the degree of Master of Science by the first author, Xing Fang. Dr. Heinz Stefan, Professor in the Department of Civil & Mineral Engineering, and Associate Director of the St. Anthony Falls Hydraulic Laboratory, was the faculty advisor and provided guidance during this study. This study directed by Dr. Stefan provided educational, research and professional experience and financial support.

Thanks are addressed to Mr. Thomas R. Johnson, Barr Engineering Company (Minneapolis, MN) for providing suggestions at particular points of this study.

The Chinese Government provided financial support for one year of study for Xing Fang.

CONTENTS

		Page No.
ABSTRACT		i
ACKNOWLEDGEMENTS		ii
LIST OF SYMBOLS		vi
LIST OF FIGURES AND TABLES		xi
Chapter I	INTRODUCTION	1
I.1	Concepts and Definitions	1
I.2	Review of Previous Investigations	3
I.3	Scope of Study	4
Chapter II	THEORY OF NON-BUOYANT SLOT JETS	5
II.1	Plane Turbulent Jet(Slot Jet) in Infinite Fluid	5
II.1.1	Analysis	5
II.1.2	Experimental results	9
II.1.3	Comparisons	12
II.2	Slot Jet Theory for Channel Discharge into Water of Finite Constant Depth and Infinite Width	13
II.2.1	Continuity and momentum equations in fully developed flow region	13
II.2.2	Local friction coefficient and entrainment coefficient	23
II.2.3	The flow development region	25
II.2.3.1	Continuity and momentum equations	25
II.2.3.2	Comparisons of analytical results with experimental data	30
II.2.4	Model synthesis and sensitivity analysis	34
II.3	Slot Jet Theory for Channel Discharge over Sloping Bottom in Infinite Fluid	44
II.3.1	Continuity and momentum equations in fully developed flow region	44
II.3.2	Local friction coefficient and entrainment coefficient	50
II.3.3	The flow development region	51
II.3.3.1	Continuity and momentum equations	51
II.3.3.2	Comparisons of analytical results with experimental data	54
II.3.4	Model synthesis and sensitivity analysis	54

Chapter III ANALYSIS OF EXPERIMENTAL DATA 62

III.1 Available Data and Simple Analysis 62

III.2 Gauss Fitting Method 67
III.2.1 Velocity distribution 67
III.2.2 Moments of velocity distribution 68
III.2.3 Numerical integration 69

III.3 Analysis of Experimental Data 73

Chapter IV BOUNDARY EFFECTS 77

IV.1 Bottom Friction Effects on Momentum 77
IV.1.1 Bottom friction effects in horizontal channel 77
IV.1.1.1 Continuity and momentum equations in fully developed flow region 80
IV.1.1.2 The flow development region 84
IV.1.2 Bottom friction effects in sloping channel 86
IV.1.2.1 Continuity and momentum equations in fully developed flow region 86
IV.1.2.2 The flow development region 96

IV.2 Wall Effects on Momentum 97
IV.2.1 Wall effects on half jet over horizontal bottom 103
IV.2.1.1 Continuity and momentum equations in fully developed flow region 105
IV.2.1.2 The flow development region 108
IV.2.2 Comparisons of the numerical results with experimental data 110

Chapter V APPLICATIONS OF COMPLETE MODEL TO LABORATORY DATA AND FIELD CONDITIONS 113

V.1 Densimetric Froude Number for Jet Flow 113

V.2 Application of Complete Model to Laboratory Data 116
V.2.1 Horizontal channel discharge 116
V.2.1 Sloping channel discharge 122

V.3 Application of Complete Model to Field Conditions 122
V.3.1 Friction coefficient c_f under field conditions 122
V.3.2 Comparison of model prediction with field data 126
V.3.3 Application and Extrapolation of model to general field conditions 127

Chapter VI SUMMARY, CONCLUSIONS AND RECOMMENDATIONS 150

REFERENCES 153

Appendix A EMPIRICAL EQUATIONS FOR DILUTION BEFORE PLUNGING 157

A.1 Introduction 157
A.2 Formulation of Inflow Model for Plunging Flow 157
A.2.1 Flow concepts, governing parameters And flow regimes 157
A.2.2 Plunging flow on a mild slope 162
A.2.2.1 Distance to plunging 162
A.2.2.2 Dilution of wall jet and free jet 164
A.2.2.3 Non–buoyant flow into strongly diverging channel or with large F_o 167
A.2.2.4 Transition from negatively buoyant flow to non–buoyant flow 167
A.2.3 Plunging flow on a steep slope 171
A.2.3.1 Governing parameters and flow regimes 171
A.2.3.2 Distance to plunging 171
A.2.3.3 Dilution at plunging 173
A.3 Application of Inflow Model 176

Appendix B FITTING METHOD ADAPTED TO FINITE DATA SETS 181

B.1 The second moment correction coefficient 181
B.2 Results of the modified fitting method 183
B.3 The first moment correction coefficient 191

Appendix C LISTING OF COMPUTER PROGRAMS AND NOTES 194

LIST OF SYMBOLS

		Units
A_o	= cross–sectional area of inflow channel = $B_o H_o$	[L^2]
A_k	= shape constant of velocity profile of jets (k=0,1,2,..11)	[–]
AR_o	= aspect ratio of inflow channel = B_o/H_o	[–]
AR_t	= transitional value of aspect ratio from the negatively buoyant flow to non–buoyant flow	[–]
B(x)	= characteristic jet width defined by the Gaussian distribution = $\sigma\sqrt{2}$	[L]
B_k	= integral constant or proportionality constant (k = 1,2,..10)	[–]
B_c	= corrected characteristic length	[L]
B_o	= width of inflow channel	[L]
b_p	= width of jet flow at plunging	[L]
b(x)	= full width of free jet from theory of slot jet	[L]
$b_o(x)$	= half width of the shear layer in the flow development region	[L]
C	= Chezy coefficient	[$\sqrt{L/T}$]
c_f	= local friction coefficient	[–]
C_f	= total friction force coefficient	[F]
C_k	= jet coefficient (k=1,2,3) and proportionality constant (k=6,7)	[–]
C_{mo}	= correction coefficient of zero moment	[–]
C_{m1}	= correction coefficient of first moment	[–]
C_{m2}	= correction coefficient of second moment	[–]
D_k	= proportionality constant (k=1,2, 23)	[–]
D_x	= total local friction force in the direction of the flow axis	[F]
D_{xb}	= local friction force on the bottom	[F]
D_{xw}	= local friction force on the wall	[F]
e	= mean height of the roughness projections	[L]

F	= densimetric Froude number at any cross section $= \frac{U}{(g'H)^{1/2}}$	[–]
F_o	= inflow densimetric Froude number $= \frac{U_o}{(g'H_o)^{1/2}}$	[–]
F_p	= densimetric Froude number at plunging	[–]
g	= acceleration due to gravity	[L/T^2]
g'	= reduced acceleration due to gravity $= \frac{\rho_a-\rho_o}{\rho_o} g$ or $\frac{\rho_a-\rho}{\rho_a} g$	[L/T^2]
H_o	= mean depth of inflow channel	[L]
H_p	= mean depth at plunging	[L]
$H(x)$	= water depth of sloping channel = $H_o + x \tan\beta$	[L]
h_d	= depth of underflow layer	[L]
k	= exponential constant (Chapter II)	[–]
k_s	= relative roughness = $e/H(x)$	[–]
L	= characteristic length in the dimensional analysis	[L]
$M(x)$	= momentum in the cross–section x	[M L/T]
M_o	= momentum of inflow (Chapter II)	[M L/T]
M_o	= zero moment $= \int_o^\infty U(y)\, dy$ (Chapter III)	[L^2/T]
M_1	= first moment $= \int_o^\infty U(y)\, y\, dy$	[L^3/T]
M_2	= second moment $= \int_o^\infty U(y)\, (y-y_o)^2\, dy$	[L^4/T]
M_3	= third moment $= \int_o^\infty U(y)\, (y-y_o)^3\, dy$	[L^5/T]
M_{oc}	= corrected zero moment	[L^2/T]
M_{1c}	= corrected first moment	[L^3/T]
M_{2c}	= corrected second moment	[L^4/T]
m_1	= M_1/M_o	[L]
m_2	= $M_2/M_o = \sigma^2$	[L^2]
m	= exponential constant (Chapter II)	[–]
n	= exponential constant (Chapter II)	[–]
n	= Manning coefficient (Chapter V)	[$T/L^{1/3}$]
N	= number of calculation steps	[–]
p	= exponent or power	[–]

q	= exponent or power	[–]
q	= flow rate per unit width	[L^2/T]
Q	= volumetric flow rate	[L^3/T]
Q_o	= volumetric inflow rate	[L^3/T]
Q_a	= volumetric ambient return flow rate	[L^3/T]
Q_{am}	= ambient return flow rate at measurement section	[L^3/T]
Q_d	= underflow rate downstream from plunging(x_p)	[L^3/T]
Q_m	= underflow rate at measurement section (x_m)	[L^3/T]
Q_p	= volumetric flow rate at plunging (x_p)	[L^3/T]
$\frac{Q(x)}{Q_o}$	= dilution ratio at cross section x	[–]
S	= bottom slope = $\tan(\beta)$	[–]
S_o	= hydraulic slope = S (normal flow)	[–]
R	= radius of a pipe	[L]
R_e	= Reynolds number = $\frac{U\ L}{\nu}$	[–]
Re_x	= local Reynolds number = $\frac{u_m(x)\ x}{\nu}$	[–]
R_{eo}	= bulk Reynolds number of inflow = $\frac{U_o H_o}{\nu}$	[–]
R_h	= hydraulic radius	[L]
Ri	= Richardson number = $\frac{\rho_d - \rho_a}{\rho_a}\ g\ h_d\ /U_d^2$	[–]
U	= mean velocity of turbulent jet in the x direction	[L/T]
U_d	= mean velocity of underflow (density current)	[L/T]
U_o	= mean velocity of channel discharge	[L/T]
U_∞	= free stream velocity outside of the boundary layer	[L/T]
u	= local velocity of jet in the x direction	[L/T]
u_s	= water surface velocity of the channel discharges	[L/T]
u_m	= the maximum velocity in the x direction	[L/T]
u/u_m	= the non–dimensional velocity distribution	[–]
v_e	= entrainment velocity of jet flow	[L/T]
v	= local velocity of jet in the y direction	[L/T]
x	= longitudinal coordinate (origin at end of inflow channel)	[L]
x_o	= length of potential core of the flow development region	[L]
x_d	= distance to underflow after plunging	[L]
x_p	= distance to plunging	[L]

y	= transverse coordinate(origin at inflow channel centerline)	[L]
y_o	= centerline of velocity profile = m_1	[L]
y_1	= transverse distance to inner edge of shear layer	[L]
y_n	= negative cut–off point in η axis	[–]
y_p	= positive cut–off point in η axis	[–]
z	= depth coordinate (origin at bottom)	[L]
α_1	= angle of the shear layer in the development region	[–]
α_e	= entrainment coefficient	[–]
$\alpha_e{}^o$	= entrainment coefficient in the flow development region	[–]
β	= bottom (beach) slope [–]	
λ	= resistance coefficient	[–]
η	= non–dimensional transverse coordinate	
	$= \frac{y}{B(x)}$ $(y_o = 0.0)$	
	$= \frac{y-y_o}{B(x)}$ $(y_o \neq 0.0)$	[–]
ξ	= non–dimensional transverse coordinate in flow development region	
	$= \frac{y-y_1}{b_o(x)}$ (Chapter II)	
	$= \frac{y-\delta(x)}{b_o(x)}$ (Chapter IV)	[–]
ζ	= non–dimensional coordinate with depth in the boundary layer	
	$= z/H_o$	[–]
δ	= diffuser half–angle (Appendix I)	[–]
$\delta(x)$	= boundary layer thickness (Chapter IV)	[–]
γ	= dilution = Q_d/Q_o	[–]
ν	= kinematic viscosity	[L^2/T]
τ_o	= shear stress of boundary layer on flat plate	[F/L^2]
τ_t	= turbulent shear stress	[F/L^2]
σ	= standard deviation	[L]
Δy	= calculation step for numerical integration	[L]
ρ	= density of water in any cross section	[M/L^3]
ρ_a	= density of ambient water	[M/L^3]
ρ_o	= density of inflow	[M/L^3]
ϵ_o	= non–dimensional density difference = $\frac{\rho_a-\rho_o}{\rho_o}$	[–]

Subscripts:

a	= ambient
d	= downstream of plunging (underflow)
m	= at measurement cross section, mixed, underflow
o	= inflow, initial
p	= at plunging

Units:

L	= length
M	= mass
T	= time
F	= force

LIST OF FIGURES AND TABLES

Chapter I:

Fig. 1–1 Plunging flow on a slope following a discharge from a channel (schematic).

Fig. 1–2 First approximation of inflow geometry: Flow into a diverging and sloping channel.

Chapter II:

Fig. 2–1 Definition sketch of plane turbulent free jets (Rajaratnam, 1976).

Fig. 2–2 Velocity distribution for plane turbulent free jets (Forthmann, 1939).

Fig. 2–3 Comparison of velocity profiles of plane turbulent free jets.

Fig. 2–4 Dimensionless velocity distribution of plane turbulent free jets (Zijnen, 1958a).

Fig. 2–5 A schematic representation of horizontal channel discharge.

Fig. 2–6 A schematic representation of the model of jet flow over horizontal bottom with finite water depth.

Fig. 2–7 Dimensionless centerline velocity and width of a non–entraining jet over a horizontal bottom with friction.

Fig. 2–8 Comparison of dilution $Q(x)/Q_o$ and dimensionless width $b(x)/B_o$ of plane turbulent free jets.

Fig. 2–9 Comparison of dimensionless centerline velocity of plane turbulent free jets.

Fig. 2–10 Fitting of experimental data to obtain entrainment coefficient α_e.

Fig. 2–11 Definition sketch of flow–development region of jet flows.

Fig. 2–12 Sensitivity of dimensionless length x_o/B_o of developing region to friction coefficient and entrainment coefficient at $AR_o = 0.5$.

Fig. 2–13 Relationship between x_o/B_o and friction coefficient c_f at $AR_o=20$.

Fig. 2–14 Dilution $Q(x)/Q_o$ versus x/B_o as AR_o increases.

Fig. 2–15 Relationship between dimensionless $b(x)/B_o$, $u_m(x)/U_o$ and x/B_o as AR_o is changed.

Fig. 2–16 Relationship between $b(x)$, $u_m(x)/U_o$ and x (ft) as AR_o is changed.

Fig. 2–17 Dilution $Q(x)/Q_o$ versus x/B_o as entrainment coefficient α_e is changed at $AR_o = 0.5$.

Fig. 2–18 Sensitivity of $b(x)/B_o$ and $u_m(x)/U_o$ to entrainment coefficient α_e at $AR_o = 0.5$.

Fig. 2–19 Dilution $Q(x)/Q_o$ versus x/B_o as entrainment coefficient α_e is changed at $AR_o = 20$.

Fig. 2–20 Sensitivity of $b(x)/B_o$ and $u_m(x)/U_o$ with entrainment coefficient α_e at $AR_o = 20$.

Fig. 2–21 Dilution $Q(x)/Q_o$ versus x/B_o as friction coefficient c_f is changed at $AR_o = 0.5$.

Fig. 2–22 Sensitivity of $b(x)/B_o$ and $u_m(x)/U_o$ with friction coefficient c_f at $AR_o = 0.5$.

Fig. 2–23 A schematic representation of the sloping channel discharge.

Fig. 2–24 A simple model of jet flow over sloping bottom with finite water depth.

Fig. 2–25 Relationship between dimensionless length x_o/B_o and slope angle β° as α_e or c_f is changed at $AR_o = 0.5$.

Fig. 2–26 Dimensionless length x_o/B_o versus slope angle β° as AR_o increases.

Fig. 2–27 Dilution $Q(x)/Q_o$ versus x/B_o as slope angle β° is changed at $AR_o = 0.5$.

Fig. 2–28 Sensitivity of $b(x)/B_o$ and $u_m(x)/U_o$ with slope angle β° at $AR_o = 0.5$.

Fig. 2–29 Dilution $Q(x)/Q_o$ versus x/B_o as slope angle β° and AR_o are changed.

Fig. 2–30 Sensitivity of $b(x)/B_o$ and $u_m(x)/U_o$ with slope angle β° as AR_o is changed.

Chapter III:

Fig. 3–1 Plan view of locations where velocity profile measurements were taken (Example). Experiments by Johnson et. al. (1988).

Fig. 3–2 Examples of velocity profiles with depth and average velocities (Experiment 21/10/1985).

Fig. 3–3 Scheme of numerical integration (Method 1).

Fig. 3–4 Examples of fitted experimental data.

Fig. 3–5 Examples of curves fitted to a data set with perfect Gaussian distribution.

Fig. 3–6 Examples of analysis of experimental data by modified fitting method.

Fig. 3–7 Examples of analysis of experimental data by modified fitting method.

Fig. 3–8 Comparison of model prediction with experimental data for $b(x)/B_0$ and $u_m(x)/U_0$.

Chapter IV:

Fig. 4–1 Schematic of horizontal channel discharge with boundary effects.

Fig. 4–2 Comparison of numerical results with experimental data for dimensions of horizontal channel discharges at $AR_0 = 0.5$.

Fig. 4–3 Comparison of numerical results with experimental data for dimensions of horizontal channel discharges at $AR_0 = 1.8$.

Fig. 4–4 Comparison of numerical results with experimental data for dilution of horizontal channel discharges.

Fig. 4–5 Sensitivity of jet dimensions to aspect ratio AR_0.

Fig. 4–6 Sensitivity of dilution to aspect ratio AR_0 in horizontal channel.

Fig. 4–7 Relationship between Reynolds number and x for different aspect ratios AR_0.

Fig. 4–8 Relationship between the local friction coefficient and x for different aspect ratios AR_0.

Fig. 4–9 Schematic of velocity distributions in sloping channel.

Fig. 4–10 Sensitivity of dilution to aspect ratio AR_0 in sloping channel.

Fig. 4–11 Sensitivity of non–dimensional centerline velocity to aspect ratio AR_0 in sloping channel discharge.

Fig. 4–12 Sensitivity of jet width to aspect ratio AR_0 in sloping channel discharge.

Fig. 4–13 Relationship between Reynolds number and x in sloping channel at different aspect ratios AR_0.

Fig. 4–14 Relationship between local friction coefficient and x in sloping channel at different aspect ratios AR_0.

Fig. 4–15 Definition sketch of plane turbulent wall jets.

Fig. 4–16 Comparison of numerical model results with experimental data for dilution and growth of the length scale b(x) of wall jets.

Fig. 4–17 Comparison of numerical model results with experimental data for variation of the velocity scale of wall jets.

Chapter V:

Fig. 5–1 Relationship between F and x/B_0 for different F_0 at AR_0 = 0.5.

Fig. 5–2 Model results and experimental data for the relationship $x_p(F_0)$. Line through experimental data and model results are for free jet
theory (frictionless).

Fig. 5–3 Model results and experimental data for the relationship $x_p(F_0)$. The model includes bottom friction effects.

Fig. 5–4 Experimental data and model results for dilution Q_p/Q_0 at β = o° and AR_0 = 0.5.

Fig. 5–5 Experimental data and model results for dilution Q_p/Q_0 at β = 0° and AR_0 = 1.8.

Fig. 5–6 Sensitivity of model results at different F_p in cartesian (top) and log–log (bottom) coordinates. The model includes effects of bottom friction.

Fig. 5–7 Prediction of dilution under laboratory conditions.

Fig. 5–8 Comparison of experimental plunging point data with model results at β = 3° and F_p = 1.0. x_p is normalized by B_0 (top) or $\sqrt{A_0}$ (bottom)

Fig. 5–9 Comparison of experimental data with numerical results of dilution Q_p/Q_0 at β = 3° [laboratory condition].

Fig. 5–10 Schematic plan view of wall jet in field condition (bottom) and cumulative effluent flow rates as a function of distance (top).

Fig. 5–11 Sensitivity of predicted distance to plunging x_p to densimetric Froude number F_0 at plunging F_p and slope angle β.

Fig. 5–12 Sensitivity of x_p/B_0 to aspect ratio AR_0 for smooth bottom.

Fig. 5–13 Prediction of dilution (top) and plunging (bottom) for smooth bottom.

Fig. 5–14 Prediction of dilution (top) and plunging (bottom) at c_f = 0.0005.

Fig. 5–15 Prediction of dilution (top) and plunging (bottom) at c_f = 0.005.

Fig. 5–16 Prediction of dilution (top) and plunging (bottom) at c_f = 0.02

Fig. 5–17 Dilution at F_0 = 15 for different AR_0 and c_f.

Fig. 5–18 Numerical results of dilution versus F_0 at c_f = 0.005, β = 0.5° for different aspect ratios AR_0.

Fig. 5–19 Numerical results of dilution versus F_0 at c_f = 0.005, β = 1° for different aspect ratios AR_0.

Fig. 5–20 Numerical results of dilution versus F_0 at c_f = 0.005, β = 2° for different aspect ratios AR_0.

Fig. 5–21 Numerical results of dilution versus F_0 at c_f = 0.005, β = 3° for different aspect ratios AR_0.

Fig. 5–22 Numerical results of dilution versus F_0 at c_f = 0.005, β = 5° for different aspect ratios AR_0.

Fig. 5–23 Prediction of relationship of dilution with F_0 at c_f = 0.005 and AR_0 = 5 as slope angle β increases from 0° to 5°.

Fig. 5–24 Prediction of relationship of dilution with $\beta°$ at c_f = 0.005 and AR_0 = 5 for different densimetric Froude number F_0.

Fig. 5–25 Sensitivity of dilution to F_0 and β at c_f = 0.005 and AR_0 = 50.

Fig. 5–26 Sensitivity of dilution to F_0 and β at c_f = 0.0005 and AR_0 = 20.

Fig. 5–27 Sensitivity of dilution to F_0 and β at c_f = 0.02 and AR_0 = 20.

Fig. 5–28 Sensitivity of dilution to F_0 and β at c_f = 0.005, AR_0 = 50 and α_e = 0.005.

Fig. 5–29 Envelope of maximum dilution for slope angle $0° \leq \beta \leq 5°$ and large aspect ratio $5 \leq AR_0 \leq 100$ at c_f = 0.005.

Fig. 5–30 Envelop of maximum dilution $(Q_p/Q_0)_{max}$ (defined at F_0 = 15) for slope angles $0° \leq \beta \leq 5°$ and aspect ratios $5 \leq AR_0 \leq 100$ with three friction coefficient normalized by $AR_0^{0.28}$.

Appendix A:

Fig. A–1 Flow parameters of plunging flow (after Akiyama et al. 1984).

Fig. A–2 Extreme cases of plunging flow: (a)No mixing on mild slope (b)Mixing on steep slope (after Akiyama et al., 1984).

Fig. A–3 Flow Regimes: (a)Attached Flow on Left, (b)Wall Jet (One Stalled Region) In Center, (c) Free Jet (Two Stalled Regions) [Johnson and Stefan, 1988].

Fig. A–4 Relationship between $Q(x)/Q_o$ and δ ($\delta \leq 10°$ Experimental Data).

Fig. A–5 Schematic representation of plunging flow in a diverging horizontal channel. A wall jet type flow is shown [Johnson et al., 1988].

Fig. A–6 Relationship of plunging point location (x_p/B_o) to inflow densimetric Froude number (F_o). Separated flows (wall jets and free jets).

Fig. A–7 Empirical formula and experimental Data at AR=0.5, $\delta \geq 45°$.

Fig. A–8 Empirical formula and experimental Data at AR=1.8, $\delta \geq 45°$.

Fig. A–9 Empirical formula and experimental Data at $\delta=10°$, $\beta=0.0°$.

Fig. A–10 Measured cumulative flow rate (Q_m/Q_o) vs. non–dimensional distance (x_m/B_o) for non–buoyant free jet and wall jet.

Fig. A–11 Relationship between AR_t and diffuser angle $\delta°$.

Fig. A–12 Plunging flow in a diverging sloping channel (schematic).

Fig. A–13 Flow patterns. Wall jets on horizontal and sloping diffuser.

Fig. A–14 Relationship between Q_p/Q_o and F_o for $\delta=10°$ and $\delta=20°$ as $\beta=3°$.

Fig. A–15 Relationship between Q_p/Q_o and F_o for $\delta=90°$, $\beta=3°$.

Fig. A–16 Relationship between Q_p/Q_o and F_o for $\delta=10°$, $\beta=0°$.

Fig. A–17 Relationship between Q_p/Q_o and F_o for $\delta=20°$, $\beta=0°$.

Fig. A–18 Relationship between Q_p/Q_o and F_o for $\delta=45°$, $\beta=0°$.

Fig. A–19 Relationship between Q_p/Q_o and F_o for $AR_o=1.8$, $\beta=3°$.

Appendix B:

Fig. B–1 The correction coefficient of the second moment versus /non–dimensional velocity at cut–off point.

Fig. B–2 A scheme of numerical integration. (Method 2).

Fig. B–3 Effects of different cut–off points with same calculation step $\Delta\eta$.

Fig. B–4 Examples of the modified Gauss fitting method with symmetric and unsymmetric cut–off points.

Fig. B–5 Examples of the modified Gauss fitting method.

Fig. B–6 Examples of effects of different calculation step $\Delta\eta$.

Fig. B–7 Analysis of error of B_c with different calculation step $\Delta\eta$.

Fig. B–8 Comparison of integration by method 1 and method 2 with a finite number of measurements.

Fig. B–9 Correction coefficient of the first moment.

TABLES:

Table 2.1 Jet coefficients.

Table 3.1 Original experimental data (Johnson et al., 1988).

Table 3.2 Average velocity at experimental points.

Table 4.1 Parameters of velocity profiles and friction coefficients.

Table 5.1 Friction coefficient c_f and Reynolds number Re_0 for field conditions.

Chapter I INTRODUCTION

I.1 Concepts and Definitions

The inflow into a reservoir or the discharge of an effluent into a lake is often not precisely of the same density as the lake or reservoir water. If the density of the inflow (ρ_{in}) is less than that of the receiving water (ρ_a) the inflow will form an overflow (surface flow); an underflow (plunging flow) will form when it is greater.

In one–dimensional (vertical) dynamic water quality models (e.g. Riley and Stefan, 1989) the surface flow is simply incorporated into the surface layer(s), but plunging flow requires an estimate of the dilution to predict into which layer in a stratified lake or reservoir an inflow will enter. Plunging flow shown in Fig. 1–1 is a transitional flow from homogeneous open channel flow to stratified, entraining underflow. In order to provide information on the dilution of plunging flows a simple integral jet model dealing primarily with discharges from sudden open channel expansions over a horizontal or sloping bottom will be reported herein.

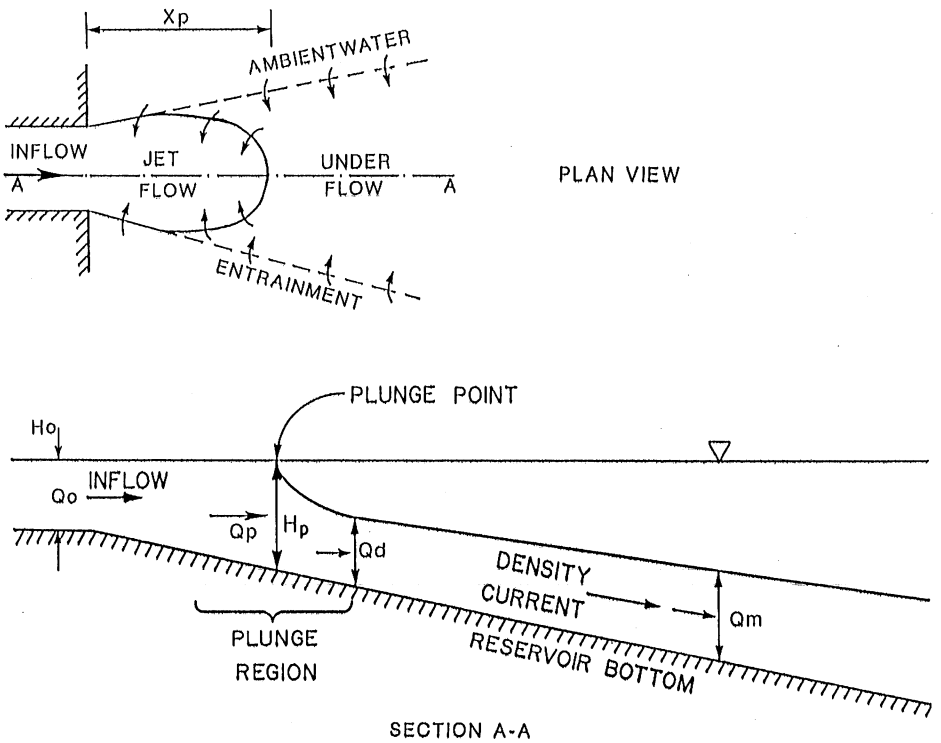

Fig. 1–1 Plunging flow on a slope following a discharge from a channel (schematic).

The flow from a channel into a lake or reservoir schematically shown in Fig. 1–1 often starts as a jet–like flow. When negative buoyancy becomes dominant, plunging occurs. Following Johnson and Stefan's (1988) data we propose to use a slot jet model to predict the distance to plunging and dilution before plunging. The definition of a jet was given by Fischer et al (1979): A jet is the discharge of fluid from an orifice or slot into a large body of same or similar fluid. Jets are classified as non–buoyant, positively buoyant and negatively buoyant jets. They are also classified as laminar and turbulent. The inflow before plunging is similar to non–buoyant turbulent jet flow.

The physical parameters governing the inflow from a channel into a lake or reservoir include inflow conditions as well as geometrical parameters. In first approximation the geometrical parameters are the inflow depth H_o, inflow width B_o, aspect ratio of inflow $AR_o = B_o/H_o$, divergence angle δ and slope angle on the bottom β (Fig. 1–2). The inflow parameters are Reynolds number of inflow Re_o, densimetric Froude number of inflow F_o and local friction coefficient c_f. The integral model uses these physical parameters to predict the dilution before plunging and the distance to plunging.

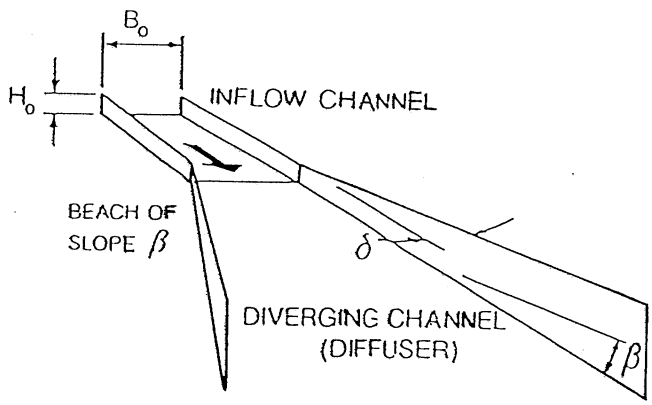

Fig. 1–2 First approximation of inflow geometry: flow into a diverging and sloping channel.

Two important differences between the channel discharge and a classical slot jet flow exist. (1) A plane turbulent free jet comes from a slot of infinite width relative to its height (or thickness). The aspect ratio of inflow AR_o of a slot jet is theoretically equal to zero because $H_o \to \infty$. The inflow channel by contrast has finite depth and typically a large or finite aspect ratio. (2) A classical free jet enters a fluid body with no or very distant boundaries and walls, whereas the channel discharge is continuously in contact with the channel bottom. For these two reasons it is therefore necessary to deal with the effects of finite water depth and wall friction on entrainment and momentum of the flow.

Despite the differences between a classical turbulent free slot jet and a discharge into a strongly diverging channel, some flow features are the same. In the axial direction there is, following the end of the channel, a flow development region, where shear penetrates inwards towards the axis of the

jet flow while there is still a (potential) core of undiminished mean velocity U_0. In the second region, known as the fully developed jet flow region, the potential core has disappeared. The fully developed region and the flow development region will be analyzed separately in this study and then combined to construct the integral model of the flow field. Bottom effects and wall effects will also be introduced in different chapters. The final results will be values for dilution of the inflow as a function of inflow parameters and geometry.

I.2 Review of Previous Investigations

Analysis and experimental observations of plane turbulent free jets, which provide the basic methods for the analysis of the channel discharge, were given by Forthmann (1934), Goertler (1942), Tollmien (1926), Albertson et al (1950), Fischer et al (1979), Zijnen (1958), Heskestad (1965), Rajaratnam (1976) and others. Plane turbulent wall jets have been studied by Forthmann (1934), Zerbe and selna (1946), Sigalla (1958), Myers et al. (1961), Schwarz and Cosart (1961), and others. These investigations focus on jet geometry velocities and momentum without effects of boundaries and friction.

Field and experimental studies of plunging flows into reservoirs have been conducted by Wunderlich and Elder (1973), Hebbert (1979), Ellison and Turner (1959), Akiyama and Stefan (1984), Johnson and Stefan (1988) and others. Akiyama and Stefan (1987), Johnson and Stefan (1988) conducted experiments in a horizontal diverging channel and in a sloping diverging channel, including negatively buoyant flows and as well as non–buoyant flows. Information about flow regimes, distance to plunging, and dilution was obtained.

The integral approach, coupled with numerical methods for solving the momentum and continuity equations, has been popular for analytical solutions. Using the similarity hypothesis for velocity profiles and the basic equations of motion, Goertler (1942), Tollmien (1926), Rajaratnam (1976) and others predicted centerline velocity, jet width and entrainment of turbulent free jets. Numerical solutions of the two–dimensional flow equations including various closure schemes for turbulence (Yuan, Song and He, 1991) have recently also been successful but are beyond the scope of this study.

MINLAKE (Riley et. al., 1988) is a dynamic, one–dimensional (in depth), unsteady lake water quality simulation model. A subroutine PDEPTH in MINLAKE is used to compute initial dilution before plunging and depth at plunging (Akiyama, 1987). Referring to Fig. 1–1 the dilution before plunging $\gamma = Q_p/Q_0$ is kept constant at

$\gamma = 1.15$ for mild slope

$\gamma = 2.80$ for steep slope.

Setting the dilution constant is however not necessarily appropriate for natural reservoirs and lakes.

An empirical model for computing dilution before plunging has been constructed from available experimental data (Johnson and Stefan, 1988) in Appendix A. This effort is, however severely limited by the fact that experiments (Akiyama, 1984 and Johnson, Stefan, 1988) were conducted with only two small aspect ratios $AR_0 = 0.5$ and 1.8, densimetric Froude numbers $F_0 \leq 4$ and two slope angles $\beta = 0°$ and 3°. It is not appropriate to use the empirical model in field conditions with large aspect ratios ($AR_0 > 5$) and any slope angle β between 0° and 6°. Instead it is necessary to describe the flow mechanisms by solution of the flow continuity and momentum equations in order to predict the complicated entrainment process without further recourse to experiments.

I.3 Scope of Study

The main objective of this study is to develop a method to predict the dilution before plunging of inflows to lakes or reservoirs if the geometry (simplified) and inflow conditions are known. Therefore the discharge from an open rectangular channel into a larger water body with horizontal or sloping bottom is investigated using the basic elements of slot jet theory. The integral analysis approach is used to deal with the flow development region (zone of flow establishment, ZFE) and the fully developed flow region. The integral analysis includes a similarity hypothesis for velocity profiles, application of the entrainment principle and consideration of the bottom friction effects on momentum. The friction and entrainment coefficients are derived from available experimental data. Wall effects on momentum are also investigated for half jets.

A general integral model has been constructed to predict the jet centerline velocity, full width and dilution of non–buoyant turbulent jet flows over horizontal and sloping bottoms in abruptly expanding channels. If the aspect ratio AR_0 of inflow, the sloping angle of the bottom $\beta°$ and inflow densimetric froude number F_0 are given, the equations presented herein can be used to predict the distance to plunging and the dilution of neutrally buoyant or negatively–buoyant inflows with large diffuser angle ($\delta \geq 45^0$).

Predictions obtained with the numerical model are compared with experimental data for jet dimensions and dilution. The model is applied to simplified field conditions to illustrate effects of inflow channel aspect ratio, friction and bottom slope. The model developed herein can be used to give a first estimate of the dilution of inflows to reservoirs and lakes in one–dimensional water quality models.

In Appendix A, empirical equations for the dilution of plunging flow are developed. Experimental results of density induced plunging flow into reservoirs and non–buoyant jet flow have been used.

In Appendix B, a Gauss fitting method to analyze finite numbers of experimental measurements in non–buoyant horizontal jets is developed.

Chapter II THEORY OF NON–BUOYANT SLOT JETS

II.1. Plane Turbulent Jet (Slot Jet) in Infinite Fluid

Let us consider a jet of water coming from a narrow slot of large length into a large water body. The width of the jet is $2b_0$ and U_0 is the uniform velocity in the jet. The jet mixes violently with the surrounding fluid creating turbulence, and the jet itself grows thicker. Figure 2–1 shows a schematic representation of the jet configuration, which is known as the plane turbulent free jet. The jet flow has two distinct regions. In the first region, close to the nozzle, known commonly as the flow development region, the turbulent shear layer penetrates inwards towards the centerline of the jet where there is a wedge–like region of mean velocity U_0. This wedge is known as the potential core and is surrounded by a mixing layer. In the second region, known as the fully developed flow region, turbulence has penetrated to the axis and the potential core has disappeared. In this section we will review the fully developed flow region and some experimental results.

In the fully developed flow region, the transverse distribution of the time averaged local velocity in the x–direction, i.e. the variation of u with y at different sections, has the same geometrical shape as shown in Fig. 2–2. Velocity distributions measured at different sections are shown on top and plotted in dimensionless from on the bottom of Fig. 2–2.

II.1.1 Analysis

The equations of motion for the plane turbulent free jet with a zero pressure gradient in the axial direction are (Rajaratnam, 1976)

$$u \frac{\partial u}{\partial x} + v \frac{\partial u}{\partial y} = \frac{1}{\rho} \frac{\partial \tau_t}{\partial y} \qquad [2\text{–}1]$$

$$\frac{\partial u}{\partial x} + \frac{\partial v}{\partial y} = 0 \qquad [2\text{–}2]$$

where u and v are, respectively, the mean (time averaged) velocity of the turbulent jet in the x–direction and y–direction, τ_t is turbulent shear stresses often written simply as τ.

A plane turbulent jet issuing into a large stagnant environment and expanding under zero pressure gradient experiences no external force and hence the momentum of the jet in the axial direction is preserved.

To derive the momentum conservation criterion we multiply [2–1] by ρ and integrate from $y = 0$ to $y = \infty$.

$$\rho \int_0^\infty u \frac{\partial u}{\partial x}\, dy + \rho \int_0^\infty v \frac{\partial u}{\partial y}\, dy = \int_0^\infty \frac{\partial \tau}{\partial y}\, dy \qquad [2\text{–}3]$$

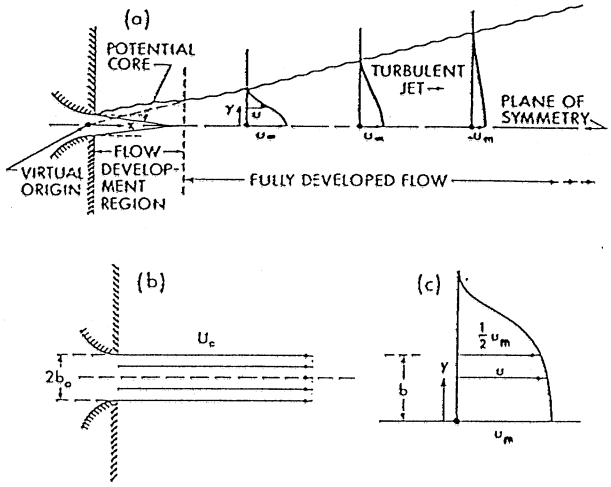

Fig. 2–1 Definition sketch of plane turbulent free jets. (Rajaratnam, 1976)

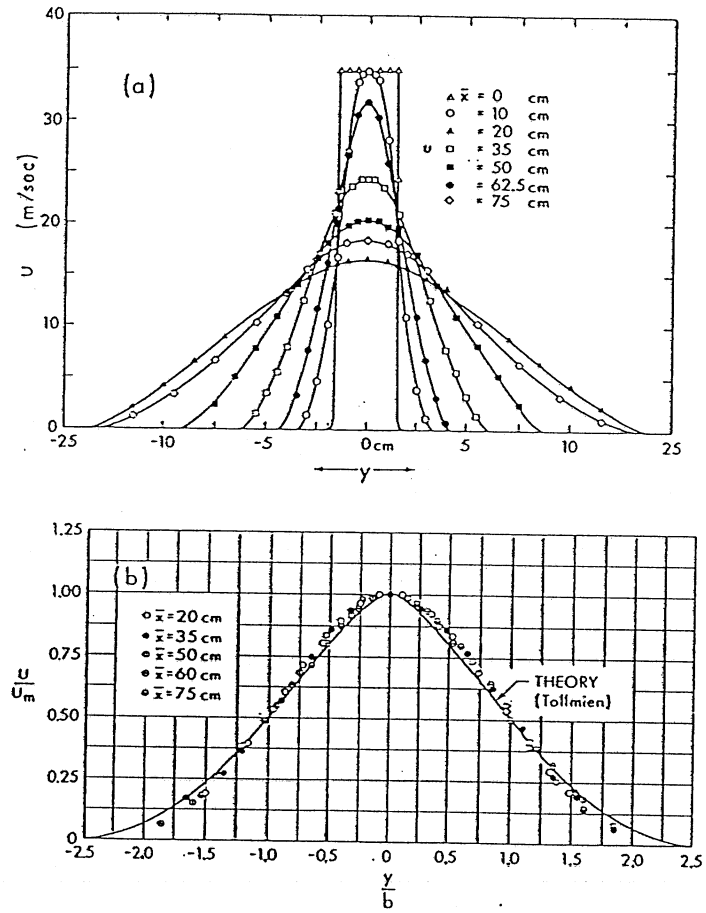

Fig. 2–2 Velocity distribution for plane turbulent free jets. (Forthmann, 1939)

Let us now consider the different terms of this equation.

$$\rho\int_0^\infty u\,\frac{\partial u}{\partial x}\,dy = \frac{1}{2}\,\frac{d}{dx}\int_0^\infty \rho u^2\,dy$$

$$\rho\int_0^\infty v\,\frac{\partial u}{\partial y}\,dy = \rho\,(|uv|_0^\infty - \int_0^\infty u\,\frac{\partial v}{\partial y}\,dy)$$

$$= \rho\,(\int_0^\infty u\,\frac{\partial u}{\partial x}\,dy)$$

$$= \frac{1}{2}\,\frac{d}{dx}\int_0^\infty \rho u^2\,dy$$

$u = u_m,\ v = 0,$ for $y = 0$

$u = 0,\ v = v_e.$ for $y \to \infty$

where v_e is a finite quantity known as the "entrainment velocity", which we will consider later.

$$\int_0^\infty \frac{\partial \tau}{\partial y}\,dy = |\tau|_0^\infty = \tau(\infty) - \tau(0) = 0$$

Since $\tau(0) = 0$ because of symmetry and $\tau(\infty)$ is zero [2–3] becomes

$$\frac{d}{dx}\int_0^\infty \rho u^2\,dy = 0 \qquad [2–4]$$

If the plane jet is issuing from an orifice of height $2b_0$ with a uniform velocity U_0, for every unit length of the orifice, the momentum flux $M_0 = 2\rho b_0 U_0^2$. Hence [2–4] after integration becomes

$$2\int_0^\infty \rho u^2\,dy = M_0\ . \qquad [2–5]$$

For the plane turbulent jet, we have seen that The velocity distribution in the fully developed region is self–similar. That is

$$\mathbf{u/u_m = f(\eta)\ ,} \qquad [2–6]$$

where $\eta = y/b$, b is the half width of jet which is from the centerline to the point with the velocity $u = \frac{1}{2} u_m$.

Assume simple forms for u_m and b as:

$$u_m = B_1 x^p \qquad [2\text{–}7]$$

$$b = B_2 x^q \qquad [2\text{–}8]$$

where p and q are unknown exponents. B_1 and B_2 are proportionality coefficients. Substituting [2–6], [2–7] and [2–8] into [2–5], gives

$$\frac{d}{dx}(bu_m^2) = 0 \qquad [2\text{–}9]$$

From [2–9], we can say that bu_m^2 is independent of x. That is:

$$x^{q+2p} = B_3 x^o \quad \text{or} \quad q+2p = 0 \qquad [2\text{–}10]$$

In order to evaluate the constant p and q, we use the entrainment hypothesis introduced by Morton et. al. (1956) in connection with the analysis of plumes (Rajaratnam, 1976). If Q is the flow rate for unit length at any cross section of the jet

$$Q = 2 \int_0^\infty u \, dy \qquad [2\text{–}11]$$

If Q_o is the flow from the nozzle, it is known from experiments that Q/Q_o is greater than unity and assumes very large values as x becomes large. We write

$$\frac{dQ}{dx} = 2 \frac{d}{dx} \int_0^\infty u \, dy = 2 v_e \qquad [2\text{–}12]$$

v_e is entrainment velocity. From dimensional considerations, suppose that the entrainment velocity v_e is proportional to the centerline velocity u_m, that is

$$v_e = \alpha_e u_m \qquad [2\text{–}13]$$

where α_e is the entrainment coefficient.

$$\frac{d}{dx} \int_0^\infty u \, dy = \alpha_e u_m \qquad [2\text{–}14]$$

Put [2–6], [2–7] and [2–8] into [2–14], and obtain

$$\frac{\frac{d}{dx}(u_m\, b)}{u_m} = B_4\, x^o$$

That is: $p + q - 1 - p = 0$ or $q = 1$
Using [2–10], we get $p = -1/2$. Hence, for the plane turbulent jet, we have

$$u_m = B_5 / \sqrt{x} \quad \text{and} \quad b = B_6\, x \qquad [2–15]$$

II.1.2 Experimental Results

The earliest systematic experiments on plane turbulent jets were apparently conducted by Forthmann(1934). Further careful measurements on the plane jet have been made by Albertson et al. (1950), Zijnen (1958a), Heskestad (1965) and others. Zijnen's experimental results were compared with the theoretical curves of Tollmien and Goertler (Fig. 1–5, Rajaratnam, 1976, Chapter 1). It has been experimentally found that the velocity distribution can be represented satisfactorily by a Gaussian curve. Tollmien(1926), Goertler(1942), Reichardt(1942), Albertson et al. (1950), Zijnen (9158a) and Schlichting(1968) among others gave equations for velocity profiles. Zijnen (1958a) gave

$$u/u_m = \exp(-a\,\lambda^2) \qquad [2–16]$$

where a was found to vary from 70.7 to 75.0 and $\lambda = y/x$. We can write [2–16] as

$$u/u_m = \exp[-0.693\,(y/b)^2] \qquad [2–17]$$

where $b = C_2\, x$, C_2 will vary from 0.096 t0 0.099, as a varies from 70.7 to 75.0. Albertson et al.(1950) found that

$$u/u_m = \exp\left(-\frac{y^2}{2\sigma^2}\right) \qquad [2–18]$$

where σ is the standard deviation of a Gaussian function, at $y = \sigma$ u takes the value $0.6065u_m$. Fischer et al. (1979) also used Gaussian curves for the velocity distribution

$$u/u_m = \exp[-(x/b_w)^2] \qquad [2–19]$$

where b_w is the value of x at which u takes the value $0.37u_m$. If we make some transformations and use the half–width b for characteristic length, all above equations are of the same Gaussian form

$$u/u_m = \exp(-0.693\,[x/b]^2)$$
$$= \exp(-0.693\,\eta^2) \qquad [2–20]$$

Fig. 2–3 shows the comparison of velocity profiles including Tollmien's numerical solution and Goertler's numerical solution (Rajaratnam, 1976), The Gaussian distribution matches Goertler's equation as $y/b < 1.0$, and Tollmien's equation as $y/b > 1.0$, according to Fig. 2.4 (Zijnen, 1958a), The Gaussian velocity distribution is better than Tollmien's and Goertler's equation, so the Gaussian velocity profile will be used in the theory of non–buoyant slot jets.

The following formula will be used to compare the characteristic coefficients of turbulent free jets:

$$u_m/U_o = C_1/[x/b_o]^{0.5} \qquad [2\text{–}21]$$

$$b/b_o = C_2\, x/b_o \qquad [2\text{–}22]$$

Put [2–21], [2–22] into [2–11], and divide by $Q_o = 2\, U_o\, b_o$, to obtain

$$Q(x)/Q_o = \frac{u_m b}{U_o b_o} \int_o^\infty f(\eta)\, d\eta$$

$$= C_1\, C_2\, [x/b_o]^{0.5} \int_o^\infty f(\eta) d\eta$$

So $$Q(x)/Q_o = C_3\, [x/b_o]^{0.5} \qquad [2\text{–}23]$$

where $$C_3 = C_1\, C_2 \int_o^\infty f(\eta)\, d\eta$$

From [2–14], we get the entrainment coefficient α_e

$$\alpha_e = \frac{1}{u_m} \frac{d}{dx} \int_o^\infty u\, dy$$

$$= 0.5\, C_2 \int_o^\infty f(\eta)\, d\eta \qquad [2\text{–}24]$$

Table 2.1 shows values of jet coefficients C_1, C_2, C_3, α_e given by several authors.

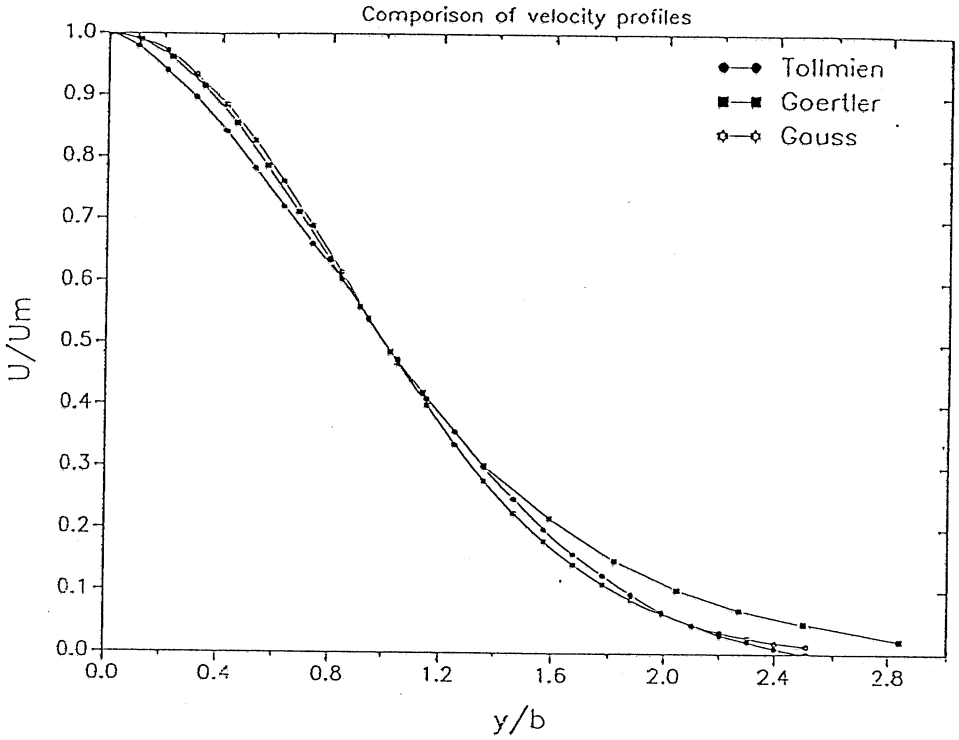

Fig. 2–3 Comparison of velocity profiles of plane turbulent free jets.

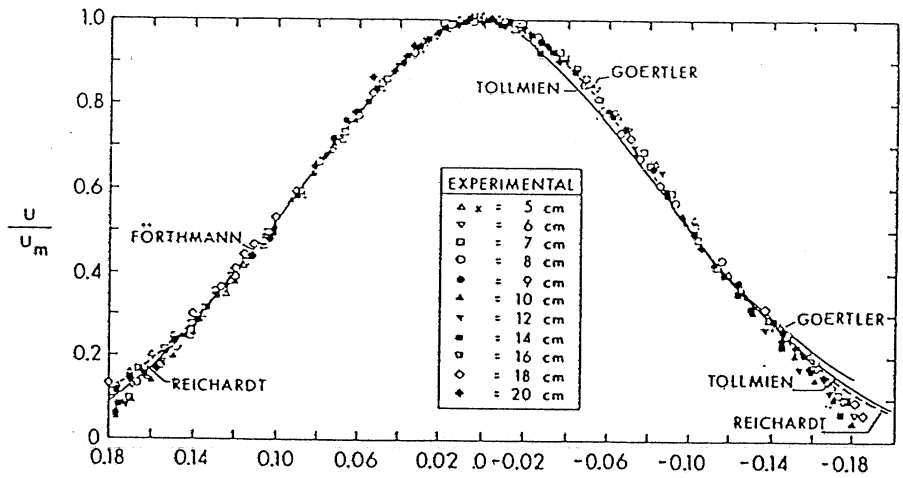

Fig. 2–4 Dimensionless velocity distribution of plane turbulent free jets (Zijnen, 1958a).

II.1.3 Comparisons

The agreement between analysis and experimental results for plane turbulent jets is good. For the analysis of non–buoyant slot jets in finite water depths (the channel discharge), we will use the concepts used for the plane turbulent free jet analysis. We will prove these to be right and useful using experimental results by Johnson & Stefan (1988). In particular we will use the following two assumptions:

(1) The transverse velocity distributions of the channel discharge are self similar and can be represented satisfactorily by a Gaussian distribution

$$u/u_m = \exp(-0.693\ \eta^2)$$

(2) The entrainment principle is applicable and the entrainment velocity v_e is proportional to the centerline velocity u_m.

$$v_e = \alpha_e\ u_m$$

These two basic assumptions will be applied for the analysis of free surface channel discharge into diverging diffusers with horizontal or sloping bottom.

Table 2.1 Jet Coefficients

Author		C_1	C_2	C_3	a_e
Abramovich (1963)		3.78	0.097	0.39	0.052
Goertler (1942)		3.30	0.114	0.41	0.060
Rajaratnam (1976)		3.50	0.100	0.37	0.053
Albertson et al. (1950)		3.22	0.128	0.44	0.068
Fischer et al. (1979)		3.41	0.097	0.35	0.051
Zijnen	0.5mm×10mm	3.51	0.096	0.36	0.051
(1958)	10mm×25mm	3.13	0.099	0.33	0.053

II.2. Slot Jet Theory for Channel Discharge into Water of Finite Constant Depth and Infinite Width

Let us consider a jet of water coming from a plane nozzle with finite water depth into a large water body with sloping angle $\beta = 0°$ (horizontal channel) and diffuser angle $\delta = 90°$. The width of inflow is B_o, the water depth of inflow is H_o. The density of the inflow water is same as the density of the ambient water. Fig. 2–5 is a schematic representation of the horizontal channel discharge. The flow has two distinct regions: a flow development region and a fully developed flow region. We will study these, respectively, using momentum integration equation.

The plane turbulent free jet has infinite water depth and a uniform velocity profile as shown in (e) of Fig. 2–6. The plane turbulent free jet has no bottom shear stress (no friction).

For the horizontal channel discharge, we must consider the effects of finite water depth. A boundary layer will form on the bottom and the velocity profile with depth will be as shown in Fig. 2–5 (b) and Fig. 2–6 (d) [dashed line], There will be a shear stress (friction) on the bottom. We will first use a simple model as shown in (c), (d) of Figure 2–6. We will analyze four cases: (A) No entrainment, no friction; (B) No entrainment, with friction; (C) Entrainment, no friction(like a plane turbulent free jet); (D) Entrainment, with friction. We will analyze the turbulent jet using the basic continuity and momentum equations.

II.2.1 Continuity and momentum equations in fully developed flow region

Using the velocity profile in the cross–section shown in Fig. 2–5 (a), write the flow rate Q(x) and momentum M(x).

$$Q(x) = 2 \int_0^\infty u(x,y)\ H_o\ dy \qquad [2\text{–}25]$$

$$M(x) = 2 \int_0^\infty \rho\ u^2(x,y)\ H_o\ dy \qquad [2\text{–}26]$$

Using the velocity similarity assumption

$$u(x)/u_m(x) = f(\eta) \qquad [2\text{–}27]$$

where $\eta = y/b(x)$ and b(x) is the full width of horizontal channel discharge shown in Fig. 2–6 (c), we get

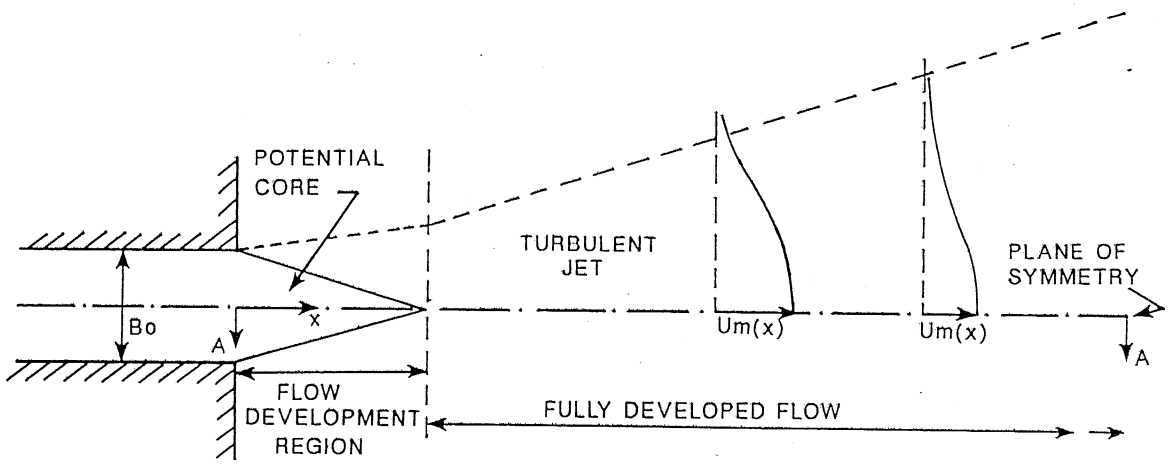

(a) PLAN VIEW

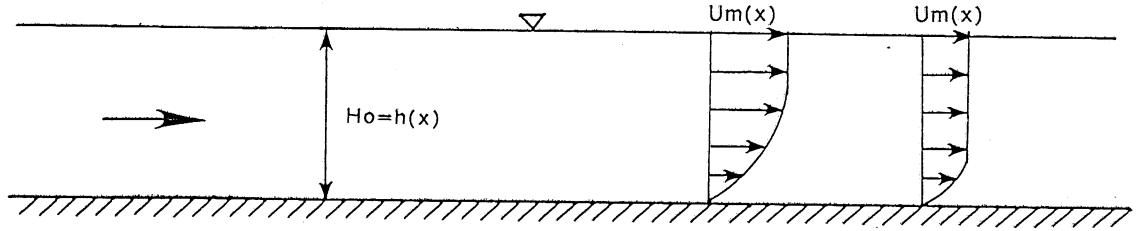

(b) SECTION A-A

Fig. 2–5 A schematic representation of horizontal channel discharge.

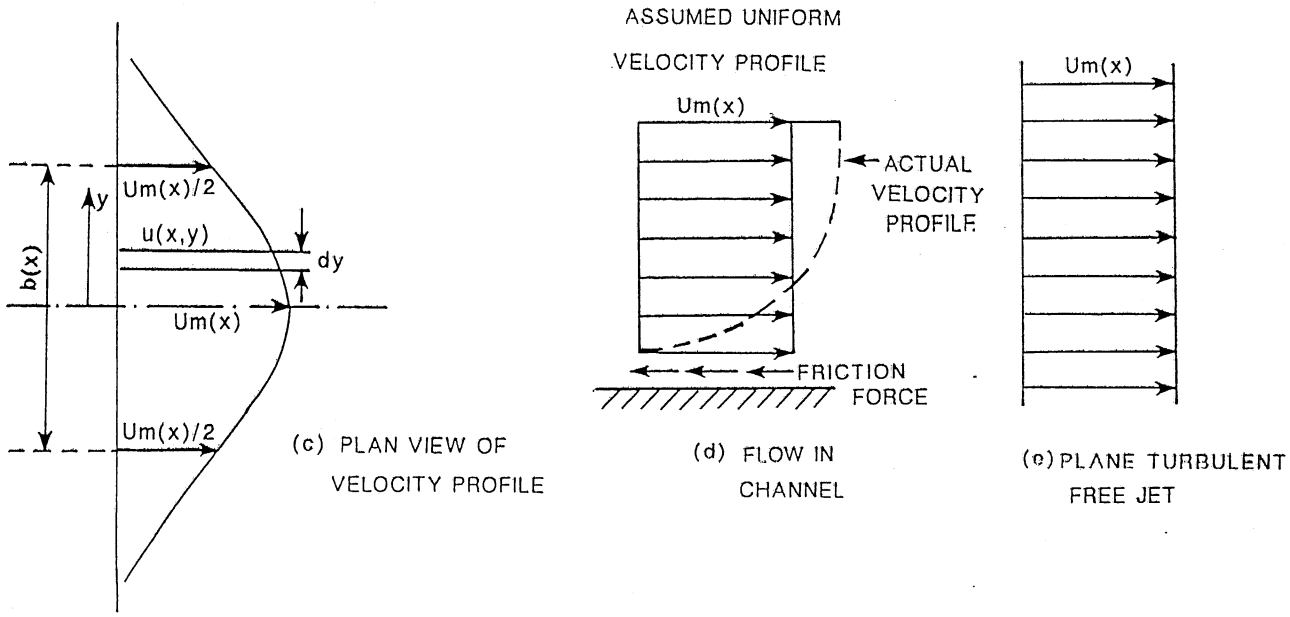

Fig. 2–6 A schematic representation of the model of jet flow over horizontal bottom with finite water depth.

$$Q(x) = 2\ H_o\ u_m(x)\ b(x) \int_0^\infty f(\eta)d\eta$$

$$= C_6\ H_o\ u_m(x)\ b(x) \qquad [2\text{–}28]$$

$$M(x) = 2\ \rho\ H_o\ u_m^2(x)\ b(x) \int_0^\infty f^2(\eta)d\eta$$

$$= C_7\ \rho\ H_o\ u_m^2(x)\ b(x) \qquad [2\text{–}29]$$

where: $$C_6 = 2 \int_0^\infty f(\eta)\ d\eta \qquad [2\text{–}30]$$

$$C_7 = 2 \int_0^\infty f^2(\eta)\ d\eta \qquad [2\text{–}31]$$

C_6, C_7 are coefficients. The rate of change of flow and momentum is

$$\frac{dQ(x)}{dx} = \frac{d}{dx}\ [\ C_6\ H_o\ u_m(x)\ b(x)\ ] \qquad [2\text{–}32]$$

$$\frac{dM(x)}{dx} = \frac{d}{dx}\ [\ C_7\ \rho\ H_o\ u_m^2(x)\ b(x)\ ] \qquad [2\text{–}33]$$

We consider four different cases according to the basic equations.

(A) No entrainment, no friction:

Suppose there is no entrainment and no friction for horizontal channel discharge. The flow rate and momentum of horizontal channel discharge should be constants, and equal to the flow rate Q_o and momentum M_o of inflow respectively. Assume the velocity of the inflow is U_o. We get

$$Q(x) = C_6\ H_o\ u_m(x)\ b(x)$$
$$= U_o\ B_o\ H_o$$
$$= Q_o \qquad [2\text{–}34]$$

$$M(x) = C_7\ \rho\ H_o\ u_m^2(x)\ b(x)$$
$$= \rho\ H_o\ U_o^2\ B_o$$
$$= M_o \qquad [2\text{–}35]$$

Solving [2–34] and [2–35], we get:

$$\mathbf{u_m(x)/U_o = A_o} \qquad \mathbf{[2\text{–}36]}$$

$$\mathbf{b(x)/B_o = A_1} \qquad \mathbf{[2\text{–}37]}$$

where: $$A_0 = \frac{\int_0^\infty f(\eta)\, d\eta}{\int_0^\infty f^2(\eta)\, d\eta} \qquad [2\text{–}38]$$

$$A_1 = \frac{\int_0^\infty f^2(\eta)\, d\eta}{2\,[\int_0^\infty f(\eta)\, d\eta]^2} \qquad [2\text{–}39]$$

No entrainment for horizontal channel discharge is an unrealistic case. $f(\eta)$ is not a Gaussian distribution, $f(\eta)$ should be

$$f(\eta) = 1 \qquad \eta = 0 \text{ to } 0.5$$

$$f(\eta) = 0 \qquad \eta > 0.5 \qquad [2\text{–}40]$$

so we get $A_0 = 1.0$, $A_1 = 1.0$. The centerline velocity u_m of the horizontal channel discharge is equal to the inflow velocity U_0 and the full width $b(x)$ is equal to the inflow width B_0.

(B) No entrainment, with friction

We use the local friction coefficient c_f to represent the effect of friction, so the shear stress τ_0 on the bottom is defined as (Schlichting, 1960, Chapter *XXI*)

$$\tau_0 = \frac{1}{2}\, c_f\, \rho\, U_\infty^2 \qquad [2\text{–}41]$$

For jet flow, U_∞ is not a constant, U_∞ should be the water surface velocity $u(x,y)$. we should write the shear stress as:

$$\tau_0(x,y) = \frac{1}{2}\, c_f\, \rho\, u^2(x,y) \qquad [2\text{–}42]$$

Because of the shear stress on the bottom, the rate of change of the momentum in a cross–section is equal to the total local friction drag D_x.

$$\frac{dM(x)}{dx} = -\, D_x$$

$$= -2 \int_0^\infty \tau_0(x,y)\, dy$$

$$= -\, c_f\, \rho\, u_m^2(x)\, b(x) \int_0^\infty f^2(\eta) d\eta \qquad [2\text{–}43]$$

The momentum of jet flow decreases in flow direction because of the friction. Suppose c_f to be a constant, according to [2–33] and [2–43], we get

$$-c_f \rho u_m^2(x) b(x) \int_0^\infty f^2(\eta) d\eta = \frac{d}{dx} [C_7 \rho H_o u_m^2(x) b(x)]$$

So we get

$$-\frac{c_f}{2H_o} = \frac{d}{dx} \{ \ln[C_7 \rho H_o u_m^2(x) b(x)] \} \qquad [2–44]$$

Solving [2–34] and [2–44], we get

$$u_m(x)/U_o = A_o \exp(-\frac{c_f}{2H_o} x) \qquad [2–45]$$

$$b(x)/B_o = A_1 \exp(\frac{c_f}{2H_o} x) \qquad [2–46]$$

A_o and A_1 are again equal to 1.0. We find that $u_m(x)$ will decrease as an exponential function of x and b(x) increases as an exponential function of x as shown in Fig. 2–7. c_f and H_o affect $u_m(x)$ and b(x) strongly.

(C) Entrainment, no friction

To account for entrainment of the horizontal channel discharge, we use the entrainment hypothesis [2–13]. The rate of change of flow rate is equal to the flow rate coming from ambient water

$$\frac{dQ(x)}{dx} = \frac{d}{dx} [C_6 H_o u_m(x) b(x)]$$

$$= 2 v_e H_o$$

$$= 2 \alpha_e u_m(x) H_o$$

So we get

$$\frac{d}{dx} \{ \ln[C_6 H_o u_m(x) b(x)] \} b(x) = 2 \frac{\alpha_e}{C_6} \qquad [2–47]$$

Suppose the entrainment coefficient α_e to be a constant, solving equations [2–35] and [2–47], we get

$$u_m(x)/U_o = [\frac{A_o}{4\alpha_e}]^{0.5} / [x/B_o]^{0.5} \qquad [2–48]$$

$$b(x)/B_o = \frac{2\alpha_e}{A_2} \frac{x}{B_o} \qquad [2–49]$$

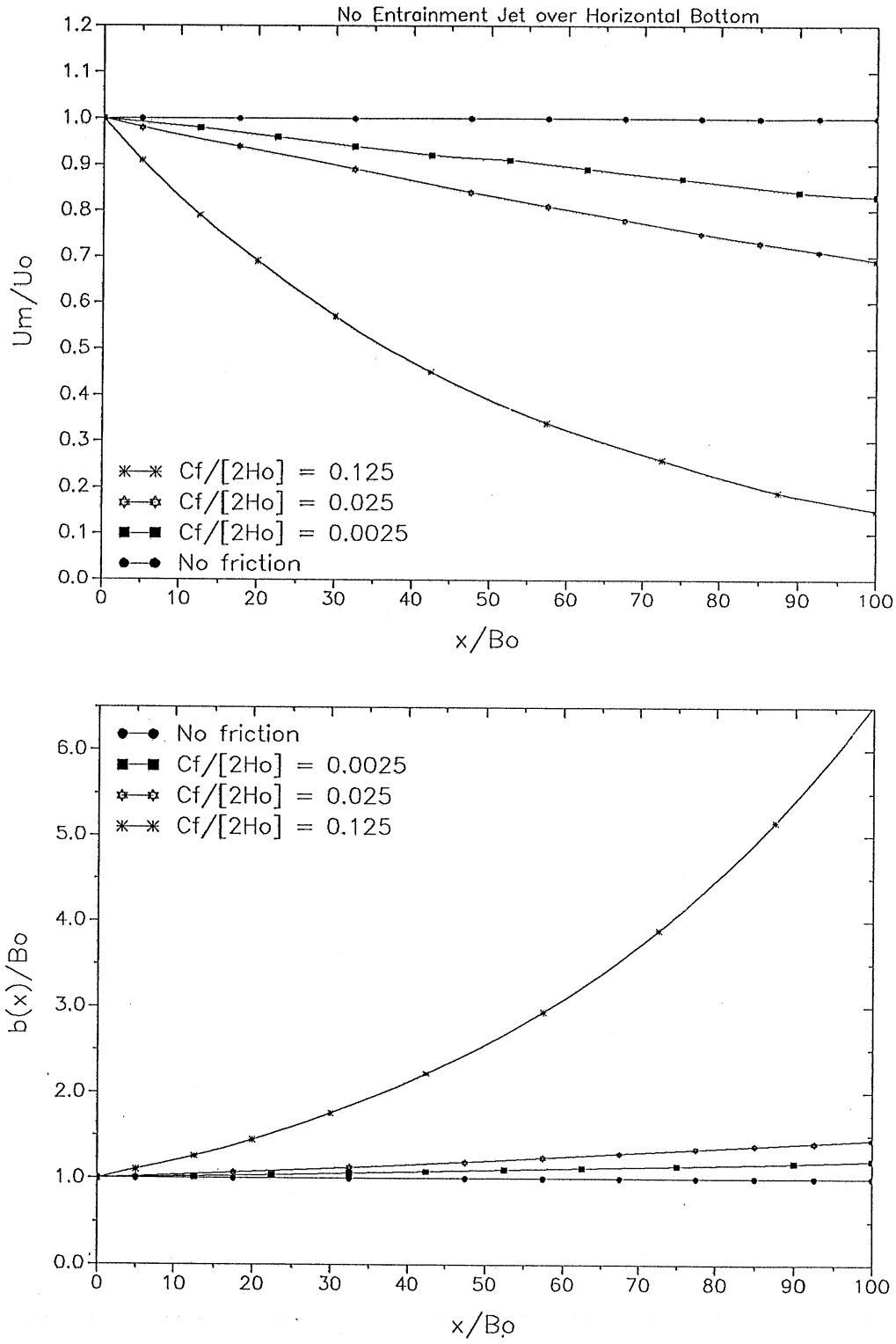

Fig. 2–7 Dimensionless centerline velocity and width of a non–entraining jet over a horizontal bottom with friction.

We use the Gaussian velocity distribution [2–17] and make the transformation $b(x) = 2b$.

$$f(\eta) = \exp(-2.772\ \eta^2) \qquad [2\text{–}50]$$

Then we get

$$A_2 = \int_0^\infty f(\eta)\ d\eta = \int_0^\infty e^{-2.772\eta^2}\ d\eta = 0.53229 \qquad [2\text{–}51]$$

$$A_3 = \int_0^\infty f^2(\eta)\ d\eta = \int_0^\infty e^{-5.544\eta^2}\ d\eta = 0.37639 \qquad [2\text{–}52]$$

From [2–38], [2–39], we get:

$$A_0 = 1.4142 \qquad [2\text{–}53]$$

$$A_1 = 0.6642 \qquad [2\text{–}54]$$

with these constants and an entrainment coefficient $\alpha_e = 0.053$ (Rajaratnam, 1976, see Table 2.1) to [2–48], [2–49], we get

$$u_m(x)/U_o = 3.65/[x/b_o]^{0.5} \qquad [2\text{–}55]$$

$$b(x)/b_o = 0.0996\ x/b_o \cong 0.10\ x/b_o \qquad [2\text{–}56]$$

The comparison between the theoretical results and the experimental data for the plane turbulent free jet is good as is shown in Fig. 2–8 and Fig. 2–9.

(D) Entrainment, with friction:

To account for simultaneous entrainment and friction by the horizontal channel discharge we solve [2–44] and [2–47]. we get

$$\frac{du_m(x)/U_o}{dx} + A_4\ \frac{u_m(x)}{U_o} + A_5\ \exp(A_4 x)\ \left[\frac{u_m(x)}{U_o}\right]^3 = 0 \qquad [2\text{–}57]$$

$$\frac{b(x)}{B_o} = \left[\frac{U_o}{u_m(x)}\right]^2 \frac{\exp(-A_4 x)}{2A_3} \qquad [2\text{–}58]$$

where:
$$A_4 = \frac{c_f}{2H_o} \qquad [2\text{–}59]$$

$$A_5 = 2\ \frac{\alpha_e}{A_o B_o} \qquad [2\text{–}60]$$

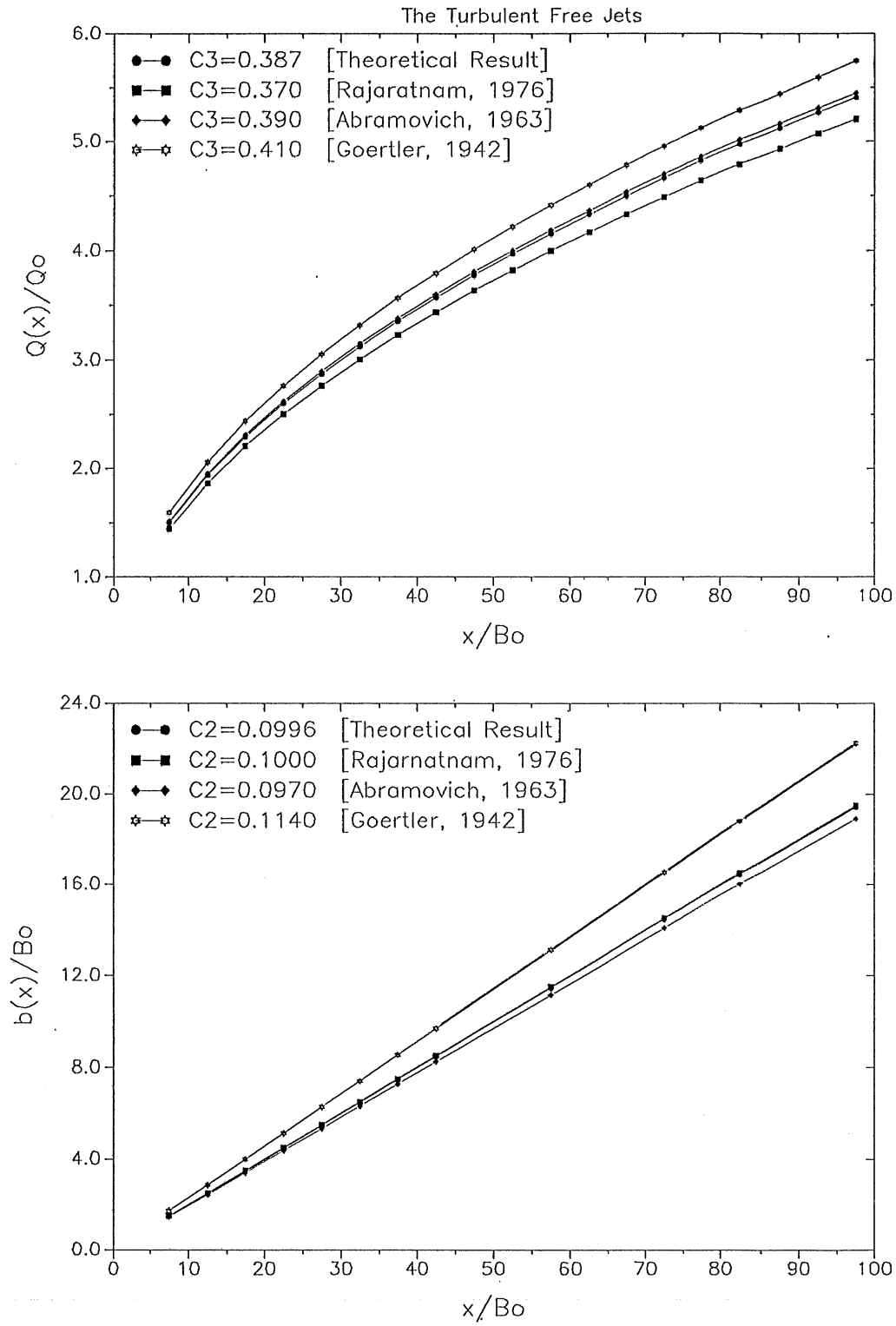

Fig. 2–8 Comparison of dilution $Q(x)/Q_o$ and dimensionless width $b(x)/B_o$ of plane turbulent free jets.

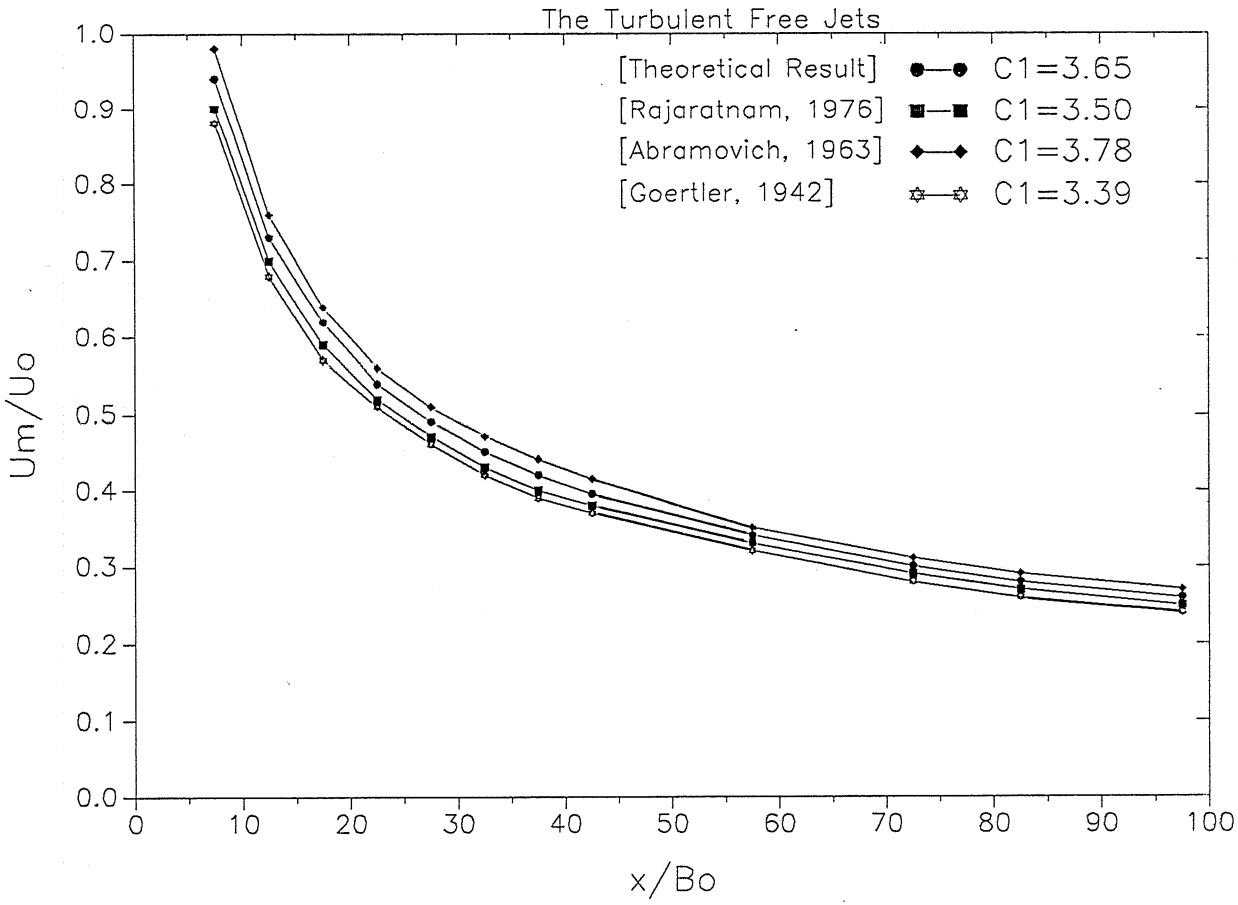

Fig. 2–9 Comparison of dimensionless centerline velocity of planeturbulent free jets.

The initial conditions of the differential equation [2–57] are:

$$x = 0.0, \quad u_m(x)/U_o = 1.0$$

Using the fourth–order Runge–Kutta methods, we can get a numerical solution for $u_m(x)/U_o$ from the differential equation [2–57], then get $b(x)/B_o$ from [2–58]. For flow with entrainment and friction, specification of values for the coefficients c_f and α_e is important in order to compare the theoretical results with experimental results. We will specify these two coefficients in section II.2.2

II.2.2 Local friction coefficient and entrainment coefficient

In applications of the above theory of non–buoyant slot jets in finite water depths, we need to specify the appropriate local friction coefficients for both experimental conditions and natural field situations.

The bottom shear stresses can be represented as a function

$$\tau_o = F(V, L, \rho, \mu, e)$$

where V is a characteristic velocity, i.e. the mean velocity in a pipe flow, or the free stream velocity U_∞ for flow over a flat plate; L is a characteristic length, i.e. the diameter of a pipe, or water depth in an open channel; ρ is the density of water; μ is the viscosity; e is a mean height of the roughness projections.

By the methods of dimensional analysis it may be easily shown that (Vennard & Street, 5th edition):

$$\tau_o = F'(\frac{VL\rho}{\mu}, \frac{e}{L})\ \rho V^2$$

and, by comparison with equation [2–42],

$$c_f = F''(R_e, \frac{e}{L}) \qquad [2–61]$$

where Re = Reynolds number of the flow = $\frac{VL}{\nu}$, ν is the kinematic viscosity. The friction factor depends only upon the Reynolds number Re of flow and upon the ratio e/L, called the relative roughness of the channel bottom.

In the experiments of Johnson et al. (1988) the experimental facility was intended to model an inflow to a lake or reservoir and to study the plunging flow. Several experiments of non–buoyant free jet flow over a horizontal bottom ($\beta = 0.0°$) and with a the diffuser angle $\delta = 90°$ were

also conducted. The experimental facility was shown schematically in Fig. II–1 (Johnson and Stefan, 1988). **The experimental water depth H_0 was about 0.3ft**; the bottom roughness of the main tank was lower than cast iron, and higher than galvanized iron. The mean roughness height e is about 0.2mm (0.00065 ft) using Fig. 9.6 of Vennard & Street, 5th edition as a guide.

In the experiments (Johnson and Stefan,1988), $9.5\times10^3 \leq Re_0 \leq 1.2\times10^4$, where $\frac{U_0H_0}{\nu}$ is Reynolds number of inflow. We use 1.1×10^4 to estimate the friction coefficient c_f. According to Fig. 21.11 and Fig. 21.12 for skin friction of a flat plate at zero incidence (Schlichting, 1960, Chapter *XXI*), the local friction factor c_f can be determined by the local Reynolds number $Re_x = U_\infty x/\nu$ and the local relative roughness $\frac{x}{k_s} = \frac{x}{e}$. For a slot jet, U_∞ should be the water surface velocity which changes with x. We will therefore analyze c_f of the inflow and at the end of the main tank.

For the inflow of slot jet, x should be the length of rectangular channel in front of main tank (6 ft). We get

$$\begin{aligned} \text{Re(inflow)} &= \frac{U_0 x}{\nu} = \frac{U_0 H_0}{\nu}\frac{x}{H_0} \\ &= 1.1\times10^4 * \frac{6.0}{0.3} \\ &= 2.2\times10^5 \end{aligned}$$

For outflow, the diffuser length should be x = 16.0 + 6.0 = 22.0 ft, we get

$$\text{Re(outflow)} = \frac{u_m\, x}{\nu} = \frac{u_m\, H_0}{\nu} * \frac{22.0}{0.3}$$

where u_m is the centerline velocity at the end of diffuser, according to further computation [next section], $u_m(\text{outflow}) \cong 20\%\ U_0$. So the Reynolds number of outflow is equal to

$$R_e(\text{outflow}) = 1.6\times10^5$$

From Fig. 21.12 (Schlichting, 1960), the experimental flow region of Johnson is in the region of a smooth flat plate where c_f is independent of the relative roughness. c_f is from 0.0048 to 0.0052, so we will use the average value

$$c_f = 0.005 \qquad [2\text{–}62]$$

in order to compare the theoretical results to experimental data. The entrainment coefficient α_e in Table 2.1 are all specified from coefficient C_1, C_2 and the velocity profile. For theoretical analysis, coefficient C_1, C_2 are unknown. **We can fit the experimental data (Johnson and Stefan, 1988) to get α_e.** The entrainment velocity v_e distribution with depth should be similar to the velocity distribution in the boundary layer, which is approximated by the 1/n–th–power velocity distribution. The entrainment velocity v_e at the

water surface is largest, the total entrainment coefficient α_e for entire depth should be less than that of the turbulent free jet [0.053]. The fitted results are shown in Fig. 2–10. If the aspect ratio AR_o is equal to 0.5, the experimental data fits the theoretical result with α_e= 0.04, but if AR_o = 1.8, the experimental data does not fit the theoretical curve; otherwise we need consider the error of experimental measurement, so we get Equation [2–63] as the fitted result:

$$\alpha_e = 0.04 \qquad [2\text{–}63]$$

II.2.3 The flow development region

Fig. 2–11 is a definition sketch of the flow–development region. The potential core is a wedge–like region with the mean velocity U_o. Outside of the potential core is the turbulent shear layer. x_o is the length of the potential core. y_1 is the half width of the potential core.

II.2.3.1 Continuity and momentum equations

The velocity in the potential core is the inflow velocity U_o. The velocity distribution in the turbulent shear layers outside of the potential core can be represented by a Gaussian function [2–17] (Rajaratnam,1976). The flow rate at a cross–section can be written as

$$\begin{aligned} Q(x) &= 2U_o y_1(x) H_o + 2 \int_{y_1}^{\infty} u(x,y)dy \; H_o \\ &= 2U_o H_o[\, y_1(x) + A_6 \, b_o(x)] \end{aligned} \qquad [2\text{–}64]$$

where: $$A_6 = \int_0^{\infty} f(\xi) \, d\xi \qquad [2\text{–}65a]$$

$$\begin{aligned} u(x,y) &= U_o \, f(\xi) \\ \xi &= [y - y_1(x)]/b_o(x) \\ f(\xi) &= \exp(-0.693 \; \xi^2) \end{aligned} \qquad [2\text{–}65b]$$

where $b_o(x)$ = half–width of the shear layer in the flow development region (Fig. 2–11). The full–width b(x) of jet flow in the flow development region is

$$b(x) = 2.0 \; [\; b_o(x) + y_1(x) \;] \qquad [2\text{–}66]$$

Using the entrainment principle, we obtain

$$\frac{dQ(x)}{dx} = 2v_e H_o = 2\alpha_e U_o H_o \qquad [2\text{–}67]$$

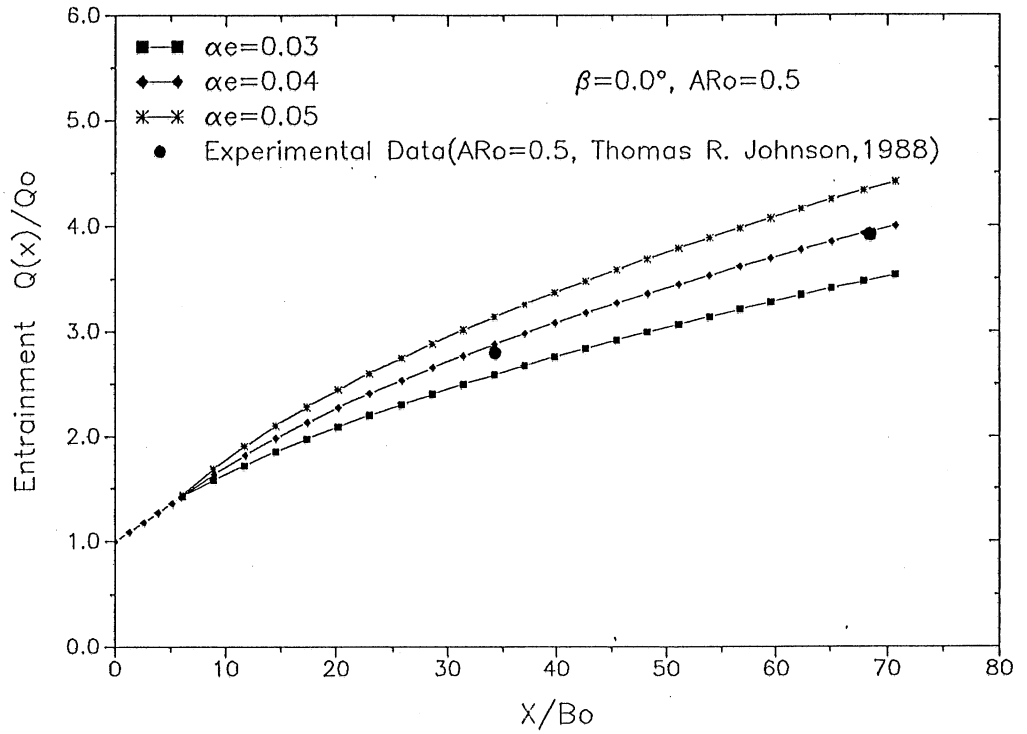

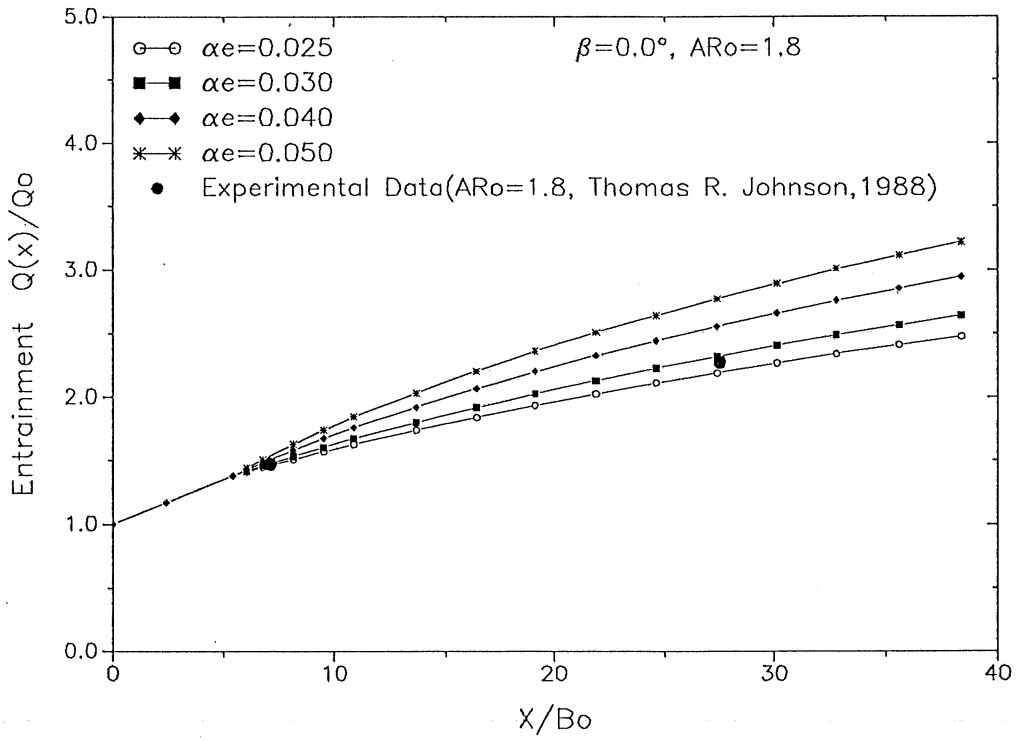

Fig. 2–10 Fitting of experimental data to obtain entrainment coefficient α_e.

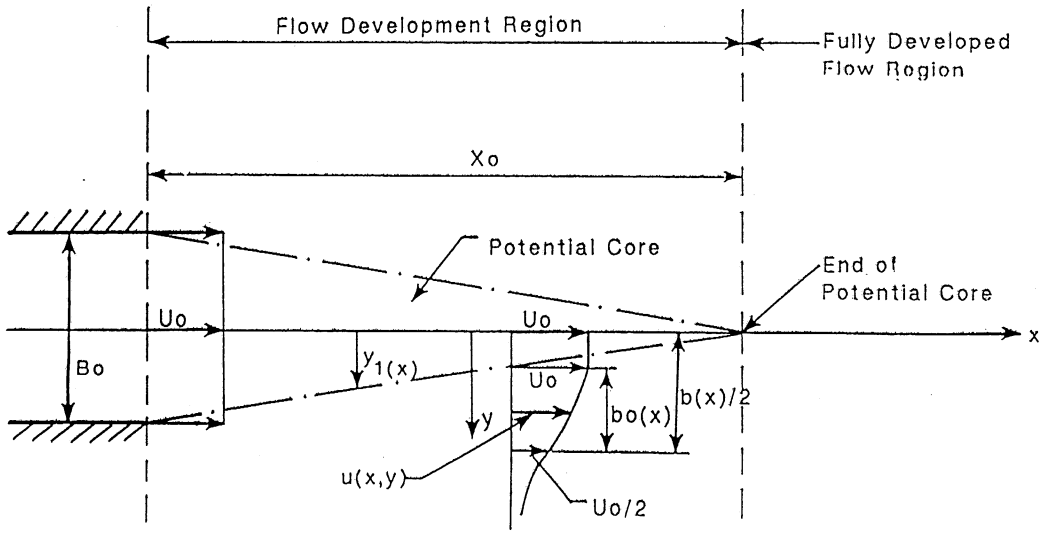

Fig. 2–11 Definition sketch of flow–development region of jet flows

where $\alpha_e{}^o$ is entrainment coefficient in the flow development region. With [2–64] into [2–67]

$$\frac{dy_1(x)}{dx} + \frac{d}{dx}[A_6 b_o(x)] = \alpha_e{}^o \qquad [2–68]$$

The momentum can be written as

$$M(x) = 2\rho U_o^2 H_o y_1(x) + b_o(x) \int_{y_1}^{\infty} \rho u^2(x,y) H_o \, dy$$

$$= 2\rho U_o^2 H_o [y_1(x) + A_7 b_o(x)] \qquad [2–69]$$

where $$A_7 = \int_0^{\infty} f^2(\xi) \, d\xi \qquad [2–70]$$

Now consider two cases: (A) without friction; (B) with friction.

(A) Without friction in the flow development region

Without friction in the flow development region, the momentum in the direction x should be constant and equal to the momentum of the inflow.

$$2\rho U_o^2 b_o H_o = 2\rho U_o^2 H_o \, [y_1(x) + A_7 b_o(x)] \qquad [2–71a]$$

$$b_o = y_1(x) + A_7 b_o(x) \qquad [2–71b]$$

Equation [2–71b] is derived as follows:

$$\frac{dy_1(x)}{dx} + \frac{d}{dx}[A_7 b_o(x)] = 0 \qquad [2–71c]$$

Solving [2–68] and [2–71c], we obtain

$$b_o(x) = \frac{\alpha_e{}^o}{A_6 - A_7} x + B_7 \qquad [2–72a]$$

$$y_1(x) = b_o - A_7 b_o(x) \qquad [2–72b]$$

where B_7 is a constant. The initial condition of the differential equation [2–71] is $b_o(0) = 0$, $y_1(0) = b_o$, B_7 must be equal to zero. The length x_o of the flow development region is given by the condition $y_1(x) = 0$ where $x = x_o$.

$$y_1(x) = b_o - \frac{A_7 \alpha_e{}^o}{A_6 - A_7} x_o = 0 \qquad [2–73]$$

The length x_o of the potential core is

$$x_o = \frac{A_6 - A_7}{A_7 \alpha_{e^o}} b_o \qquad [2\text{–}74]$$

where $$A_6 = \int_0^\infty e^{-0.693\xi^2} d\xi = 1.065 \qquad [2\text{–}75a]$$

$$A_7 = \int_0^\infty e^{-1.386\xi^2} d\xi = 0.753 \qquad [2\text{–}75b]$$

From equation [2–74], x_o/B_o is independent of aspect ratio AR_o in the flow development region without friction.

(B) With friction in the flow development region

The rate of change of momentum with x is equal to the local total friction force. Using [2–42], we get

$$\frac{dM(x)}{dx} = -D_x$$

$$= -2\int_0^\infty \frac{1}{2} c_f \rho u^2(x,y) dy$$

$$= -2[\frac{1}{2} c_f \rho U_o^2 y_1(x) + \int_{y_1}^\infty \frac{1}{2} c_f \rho u^2(x,y)\, dy]$$

$$= -c_f \rho U_o^2 [y_1(x) + A_7 b_o(x)]$$

$$= 2\rho U_o^2 H_o \{\frac{dy_1(x)}{dx} + \frac{d}{dx}[A_7 b_o(x)]\} \qquad [2\text{–}76a]$$

From [2–76a], we write:

$$-\frac{C_f}{2H_o}[y_1(x) + A_7 b_o(x)] = \frac{dy_1(x)}{dx} + \frac{d}{dx}[A_7 b_o(x)] \qquad [2\text{–}76b]$$

Solving equation [2–71] and [2–76b], we obtain two differential equations

$$(A_6 - A_7)\frac{db_o(x)}{dx} = \alpha_{e^o} + \frac{C_f}{2H_o}[y_1(x) + A_7 b_o(x)] \qquad [2\text{–}77a]$$

$$\frac{A_7 - A_6}{A_6} \frac{dy_1(x)}{dx} = \frac{A_7}{A_6} \alpha_{e^o} + \frac{C_f}{2H_o}[y_1(x) + A_7 b_o(x)] \qquad [2\text{–}77b]$$

Using a 4th order Runge–Kutta method, we can get a numerical solution.

II.2.3.2 Comparison of analytical results with experimental data

With reference to Fig. 2–12, the flow rate at a distance x from the nozzle can be written as

$$Q(x) = 2H_0 \left[U_0 (x_0 - x) \tan \alpha_1 + U_0 b_0(x) \int_0^\infty f(\xi) d\xi\right] \qquad [2–78a]$$

where $f(\xi) = u(x,y)/U_0$ and $\xi = (y-y_1)/b_0(x)$. $f(\xi)$ is represented, for convenience, as a Gaussian profile [2–17]. we have the relationship

$$B_0 = 2 x_0 \tan \alpha_1$$

$$b_0(x) = C_0 x$$

With inflow rate $Q_0 = U_0 B_0 H_0$, we get

$$Q(x)/Q_0 = 1.0 + 2 (C_0 A_6 - \tan \alpha_1) \frac{x}{B_0} \qquad [2–78b]$$

Comparing [2–78b] with [2–67], We can therefore say that the entrainment coefficient $\alpha_e{}^o$ in the flow–development region is

$$\alpha_e{}^o = C_0 A_6 - \tan \alpha_1 \qquad [2–79]$$

Experimental observations of the plane turbulent shear layer have been made by Reichardt (1942), Lipemann and Laufer (1947), Albertson et al. (1950), and Wygnanski and Fiedler (1970). Albertson et al. (1950) found experimentally that:

$$x_0/B_0 = 5.175 \qquad [2–80a]$$

$$\alpha_1 = \tan^{-1}(1/10.4) = 5.49° \qquad [2–80b]$$

$$Q(x)/Q_0 = 1.0 + 0.080 (x/B_0) \qquad [2–80c]$$

We know $\frac{dQ(x)}{dx} = 2 \alpha_e{}^o U_0 H_0$. From the entrainment principle, it is easy to show that

$$\alpha_e{}^o = 0.04$$

$$b_0(x) = 0.128 x$$

Using $\alpha_e{}^o = 0.040$, Comparison of the analytical results with experimental data, equation [2–74] gives

$$x_0/B_0 = 5.18 \qquad [2–81a]$$

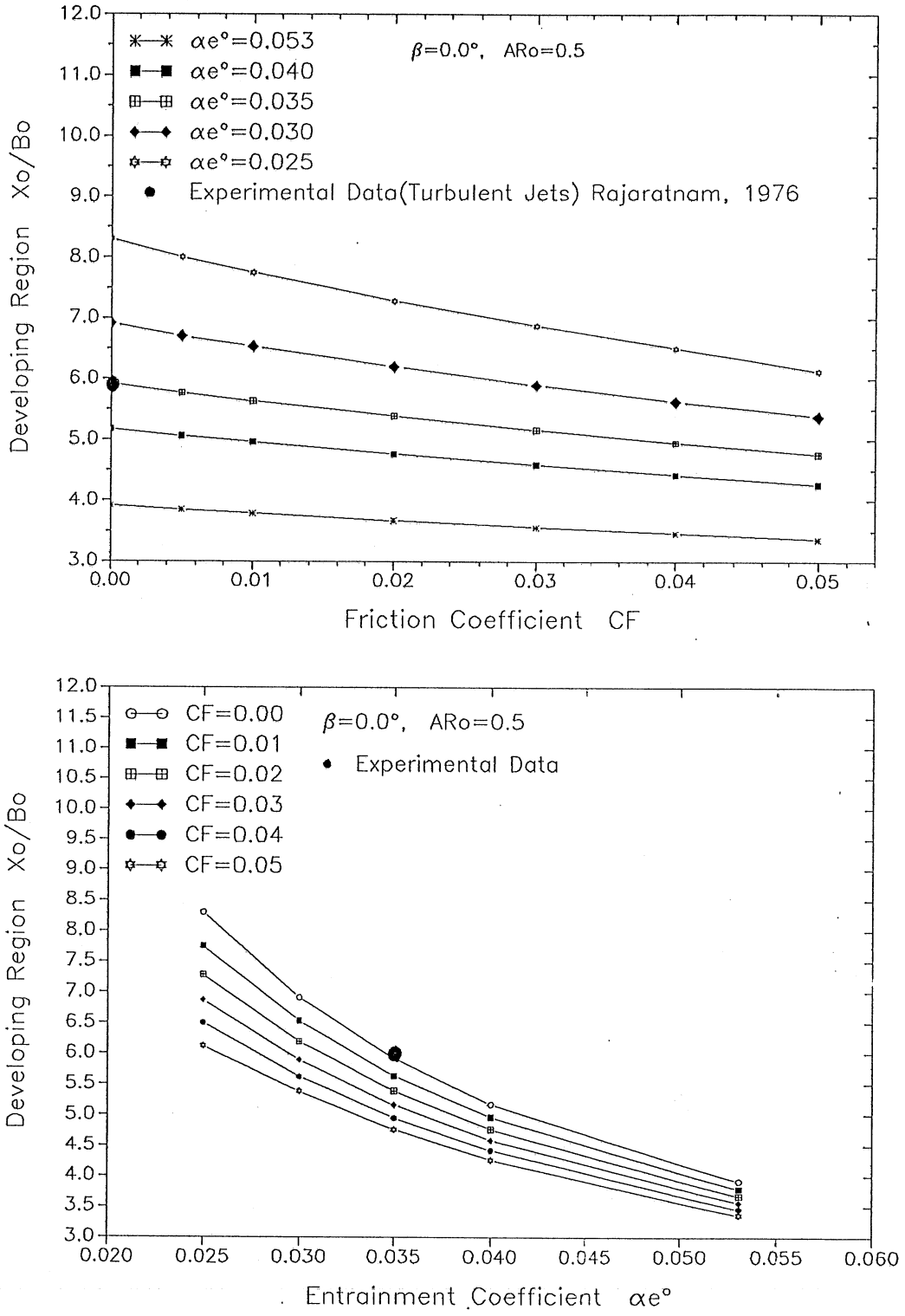

Fig. 2–12 Sensitivity of dimensionless length x_o/B_o of developing region to friction coefficient and entrainment coefficient at $AR_o = 0.5$.

From experimental observations of the plane turbulent shear layer, Rajaratnam (1976) found

$$x/B_0 = 0.5 \tan \alpha_1 = 0.5 \tan 4.8^\circ = 6.0 \qquad [2\text{–}81b]$$

$$Q(x)/Q_0 = 1 + 0.070\ x/B_0 \qquad [2\text{–}81c]$$

We can say that $\alpha_e{}^o = 0.035$. Using $\alpha_e{}^o = 0.035$, comparison of the analytical results with experimental data, equation [2–74] gives

$$x_0/B_0 = 5.92$$

$$\alpha_1 = \tan^{-1}[1.0/11.84] = 4.83^\circ \qquad [2\text{–}81d]$$

The model solutions fit very well Rajaratnam's (1976) and Albertson's (1950) experimental data. **So in the flow development region, the entrainment coefficient of the shear layer is assumed constant and equal to 0.035 (Rajaratnam, 1976).**

The above theoretical solutions and experimental data are with no friction in the flow development region (plane turbulent free jet). For jet flow with finite water depth, the length x_0 of the flow development region depends on the local friction coefficient c_f and the entrainment coefficient $\alpha_e{}^o$.

Some useful results from the numerical solution of equations [2–77a] and [2–77b] are as follows: Fig. 2–12 (top) shows changes of the length x_0/B_0 in the flow development region with friction coefficient c_f at $AR_0 = 0.5$. As c_f increases, x_0/B_0 decreases because the friction causes a loss of inflow momentum and therefore makes the potential core disappear earlier. x_0/B_0 is not very sensitive to the local friction coefficient, especially as $\alpha_e{}^o$ is lager. In Fig. 2–12 (bottom) it was shown that x_0/B_0 is sensitive to the entrainment coefficient at $AR_0 = 0.5$. With larger entrainment more surrounding water to the turbulence penetrates more rapidly towards the axis, so that the potential core disappears earlier.

Fig. 2–13 shows the relationship between x_0/B_0 and friction coefficient c_f at $AR_0 = 20$. If AR_0 is large, even though x_0 increases, x_0/B_0 decreases. The theoretical results for the flow development region clearly show changes of x_0/B_0 with entrainment and friction.

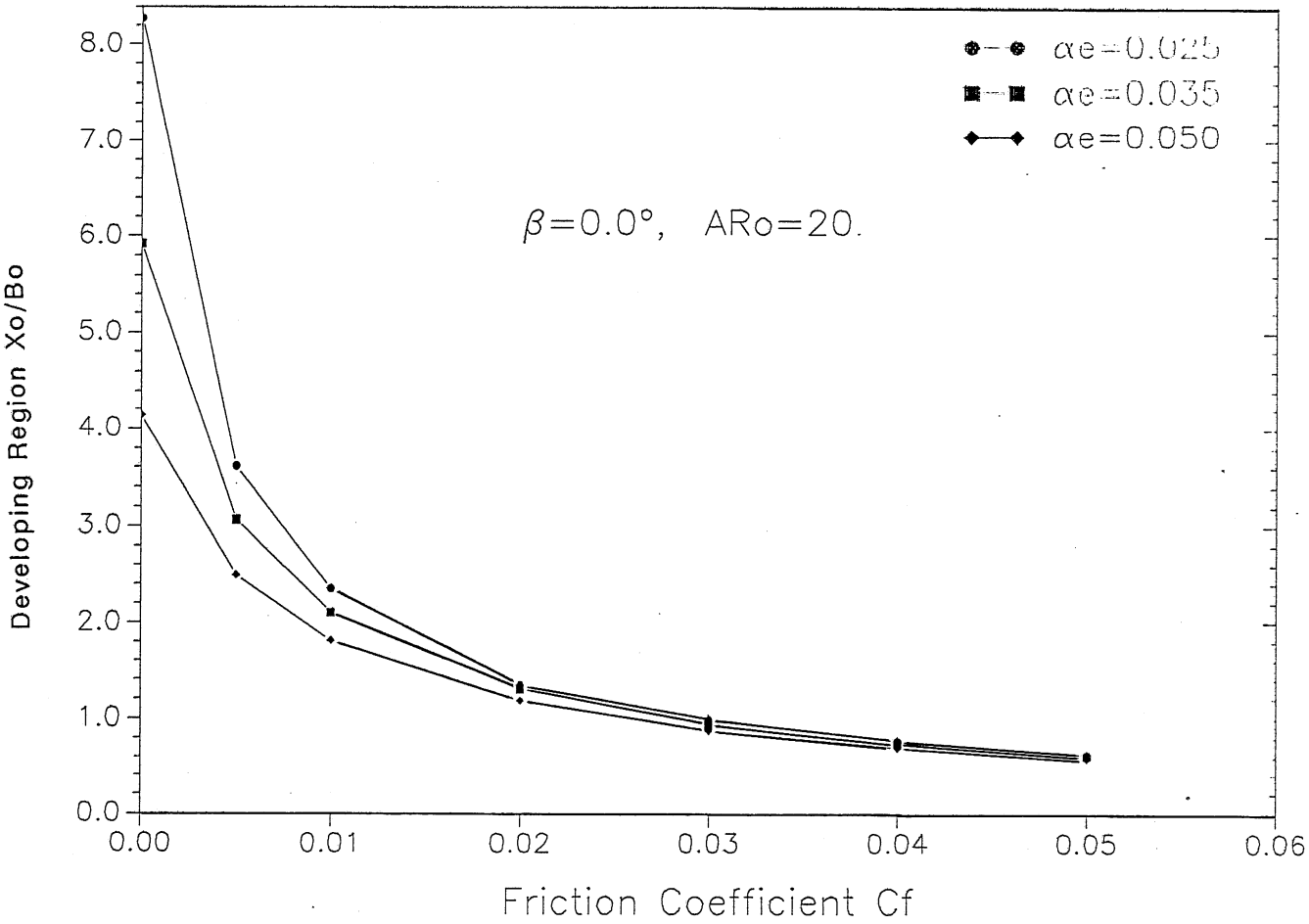

Fig. 2–13 Relationship between x_o/B_o and friction coefficient c_f at AR_o=20.

II.2.4 Model synthesis and sensitivity analysis

By combining the flow development region with the fully developed flow region, the model of jet flow over a horizontal bottom with finite water depth is formed. In order to combine the two parts, some modifications of the initial condition of the differential equations in the fully developed flow region, i.e., equations [2–47] and [2–57], are needed. The initial conditions should be:

$$x = x_0: \qquad u_m(x) = U_0$$

$$b(x) = b_0(x_0)$$

Equation [2–48] and [2–49] become:

$$u_m(x)/U_0 = [1 + \frac{4\alpha_e}{A_0 B_0}(x - x_0)]^{-0.5}$$

$$b(x)/B_0 = \frac{1}{2A_3} + 2\frac{\alpha_e}{A_2}(x - x_0)$$

The sensitivity of the model of jet flow over a horizontal bottom with finite water depth is shown in Fig. 2–14 to Fig. 2–22. The effects of inflow channel aspect ratio AR_0, entrainment coefficient α_e and friction factor c_f are illustrated.

As the aspect ratio AR_0 is very large, entrainment in the fully developed flow region is small as is shown in Fig. 2–14. Dimensionless width $b(x)/B_0$ and centerline velocity $u_m(x)/U_0$ of jet flow changes rapidly as is shown in Fig. 2–15. A relationship of $b(x)$ versus x as AR_0 increases is shown in Fig. 2–16. The potential core increases and curves of $b(x)$ versus x are parallel lines in the flow–development and fully developed flow regions as AR_0 increases.

Dilution $Q(x)/Q_0$ and dimensions of jet flow is sensitive to the entrainment coefficient α_e shown in Fig. 2–17 to 2–20. As α_e increases more ambient water is entrained by the jet, and width of the jet increases.

Fig. 2–20 and Fig. 2–22 show the relationship between dilution, and dimensions of jet and the local friction coefficient c_f. As c_f increases, dilution and centerline velocity decrease because the friction causes a loss of inflow momentum. Width $b(x)$ increases slowly. For field situations, the local friction coefficient varies generally hence dilution and dimensions of the jet are sensitive to the friction coefficient on the bottom as AR_0 is large. Overall the integral model gives much useful information for jet flow over horizontal bottom with finite depth.

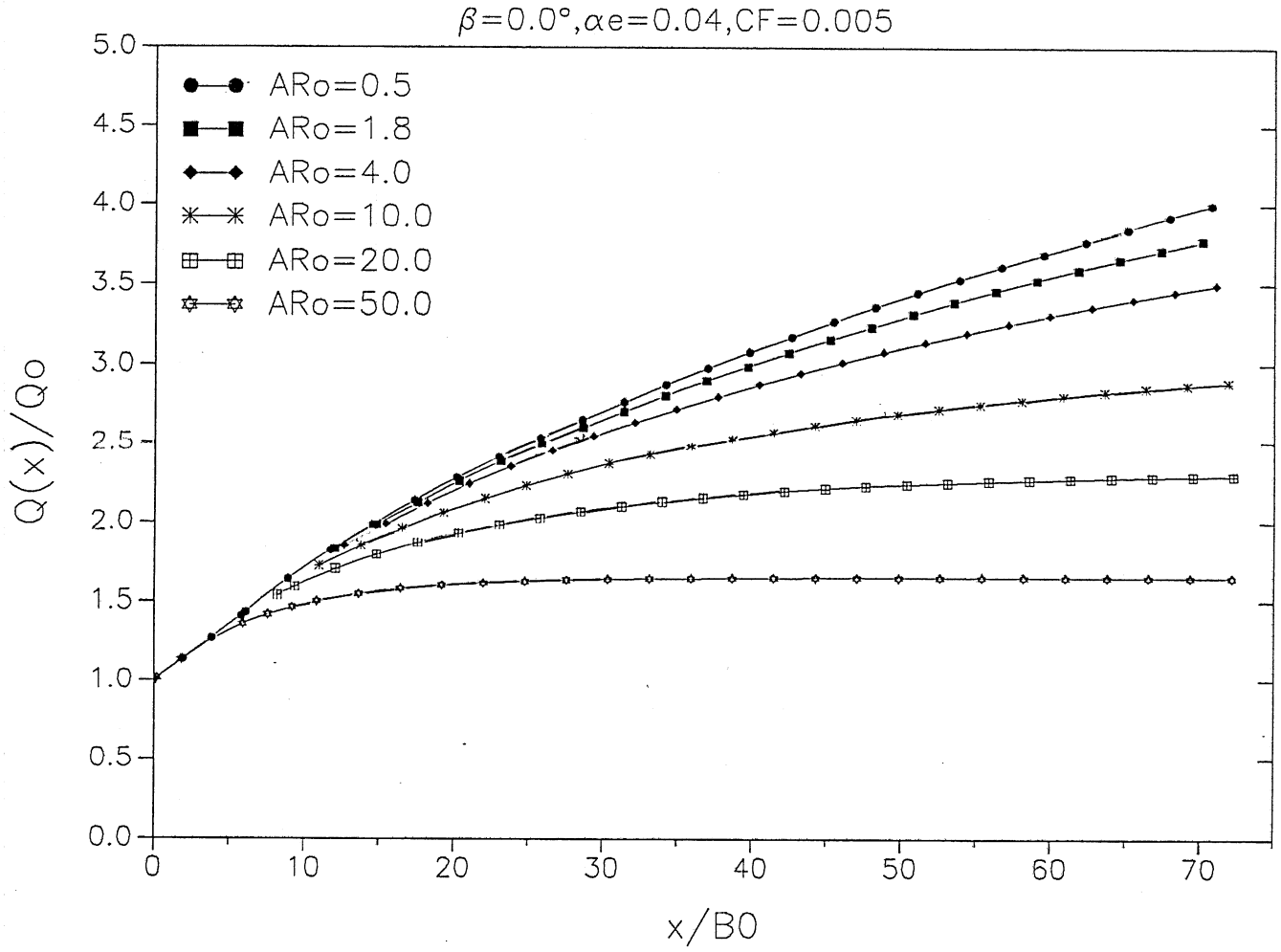

Fig. 2–14 Dilution $Q(x)/Q_0$ versus x/B_0 as AR_0 increases.

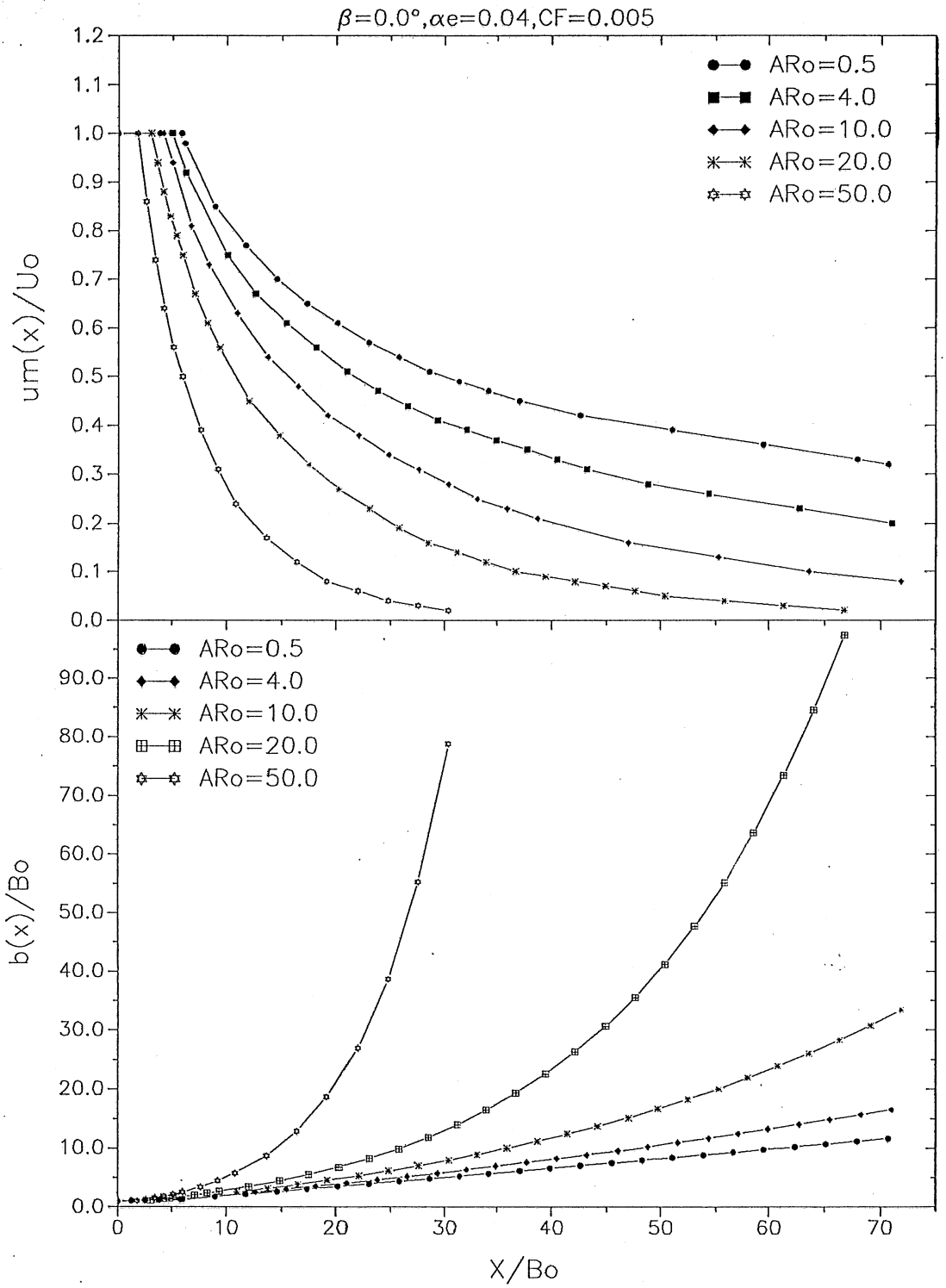

Fig. 2–15 Relationship between dimensionless $b(x)/B_o$, $u_m(x)/U_o$ and x/B_o as AR_o is changed.

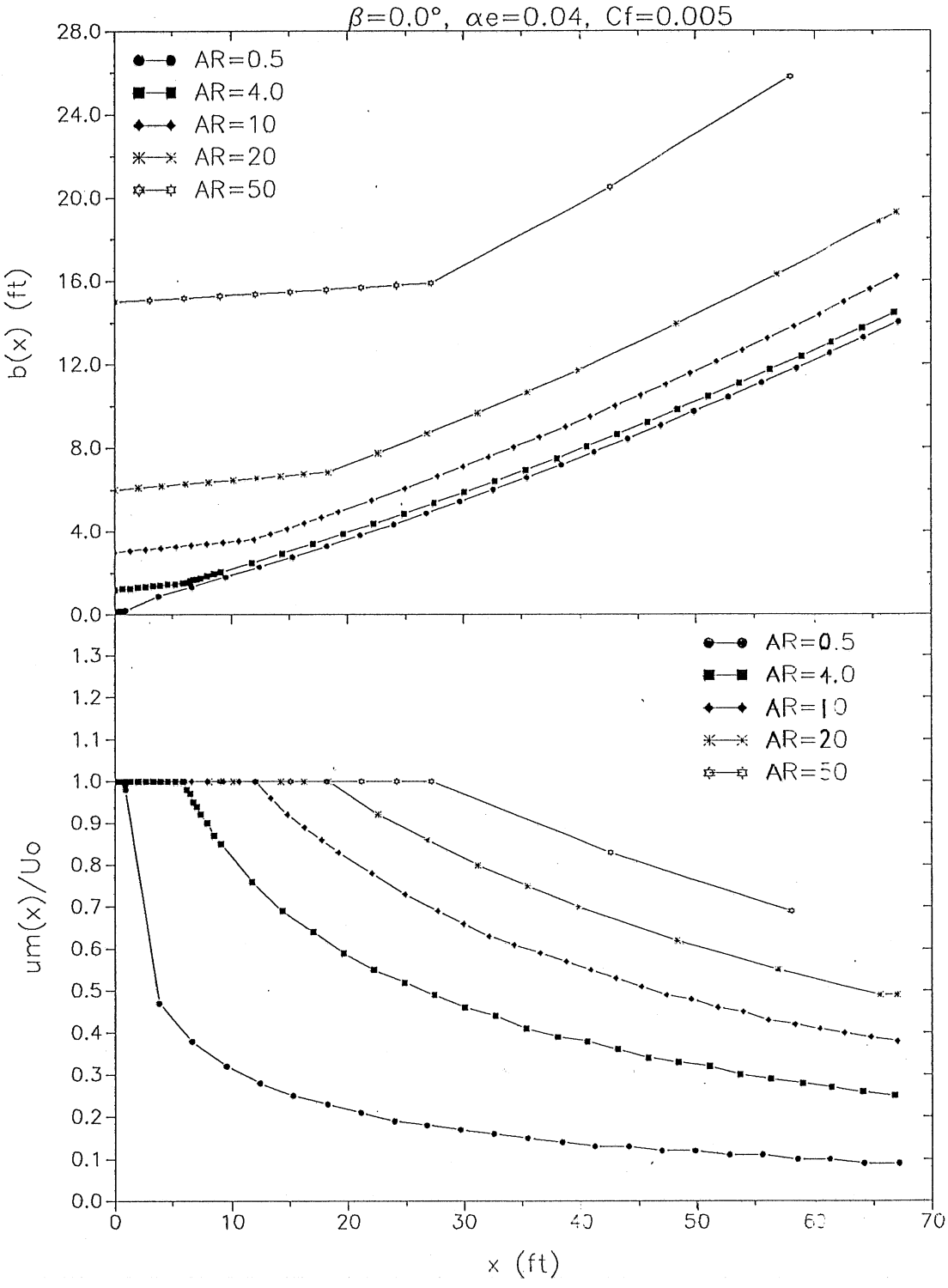

Fig. 2–16 Relationship between b(x), $u_m(x)/U_o$ and x (ft) as AR_o is changed.

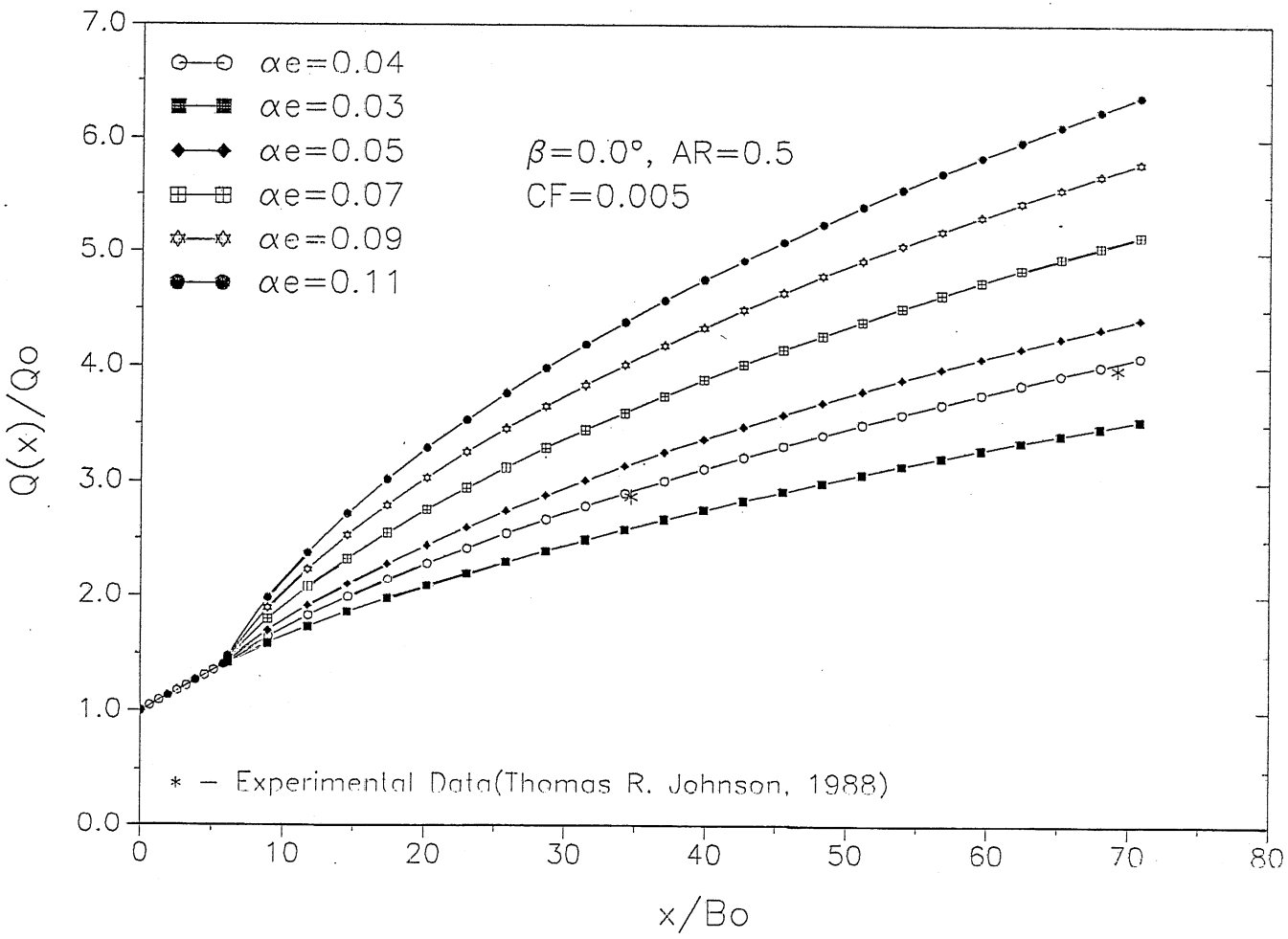

Fig. 2–17 Dilution $Q(x)/Q_0$ versus x/B_0 as entrainment coefficient α_e is changed at $AR_0 = 0.5$.

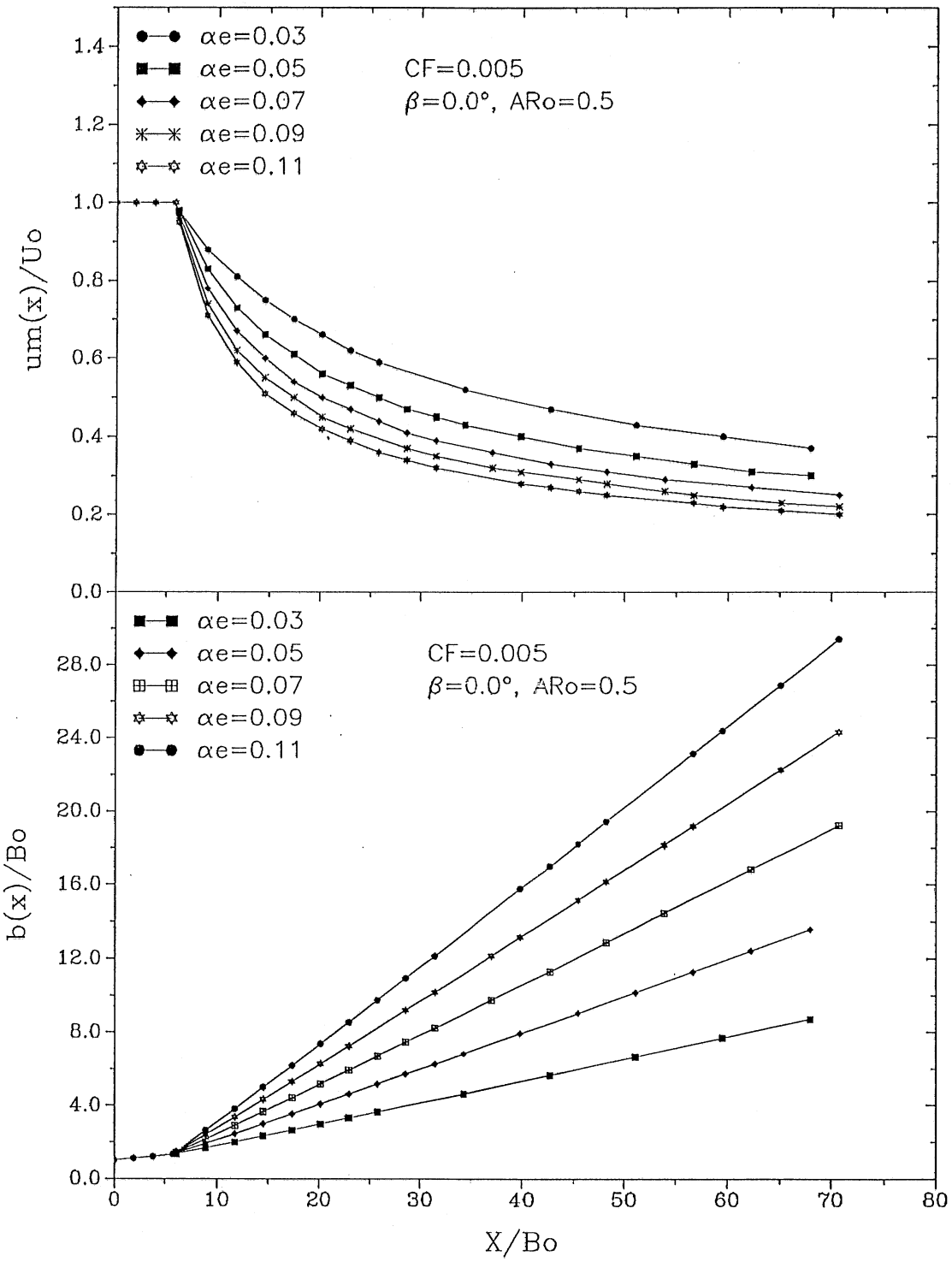

Fig. 2–18 Sensitivity of $b(x)/B_o$ and $u_m(x)/U_o$ to entrainment coefficient α_e at $AR_o = 0.5$.

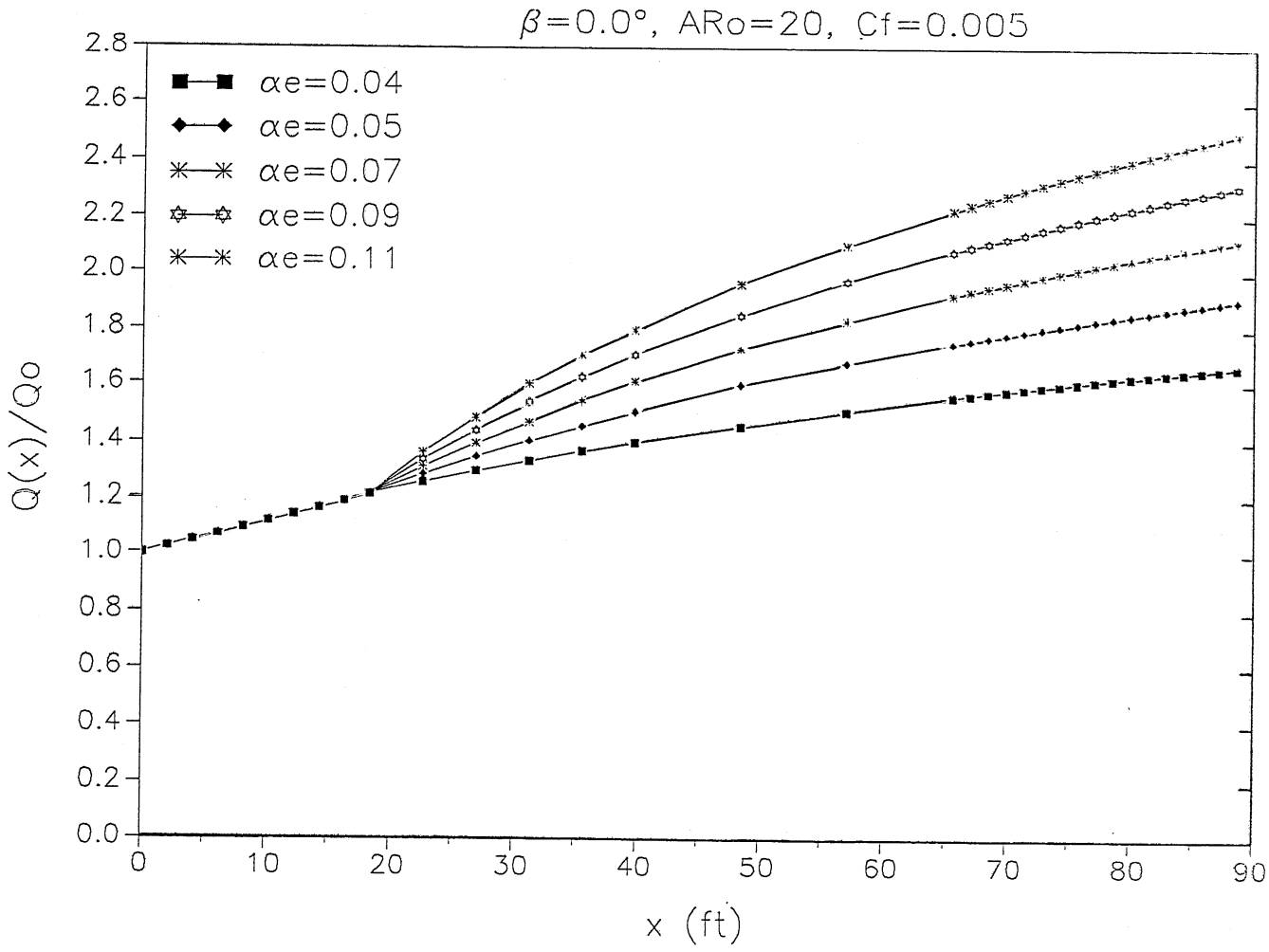

Fig. 2–19 Dilution $Q(x)/Q_o$ versus x/B_o as entrainment coefficient α_e is changed at $AR_o = 20$.

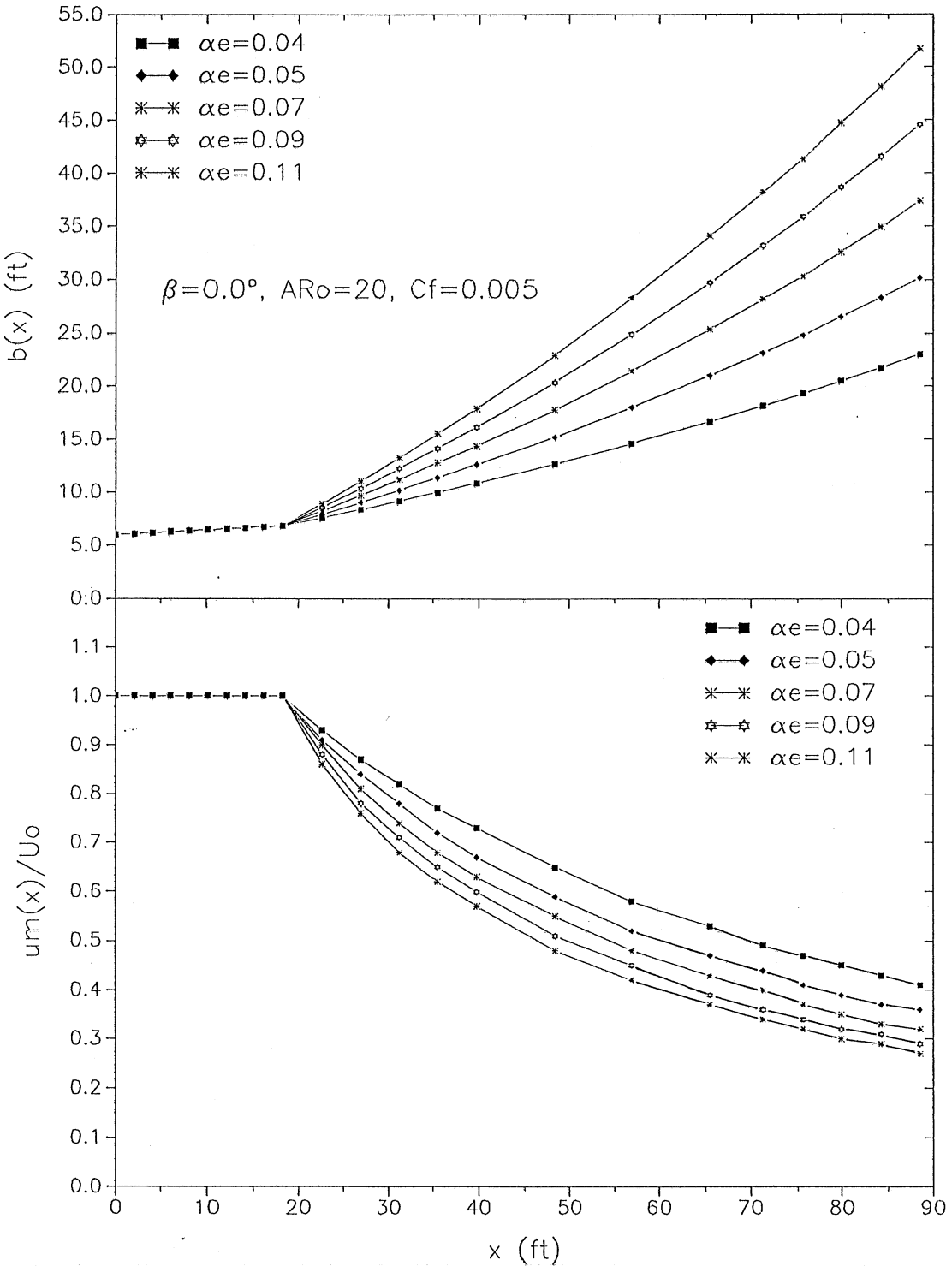

Fig. 2–20 Sensitivity of $b(x)/B_o$ and $u_m(x)/U_o$ with entrainment coefficient α_e at $AR_o = 20$.

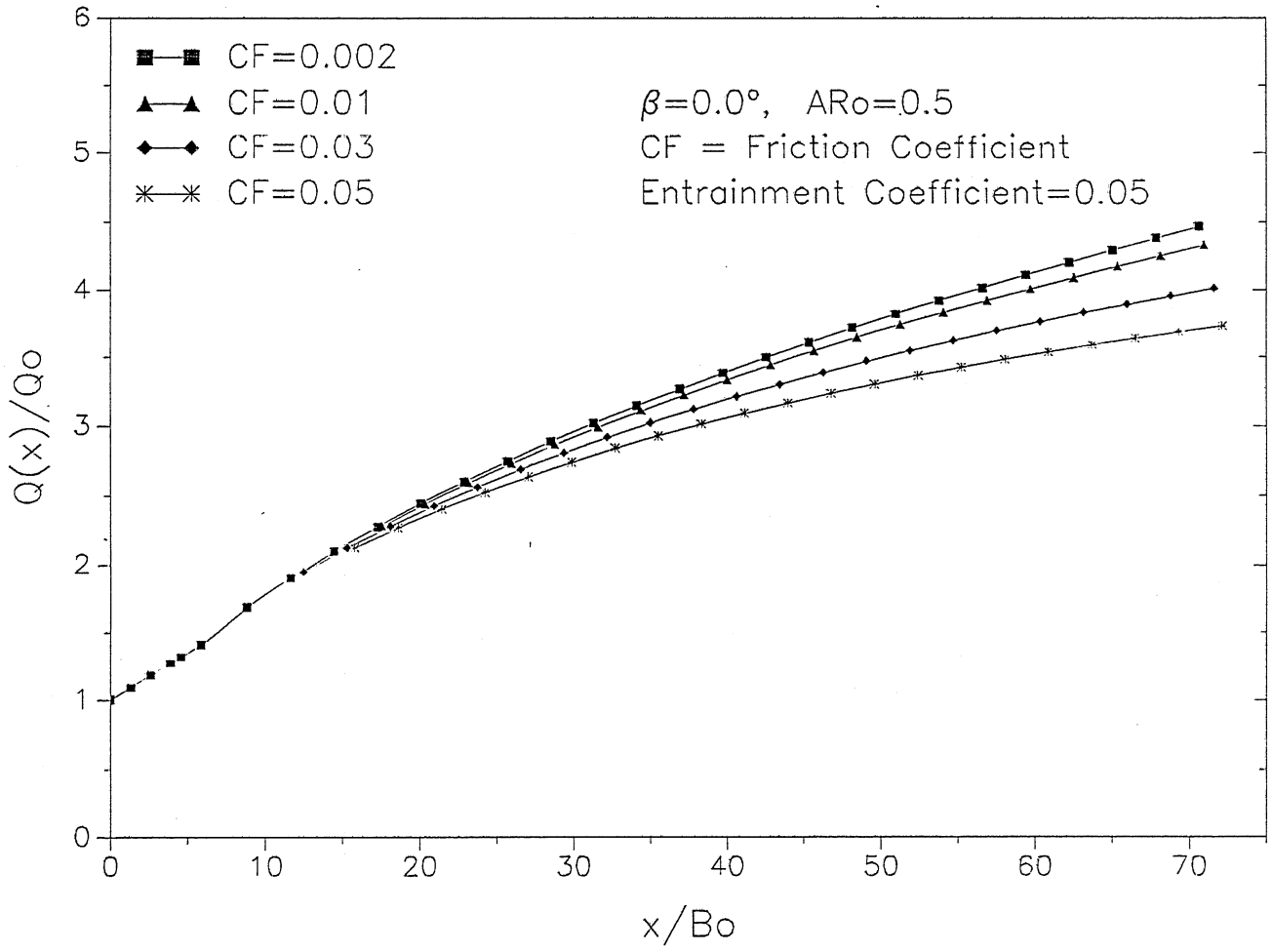

Fig. 2–21 Dilution $Q(x)/Q_0$ versus x/B_0 as friction coefficient c_f is changed at $AR_0 = 0.5$.

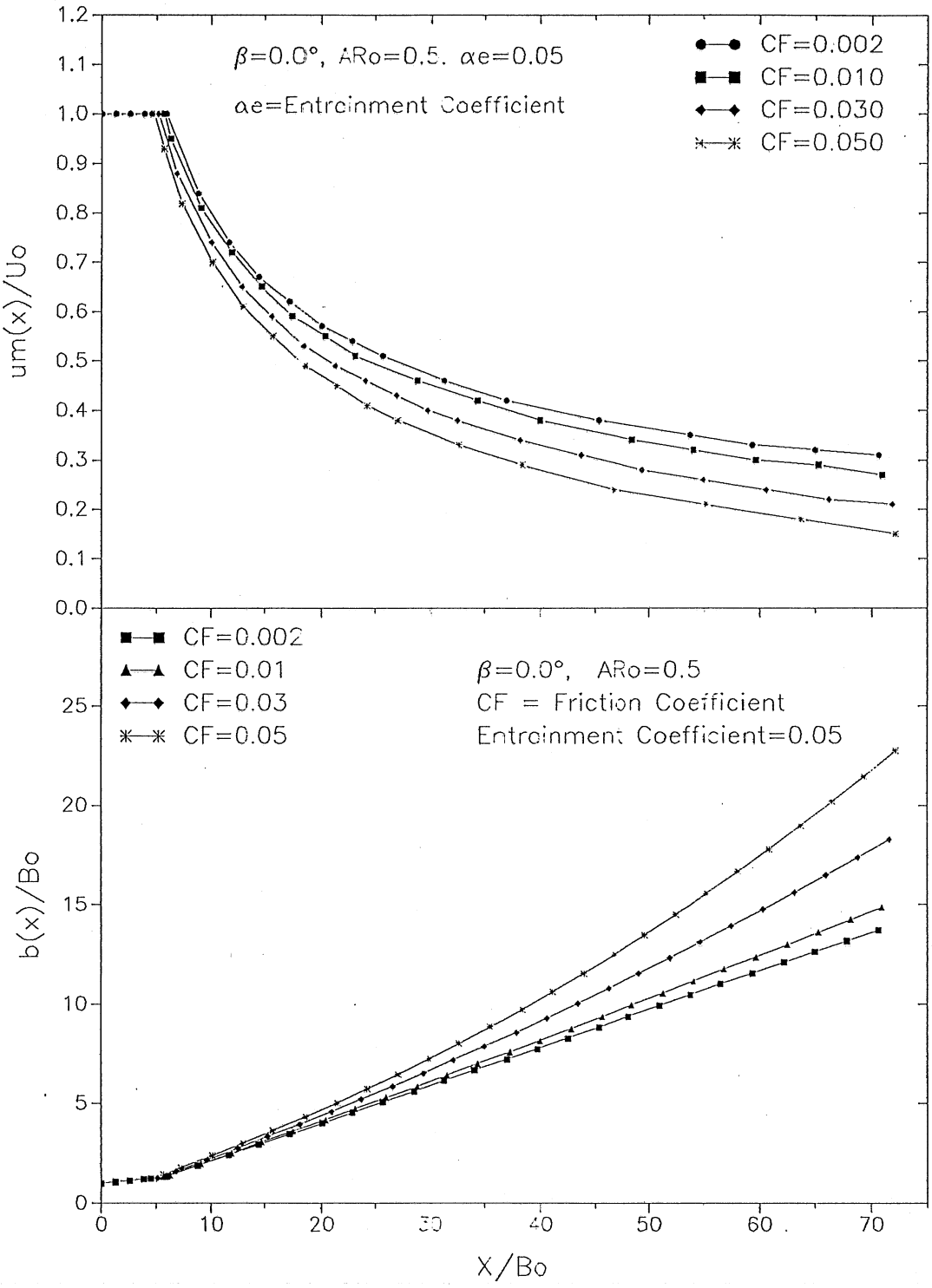

Fig. 2–22 Sensitivity of $b(x)/B_o$ and $u_m(x)/U_o$ with friction coefficient c_f at $AR_o = 0.5$.

II.3 Slot Jet Theory for Channel Discharge over Sloping Bottom in Infinite Fluid

In typical lake or reservoir situations the channel bottom would be sloping. Therefore we will consider a jet of water coming from a plane nozzle with finite water depth into a wide water body $\delta = 90°$ with a sloping bottom ($\beta > 0°$). The water depth is increasing in flow direction.

$$H(x) = H_0 + x \tan\beta \qquad [2\text{–}82]$$

We must also consider friction on the bottom. The velocity profile with depth is schematically shown in Fig. 2–23 (b). For most of practical cases the sloping angle β is much less than 10°. therefore the simple model shown in Fig. 2–24 will be used. It assumes that the velocity is a constant over depth H(x), velocity is in the horizontal direction, the transverse velocity profile is similar for different depths, and a shear stress exists on the bottom of sloping channel. The continuity and momentum equations are again used to construct the theoretical model to analyze the flow development region and fully developed flow region.

II.3.1 Continuity and momentum equations in fully developed flow region

Using the similarity hypothesis for the velocity profiles, the flow rate Q(x) and momentum M(x) are

$$Q(x) = 2 \int_0^\infty u(x,y)\ H(x)\ dy \qquad [2\text{–}83]$$

$$M(x) = 2 \int_0^\infty \rho\ u^2(x,y)\ H(x)\ dy \qquad [2\text{–}84]$$

Using the velocity similarity assumption [2–27], we have

$$\begin{aligned} Q(x) &= 2\ u_m(x)\ b(x)\ H(x) \int_0^\infty f(\eta)d\eta \\ &= C_6\ u_m(x)\ b(x)\ H(x) \end{aligned} \qquad [2\text{–}85]$$

$$\begin{aligned} M(x) &= 2\ \rho\ u_m^2(x)\ b(x)\ H(x) \int_0^\infty f^2(\eta)d\eta \\ &= C_7\ \rho\ u_m^2(x)\ b(x)\ H(x) \end{aligned} \qquad [2\text{–}86]$$

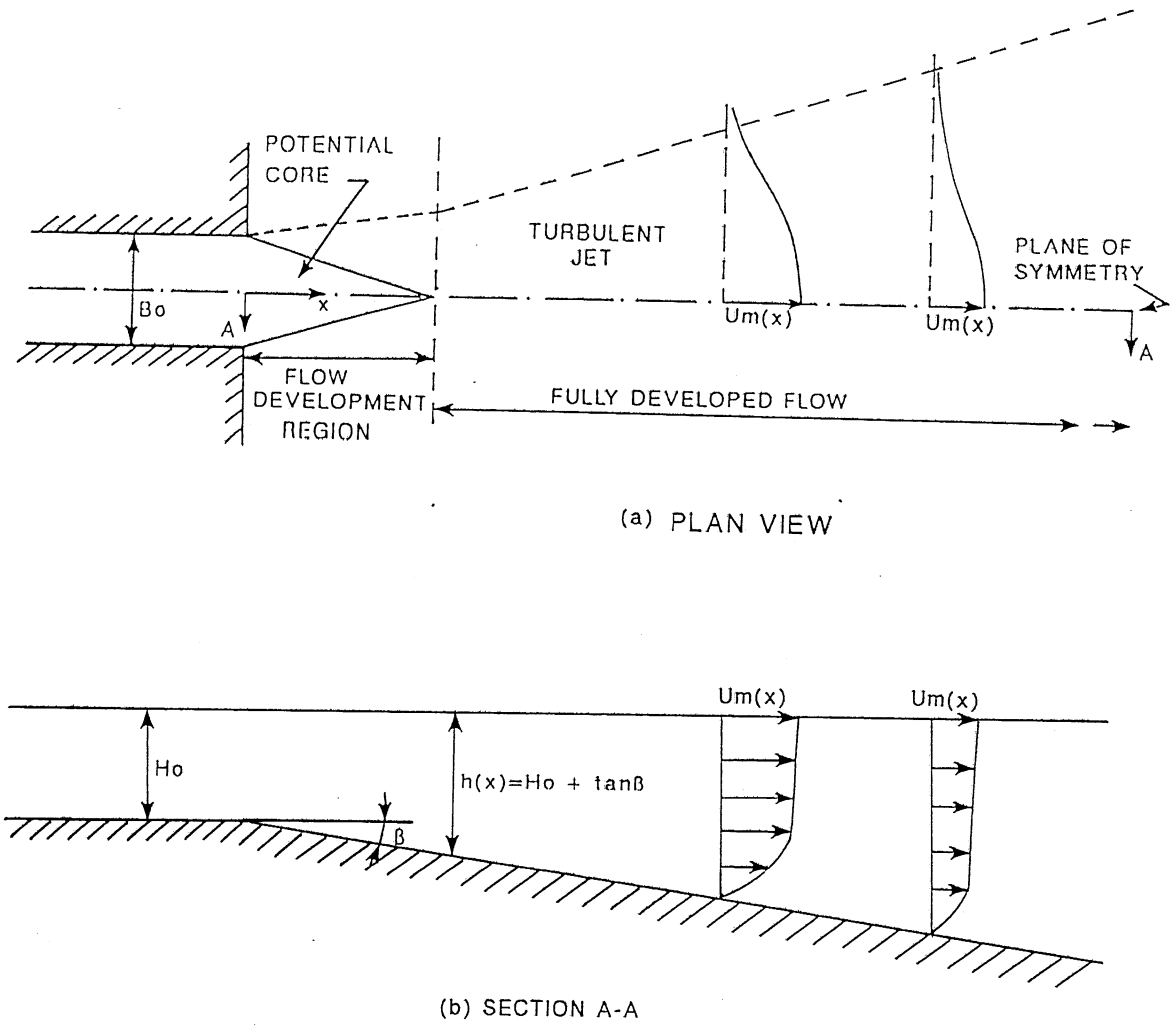

Fig. 2–23 A schematic representation of the sloping channel discharge.

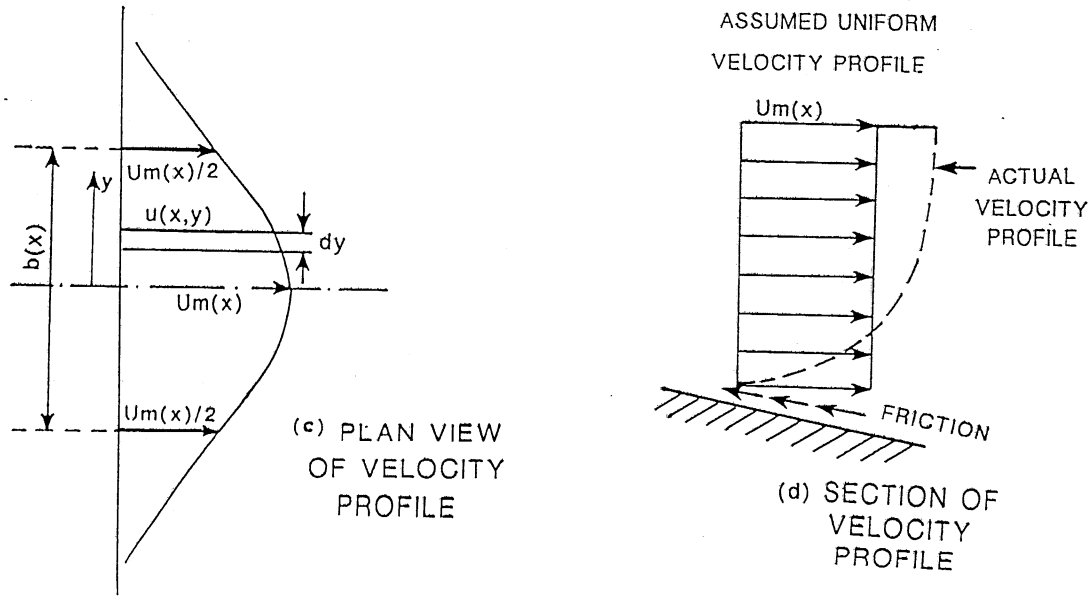

Fig. 2–24 A simple model of jet flow over sloping bottom with finite water depth.

where C_6, C_7 are velocity profile constants defined by equations [2–30] and [2–31]. The rate of change of flow rate and momentum is

$$\frac{dQ(x)}{dx} = \frac{d}{dx}\left[C_6\ u_m(x)\ b(x)\ H(x)\right] \qquad [2–87]$$

$$\frac{dM(x)}{dx} = \frac{d}{dx}\left[C_7\ \rho\ u_m^2(x)\ b(x)\ H(x)\right] \qquad [2–88]$$

For sloping channel discharge, we also consider four different cases as have been discussed for horizontal channel discharge.

(A) No entrainment, no friction:

Suppose there is no entrainment and no friction for sloping channel discharge. The flow rate and momentum of sloping channel discharge should be constants, and equal to the flow rate Q_o and momentum M_o of inflow, respectively. Assume the velocity of the inflow is U_o

$$\begin{aligned} Q(x) &= C_6\ u_m(x)\ b(x)\ H(x) \\ &= U_o\ B_o\ H_o \\ &= Q_o \end{aligned} \qquad [2–89]$$

$$\begin{aligned} M(x) &= C_7\ \rho\ u_m^2(x)\ b(x)\ H(x) \\ &= \rho\ H_o\ U_o^2\ B_o \\ &= M_o \end{aligned} \qquad [2–90]$$

Solving [2–89] and [2–90], we obtain

$$u_m(x)/U_o = A_o \qquad [2–91]$$

$$b(x)/B_o = A_1/[1 + x\ \tan\beta/H_o] \qquad [2–92]$$

where A_o and A_1 are constants defined as [2–38] and [2–39]. $f(\eta)$ should be [2–40]

$$f(\eta) = 1 \qquad \eta = 0 \text{ to } 0.5$$

$$f(\eta) = 0 \qquad \eta > 0.5$$

$$A_o = 1.0, \qquad A_1 = 1.0$$

The centerline velocity u_m is equal to the inflow velocity U_o and the full width b(x) of the sloping channel discharge is less than inflow width B_o because of effects of sloping angle β. As β and x increase, b(x) decreases.

(B) No entrainment, with friction

Using equations [2–41], [2–42] to consider the friction effects on momentum, the rate of change of the momentum is

$$\frac{dM(x)}{dx} = - c_f \rho u_m^2(x) b(x) \int_0^\infty f^2(\eta) d\eta$$

$$= \frac{d}{dx}[C_7 \rho u_m^2(x) b(x) H(x)] \qquad [2–93]$$

Where minus sign indicates that the momentum of the discharge decreases because of friction. Suppose c_f to be a constant, [2–93] can be written as

$$2 \frac{d}{dx} \{\ln[C_7 \rho u_m^2(x) b(x) H(x)]\} = - \frac{c_f}{H(x)}$$

and $$- \frac{c_f}{H(x)} = - \frac{c_f}{\tan\beta} \frac{d}{dx}\{\ln[H(x)]\}$$

Finally, [2–93] is

$$C_7 u_m^2(x) b(x) [H(x)]^w = U_0^2 B_0 [H_0]^w \qquad [2–94a]$$

where: $$w = \frac{c_f + 2 \tan\beta}{2 \tan\beta} \qquad [2–94b]$$

Solving [2–89] and [2–94], gives

$$u_m(x)/U_0 = A_0 (1 + x \tan\beta/H_0)^{-m} \qquad [2–95]$$

$$b(x)/B_0 = A_1 (1 + x \tan\beta/H_0)^k \qquad [2–96a]$$

where: $$m = \frac{c_f}{2 \tan\beta} \qquad [2–96b]$$

$$k = \frac{c_f - 2 \tan\beta}{2 \tan\beta} = m - 1 \qquad [2–96c]$$

Where constants A_0 and A_1 are equal to 1.0. So $u_m(x)/U_0$ and $b(x)/B_0$ are functions of β, AR_0, c_f, x, as shown in Fig. 2–21 to Fig. 2–23. Results are sensitive to the aspect ratio AR_0.

(C) **Entrainment, no friction:**

Using the entrainment hypothesis [2–13], the rate of change of flow should be equal to the flow rate coming from ambient water

$$\frac{dQ(x)}{dx} = \frac{d}{dx}\left[C_6\, u_m(x)\, b(x)\, H(x)\right]$$

$$= 2\, v_e\, H(x)$$

$$= 2\, \alpha_e\, u_m(x)\, H(x) \qquad [2\text{–}97a]$$

Hence

$$\frac{d}{dx}\left\{\ln[C_6 u_m(x) b(x)]\right\} b(x) = 2\,\frac{\alpha_e}{C_6} \qquad [2\text{–}97b]$$

Suppose the entrainment coefficient α_e is a constant, solving equations [2–90] and [2–97], using the initial condition x=0, $u_m(x)=A_o U_o$, we obtain

$$u_m(x)/U_o = A_o\left[1 + 4\alpha_e A_o\left(\frac{x}{B_o} + \frac{x^2 \tan\beta}{B_o H_o}\right)\right]^{-0.5} \qquad [2\text{–}98]$$

$$b(x)/B_o = \frac{2\alpha_e}{B_o C_6 H(x)}\left[H_o x + \frac{x^2}{2}\tan\beta\right] + \frac{A_1 H_o}{H(x)} \qquad [2\text{–}99]$$

we use again Gaussian velocity distributions [2–50]. Constants C_6, A_o, A_1 are given by equation [2–30], [2–38] and [2–39].

(D) **Entertainment, with friction:**

If both entrainment and friction on the sloping channel bottom are considered. Equations [2–93] and [2–97a] can be written as

$$\frac{du_m(x)/U_o}{dx} + A_8\,\frac{u_m(x)}{U_o} + A_5\left[1 + x\frac{\tan\beta}{H_o}\right]^w \left[\frac{u_m(x)}{U_o}\right]^3 = 0 \qquad [2\text{–}100]$$

$$\frac{b(x)}{B_o} = \frac{U_o}{C_7 u_m^2(x)}\left[1 + x\,\frac{\tan\beta}{H_o}\right]^{-w} \qquad [2\text{–}101]$$

where $A_8 = \frac{c_f}{2}$ [2–102]

Constants A_5, C_7, and power w are defined by [2–60], [2–39] and [2–94b] respectively. The initial conditions of the differential equation [2–100] are

$$x = 0.0, \quad u_m(x)/U_o = 1.0$$

Using a fourth–order Runge–Kutta method a numerical solution for $u_m(x)/U_0$ can be obtained from the differential equation [2–100], then $b(x)/B_0$ is found from [2–102]. For sloping channel discharge with entrainment and friction, c_f and α_e are unknown and specified in the next section.

II.3.2 Local friction coefficient and entrainment coefficient

Unfortunately no experimental data for non–buoyant sloping channel discharge are not yet available, but we hope using the available experimental facility (Johnson and Stefan, 1988) to conduct some further experiments for non–buoyant and negatively buoyant sloping channel discharges in order to validate theoretical results. In the meantime we use experimental data for negatively buoyant sloping channel discharges (Johnson and Stefan, 1988) to specify the local friction coefficient. A procedure and some information necessary for specifying c_f has been given in the section II.2.2.

In the experiments (Johnson and Stefan, 1988), the mean height of roughness projections e is about 0.20mm (0.00065 ft). $Re_0 \cong 1.0\times10^4$, where $Re_0 = \frac{U_0 H_0}{\nu}$ is the Reynolds number of the inflow. The local friction factor c_f can be determined by the local Reynolds number $Re_x = U_\infty x/\nu$ and the local relative roughness $\frac{x}{e}$. U_∞ should be the water surface velocity which changes with x. We analyze c_f at the inflow and the end of the main tank.

For the inflow, x should be the length of rectangular inflow channel (6 ft). Hence

$$\text{Re(inflow)} = \frac{U_0 x}{\nu} = \frac{U_0 H_0}{\nu}\frac{x}{H_0}$$

$$= 1.0\times10^4 * \frac{6.0}{0.3}$$

$$= 2.0\times10^5$$

For outflow, the length should be x = 16.0 + 6.0 = 22.0 ft. We get

$$\text{Re(outflow)} = \frac{u_m\, x}{\nu} = \frac{u_m\, H_0}{\nu} * \frac{22.0}{0.3}$$

where u_m is the centerline velocity at the end of diffuser. According to further computation, u_m(outflow) $\cong$ 10% U_0, so the Reynolds number of outflow is equal to

$$\text{Re(outflow)} = 7.4\times10^4$$

From Fig. 21.12 (Schlichting, 1960), the experimental flow region (Johnson and Stefan, 1988) is in the region of a smooth flat plate and c_f is independent of the relative roughness. c_f is from 0.0048 to 0.0062 with the average value

$$c_f \approx 0.0055 \qquad \text{[2–103]}$$

For the entrainment coefficient α_e, we use $\alpha_e = 0.004$ which is the same as the entrainment coefficient of a horizontal channel discharge.

II.3.3 The flow development region

Fig. 2–11 can serve as a definition sketch of the flow–development region of sloping channel discharge. All symbols are the same as in section II.2.3, but it is necessary to consider the changeable depth H(x) effects for sloping channel discharge.

II.3.3.1 Continuity and momentum equations

The velocity in the potential core is the inflow velocity U_o. The velocity distribution in the turbulent shear layers can again be represented as a Gaussian function [2–17] (Rajaratnam, 1967, [5–47]). The flow rate is

$$Q(x) = 2U_o y_1(x)H(x) + 2\int_{y_1}^{\infty} u(x,y)\, dy\, H(x)$$

$$= 2U_o H(x)[\, y_1(x) + b_o(x)\, A_6] \qquad \text{[2–104]}$$

where: $A_6 = \int_0^{\infty} f(\xi)\, d\xi$

$$u(x,y) = U_o\, f(\xi)$$

$$\xi = [y - y_1(x)]/b_o(x)$$

$$f(\xi) = \exp(-0.693\ \xi^2)$$

The rate of change of flow rate Q(x) is

$$\frac{dQ(x)}{dx} = 2U_o\{H(x)[\frac{dy_1(x)}{dx} + A_6\frac{db_o(x)}{dx}]$$

$$+ \tan\beta[y_1(x) + A_6 b_o(x)]\} \qquad \text{[2–105]}$$

For the flow development region, we must consider the entrainment coefficient of the shear layer, $\alpha_e{}^o \approx 0.035$ (Rajaratnam, 1976).

$$\frac{dQ(x)}{dx} = 2v_eH(x) = 2\alpha_e{}^oU_oH(x) \qquad [2\text{–}106]$$

With [2–105] into [2–106], we obtain

$$\frac{dy_1(x)}{dx} + A_6\frac{db_o(x)}{dx} + \tan\beta\left[\frac{y_1(x)}{H(x)} + A_6\frac{b_o(x)}{H(x)}\right] = \alpha_e{}^o \qquad [2\text{–}107]$$

The momentum equation can written as

$$M(x) = 2\rho U_o^2H(x)y_1(x) + b_o(x)\int_{y_1}^{\infty}\rho u^2(x,y)H(x)\,dy$$
$$= 2\rho U_o^2H(x)[y_1(x) + A_7b_o(x)] \qquad [2\text{–}108]$$

where: $A_7 = \int_o^{\infty} f^2(\xi)d\xi$

Now we consider two cases in flow development region: (A) Without friction; (B) With friction.

(A) Without friction in the flow development region

Without friction in the flow development region, the momentum should be conservative and equal to the momentum of the inflow.

$$2\rho U_o^2b_oH_o = 2\rho U_o^2H(x)\,[y_1(x) + A_7b_o(x)]$$
$$b_oH_o = H(x)\,[y_1(x) + A_7b_o(x)] \qquad [2\text{–}109]$$

The derivation of equation [2–109] is as follows:

$$H(x)[\frac{dy_1(x)}{dx} + A_7\frac{db_o(x)}{dx}] + \tan\beta[y_1(x) + A_7b_o(x)] = 0 \qquad [2\text{–}110]$$

Solving [2–105] and [2–110], we get

$$\frac{db_o(x)}{dx} = \frac{\alpha_e{}^o}{A_6\text{–}A_7} - \frac{b_o(x)\tan\beta}{H_o + x\tan\beta} \qquad [2\text{–}111]$$

$$\frac{dy_1(x)}{dx} = -\frac{A_7\alpha_e{}^o}{A_6\text{–}A_7} - \frac{y_1(x)\tan\beta}{H_o + x\tan\beta} \qquad [2\text{–}112]$$

If the sloping angle $\beta = 0°$, the result of sloping channel discharge in the flow development is the same as that of horizontal channel discharge. As β increases, the decrease of $y_1(x)$ in the sloping channel is much faster than that of $y_1(x)$ in the horizontal channel discharge. The length of the flow development region x_o should decrease. The initial conditions of the above equation are

$$x = 0 \qquad b_o(x) = B_o/2$$

$$y_1(x) = B_o/2$$

At $y_1(x) = 0$ the potential core disappears (end of the flow development region).

(B) With friction in the flow development region

Because of friction, the rate of change of the momentum is equal to the local total friction force. Using [2–42], we get

$$\frac{dM(x)}{dx} = -D_x$$

$$= -2\int_0^\infty \frac{1}{2} c_f \rho u^2(x,y)\, dy$$

$$= -c_f \rho U_o^2 y_1(x) + \int_{y_1}^\infty c_f \rho u^2(x,y)\, dy$$

$$= -c_f \rho U_o^2 [y_1(x) + A_7 b_o(x)] \qquad [2–113]$$

with [2–108], the rate of change of momentum can be written as

$$\frac{dM(x)}{dx} = 2\rho U_o^2 \{H(x)[\frac{dy_1(x)}{dx} + A_7 \frac{db_o(x)}{dx}]$$

$$+ \tan\beta [y_1(x) + A_7 b_o(x)]\} \qquad [2–114]$$

with [2–79a], we can write

$$\frac{C_f/2 + \tan\beta}{H(x)} [y_1(x) + A_7 b_o(x)] + \frac{dy_1(x)}{dx} + A_7 \frac{db_o(x)}{dx} = 0 \qquad [2–115]$$

Solving [2–107] and [2–115], we obtain two simple differential equations:

$$(A_6 - A_7)\frac{db_o(x)}{dx} = \frac{1}{2H(x)} [c_f y_1(x) + A_9 b_o(x)] + \alpha_e{}^o \qquad [2–116]$$

$$(A_7 - A_6)\frac{dy_1(x)}{dx} = \frac{1}{2H(x)} [A_{10} y_1(x) + A_{11} b_o(x)] + A_7 \alpha_e{}^o \qquad [2–117]$$

Where $A_9 = A_7 c_f + 2\tan\beta[A_7 - A_6]$

$A_{10} = A_6 c_f + 2\tan\beta[A_6 - A_7]$

$A_{11} = c_f A_6 A_7$

Using a 4th order Runge–Kutta method, we can obtain a numerical solution.

II.3.3.2 Comparisons of analytical results with experimental data

No experimental data for sloping angle $\beta > 0^\circ$ are available. If we use the same friction coefficient $c_f = 0.0$ and the same entrainment coefficient $\alpha_e^\circ = 0.035$ in both the flow development and the developed region, the non–dimensional numerical result x_0/B_0 is the same as for $\beta = 0^\circ$. It is shown in Fig. 2–25

Fig. 2–25 shows the relationship between the dimensionless length x_0/B_0 of the flow development region and the sloping angle β. The theoretical results for the flow development region clearly show changes of x_0 with entrainment, friction and sloping angle β. x_0/B_0 is sensitive to the change of entrainment coefficient α_e°. Because of entrainment the potential core disappears earlier. As slope angle β increases x_0/B_0 decrease because of effects of weight force. Fig. 2–26 shows relationship between x_0/B_0 and slope angle β with large aspect ratio AR_0 of inflow. x_0/B_0 is very sensitive to aspect ratio AR_0. x_0/B_0 decreases slowly as β° increases. Comparison of [2–13] with [2–26], x_0/B_0 in sloping channel discharge is less than that in horizontal channel discharge as $AR_0 = 20$.

II.3.4 Model synthesis and sensitivity analysis

The flow development model is combined with the fully developed flow model. The initial conditions of the differential equations [2–97] and [2–100] in the fully developed flow region need to be modified to

$$u_m(x) = U_0, \quad b(x) = b_0(x_0) \quad \text{at } x = x_0.$$

Equations [2–98] and [2–99] become

$$u_m(x)/U_0 = \left[1 + \frac{4\alpha_e}{A_0}\frac{x-x_0}{B_0} + \frac{\tan\beta}{B_0 H_0}(x^2 - x_0^2)\right]^{-0.5}$$

$$b(x)/B_0 = \frac{2\alpha_e}{C_6 H(x)}\left[\frac{H_0}{B_0}(x-x_0) + \frac{\tan\beta}{2B_0}(x^2 - x_0^2)\right] + \frac{H_0}{2A_3 H(x)},$$

where A_0, A_3, and C_6 are defined by [2–38], [2–52], and [2–30].

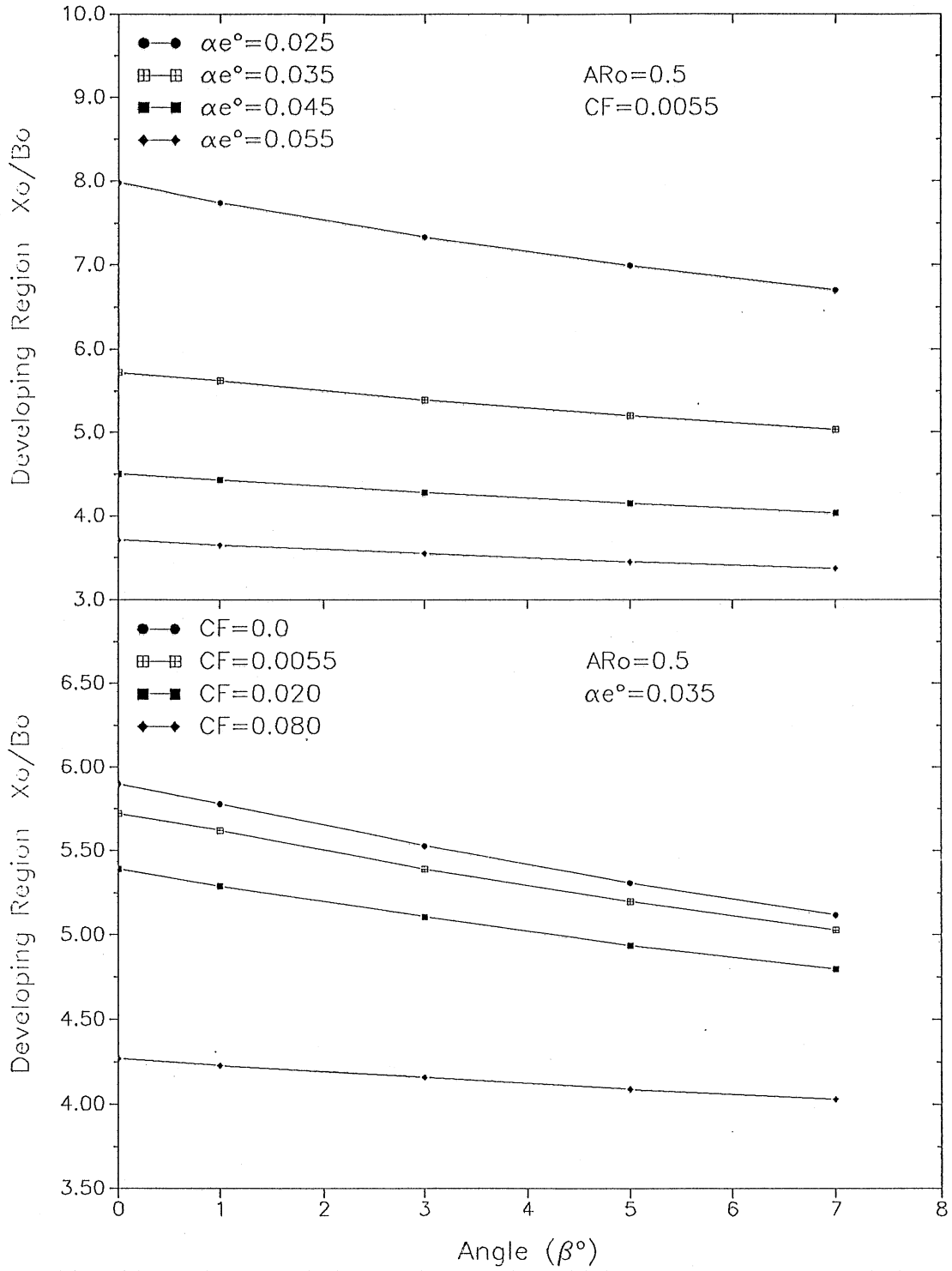

Fig. 2–25 Relationship between dimensionless length x_o/B_o and slope angle β° as α_e or c_f is changed at $AR_o = 0.5$.

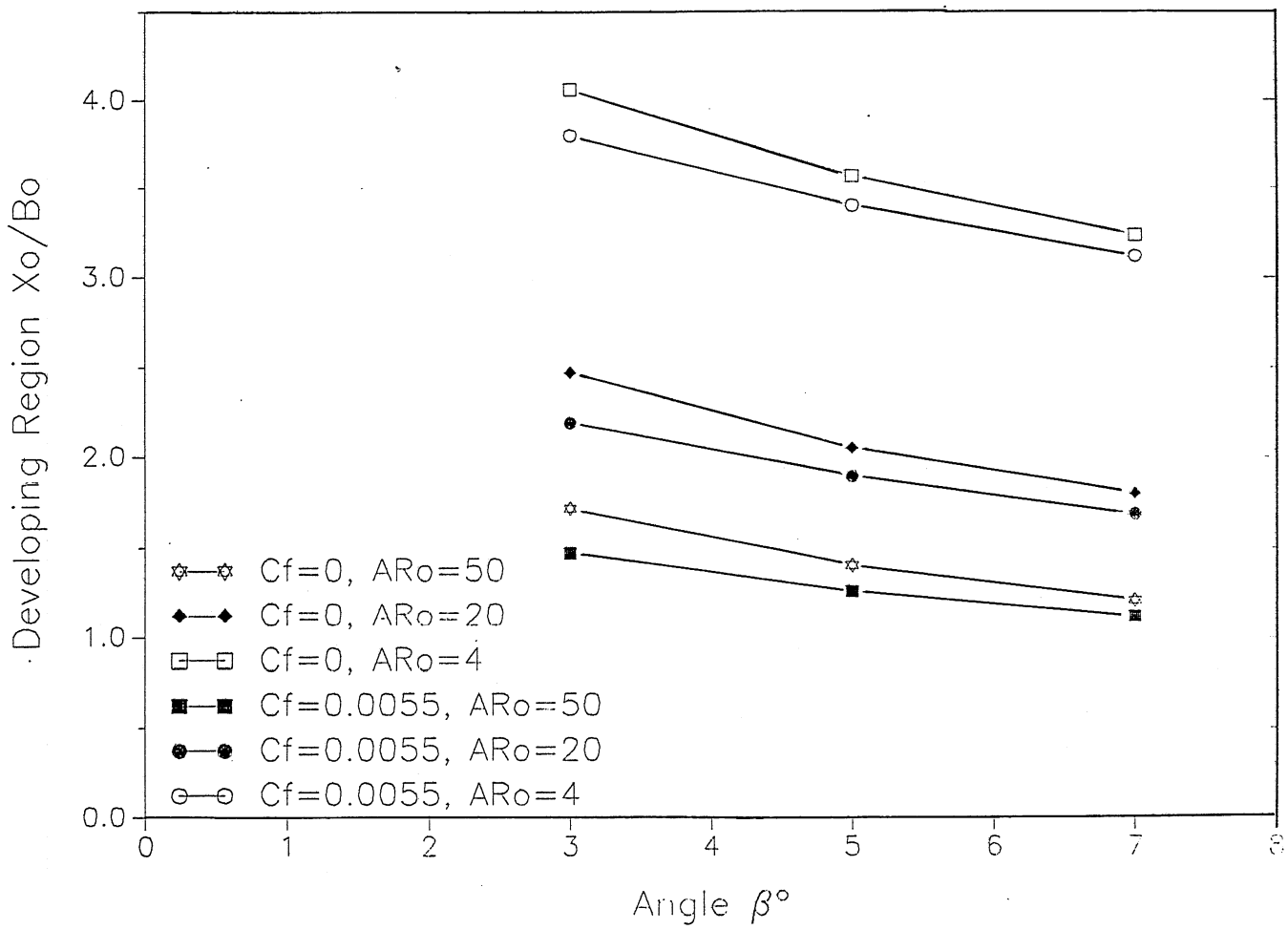

Fig. 2–26 Dimensionless length x_o/B_o versus slope angle $\beta°$ as AR_o increases.

The sensitivity of the model of jet flow over a sloping bottom is shown in Fig. 2–27 to Fig. 2–30. Relationships between $Q(x)/Q_o$, $b(x)/B_o$, and $u_m(x)/U_o$ and effects of entrainment and friction coefficients in sloping channel discharge are the same as those in the horizontal channel discharge. Comparing horizontal channel discharge with sloping channel discharge, dilution increases and dimensionless width $b(x)/B_o$ and velocity $u_m(x)/U_o$ decrease because of effects of the sloping bottom.

As aspect ratio AR_o becomes larger than 4 and as slope angle β becomes larger than 3°, width b(x) of jet in flow–development region decreases as shown in Fig. 2–30. In the fully developed flow region width b(x) increases linearly for different aspect ratios and slope angles.

In this chapter we have constructed a simple integral model of inflow to a lake or reservoir over a horizontal or sloping bottom. Some theoretical predictions have been made with the model.

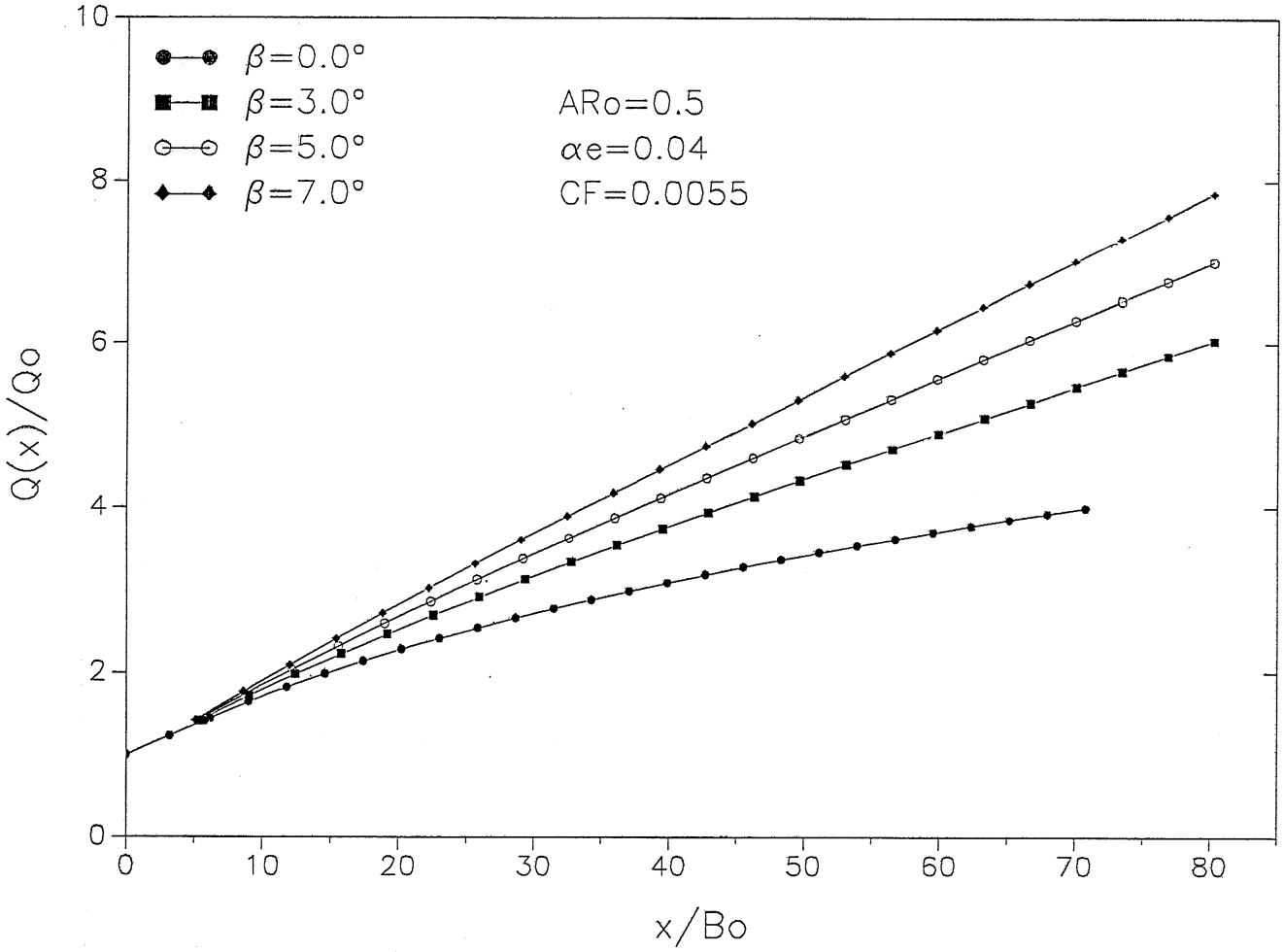

Fig. 2–27 Dilution $Q(x)/Q_o$ versus x/B_o as slope angle $\beta°$ is changed at $AR_o = 0.5$.

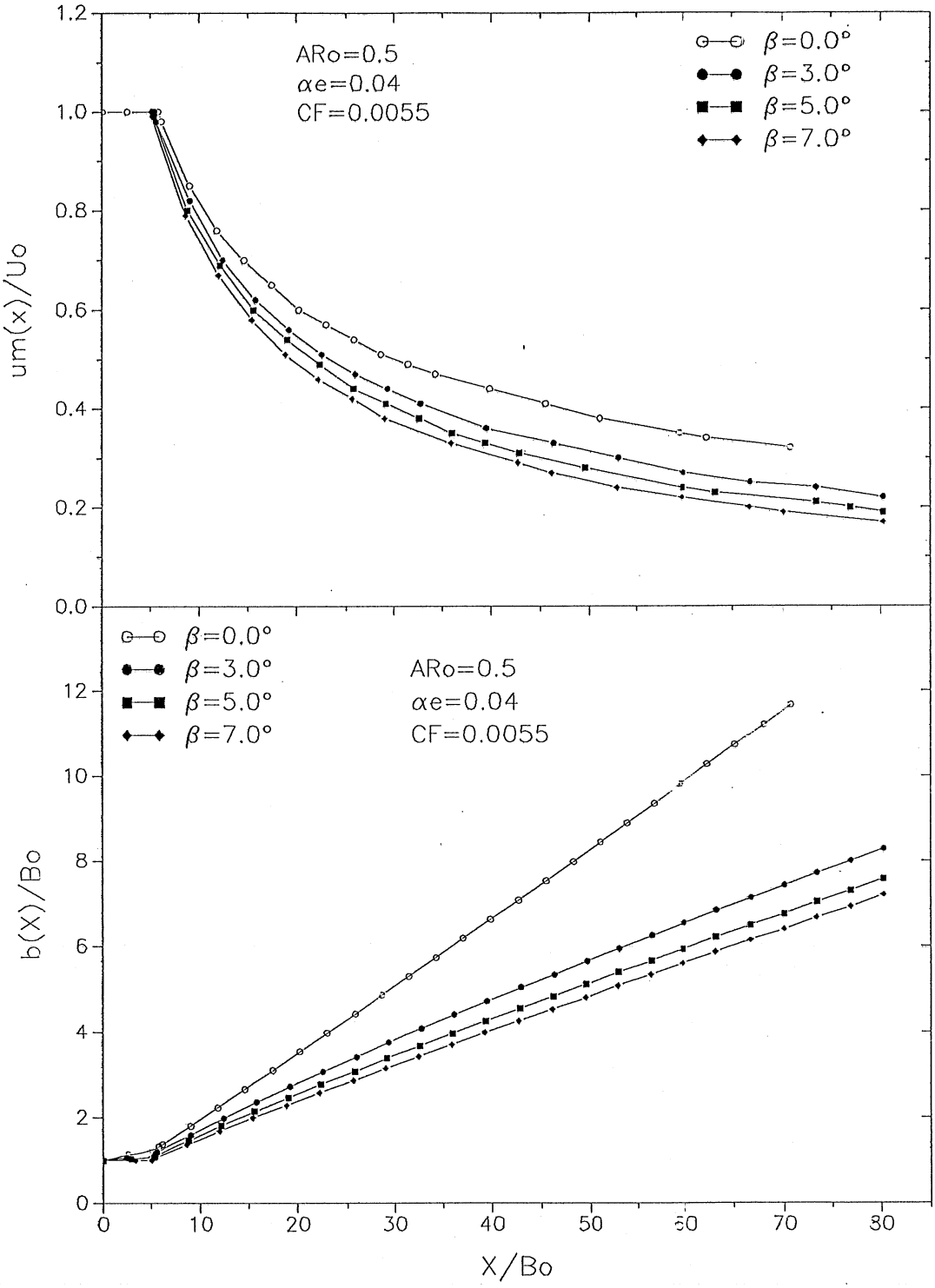

Fig. 2–28 Sensitivity of $b(x)/B_o$ and $u_m(x)/U_o$ with slope angle β° at $AR_o = 0.5$.

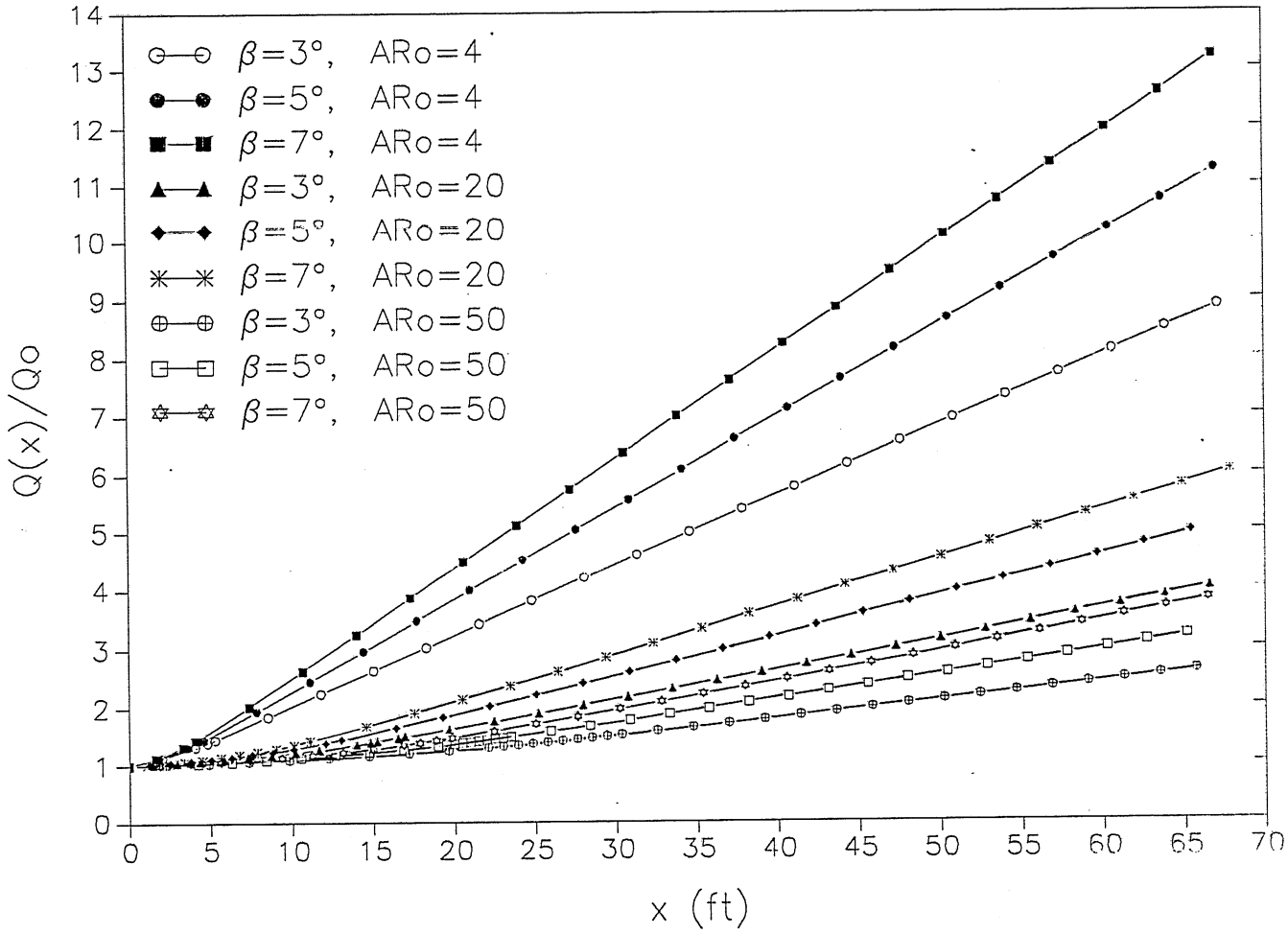

Fig. 2–29 Dilution $Q(x)/Q_o$ versus x/B_o as slope angle $\beta°$ and AR_o are changed.

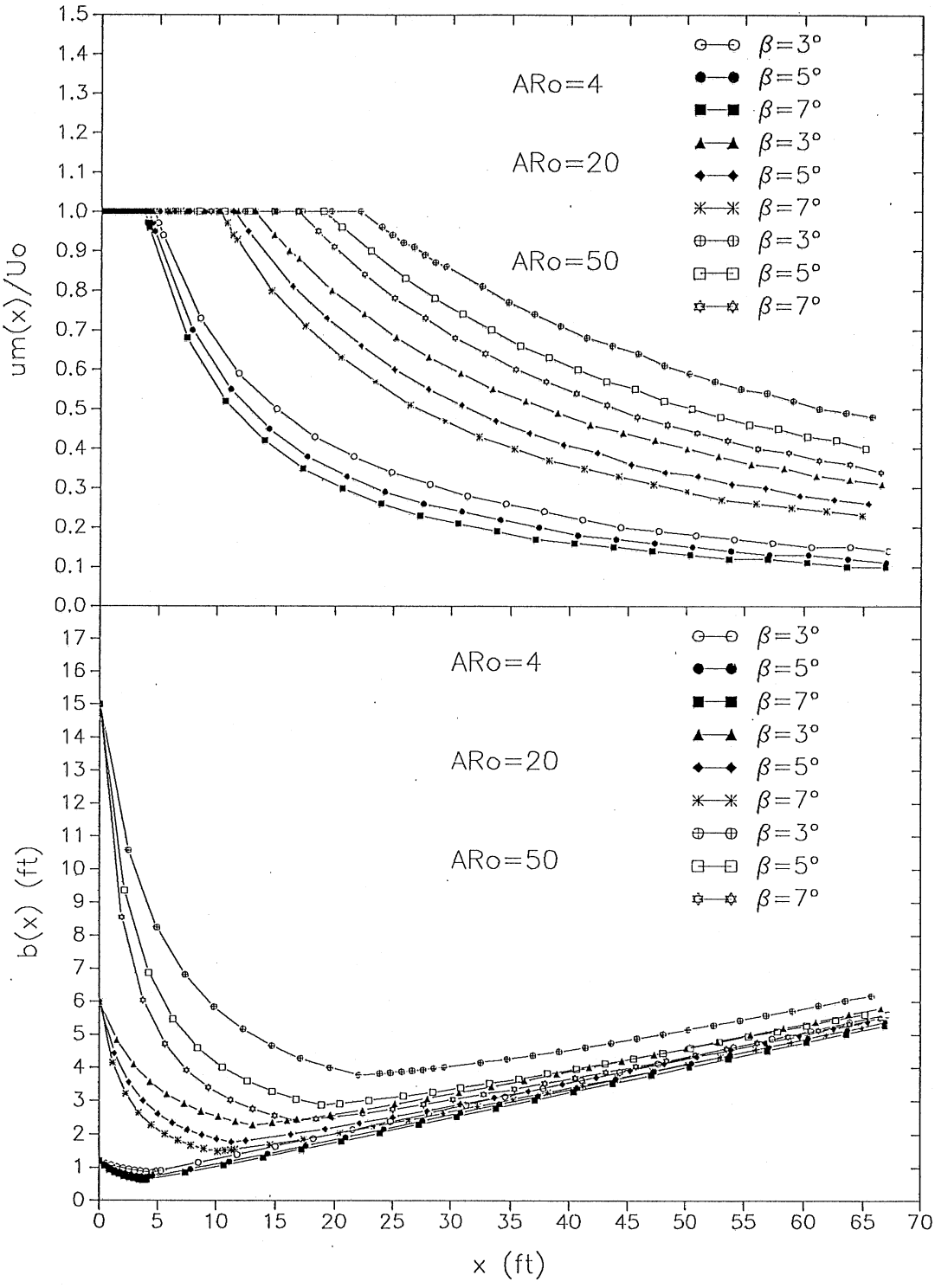

Fig. 2–30 Sensitivity of $b(x)/B_o$ and $u_m(x)/U_o$ with slope angle β° as AR_o is changed.

Chapter III ANALYSIS OF EXPERIMENTAL DATA

An integral analysis of non–buoyant slot jets discharged into diverging or sloping channels with finite water depth has been presented in chapter II. It is necessary to compare these results with available experimental data. Experimental data were available from studies by Johnson and Stefan (1988). Gaussian distributions are fitted to the experimental data of jet–like flow (Rajaratnam, 1976). A Gauss fitting method has been used to analyze finite numbers of experimental measurements in non–buoyant horizontal jets with finite water depth as will be described in Appendix B.

III.1 Available Data and Simple Analysis

Johnson et al. (1988) conducted several experiments with non–buoyant free surface channel discharges with diverging angle δ=90°. No density differences exist in non–buoyant flows. When the inflow densimetric Froude number $F_0 = U_0 (g' H_0)^{-0.5}$ is larger than 10, experiments of Johnson et al. were considered as non–buoyant flow. Johnson et al. measured velocity at different depths and in different cross–sections. The original experimental data are reported in Table 3–1. Fig. 3–1 shows an example of locations where velocity profiles were measured. Eqn. [3–1] is used to calculate the depth averaged velocity at point (x,y):

$$U(x,y) = \frac{\sum_{i=1}^{N-1} \frac{u(z_i)+u(z_{i+1})}{2} (z_{i+1} - z_i)}{\sum_{i=1}^{N-1} (z_{i+1} - z_i)} \qquad [3–1]$$

where z_i is depth of measurement point i, $u(z_i)$ is the x–direction velocity component at the measurement point (x,y,z_i). Average velocities are shown in Table 3–2. Fig. 3–2 shows examples of velocity profiles with depth and average velocities.

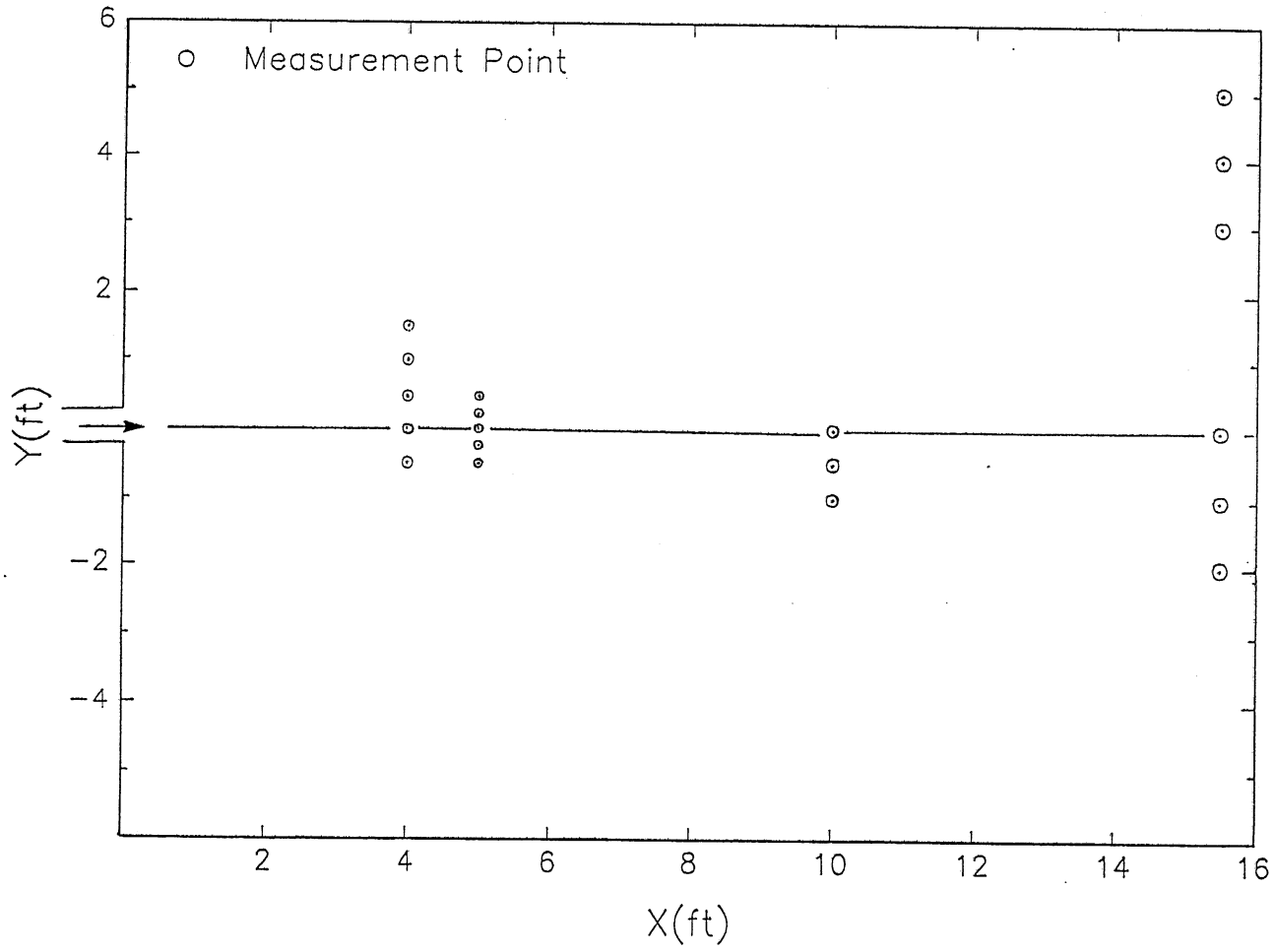

Fig. 3–1 Plan view of locations where velocity profile measurements were taken. (Example) Experiments by Johnson et. al. (1988).

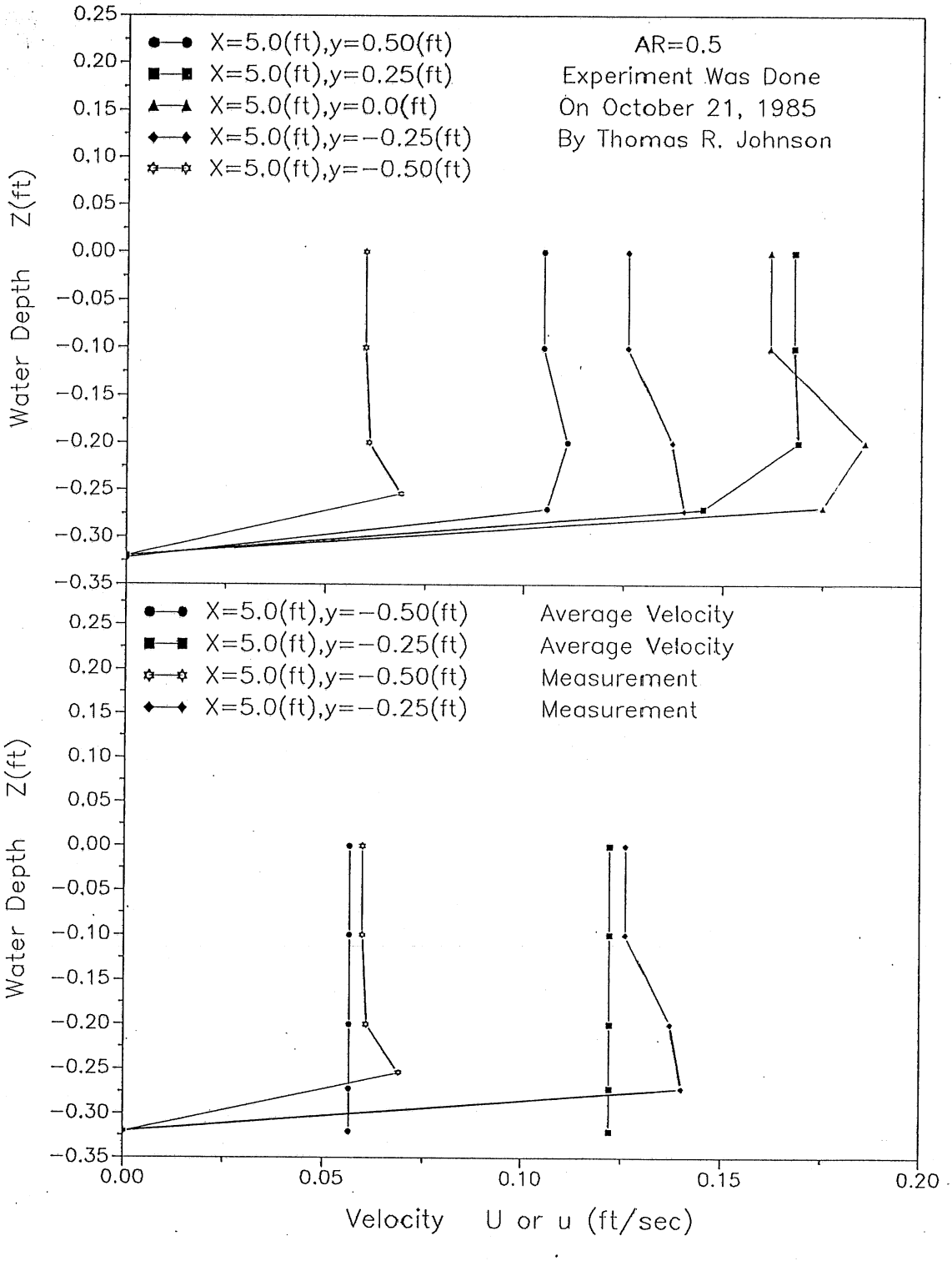

Fig. 3–2 Examples of velocity profiles with depth and average velocities (Experiment 21/10/1985).

Table 3.1 The Original Experimental Data(Johnson et al. 1988)

Date	October 21, 1985			ARo = 0.5			
x=5.00	y=0.50	x=5.00	y=0.25	x=5.00	y=0.00	x=5.00	y=-0.25
Z(ft)	u(ft/sec)	Z(ft)	u(ft/sec)	Z(ft)	u(ft/sec)	Z(ft)	u(ft/sec)
0.000	0.105	0.000	0.168	0.000	0.162	0.000	0.126
0.100	0.105	0.100	0.168	0.100	0.162	0.100	0.126
0.200	0.111	0.200	0.169	0.200	0.186	0.200	0.137
0.270	0.106	0.270	0.145	0.268	0.175	0.272	0.140
0.322	0.000	0.320	0.000	0.320	0.000	0.320	0.000
x=5.00	y=-0.50	x=10.0	y=0.00	x=10.0	y=-0.50	x=10.0	y=-1.00
Z(ft)	u(ft/sec)	Z(ft)	u(ft/sec)	Z(ft)	u(ft/sec)	Z(ft)	u(ft/sec)
0.000	0.060	0.000	0.120	0.000	0.099	0.000	0.110
0.100	0.060	0.100	0.120	0.100	0.099	0.100	0.110
0.200	0.061	0.200	0.119	0.200	0.094	0.200	0.075
0.254	0.069	0.273	0.101	0.272	0.074	0.268	0.072
0.320	0.000	0.319	0.000	0.321	0.000	0.321	0.000
Date	May 31, 1985			ARo = 1.8			
x=4.00	y=-0.50	x=4.00	y=0.00	x=4.00	y=0.50	x=4.00	y=1.00
Z(ft)	u(ft/sec)	Z(ft)	u(ft/sec)	Z(ft)	u(ft/sec)	Z(ft)	u(ft/sec)
0.000	0.000	0.001	0.179	0.001	0.288	0.001	0.117
0.053	0.000	0.049	0.179	0.050	0.288	0.048	0.117
0.103	0.055	0.099	0.238	0.100	0.312	0.098	0.111
0.163	0.075	0.159	0.238	0.160	0.320	0.158	0.112
0.223	0.105	0.219	0.271	0.220	0.322	0.218	0.170
0.276	0.089	0.276	0.314	0.280	0.296	0.278	0.126
0.321	0.000	0.321	0.000	0.325	0.000	0.323	0.000
x=4.00	y=1.50	x=15.5	y=3.00	x=15.5	y=4.00	x=15.5	y=5.00
Z(ft)	u(ft/sec)	Z(ft)	u(ft/sec)	Z(ft)	u(ft/sec)	Z(ft)	u(ft/sec)
0.001	0.069	0.001	0.068	0.001	0.188	0.001	0.165
0.046	0.069	0.023	0.068	0.001	0.188	0.022	0.165
0.096	0.079	0.043	0.108	0.042	0.188	0.052	0.155
0.156	0.075	0.084	0.055	0.082	0.148	0.092	0.193
0.216	0.071	0.123	0.071	0.122	0.125	0.132	0.200
0.276	0.068	0.163	0.078	0.162	0.151	0.172	0.187
0.321	0.000	0.203	0.085	0.202	0.150	0.212	0.127
		0.243	0.053	0.242	0.174	0.242	0.174
		0.274	0.086	0.273	0.154	0.269	0.210
		0.316	0.000	0.315	0.000	0.311	0.000

Table 3.1 The Original Experimental Data(continued)

Date	June 5, 1985			ARo = 1.8			
x=4.00	y=0.50	x=4.00	y=0.00	x=4.00	y=-0.50	x=15.5	y=1.00
Z(ft)	u(ft/sec)	Z(ft)	u(ft/sec)	Z(ft)	u(ft/sec)	Z(ft)	u(ft/sec)
0.001	0.078	0.001	0.296	0.001	0.177	0.001	0.000
0.048	0.078	0.051	0.296	0.056	0.177	0.047	0.000
0.098	0.064	0.101	0.353	0.106	0.191	0.087	0.112
0.158	0.122	0.161	0.324	0.166	0.183	0.147	0.123
0.218	0.102	0.221	0.347	0.116	0.213	0.207	0.078
0.282	0.092	0.277	0.321	0.277	0.196	0.267	0.086
0.327	0.000	0.322	0.000	0.322	0.000	0.312	0.000
x=15.5	y=0.00	x=15.5	y=-1.0	x=15.5	y=-2.00	x=15.5	y=-3.00
Z(ft)	u(ft/sec)	Z(ft)	u(ft/sec)	Z(ft)	u(ft/sec)	Z(ft)	u(ft/sec)
0.001	0.073	0.001	0.166	0.001	0.119		
0.049	0.073	0.063	0.166	0.060	0.119		
0.089	0.116	0.093	0.166	0.090	0.162		
0.149	0.160	0.153	0.156	0.150	0.144		
0.209	0.086	0.213	0.133	0.210	0.118		
0.266	0.152	0.281	0.140	0.273	0.142		
0.311	0.000	0.326	0.000	0.318	0.318		

Table 3.2 Average Velocity at Experimental Points

Date	October 21, 1985			ARo = 0.5		
x(ft)		y(ft)	U(ft/sec)	x(ft)	y(ft)	U(ft/sec)
5.00		0.50	0.0983	10.0	0.00	0.1075
5.00		0.25	0.1508	10.0	-0.50	0.0854
5.00		0.00	0.1575	10.0	-1.00	0.0846
5.00		-0.25	0.1221			
5.00		-0.50	0.0567			
Date	June 5, 1985			ARo = 1.8		
x(ft)		y(ft)	U(ft/sec)	x(ft)	y(ft)	U(ft/sec)
4.00		0.50	0.0850	15.5	1.00	0.7110
4.00		0.00	0.3025	15.5	0.00	0.1066
4.00		-0.500	0.1766	15.5	-1.00	0.1412
				15.5	-2.00	0.1247
Date	May 31, 1985			ARo = 1.8		
x(ft)		y(ft)	U(ft/sec)			
4.00		-0.50	0.0555			
4.00		0.00	0.2253			
4.00		0.50	0.2846			
4.00		1.00	0.1179			
4.00		1.50	0.0670			

III.2 Gauss Fitting Method

III.2.1 Velocity distribution

A Gaussian velocity profile (Eqn. 3–2) was used.

$$\frac{u(x)}{u_m(x)} = e^{[-2.772\ (\frac{y}{b(x)})^2]} \qquad [3\text{–}2]$$

As an alternative Eqn. [3–3] can be used.

$$\frac{u(x)}{u_m(x)} = e^{(-\eta^2)}$$

$$= e^{[\ -\ (\frac{y}{B(x)})^2\ ]} \qquad [3\text{–}3]$$

b(x) is the full width of the free jet which is defined by $\frac{u(x,b)}{u_m(x)} = 0.5$. B(x) is the characteristic length.

Equation [3–2] is the same as Eqn. [3–3]. This can be shown by the following transformation: In Eqn. [3–3], set $u(x)/u_m(x) = 0.5$

$$y_{[u/u_m(x)=0.5]} = B(x)\ \text{SQRT}[-\ln(0.5)]$$

$$= 0.832\ B(x)$$

$$= \frac{b(x)}{2}$$

$$\text{Full width } b(x) = 1.664\ B(x)$$

$$u(x)/u_m(x) = e^{(-\eta^2)}$$

$$= e^{[-2.772\ (\frac{y}{1.664\ B(x)})^2]}$$

$$= e^{[-2.772\ (\frac{y}{b(x)})^2]}$$

Equation [3–3] is used in the analysis of the experimental data and the Gauss fitting method.

III.2.2 Moments of velocity distribution

The characteristic length B(x), the centerline of velocity profile, the standard deviation σ and centerline velocity u_m will be calculated from the moments of the velocity distribution. The moments of a velocity distribution are defined as:

Zero moment: $$M_0 = \int_{-\infty}^{+\infty} u_x(y)\, dy \qquad [3\text{–}4]$$

First moment: $$M_1 = \int_{-\infty}^{+\infty} u_x(y)\, y\, dy \qquad [3\text{–}5]$$

Second moment: $$M_2 = \int_{-\infty}^{+\infty} u_x(y)\, (y-y_0)^2\, dy \qquad [3\text{–}6]$$

Third moment: $$M_3 = \int_{-\infty}^{+\infty} u_x(y)\, (y-y_0)^3\, dy \qquad [3\text{–}7]$$

Where y_0 is transverse coordinate of the centerline (maximum velocity). The value of y_0 and standard deviation σ are obtained from

$$y_0 = M_1 / M_0 \qquad [3\text{–}8]$$

$$\sigma^2 = M_2 / M_0 \qquad [3\text{–}9]$$

If the velocity distribution is $u(x)/u_m(x) = e^{(-\eta^2)}$, then

$$M_0 = u_m(x)\, B(x) \int_{-\infty}^{+\infty} e^{-\eta^2}\, d\eta$$

$$= \frac{\sqrt{\pi}}{2}\, u_m(x)\, B(x) \qquad [3\text{–}10]$$

$$M_1 = u_m(a)\, B(x)^2 \int_{-\infty}^{+\infty} e^{-\eta^2}\, \eta\, d\eta$$

$$= 0.0 \qquad [3\text{–}11]$$

$$M_2 = u_m(x)\, B(x)^3 \int_{-\infty}^{+\infty} e^{-\eta^2}\, \eta^2\, d\eta$$

$$= \frac{\sqrt{\pi}}{4}\, u_m(x)\, B(x)^3 \qquad [3\text{–}12]$$

Centerline $$y_0 = M_1 / M_0 = 0.0 \qquad [3\text{–}13]$$

Standard deviation σ^2

$$= M_2 / M_0$$

$$= \frac{B(x)^2}{2} \qquad [3\text{–}14]$$

The characteristic length B(x) of a free jet with Gaussian velocity distribution is $\sigma \sqrt{2}$.

III.2.3 Numerical integration

Numerical integration is used to calculate moments of experimental velocity data. Fig. (3–3) is a scheme for numerical integration. Numerical integration formulas are:

$$M_0 = \sum_{i=1}^{N} u(i)\ \Delta y(i) \qquad [3\text{–}15]$$

$$M_1 = \sum_{i=1}^{N} u(i)\ y_i\ \Delta y(i) \qquad [3\text{–}16]$$

$$m_1 = y_0 = M_1 / M_0 \qquad [3\text{–}17]$$

$$M_2 = \sum_{i=1}^{N} u(i)\ (y_i - y_0)^2\ \Delta y(i) \qquad [3\text{–}18]$$

$$M_3 = \sum_{i=1}^{N} u(i)\ (y_i - y_0)^2\ \Delta y(i) \qquad [3\text{–}19]$$

where $\Delta y(i) = y_{i+1} - y_i$ As i=2 to N–1

$$\Delta y(i) = \frac{y_{i+1} - y_i}{2} \qquad \text{As i=1 and N} \qquad [3\text{–}20]$$

The non–dimensional terms m_1, $m_2 = \frac{M_2}{M_0} = \sigma^2$, $m_3 = \frac{M_3}{M_0}$ were introduced. Two examples of fitted experimental data (Johnson and Stefan, 1988) are shown in Fig. 3–4. Almost all experimental data are outside of the fitted Gauss distributions. This is unreasonable and the main cause is that a finite number of experimental data are used in the fitting method. The method needs to be adjusted for finite (sparse) data which are near the centerline.

To make the adjustment consider that the experimental data follow an exact Gaussian velocity distribution (Eqn. 3–3). The Gauss fitting method should then give a perfect match. Two examples are shown in Fig. [3–5]. When the data are cut–off near the center of the distribution, the fit is very

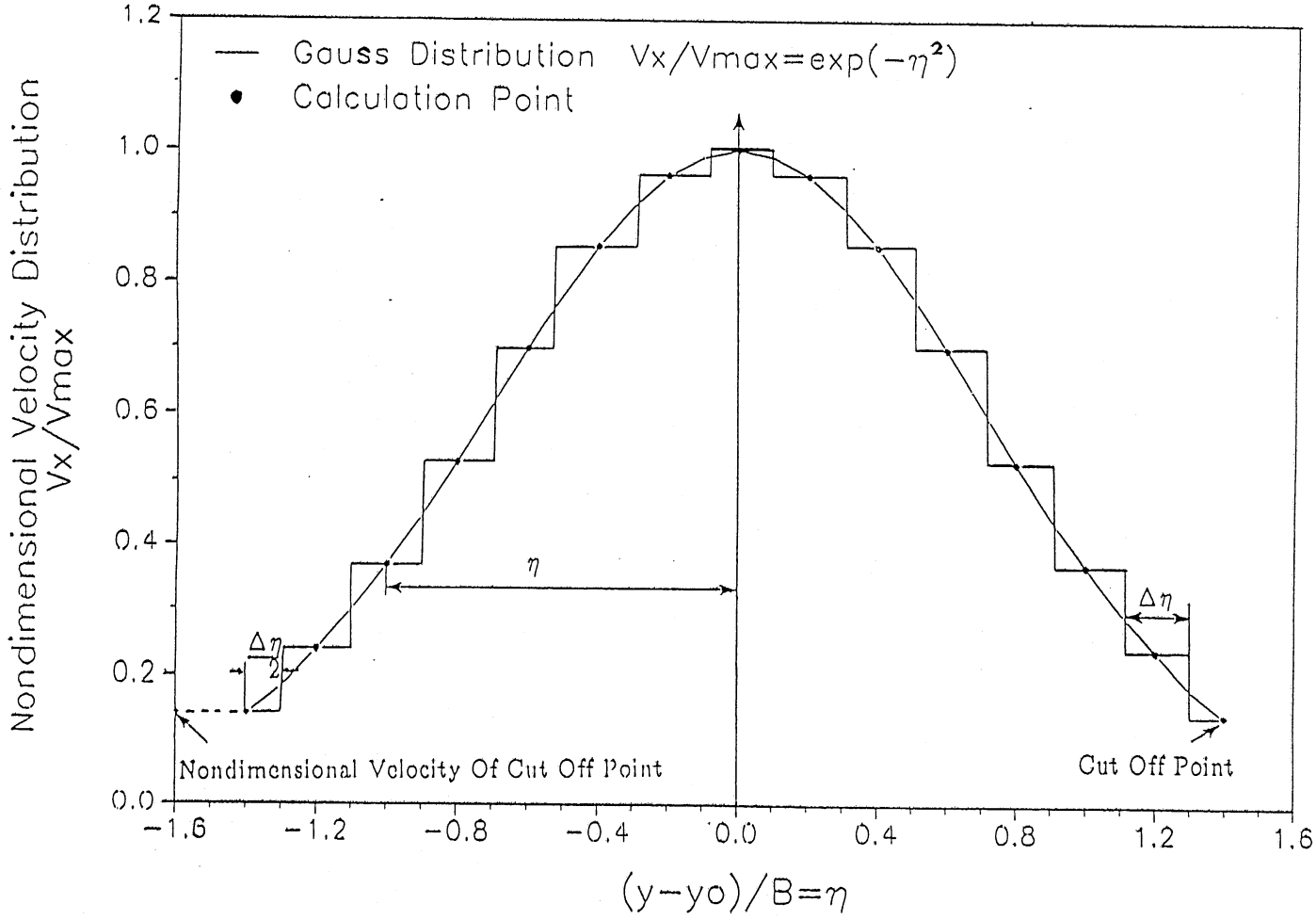

Fig. 3–3 Scheme of numerical integration (Method 1).

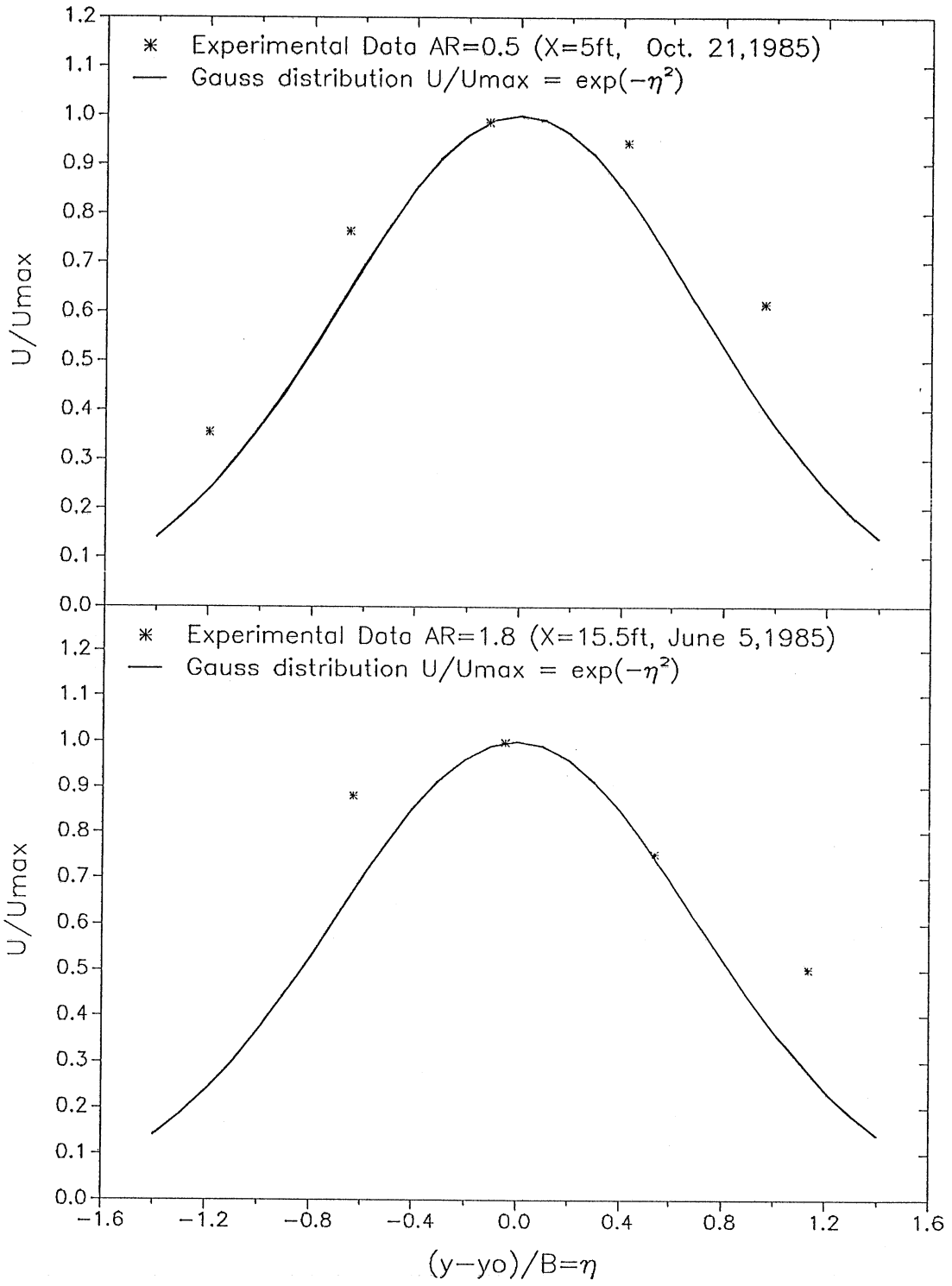

Fig. 3–4 Examples of fitted experimental data.

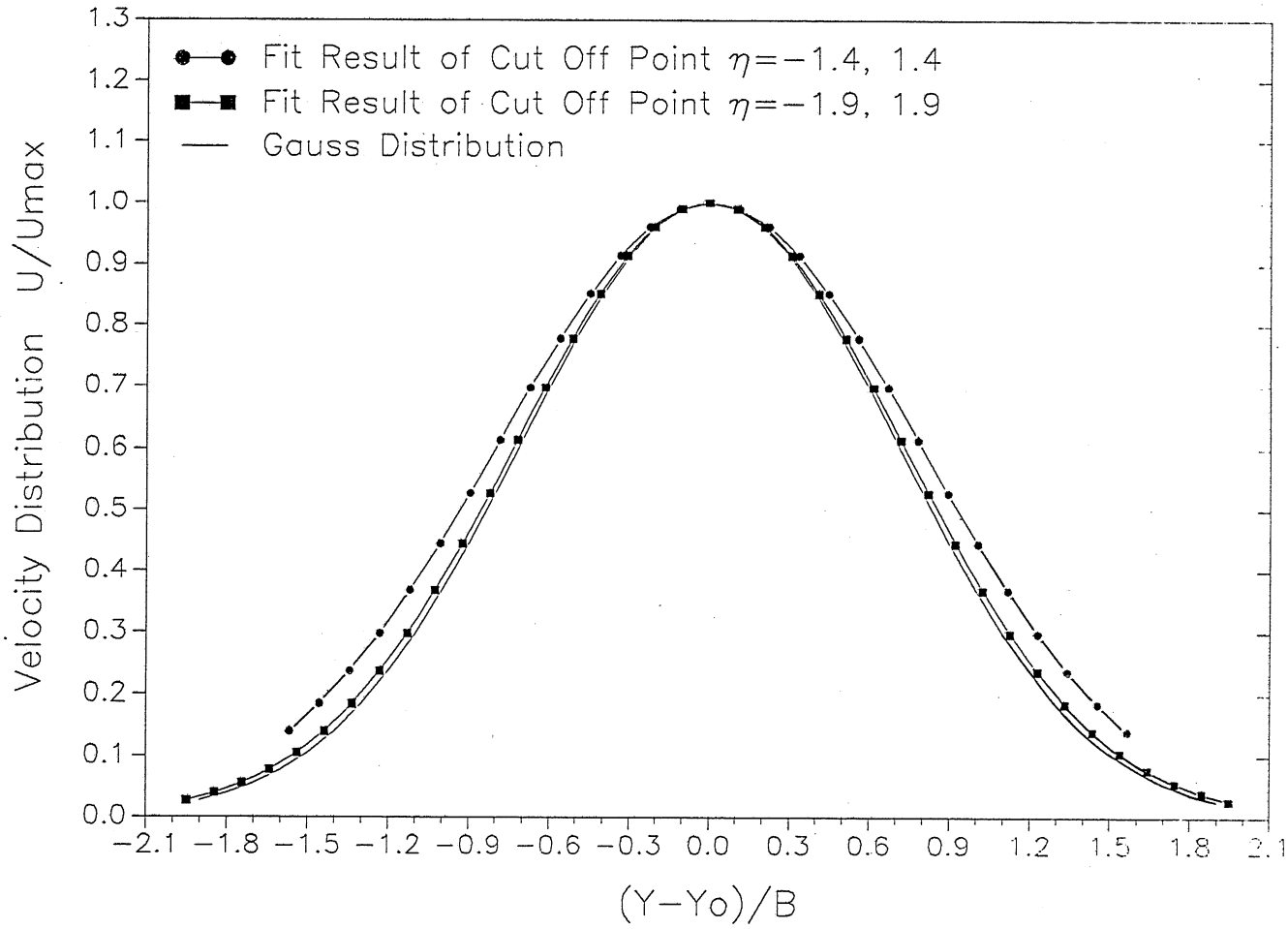

Fig. 3–5 Examples of curves fitted to a data set with perfect Gaussian distribution.

bad. If the data cut–off point is further away from center, the fit is better. The Gauss fitting method used here needs to be adapted to finite (sparse) experimental data.

III.3 Analysis of Experimental Data

Analysis of experimental data can provide centerline velocity $u_m(x)$ and full width $b(x)$.

A Gauss fitting method to analyze finite experimental data has been reported in Appendix B. Results are shown in Fig. 3–6 and Fig. 3–7. The data fit the Gaussian velocity profile well, even though the experimental data are few. The fitted result is much better than that by the standard Gauss fitting Method.

If the full width $b(x)$ of the slot jet is the distance of two points with half centerline, we have

$$b(x) = 1.664\ B(x) = 1.664\ \sigma \sqrt{2} = 2.354\ \sigma \qquad [3–21]$$

The full width $b(x)$ and the centerline velocity for the available experimental data can be obtained by the Gauss fitting method. Comparison of experimental data with the slot jet model (chapter II) is shown in Fig. 3–8. The theoretical result does not fit the experimental data. We therefore need to consider the measurement error in the experiments and the theoretical model also needs to be improved.

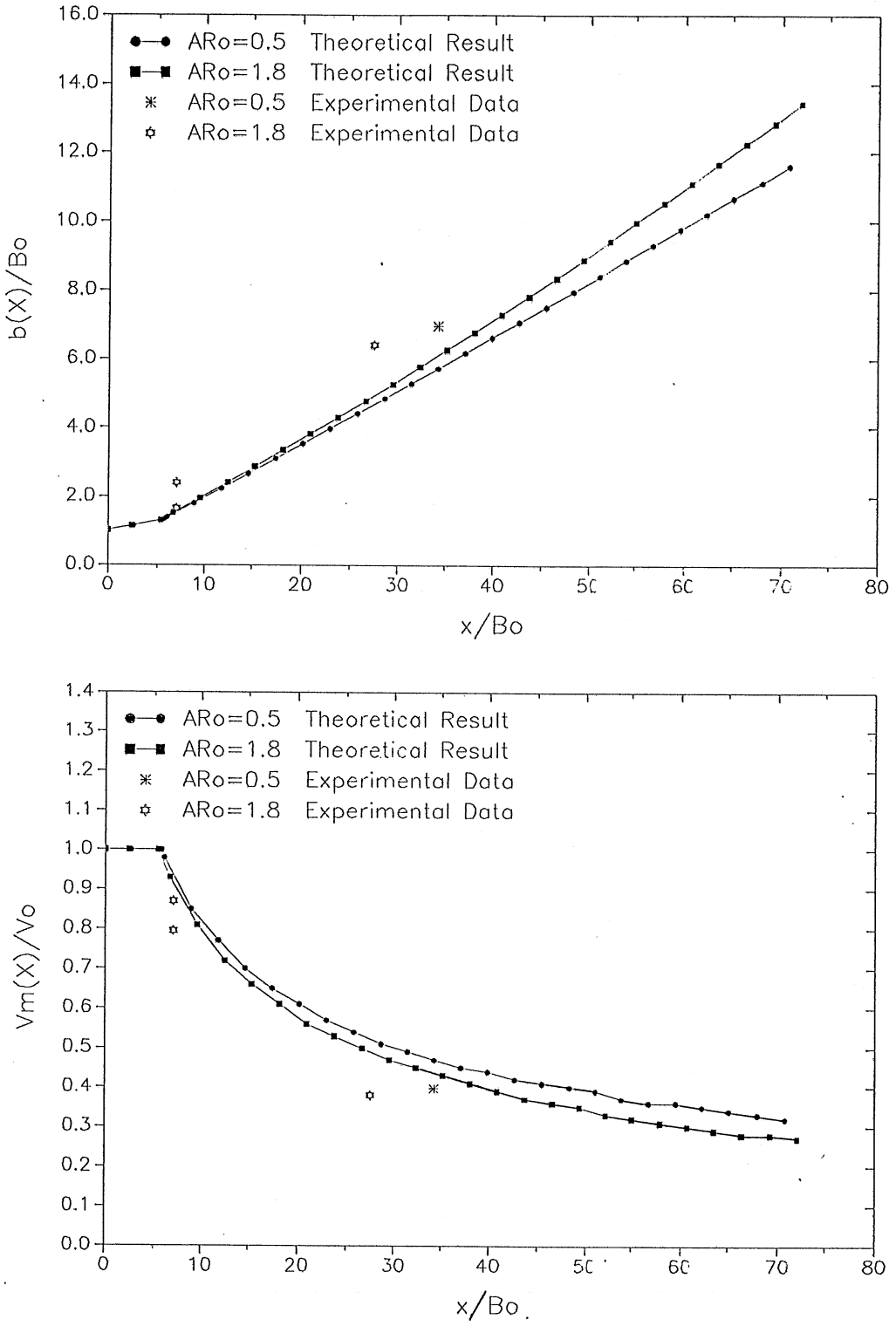

Fig. 3–6 Examples of analysis of experimental data by modified fitting method.

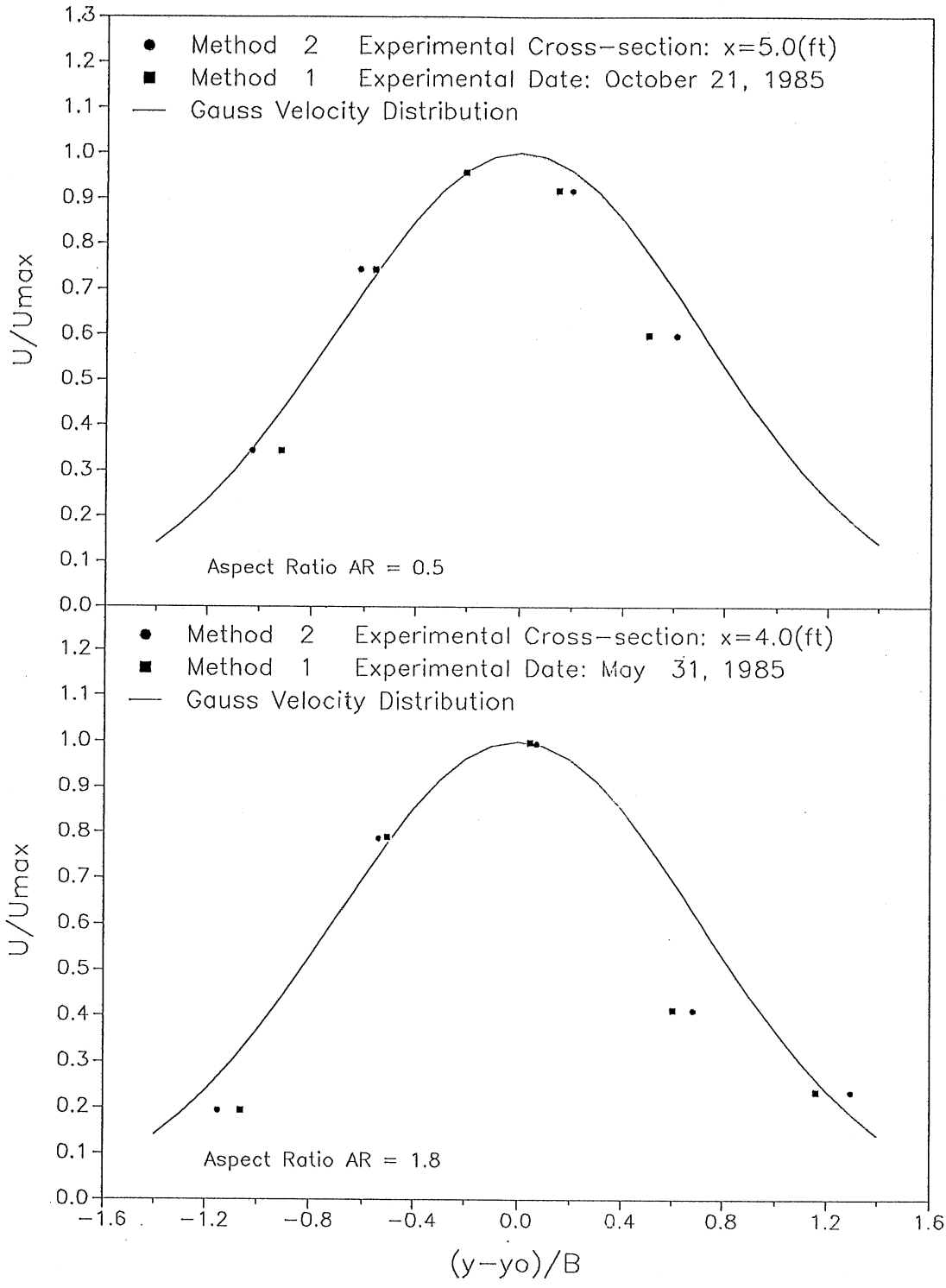

Fig. 3–7 Examples of analysis of experimental data by modified fitting method.

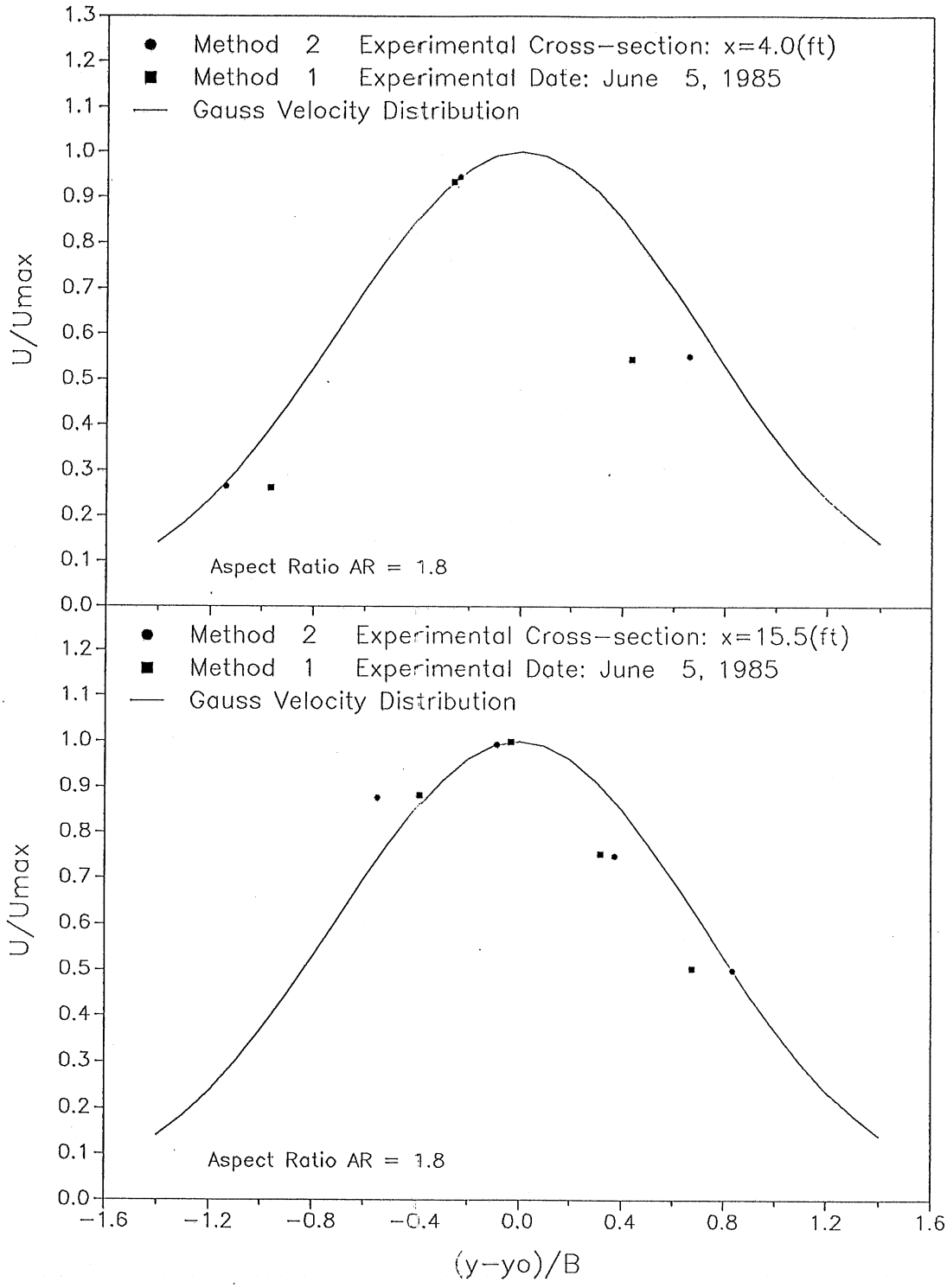

Fig. 3–8 Comparison of model prediction with experimental data for $b(x)/B_0$ and $u_m(x)/U_0$.

Chapter IV BOUNDARY EFFECTS

An integral model for a discharge into a diffuser with horizontal or sloping bottom has been developed in Chapter II. A depth averaged velocity and a constant local friction coefficient c_f were used. In a discharge with finite water depth, the vertical velocity profile is the velocity distribution in a boundary layer which can be approximated by the n–th–power law. Similarly for a discharge along a wall (wall jet) the transverse velocity profile is affected by wall friction. The local friction coefficient c_f is a function of the relative roughness and the local Reynolds number Re_x. In this chapter, the boundary effects, which include bottom effects and wall effects on momentum, will be studied.

IV.1 Bottom Effects on Momentum

Bottom effects include vertical velocity profile effects and shear stress on the wall. The velocity profile in the boundary layer is dependent on the inflow Reynolds number $Re_0 = \frac{U_0 H_0}{\nu}$. The local friction coefficient c_f for shear stress is dependent on Re_0 and the relative roughness. With reference to Fig. 20.18 and Fig. 21.11 (Schlichting, 1960), it is necessary to consider three regimes: *hydraulically smooth regime; transition regime; completely rough regime.* In this study, we consider two regimes: *hydraulically smooth regime* and *completely rough regime.* We assume that *the completely rough regime* includes *the transition regime.* For *smooth regime*, the local friction coefficient is independent of relative roughness but dependent on Reynolds number, as shown in equations [4–5] and [4–6]. For *completely rough regime*, c_f is independent of Reynolds number, but dependent on relative roughness.

IV.1.1 Bottom effects in horizontal channel

The turbulent flow in a channel of finite water depth is different from turbulent flow over a flat plate (Schlichting, 1960), where water depth is infinite and free stream velocity U_∞ is a constant. The boundary layer in a channel is confined to finite water depth and is similar to the turbulent flow through a pipe. The characteristic length of a pipe is the diameter 2R, but the characteristic length of a channel discharge is the water depth H_0. An empirical turbulent velocity profile in a pipe is

$$\frac{u}{U_\infty} = \left(\frac{y}{R}\right)^{\frac{1}{n}} \qquad [4\text{–}1a]$$

where the exponent 1/n varies slightly with the Reynolds number as shown in Fig. 20.3 (Schlichting, 1960). Reynolds number of inflow in the experiments (Johnson and Stefan, 1988) is

$$Re_0 = \frac{U_0 H_0}{\nu} \approx 1.0 \times 10^4$$

Reynolds number of an equivalent pipe flow is

$$Re = \frac{U_0 2R}{\nu} = 2 \frac{U_0 H_0}{\nu} = 2 Re_0$$

According to Fig. 20.3 (Schlichting, 1960), n ≈ 6.6 for the laboratory studies by Johnson and Stefan, 1988. For field studies, assuming U_0 = 1.0 ft/s, H_0 = 1.0 ft as lower bounds, and $\nu = 10^{-5}$ ft²/s, we obtain

$$Re_0 \approx \frac{1.0 \times 1.0}{10^{-5}} = 1.0 \times 10^5$$

The exponent n ≈ 7 seem appropriate for field studies. Velocity U_0 and water depth H_0 are different from one field situation to another. Therefore in this model n can be changed according to Reynolds number Re_0. For the laboratory studies (Johnson and Stefan, 1988), we will use a constant n = 7. In developing flow the velocity profile is (Schlichting, 1960)

$$\frac{u}{U_\infty} = (z/\delta)^{\frac{1}{n}} \qquad [4\text{–}1b]$$

where $\delta = \delta(x)$ denotes the boundary layer thickness, z is depth coordinate (origin at the bottom). **U_∞ is the water surface velocity $u_s(x,y)$** and u is the local velocity u(x,y,z) at point (x,y,z).

The boundary layer thickness $\delta(x)$ is the water depth when the flow is fully developed as in the case of a long channel. The inflow into lakes or reservoirs and the experimental channel discharge are a fully developed turbulent flow. In a horizontal channel therefore

$$\delta(x) = H_0 = \text{constant} \qquad [4\text{–}2a]$$

In a sloping channel, both boundary layer thickness $\delta(x)$ and water depth H(x) change with distance x. For most practical cases the sloping angle β is much less than 10° and we can assume

$$\delta(x) = H(x) = H_0 + x \tan\beta \qquad [4\text{–}2b]$$

One can easily derive by integration the ratio of mean velocity to free shear velocity U/U_∞ from [4–1b] (Schlichting, 1960)

$$U/U_\infty = \frac{2n^2}{(n+1)(2n+1)} = \chi \qquad [4\text{–}3]$$

where U is mean flow velocity. χ is a coefficient which is dependent on velocity profile [4–1b].

In the boundary layer, the shear stress on the wall can be written as

$$\tau_0 = \frac{1}{8} \lambda \rho U^2 . \qquad [4\text{–}4a]$$

The frictional resistance coefficient λ of a smooth pipe, according to *Blasius formula* (Schlichting, 1960) is

$$\lambda = 0.3164 \left(\frac{U\ 2R}{\nu} \right)^{-\frac{1}{4}} . \qquad [4\text{–}4b]$$

Substituting equation [4–4b] into [4–4a], the shear stress is

$$\tau_0 = 0.03325\ \rho\ U^{7/4}\ \nu^{1/4}\ R^{-1/4} \qquad [4\text{–}4c]$$

Using equation [4–3] and substituting boundary layer thickness $\delta(x)$ into R, the local friction coefficient c_f for channel discharges is

$$\begin{aligned} c_f/2 &= \frac{\tau_0}{\rho\ U_\infty^2} \\ &= 0.03325 \left(\frac{U}{U_\infty} \right)^{7/4} \left(\frac{\nu}{U_\infty \delta(x)} \right)^{1/4} \\ &= 0.03325\ \chi^{7/4} \left(\frac{\nu}{U_\infty \delta(x)} \right)^{1/4} \\ &= \theta \left(\frac{\nu}{U_\infty \delta(x)} \right)^{1/4} \end{aligned} \qquad [4\text{–}4d]$$

where $\theta = 0.03325\ \chi^{7/4}$. Typical Re_0, n, χ, and θ values are shown in Table 4.1. Coefficient θ is moderately sensitive to exponent n.

Table 4.1 Parameters of velocity profile and friction coefficients.

Re_0	n	χ	θ	Situation
2.0×10^3	6.0	0.791	0.022	Laboratory
1.7×10^4	6.6	0.807	0.023	Laboratory
5.5×10^4	7.0	0.817	0.024	
5.5×10^5	8.8	0.850	0.025	Field
1.0×10^6	10	0.865	0.026	Field
1.6×10^6	10	0.865	0.026	Field

For experimental conditions, Reynolds numbers are the order of 10^4. For field conditions, Reynolds numbers are typically larger than 10^5. For a horizontal channel discharge, substituting [4–2a] into [4–4d], gives

$$c_f/2 = \theta \left(\frac{\nu}{u_s(x,y)\ H_o} \right)^{1/4} \qquad [4–5]$$

For a sloping channel discharge, substituting [4–2b] into [4–4d], gives

$$c_f/2 = \theta \left(\frac{\nu}{u_s(x,y)\ (H_o + x \tan\beta)} \right)^{1/4} \qquad [4–6]$$

For a water temperature of about 15° C to 20° C, which is in the range of water temperatures in the experiments of Johnson et al. (1988), we use

$$\nu = 1.2 \times 10^{-5}\ (ft^2/sec)$$

IV.1.1.1 Continuity and momentum equations in fully developed flow region

In order to consider velocity profile effects on momentum, a schematic for a horizontal channel discharge is show in Fig. 4–1. The momentum has to be corrected to account for the vertical velocity distribution profile. For the transverse velocity profile a Gaussian velocity distribution in the cross–section is used again. The flow rate Q(x) and momentum M(x) can be written as

$$Q(x) = 2 \int_0^{\infty} dy \int_0^{H_o} u(x,y,z)\ dz \qquad [4–7]$$

$$M(x) = 2 \int_0^{\infty} dy \int_0^{H_o} \rho\ u^2(x,y,z)\ dz \qquad [4–8]$$

The velocity similarity assumptions are

$$u(x,y,z)/u_s(x,y) = g(\zeta) \qquad [4–9]$$

$$u_s(x,y)/u_m(x) = f(\eta) \qquad [4–10]$$

where $\eta = y/b(x)$ and $\zeta = z/H_o$. b(x) is the width of the horizontal discharge shown in Fig. 4–1 (a). Using [4–9] and [4–10], we obtain

$$Q(x) = 2\ H_o\ u_m(x)\ b(x) \int_0^{\infty} f(\eta)d\eta \int_0^{1} g(\zeta)d\zeta$$

$$= D_3\ H_o\ u_m(x)\ b(x) \qquad [4–11]$$

$$M(x) = 2\rho H_o\ u_m^2(x)\ b(x) \int_0^{\infty} f^2(\eta)d\eta \int_0^{1} g^2(\zeta)d\zeta$$

$$= D_4\ \rho\ H_o\ u_m^2(x)\ b(x) \qquad [4–12]$$

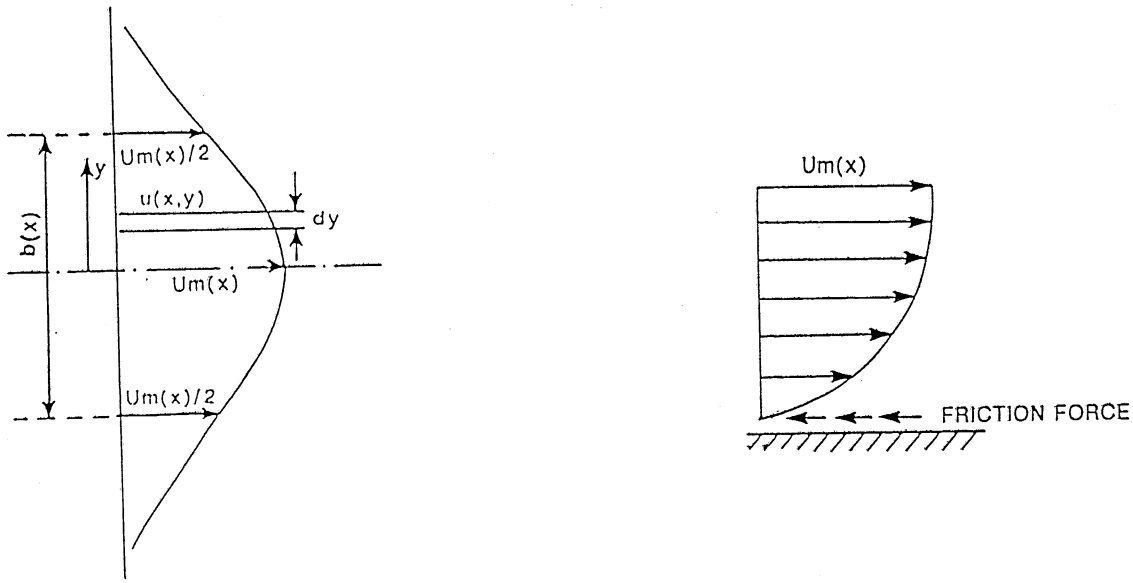

Fig. 4–1 Schematic of horizontal channel discharge with boundary effects.

where $$D_1 = \int_0^1 g(\zeta)d\zeta \qquad [4\text{–}13]$$

$$D_2 = \int_0^1 g^2(\zeta)d\zeta \qquad [4\text{–}14]$$

$$D_3 = 2 \int_0^\infty f(\eta)d\eta \int_0^1 g(\zeta)d\zeta = C_6 D_1 \qquad [4\text{–}15]$$

$$D_4 = 2 \int_0^\infty f^2(\eta)d\eta \int_0^1 g^2(\zeta)d\zeta = C_7 D_2 \qquad [4\text{–}16]$$

D_1, D_2 are coefficients dependent on the velocity profile. C_6 and C_7 are defined in Chapter II. Considering entrainment and friction, the rate of change of flow rate and momentum are, respectively

$$\begin{aligned}\frac{dQ(x)}{dx} &= \frac{d}{dx}\left[D_3 H_o u_m(x) b(x) \right] \\ &= D_3 H_o \left[u_m(x) \frac{db(x)}{dx} + b(x) \frac{du_m(x)}{dx} \right] \\ &= \int_0^{H_o} 2 v_e dz \\ &= 2 \alpha_e D_1 u_m(x) H_o \end{aligned} \qquad [4\text{–}17]$$

and

$$\begin{aligned}\frac{dM(x)}{dx} &= \frac{d}{dx}\left[D_4 \rho H_o u_m^2(x) b(x) \right] \\ &= \rho D_4 H_o \left[b(x) 2u_m(x) \frac{du_m(x)}{dx} + u_m^2(x) \frac{db(x)}{dx} \right] \\ &= -D_x \\ &= -2 \int_0^\infty \tau_o(x,y)dy \end{aligned} \qquad [4\text{–}18]$$

If the friction factor is for a smooth wall as is appropriate for the laboratory experiments, [4–18] is

$$\begin{aligned}\frac{dM(x)}{dx} &= -2 \int_0^\infty \rho c_f/2 \, u_s(x,y)^2 \, dy \\ &= -2\rho \int_0^\infty \theta \left[u_s(x,y)H_o/\nu\right]^{-0.25} u_s(x,y)^2 \, dy \\ &= -2\theta\rho \left[H_o/\nu\right]^{-0.25} u_m(x)^{1.75} b(x) \int_0^\infty f(\eta)^{1.75}d\eta \end{aligned} \qquad [4\text{–}19a]$$

If the local friction coefficient c_f is in the *completely rough regime*, equation [4–18] is

$$\frac{dM(x)}{dx} = -2 \int_0^\infty \rho c_f/2 \; u_s(x,y)^2 \; dy$$

$$= -\rho c_f \int_0^\infty u_s(x,y)^2 \; dy$$

$$= -\rho c_f \; u_m(x)^2 \; b(x) \int_0^\infty f(\eta)^2 d\eta \qquad [4–19b]$$

[4–17] with [4–19a], gives

$$u_m(x) \frac{db(x)}{dx} + b(x) \frac{du_m(x)}{dx} = D_5 \; u_m(x) \qquad [4–20a]$$

$$2b(x) \frac{du_m(x)}{dx} + u_m(x) \frac{db(x)}{dx} = D_6 D_7 \; u_m(x)^{0.75} \; b(x) \qquad [4–20b]$$

[4–17] with [4–19b], gives

$$\frac{d}{dx} \{ \ln[C_6 H_o \; u_m(x) \; b(x)] \} \; b(x) = D_5 \qquad [4–20c]$$

$$\frac{d}{dx} \{C_7 \rho H_o u_m^2(x) b(x)] \} = D_{6o} \qquad [4–20d]$$

where $$D_5 = 2 \frac{D_1}{D_3} \alpha_e = 2 \frac{\alpha_e}{C_6} \qquad [4–21]$$

$$D_6 = - \frac{2\theta}{D_4} H_o^{-1.25} \nu^{0.25} \qquad [4–22]$$

$$D_7 = \int_0^\infty f(\eta)^{1.75} d\eta \qquad [4–23a]$$

$$D_{6o} = - 0.5 \; c_f \frac{C_7}{D_4 H_o} = - \frac{c_f}{2 D_2 H_o} \qquad [4–23b]$$

Rearranging [4–20a] and [4–20b], we obtain

$$\frac{du_m(x)}{dx} = D_6 D_7 \; u_m(x)^{0.75} - D_5 \frac{u_m(x)}{b(x)} \qquad [4–24a]$$

$$\frac{db(x)}{dx} = 2D_5 - D_6 D_7 \; b(x) \; u_m(x)^{-0.25} \qquad [4–24b]$$

Rearranging [4–20c] and [4–20d], we obtain

$$\frac{d}{dx} \left[\frac{u_m(x)}{U_o}\right] + D_{6o} \frac{u_m(x)}{U_o} + D_5 A_3 \exp(D_{6o} x) \left[\frac{u_m(x)}{U_o}\right]^3 = 0 \qquad [4–25a]$$

$$\frac{b(x)}{B_o} = \left[\frac{U_o}{u_m(x)}\right]^2 \frac{\exp(-D_{6o} x)}{C_7} \qquad [4–25b]$$

Using the 4th order Runge–Kutta method, we can obtain a numerical solution for $u_m(x)$ and $b(x)$ from differential equations [4–24] and [4–25]. Using the velocity distribution function [4–2], coefficients are

$$D_1 = \int_0^1 g(\zeta)\, d\zeta = \int_0^1 \zeta^{1/n}\, d\zeta = \frac{n}{n+1}$$

$$D_2 = \int_0^1 g^2(\zeta)\, d\zeta = \int_0^1 \zeta^{2/n}\, d\zeta = \frac{n}{n+2}$$

$$D_7 = \int_0^\infty f(\eta)^{1.75} d\eta = \int_0^\infty [e^{-2.772\eta^2}]^{1.75}\, d\eta = 0.4024$$

We will consider the flow development region separately in the next section, and then obtain the complete model of a horizontal channel discharge.

IV.1.1.2 The flow development region

Fig. 2–11 is a definition sketch of the flow–development region. All symbols used here are the same as in section II.2.3, but it is necessary to consider the effects of the velocity profile with depth. The flow rate and momentum in the cross section are, respectively,

$$\begin{aligned} Q(x) &= 2\int_0^{H_0} u(x,y,z)dz\; y_1(x) + 2\int_0^{H_0} dz \int_{y_1}^\infty u(x,y,z)dy \\ &= 2D_1U_0H_0\,[\, y_1(x) + A_6\, b_0(x)] \end{aligned} \qquad [4–26]$$

$$\begin{aligned} M(x) &= 2\int_0^{H_0} \rho u(x,y,z)^2 dz\; y_1(x) + 2\int_0^{H_0} dz \int_{y_1}^\infty \rho u(x,y,z)^2 dy \\ &= 2\rho D_2 U_0^2 H_0\,[\, y_1(x) + A_7\, b_0(x)] \end{aligned} \qquad [4–27]$$

where $A_6 = \int_0^\infty f(\xi)\, d\xi$

$$u_s(x,y) = U_0\, f(\xi)$$

$$\xi = [y - y_1(x)]/b_0(x)$$

$$f(\xi) = \exp(-0.693\, \xi^2)$$

where $b_o(x)$ is a half–width of the shear layer in the flow development region shown in Fig. 2–11. Considering entrainment and friction, we obtain

$$\frac{dQ(x)}{dx} = 2D_1U_oH_o \{\frac{dy_1(x)}{dx} + \frac{d}{dx}[A_6b_o(x)]\}$$
$$= \int_o^{H_o} 2\ v_e\ dz$$
$$= 2\ D_1\ \alpha_e{}^o\ U_o\ H_o \qquad [4–28]$$

and

$$\frac{dM(x)}{dx} = 2\rho D_2U_o^2H_o\{\frac{dy_1(x)}{dx} + \frac{d}{dx}[A_7b_o(x)]\}$$
$$= -2\int_o^{\infty} \frac{1}{2}c_f\rho u_s(x,y)^2\ dy \qquad [4–29a]$$

If the friction factor is for smooth wall, [4–29a] is

$$\frac{dM(x)}{dx} = -2\int_o^{\infty} \theta\ [u_s(x,y)H_o/\nu]^{-0.25}\rho u_s(x,y)^2\ dy$$
$$= -\ 2\theta\rho\ [H_o/\nu]^{-0.25} \int_o^{\infty} u_s(x,y)^{1.75}\ dy$$
$$= -\ 2\theta\rho\ [H_o/\nu]^{-0.25}U_o{}^{1.75}[y_1(x) + D_{70}b_o(x)] \qquad [4–29b]$$

where $D_{70} = \int_o^{\infty} f(\xi)^{1.75}d\xi = 2\ D_7$.

If c_f is a constant in *the completely rough regime*, [4–29a] is

$$\frac{dM(x)}{dx} = -\rho c_f\ U_o{}^2\ [y_1(x) + A_7b_o(x)] \qquad [4–30]$$

and with [4–28]

$$\frac{dy_1(x)}{dx} + \frac{d}{dx}[A_6b_o(x)] = \alpha_e{}^o \qquad [4–31]$$

[4–29b] can be written as

$$D_8\ [y_1(x) + D_{70}\ b_o(x)] = \frac{dy_1(x)}{dx} + \frac{d}{dx}[A_7b_o(x)] \qquad [4–32a]$$

where $D_8 = -\ \frac{\theta}{D_2}\ H_o{}^{-1.25}\ [U_o/\nu]^{-0.25}$. [4–32b]

With [4–30], we have

$$D_{6o}\ [y_1(x) + A_7\ b_o(x)] = \frac{dy_1(x)}{dx} + \frac{d}{dx}[A_7b_o(x)] \qquad [4–33]$$

With [4–31] and [4–32a], two differential equations are

$$(A_6–A_7)\frac{db_o(x)}{dx} = \alpha_e^o - D_8[y_1(x) + D_{70}\, b_o(x)] \qquad [4–34]$$

$$(A_6–A_7)\frac{dy_1(x)}{dx} = - A_7\, \alpha_e^o + D_8A_6[y_1(x) + D_{70}\, b_o(x)] \qquad [4–35]$$

with [4–31] and [4–33], we have two differential equations

$$(A_6–A_7)\frac{db_o(x)}{dx} = \alpha_e^o - D_{60}[y_1(x) + A_7\, b_o(x)] \qquad [4–36]$$

$$(A_6–A_7)\frac{dy_1(x)}{dx} = - A_7\, \alpha_e^o + D_{60}A_6[y_1(x) + A_7\, b_o(x)] \qquad [4–37]$$

By combining the flow development region with the fully developed flow region, a model of jet–like free surface flow over horizontal bottom is formed. We assume n =7 for the boundary layer velocity profile for the laboratory study. Figs. 4–2 to Fig. 4–4 show a comparison of the numerical results with experimental data (Johnson and Stefan, 1988). Experimental data match the numerical results with the 1/7–th–power law better than those with a constant velocity over depth as presented in Chapter II. Fig. 4–5 shows the effect of aspect ratio AR_o on jet dimensions. Fig. 4–6 shows the relationship between dilution $Q(x)/Q_o$ and aspect ratio AR_o. Figs. 4–7 and Fig. 4–8 show the changes of Reynolds number ($Re = \frac{u_m(x)\, H_o}{\nu}$) and local friction coefficient c_f with x. For more exact theoretical studies, n = constant is not the very best choice because Re decreases with x. n should decrease with x, especially, for small AR_o. Similarly c_f = constant is not fully exact because c_f increases with x. However, the variations of both n and c_f are small and therefore not considered herein.

IV.1.2 Bottom effects in sloping channel

In typical lake or reservoir situations the channel bottom would be sloping. A schematic of a sloping channel shown in Fig. 4–9 is used to consider the increasing water depth. The local friction coefficient c_f has been shown in equation [4–6]. We will analyze the sloping channel discharge beginning with the basic equations of motion.

IV.1.2.1 Continuity and momentum equations in fully developed flow region

Using the similarity hypothesis for velocity profiles the flow rate Q(x) and momentum M(x) in the cross–section are, respectively,

$$\begin{aligned} Q(x) &= 2 \int_0^{H(x)} dz \int_0^{\infty} u(x,y,z)dy \\ &= 2\, u_m(x)\, b(x)\, H(x) \int_0^1 g(\zeta)d\zeta \int_0^{\infty} f(\eta)d\eta \\ &= D_3\, u_m(x)\, b(x)\, H(x) \end{aligned} \qquad [4–38]$$

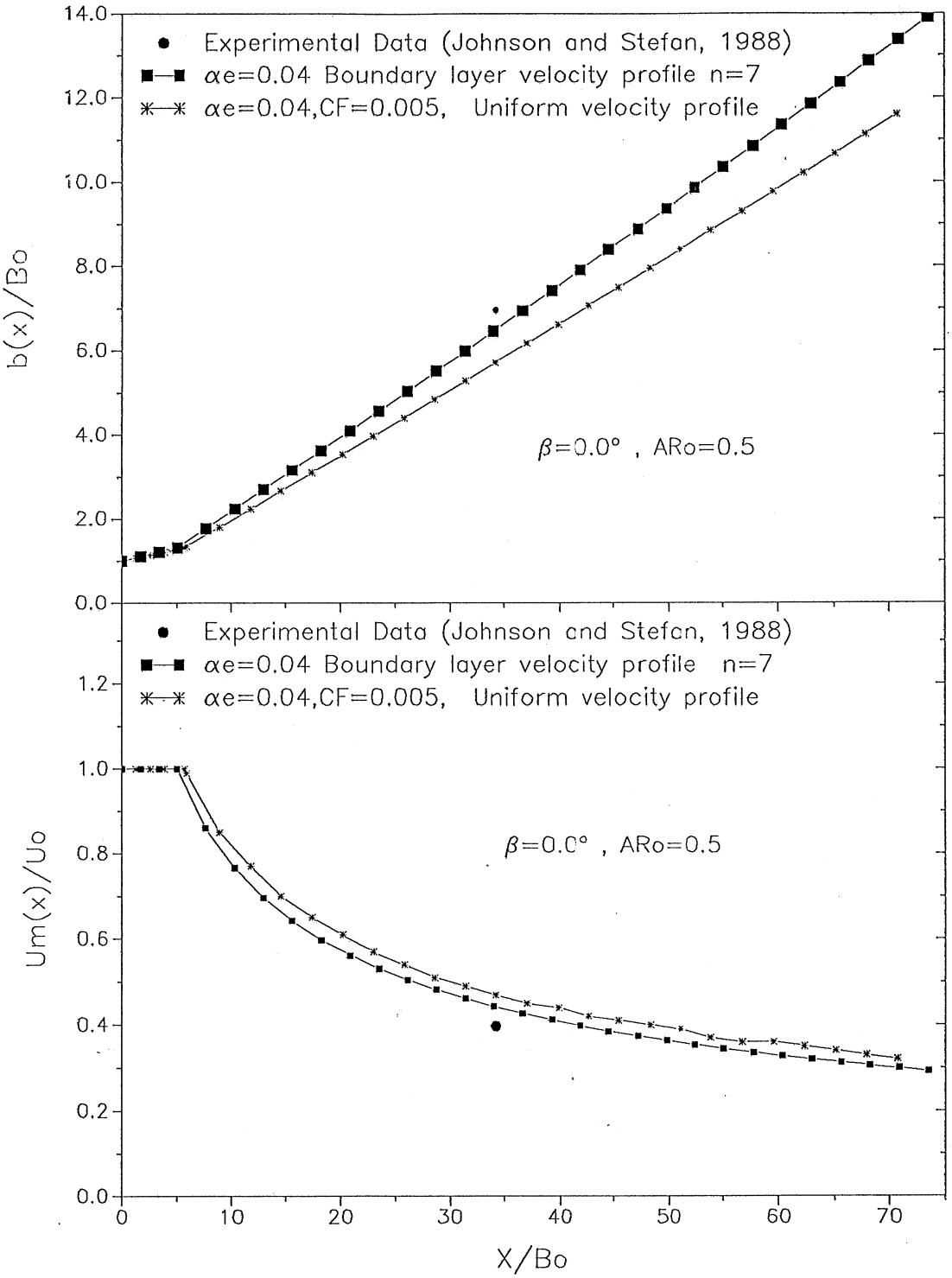

Fig. 4–2 Comparison of numerical results with experimental data for dimensions of horizontal channel discharges at $AR_o = 0.5$.

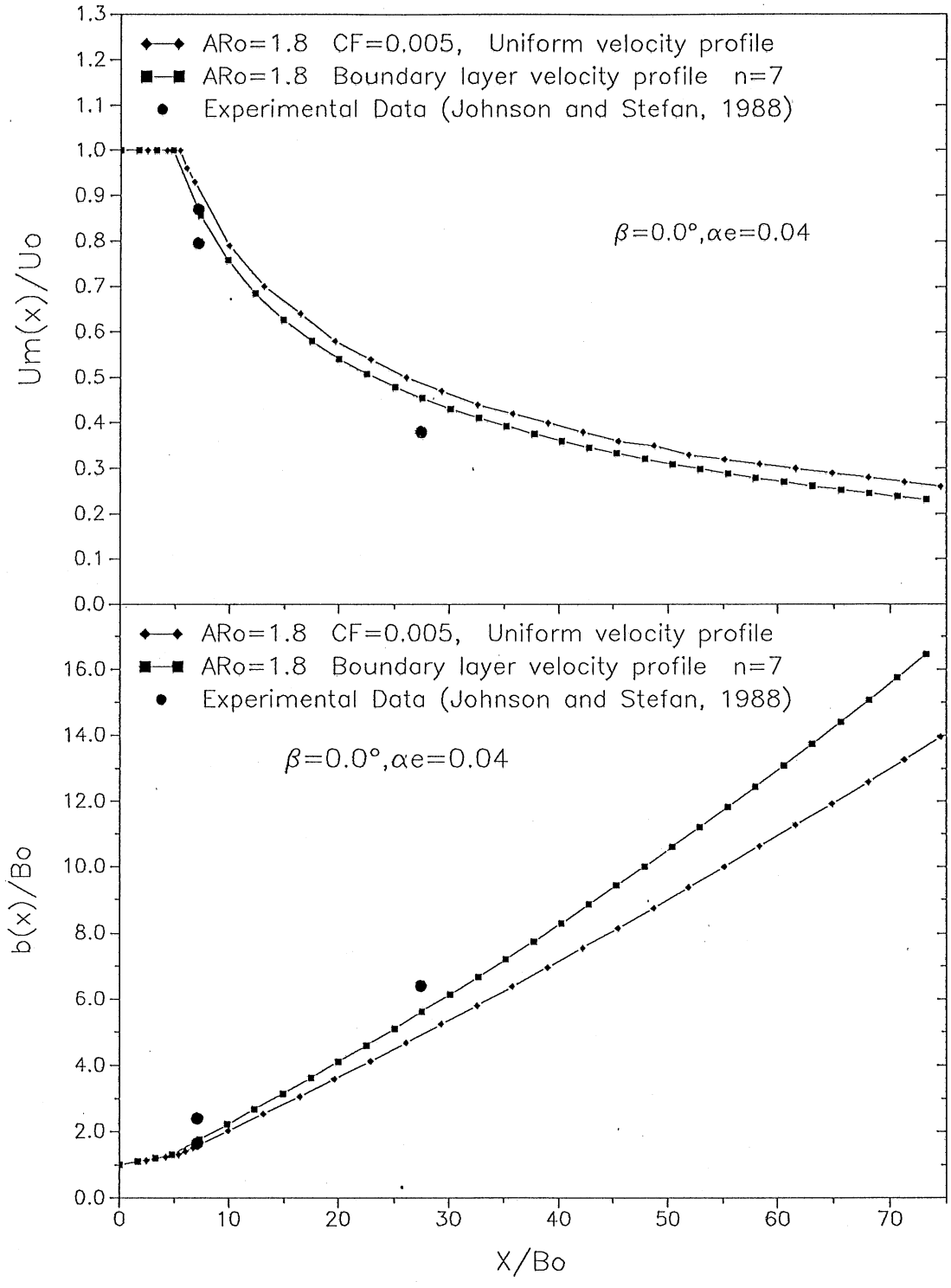

Fig. 4–3 Comparison of numerical results with experimental data for dimensions of horizontal channel discharges at $AR_o = 1.8$.

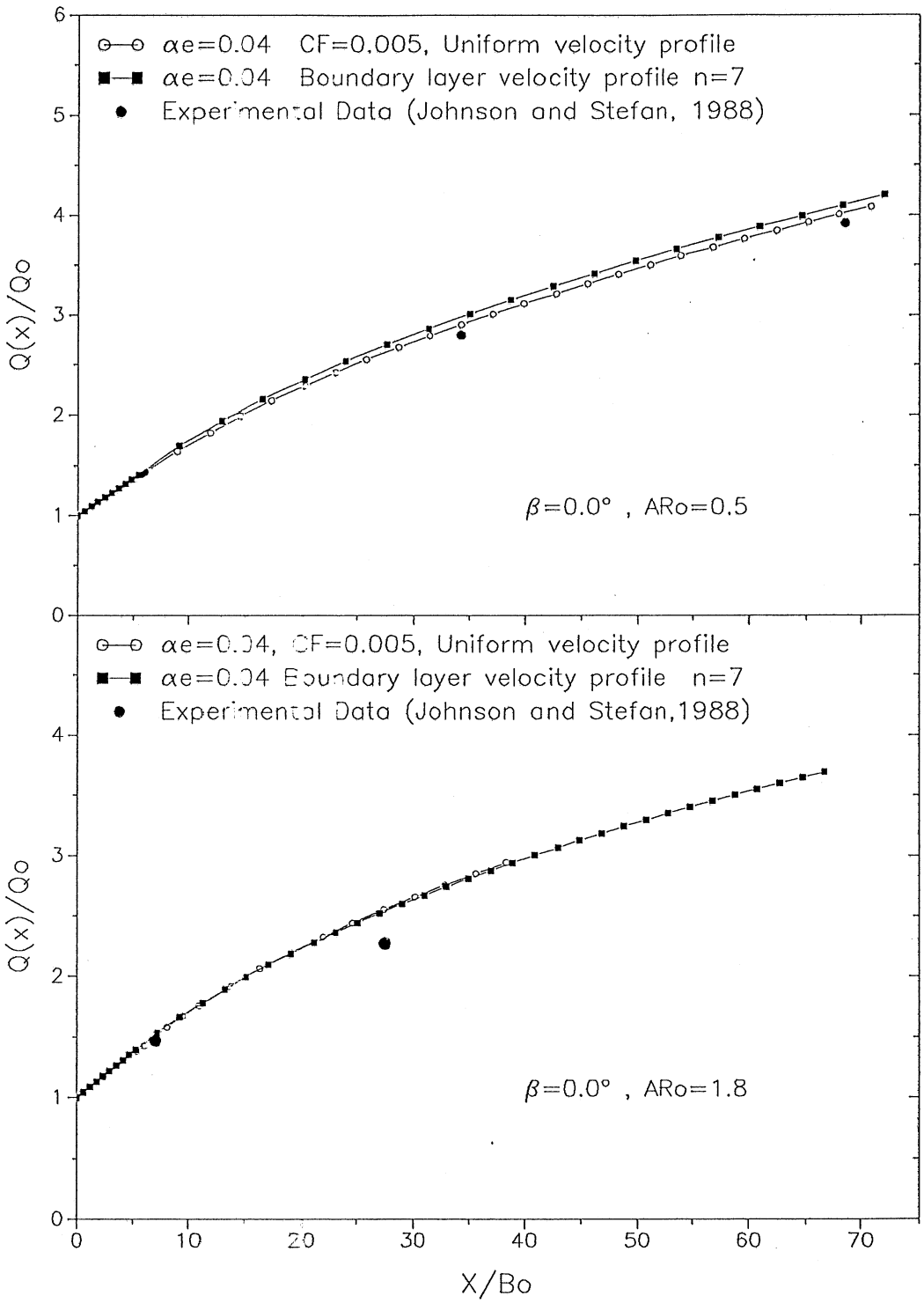

Fig. 4–4 Comparison of numerical results with experimental data for dilution of horizontal channel discharges.

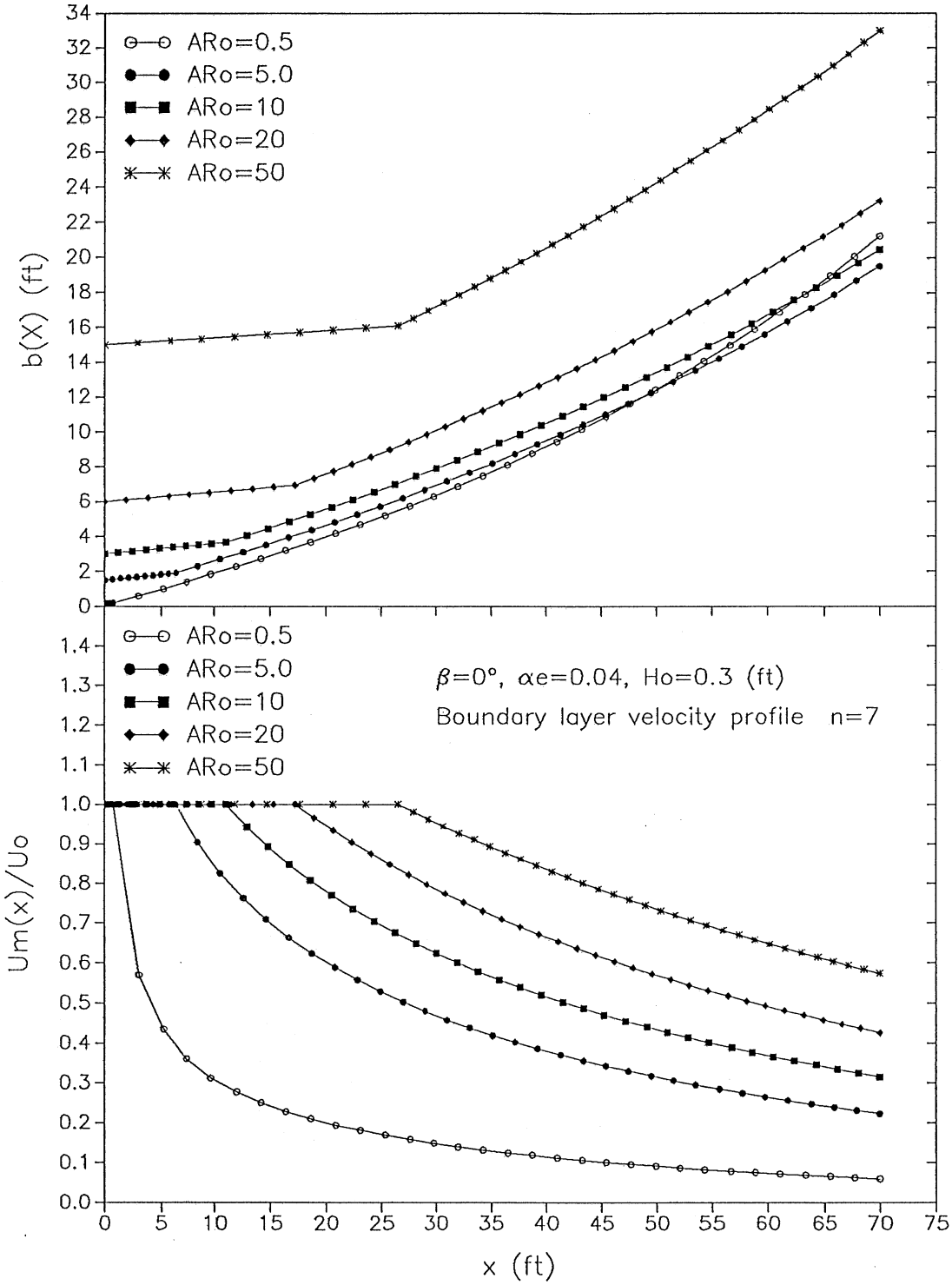

Fig. 4–5 Sensitivity of jet dimensions to aspect ratio AR_o.

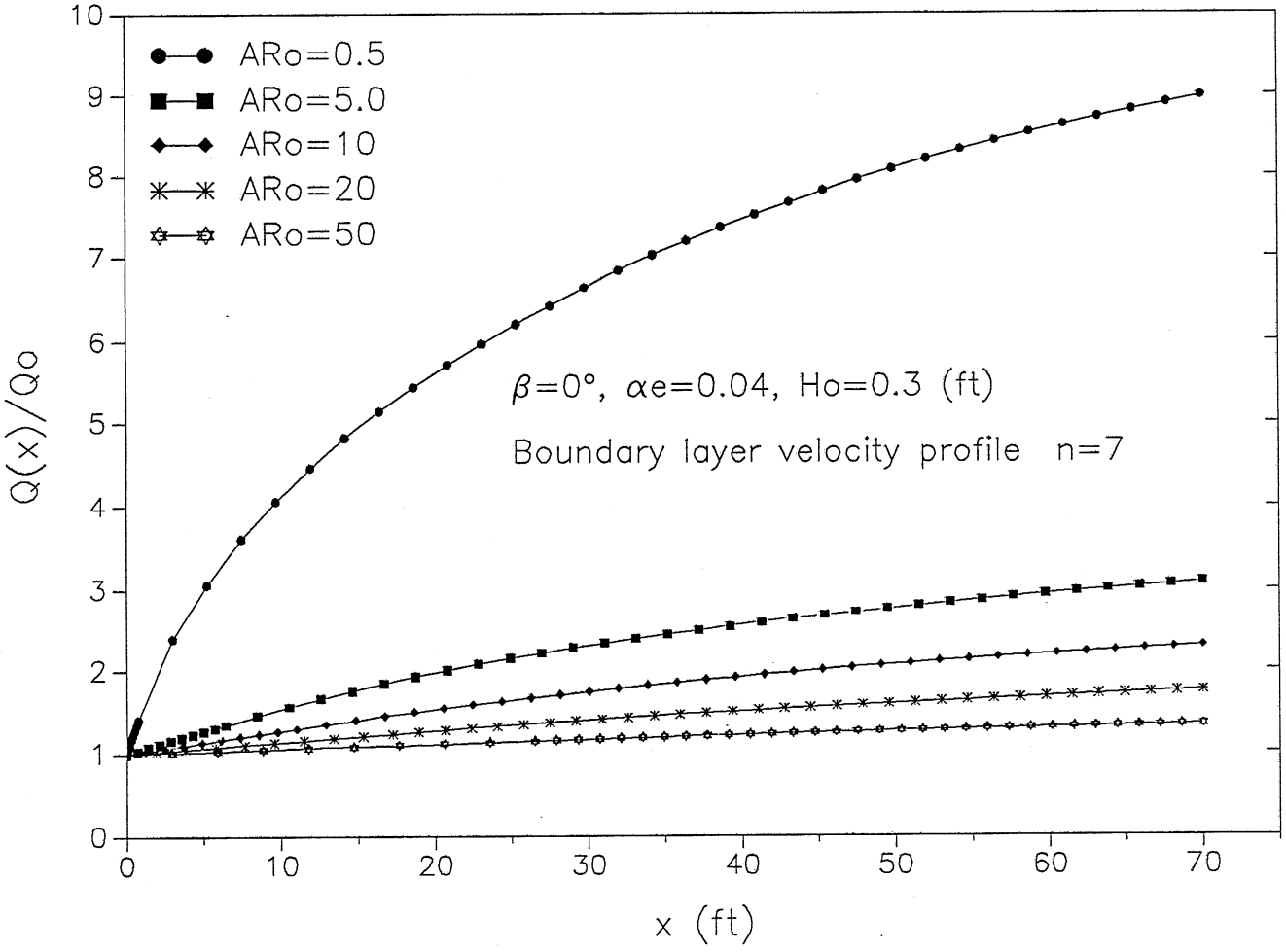

Fig. 4–6 Sensitivity of dilution to aspect ratio AR_o in horizontal channel.

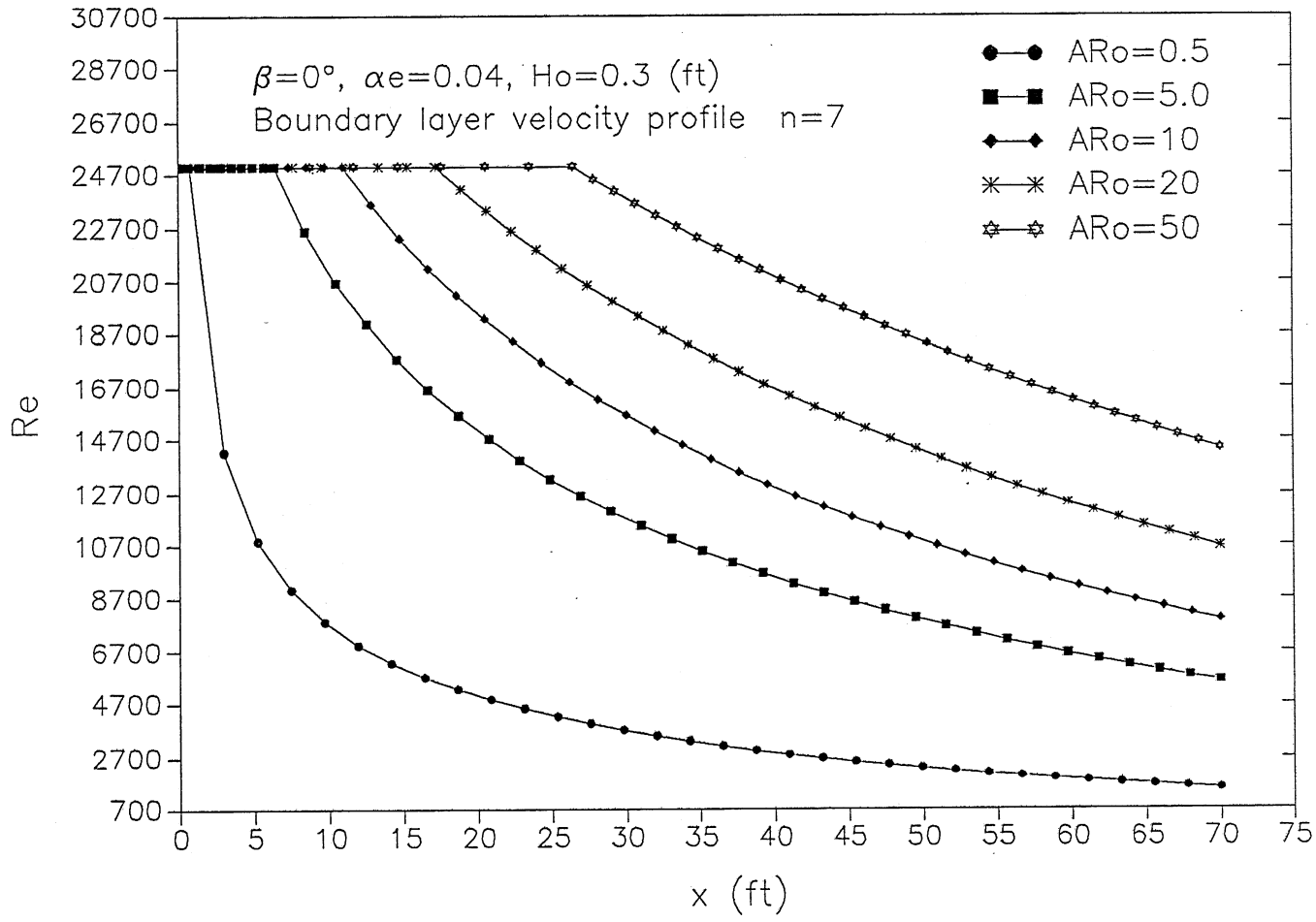

Fig. 4–7 Relationship between Reynolds number and x for different aspect ratios AR_o.

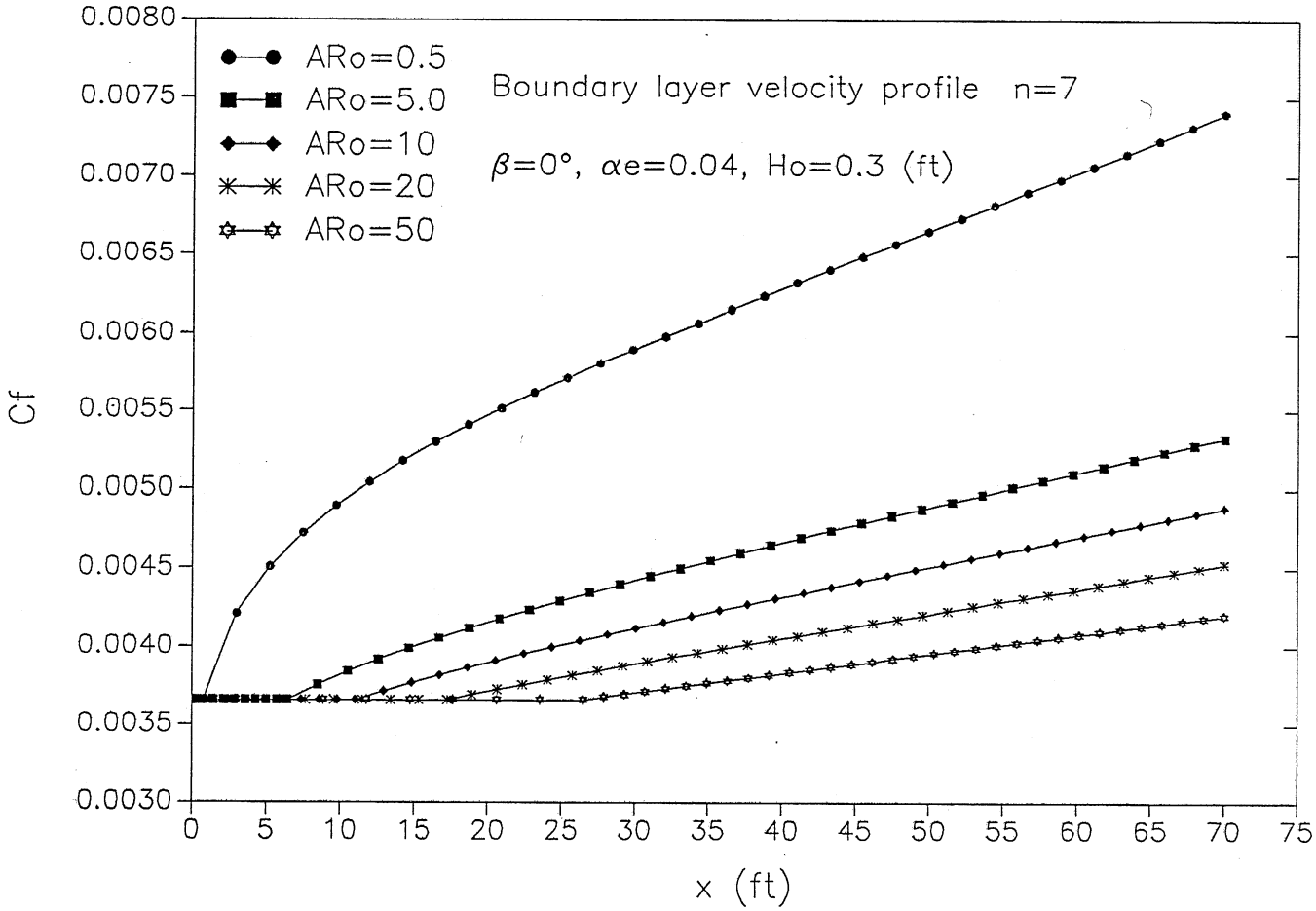

Fig. 4–8 Relationship between the local friction coefficient and x for different aspect ratios AR_o.

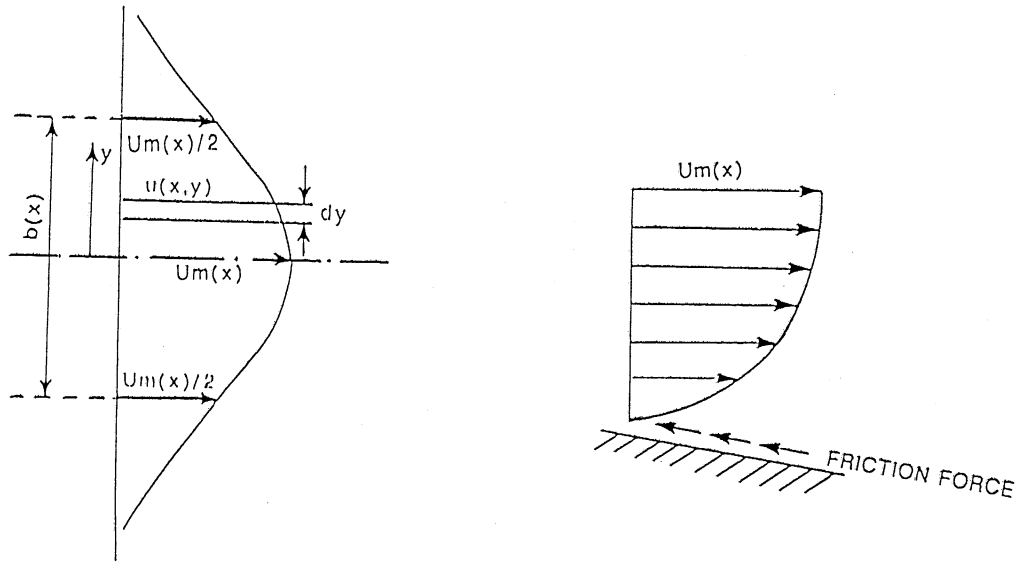

Fig. 4–9 Schematic of velocity distributions in sloping channel.

$$M(x) = 2 \int_0^{H(x)} dz \int_0^{\infty} \rho u^2(x,y) dy$$

$$= 2\rho\ u_m^2(x)\ b(x)\ H(x) \int_0^1 g^2(\zeta) d\zeta \int_0^{\infty} f^2(\eta) d\eta$$

$$= D_4\ \rho\ u_m^2(x)\ b(x)\ H(x) \qquad [4\text{–}39]$$

With entrainment and friction in the sloping channel, the rate of change of flow rate and momentum are, respectively,

$$\frac{dQ(x)}{dx} = \frac{d}{dx} [\ D_3\ u_m(x)\ b(x)\ H(x)]$$

$$= \int_0^{H(x)} 2\ v_e\ dz$$

$$= 2\ D_1\ \alpha_e\ u_m(x)\ H(x) \qquad [4\text{–}40]$$

$$\frac{dM(x)}{dx} = \frac{d}{dx} [\ D_4\ \rho\ u_m^2(x)\ b(x)\ H(x)]$$

$$= 2 \int_0^{\infty} \tau_o(x,y) dy$$

$$= -\ 2\theta\rho\ D_7 [H(x)/\nu]^{-0.25} u_m(x)^{1.75} b(x) \qquad [4\text{–}41a]$$

If c_f is a constant in *the completely rough regime*, [4–41a] is

$$\frac{dM(x)}{dx} = \frac{d}{dx} [\ D_4\ \rho\ u_m^2(x)\ b(x)\ H(x)]$$

$$= -\ 0.5\ \rho c_f\ C_7\ u_m(x)^2\ b(x) \qquad [4\text{–}41b]$$

From [4–40] and [4–41a], we have two differential equations

$$\frac{du_m(x)}{dx} = -\ \{\frac{D_9}{H(x)} [H(x)\ u_m(x)]^{-0.25} + \frac{D_5}{b(x)}\}\ u_m(x) \qquad [4\text{–}42a]$$

$$\frac{db(x)}{dx} = 2D_5 + \{D_9\ [H(x)\ u_m(x)]^{-0.25} - \tan\beta\}\ \frac{b(x)}{H(x)} \qquad [4\text{–}42b]$$

where $D_9 = -\ 2\theta\ \nu^{0.25}\ D_7/D_4$ [4–43]

with [4–40] and [4–41b], two differential equation are

$$\frac{du_m(x)/U_o}{dx} + D_{2o}\ \frac{u_m(x)}{U_o} + D_5 A_3\ [1 + x\frac{\tan\beta}{H_o}]^w\ [\frac{u_m(x)}{U_o}]^3 = 0 \qquad [4\text{–}44a]$$

$$\frac{b(x)}{B_o} = \frac{U_o}{C_7 u_m^2(x)}\ [1 + x\ \frac{\tan\beta}{H_o}]^{-w} \qquad [4\text{–}44b]$$

where $D_{2o} = \frac{c_f C_7}{2D_4} = \frac{c_f}{2D_2}$ and w is defined [2–94b].

Before we discuss these results, we also need to consider the flow development region.

IV.1.2.2 The flow development region

With reference to Fig. 2–11, which is a definition sketch of the flow development region. The potential core is a wedge–like region with the mean velocity U_o. The flow rate in a cross–section can be written as

$$Q(x) = 2\int_0^{H(x)} u(x,y,z)dz\ y_1(x) + 2\int_0^{H(x)} dz \int_{y_1}^{\infty} u(x,y,z)dy$$

$$= 2D_1U_oH(x)[\ y_1(x) + A_6\ b_o(x)] \qquad [4–45]$$

$$M(x) = 2\int_0^{H(x)} u^2(x,y,z)dz\ y_1(x) + \int_0^{H(x)} dz \int_{y_1}^{\infty} \rho u^2(x,y)H(x)dy$$

$$= 2\rho D_2U_o^2H(x)[y_1(x) + A_7b_o(x)] \qquad [4–46]$$

Considering entrainment and friction, the rate of changes of flow rate Q(x) and momentum M(x) are, respectively

$$\frac{dQ(x)}{dx} = 2D_1U_o\{H(x)[\frac{dy_1(x)}{dx} + A_6\frac{db_o(x)}{dx}] + \tan\beta[y_1(x) + A_6b_o(x)]\}$$

$$= \int_0^{H(x)} 2\ v_e\ dz$$

$$= 2\ D_1\ \alpha_e{}^o\ U_o\ H(x) \qquad [4–47]$$

and

$$\frac{dM(x)}{dx} = 2\rho D_2U_o^2\{H(x)[\frac{dy_1(x)}{dx} + A_7\frac{db_o(x)}{dx}] + \tan\beta[y_1(x) + A_7b_o(x)]\}$$

$$= -D_x$$

$$= -2\int_0^{\infty} \tau_o(x,y)dy$$

$$= -\ 2\theta\rho\ [H(x)/\nu]^{-0.25}U_o{}^{1.75}[y_1(x) + D_7b_o(x)] \qquad [4–48]$$

If c_f is a constant in *the completely rough regime*, equation [4–48] is

$$\frac{dM(x)}{dx} = 2\rho D_2U_o^2\{H(x)[\frac{dy_1(x)}{dx} + A_7\frac{db_o(x)}{dx}] + \tan\beta[y_1(x) + A_7b_o(x)]\}$$

$$= -\ \rho\ c_f\ U_o^2\ [y_1(x) + A_7b_o(x)] \qquad [4–49]$$

From [4–47] and [4–48], we obtain

$$H(x)[\frac{dy_1(x)}{dx} + A_6\frac{db_o(x)}{dx}] + \tan\beta[y_1(x) + A_6 b_o(x)]$$

$$= \alpha_e{}^o H(x) \qquad [4–50]$$

$$\tan\beta[y_1(x) + A_7 b_o(x)] + H(x)[\frac{dy_1(x)}{dx} + A_7\frac{db_o(x)}{dx}]$$

$$= -\frac{2\theta}{D_2}[U_o H(x)/\nu]^{-0.25}[y_1(x) + D_{70}\, b_o(x)] \qquad [4–51]$$

Rearranging [4–50] and [4–51], gives

$$\frac{db_o(x)}{dx} = \frac{D_{1o}}{D_{11}}H(x)^{-1.25}[y_1(x) + D_{70}\, b_o(x)] - \frac{b_o(x)}{H(x)}\tan\beta + \frac{\alpha_e{}^o}{D_{11}} \qquad [4–52a]$$

$$\frac{dy_1(x)}{dx} = -A_6\frac{D_{1o}}{D_{11}}H(x)^{-1.25}[y_1(x) + D_{70}b_o(x)] - \frac{y_1(x)}{H(x)}\tan\beta - \frac{\alpha_e{}^o A_7}{D_{11}} \qquad [4–52b]$$

where $$D_{1o} = \frac{\theta}{D_2}\theta\,[U_o/\nu]^{-0.25}$$

$$D_{11} = A_6 - A_7\ .$$

with [4–50] and [4–48b], two differential equation are

$$\frac{db_o(x)}{dx} = \frac{D_{2o}}{D_{11}}H(x)^{-1}\,[y_1(x) + A_7 b_o(x)] - \frac{b_o(x)}{H(x)}\tan\beta + \frac{\alpha_e{}^o}{D_{11}} \qquad [4–53a]$$

$$\frac{dy_1(x)}{dx} = -A_6\frac{D_{2o}}{D_{11}}H(x)^{-1}[y_1(x) + A_7 b_o(x)] - \frac{y_1(x)}{H(x)}\tan\beta - \frac{\alpha_e{}^o A_7}{D_{11}} \qquad [4–53b]$$

The flow development model is combined with the fully developed flow model. Fig. 4–10 to Fig. 4–12 show the dilution and jet dimensions for different aspect ratios AR_o at sloping angle $\beta = 3°$ and $n = 7$. In the flow development region, the development of half–with $b_o(x)$ is of interest. The full with $b(x)$ decreases because the potential core decreases and depth increases. Comparison of the horizontal and the sloping channel discharge shows that dilution on sloping bottom is larger than dilution on horizontal bottom. but jet width on sloping bottom is smaller than jet width on horizontal bottom. Fig. 4–13 and Fig. 4–14 show changes of Re and c_f with x. Re and c_f are nearly constant in the fully developed flow region. It is reasonable in the fully developed flow region to assume n and c_f to be constants. Re and c_f are not constants in the flow development region.

IV.2 Wall Effects on Momentum

In Chapter II and the preceding section IV.1, we have developed simple models for discharges into strongly diverging horizontal or sloping channels. In some cases the inflow at the head of a reservoir or the effluent into a lake in along a bank. In this section, a simple wall jet or half–jet model is applicable.

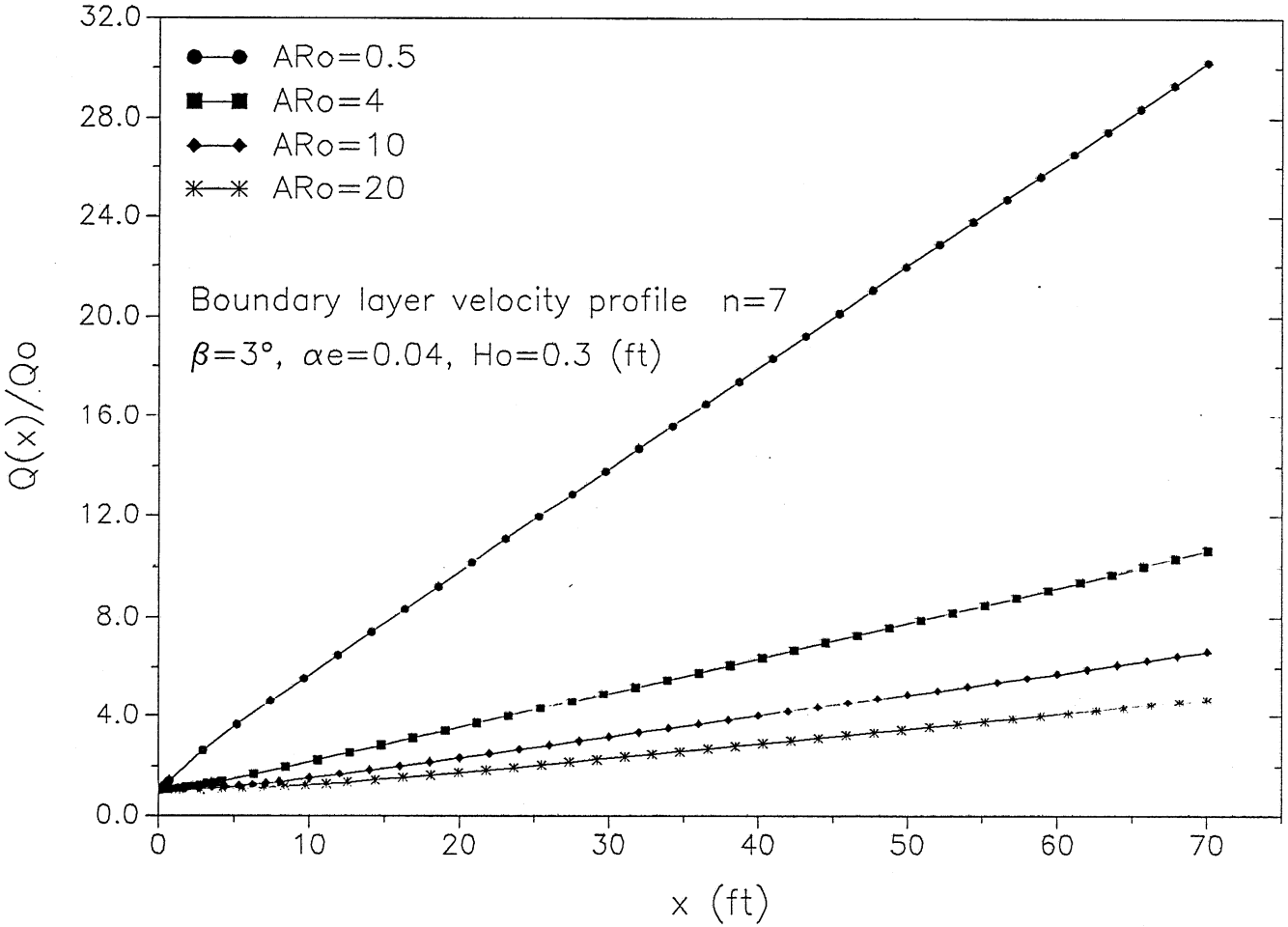

Fig. 4–10 Sensitivity of dilution to aspect ratio AR_o in sloping channel.

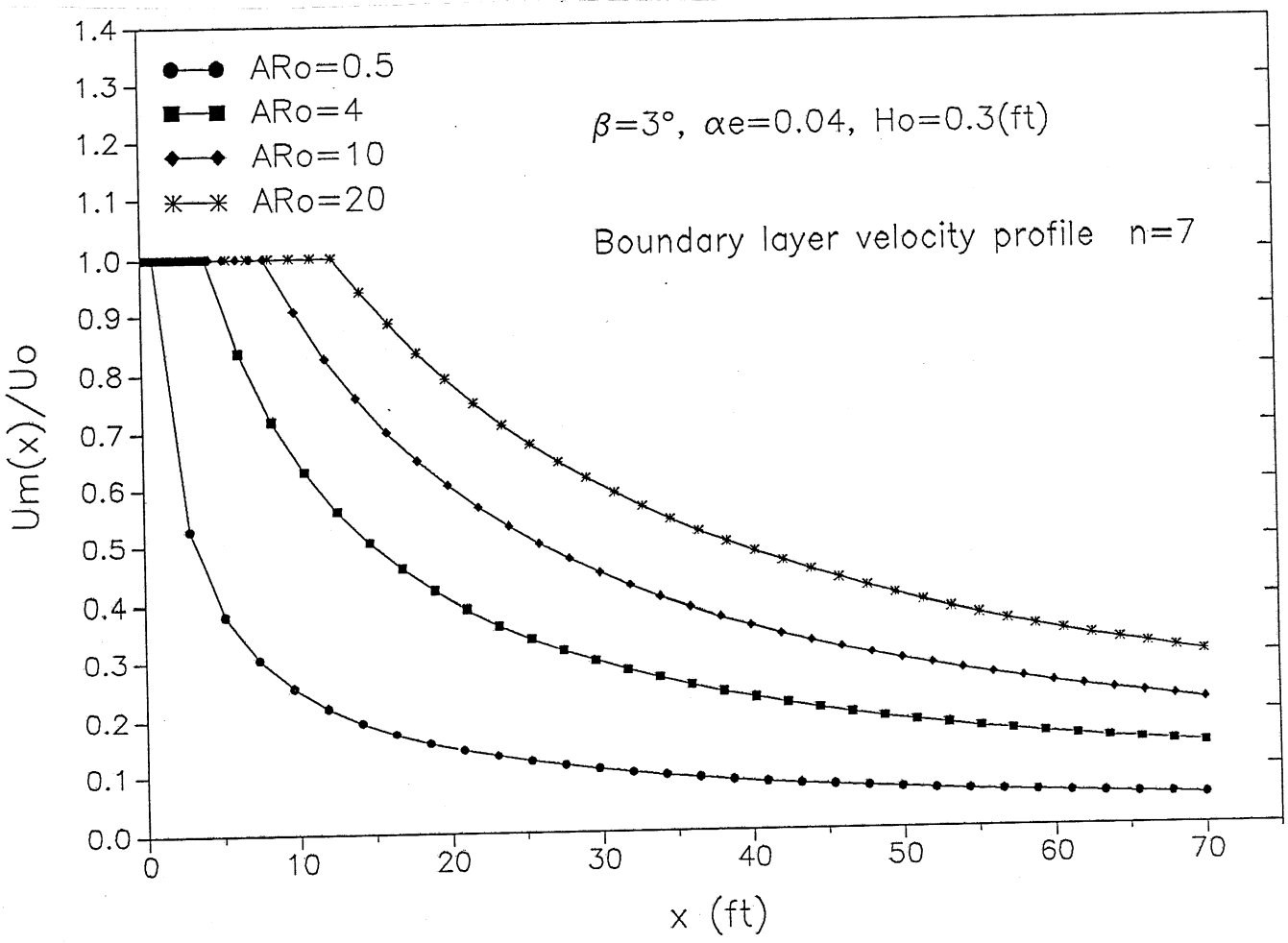

Fig. 4–11 Sensitivity of non–dimensional centerline velocity to aspect ratio AR_o in sloping channel discharge.

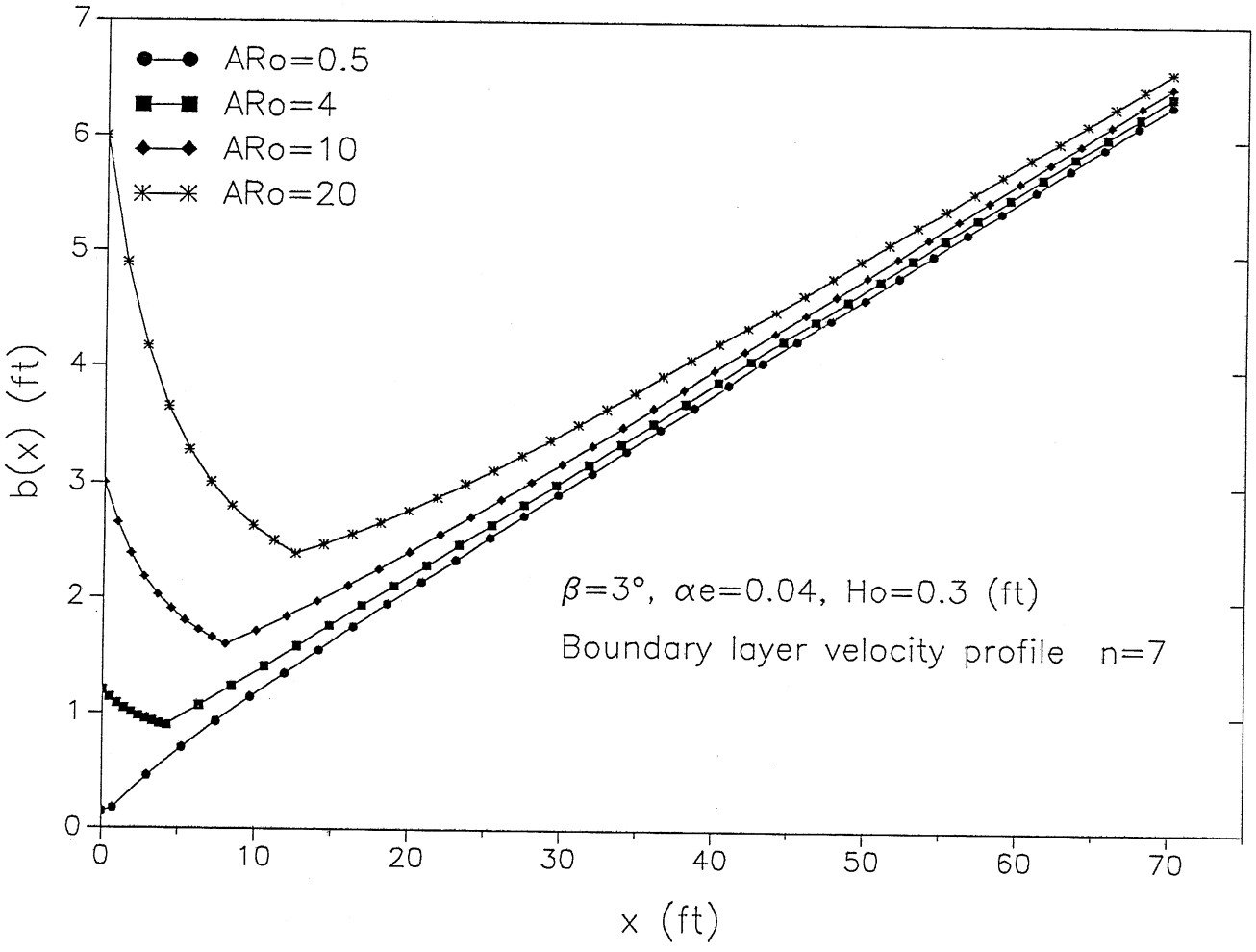

Fig. 4–12 Sensitivity of jet width to aspect ratio AR_o in sloping channel discharge.

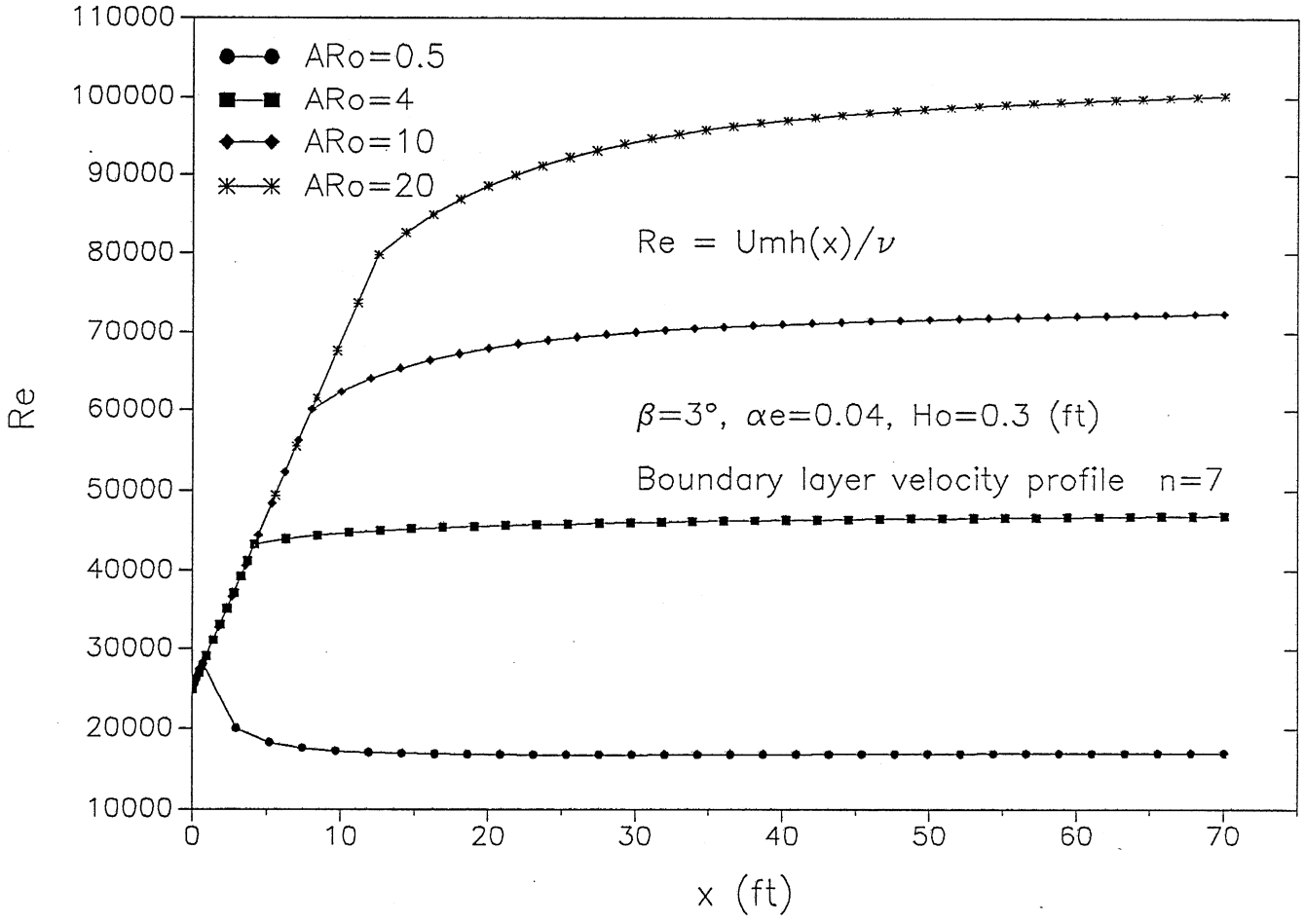

Fig. 4–13 Relationship between Reynolds number and x in sloping channel at different aspect ratios AR_o.

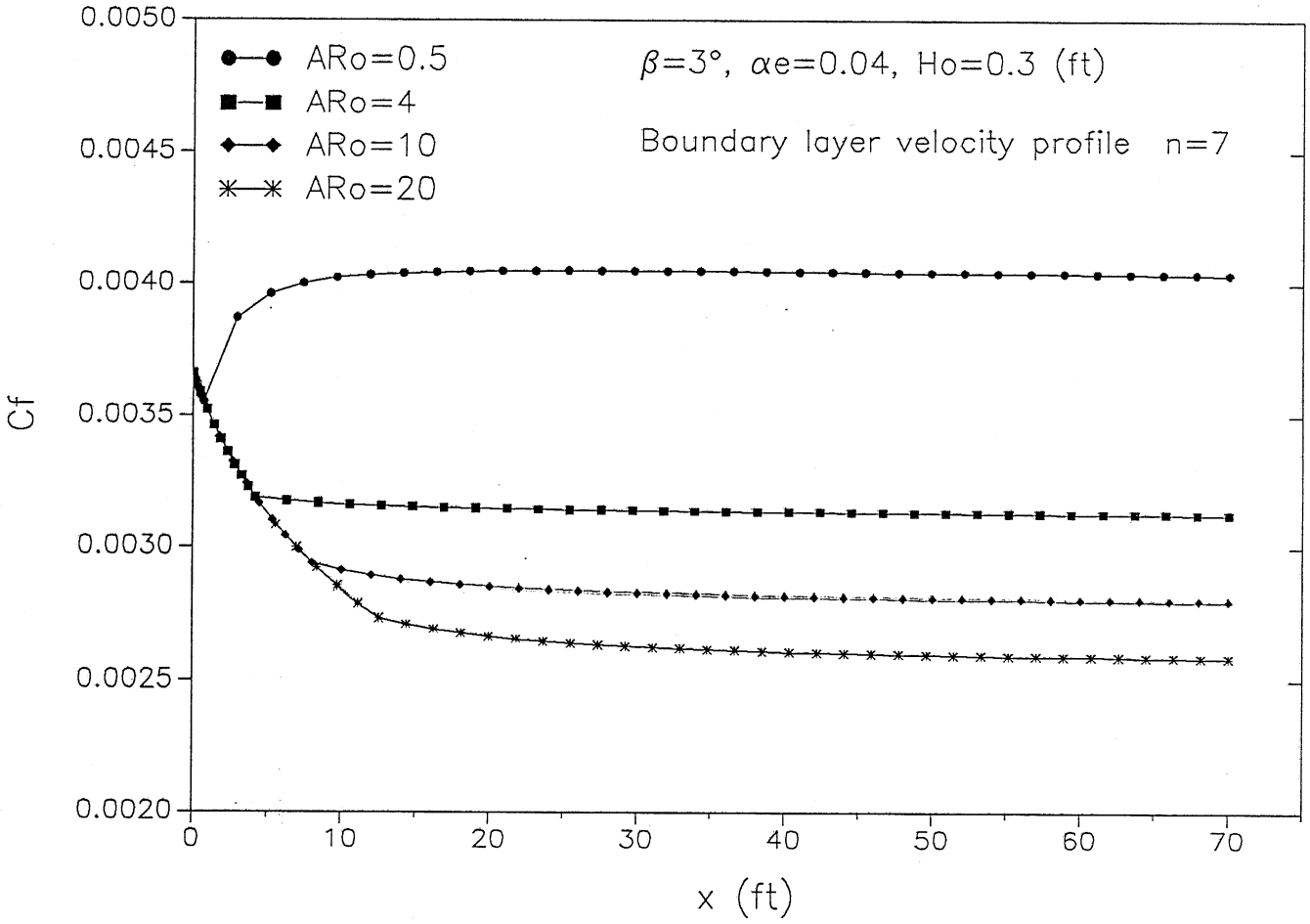

Fig. 4–14 Relationship between local friction coefficient and x in sloping channel at different aspect ratios AR_o.

The first experimental study of a plane turbulent wall jet appears to have been made by Forthmann in 1934. His observations indicate that the velocity distributions become similar for y greater than about 20 b_o. In general at any x–station, u increases from zero at the wall to a maximum value of u_m at $y = \delta(x)$ and then decreases to zero at some large value of y. The region from the wall to the maximum velocity level is known as the boundary layer and the region beyond this is called as the free mixing region.

The simple half–wall jet flow over horizontal bottom is shown in Fig. 4–15. A horizontal channel discharge of uniform velocity U_o is coming out of an open channel tangentially to a smooth flat wall which is submerged in a semi–finite expanse of the same fluid. Fig. 4–15 (a) assumes that the vertical velocity profile follows the 1/7–th–power law as a first approximation. The transverse velocity profile in Fig. 4–15 (b) is the 1/7–th–power law if y is less than the boundary layer thickness $\delta(x)$, and is Gaussian distribution if y is greater than $\delta(x)$.

IV.2.1 Wall effects on half jet over horizontal bottom

Both friction on the bottom and on the wall must be considered for the half jet.

$$D_x = D_{xb} + D_{xw} \qquad [4–54]$$

where D_x = total friction force in the axial (x) direction
D_{xb} = bottom friction force
D_{xw} = wall friction force

Using velocity profile [4–2] with depth, from equation [4–5], D_{xb} is

$$\begin{aligned} D_{xb} &= \int_0^\infty c_f/2\ \rho u_s(x,y)^2 dy \\ &= \int_0^\infty \theta\ [u_s(x,y)H_o/\nu]^{-0.25} \rho u_s(x,y)^2 dy \\ &= \theta\ \rho\ [H_o/\nu]^{-0.25} \int_0^\infty u_s(x,y)^{1.75} dy \\ &= D_{12}\ u_m(x)^{1.75} [\delta(x) \int_0^1 g(\zeta)^{1.75} d\zeta + b_o(x) \int_0^\infty f(\eta)^{1.75} d\eta] \\ &= D_{12}\ u_m(x)^{1.75} [\ \delta(x) \int_0^1 g(\zeta)^{1.75} d\zeta + D_7\ b_o(x)] \end{aligned} \qquad [4–55]$$

where $D_{12} = \theta\ \rho\ [H_o/\nu]^{-0.25}$

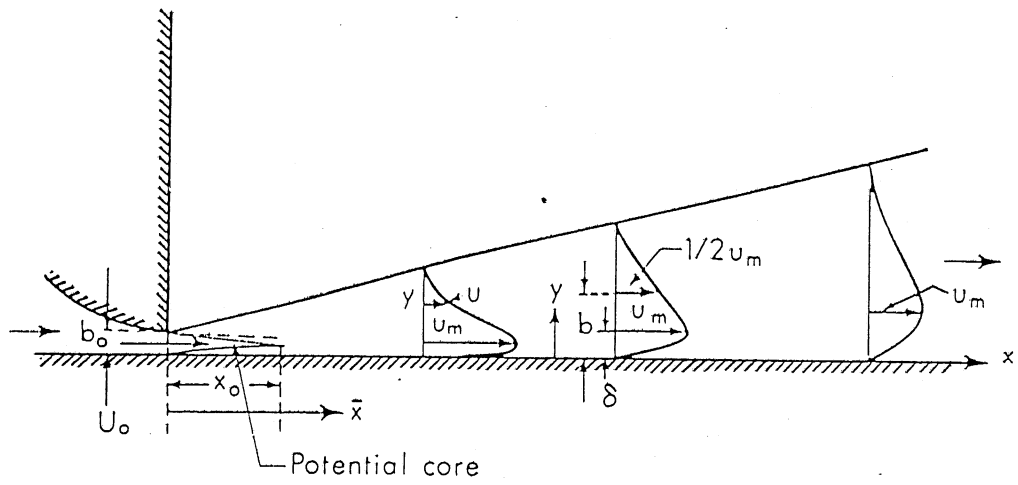

Fig. 4–15 Definition sketch of plane turbulent wall jets. (N. Rajaratnam, 1976)

Using velocity profile [4–2] on the wall, D_{xw} is

$$D_{xw} = \int_0^1 c_{fw}/2 \ \rho u_m(x,z)^2 dz$$

$$= \int_0^1 g^2(\zeta) d\zeta \ \rho H_o c_{fw}/2 \ u_m(x)^2 \qquad [4–56]$$

where c_{fw} is the friction coefficient on the wall.

In the flow development region, boundary layer thickness $\delta(x)$ and D_{xw} are, respectively,

$$\delta(x) = 0.37 \ x \ [U_o x/\nu]^{-0.2} \qquad [4–57]$$

$$D_{xw} = \rho H_o \ 0.0296 \ [U_o x/\nu]^{-0.2} \ U_o^2 \int_0^1 g^2(\zeta) d\zeta$$

$$= 0.0296 \ \rho \ H_o \ D_2 \ U_o^{1.8} \ [x/\nu]^{-0.2} \qquad [4–58]$$

In the fully developed flow region, we have

$$\delta(x) = 0.37 \ x \ \left[\frac{u_m(x) \ x}{\nu}\right]^{-0.2} \qquad [4–59]$$

$$D_{xw} = \rho H_o \ 0.0296 \ [u_m(x) \ x/\nu]^{-0.2} \ u_m(x)^2 \int_0^1 g^2(\zeta) d\zeta$$

$$= 0.0296 \ \rho H_o \ D_2 \ u_m(x)^{1.8} \ [x/\nu]^{-0.2} \qquad [4–60]$$

IV.2.1.1 Continuity and momentum equations in fully developed flow region

Using the similarity hypothesis for velocity profiles, the flow rate Q(x) and momentum M(x) can be written, respectively as

$$Q(x) = \int_0^\infty dy \int_0^{H_o} u(x,y,z) \ dz$$

$$= H_o \left[\int_0^{\delta(x)} u(x,y) dy + \int_{\delta(x)}^\infty u(x,y) dy\right] \int_0^1 g(\zeta) d\zeta$$

$$= H_o D_1 \ [D_1 \delta(x) u_m(x) + A_6 u_m(x) b_o(x)]$$

$$= H_o D_1 u_m(x) \ [D_1 \delta(x) + A_6 b_o(x)] \qquad [4–61]$$

and $$M(x) = \int_0^{\infty} dy \int_0^{H_o} \rho\ u^2(x,y,z)dz$$

$$= \rho H_o \left[\int_0^{\delta(x)} u^2(x,y)dy + \int_{\delta(x)}^{\infty} u(x,y)dy\right] \int_0^1 g^2(\zeta)d\zeta$$

$$= \rho H_o D_2 \left[D_2\delta(x)\ u_m(x)^2 + A_7 b_o(x) u_m(x,y)^2\right]$$

$$= \rho H_o D_2 u_m(x)^2 \left[D_2\delta(x) + A_7 b_o(x)\right] \qquad [4\text{–}62]$$

Where $$A_6 = \int_0^{\infty} f(\xi)d\xi$$

$$A_7 = \int_0^{\infty} f^2(\xi)d\xi$$

$$\xi = [y - \delta(x)]/b_o(x)$$

Considering entrainment and friction, the rate of change of flow rate and momentum are, respectively

$$\frac{dQ(x)}{dx} = \frac{d}{dx}\ \{\ H_o D_1 u_m(x)\ [D_1\delta(x) + A_6 b_o(x)]\}$$

$$= H_o D_1\{\ \frac{du_m(x)}{dx}[D_1\delta(x) + A_6 b_o(x)] + u_m(x)[D_1\frac{d\delta(x)}{dx} + A_6\frac{db_o(x)}{dx}]\}$$

$$= \int_0^{H_o} v_e\ dz$$

$$= \alpha_e\ u_m(x)\ H_o\ D_1 \qquad [4\text{–}63]$$

$$\frac{dM(x)}{dx} = \frac{d}{dx}\ \{\rho H_o D_2 u_m^2(x)\ [D_2\delta(x) + A_7 b_o(x)]\}$$

$$= \rho D_2 H_o u_m(x)\{\ 2\frac{du_m(x)}{dx}[D_2\delta(x) + A_7 b_o(x)]$$

$$+ u_m(x)[D_2\frac{d\delta(x)}{dx} + A_7\frac{db_o(x)}{dx}]\}$$

$$= -\ (D_{xb} + D_{xw})$$

$$= -\ \theta\ \rho[H_o/\nu]^{-0.25}\int_0^{\infty} u_s(x,y)^{1.75}dy - 0.0296\rho H_o D_2\ u_m(x)^{1.8}\ [x/\nu]^{-0.2}$$

$$= \rho H_o u_m(x)^{1.75}\{D_{13}\delta(x) + D_{14}b_o(x) + D_{15}\ u_m(x)^{0.05}x^{-0.2}\}$$

$$= \rho H_o u_m(x)^{1.75}\ F[x,\ \delta(x),\ b_o(x),\ u_m(x)] \qquad [4\text{–}64]$$

where $D_{13} = -\theta\,[H_0^5/\nu]^{-0.25}\int_0^1 g(\zeta)^{1.75}d\zeta$

$D_{14} = -\theta\,D_{70}\,[H_0^5/\nu]^{-0.25}$

$D_{15} = -0.0296\,D_2\,\nu^{0.2}$

$F[x,\ \delta(x),\ b_o(x),\ u_m(x)] = D_{13}\delta(x) + D_{14}b_o(x) + D_{15}\,u_m(x)^{0.05}x^{-0.2}$

From [4–59], we obtain the rate change of the boundary layer thickness $\delta(x)$ in the fully developed flow region

$$\frac{d\delta(x)}{dx} = 0.296\left(\frac{u_m(x)\,x}{\nu}\right)^{-0.2} - 0.074u_m(x)^{-1.2}\nu^{-0.2}x^{0.8}\,\frac{du_m(x)}{dx} \qquad [4\text{–}65]$$

We multiply [4–63] by D_2A_7 and multiply [4–64] by A_6, and then subtract [4–64] from [4–63], substitute [4–65] into the result and rearrange to obtain

$$[D_{16}\,\delta(x) + D_{17}\,b_o(x)]\,\frac{du_m(x)}{dx} + D_{18}u_m(x)\frac{d\delta(x)}{dx}$$

$$= [(D_{16} - 0.2\,D_{18})\,\delta(x) + D_{17}\,b_o(x)]\,\frac{du_m(x)}{dx} + 0.8\,D_{18}\,u_m(x)\,\frac{\delta(x)}{x}]$$

$$= E[x,\ \delta(x),\ b_o(x)]\,\frac{du_m(x)}{dx} + 0.8\,D_{18}\,u_m(x)\,\frac{\delta(x)}{x}]$$

$$= \alpha_e D_2A_7u_m(x) - A_6u_m(x)^{0.75}\,F[x,\ \delta(x),\ b_o(x),\ u_m(x)]$$

$$= G[x,\ \delta(x),\ b_o(x),\ u_m(x)] \qquad [4\text{–}66]$$

where $D_{16} = D_2\,[D_1A_7 - 2D_2A_6]$

$D_{17} = -D_2\,A_6\,A_7$

$D_{18} = D_2\,[D_1A_7 - D_2A_6]$

$E[x,\ \delta(x),\ b_o(x)] = (D_{16} - 0.2\,D_{18})\,\delta(x) + D_{17}\,b_o(x)$

with [4–66], gives

$$\frac{du_m(x)}{dx} = \frac{G[x,\ \delta(x),\ b_o(x),\ u_m(x)] - 0.8\,D_{18}\,u_m(x)\,\delta(x)/x}{E(x,\ \delta(x),\ b_o(x)\,]} \qquad [4\text{–}67]$$

Rearranging [4–63], we obtain

$$u_m(x)\ A_6\frac{db_o(x)}{dx}$$

$$= \alpha_e u_m(x) - D_1\ [\delta(x)\frac{du_m(x)}{dx} + u_m(x)\frac{d\delta(x)}{dx}] - A_6 b_o(x)\frac{du_m(x)}{dx}$$

$$= \alpha_e u_m(x) - 0.8\ D_1\ [\delta(x)\frac{du_m(x)}{dx} + u_m(x)\ \frac{\delta(x)}{x}] - A_6 b_o(x)\frac{du_m(x)}{dx}$$

We have

$$\frac{db_o(x)}{dx} = \frac{\alpha_e}{A_6} - \frac{0.8D_1}{A_6 u_m(x)}\ [\frac{du_m(x)}{dx} + \frac{u_m(x)}{x}] - \frac{b_o(x)}{u_m(x)}\ \frac{du_m(x)}{dx} \qquad [4–68]$$

Using a 4th order Runge–Kutta method, we obtain a numerical solution for equations [4–67] and [4–68]. The initial conditions are given in section IV.2.1.2.

IV.2.1.2 The flow development region

With reference to Fig. 2–11, the flow rate Q(x) and momentum M(x) can be written respectively as

$$Q(x) = \int_0^{\infty} dy \int_0^{H_o} u(x,y,z)\ dz$$

$$= H_o \int_0^1 g(\zeta)d\zeta\ [\int_0^{\delta(x)} u(x,y)dy + \int_{\delta(x)}^{y_1(x)} u(x,y)dy + \int_{y_1(x)}^{\infty} u(x,y)dy]$$

$$= H_o D_1\ [D_1\delta(x)U_o + U_o\ (y_1(x) - \delta(x)] + A_6 U_o\ b_o(x)]$$

$$= H_o D_1 U_o\ [D_1\delta(x) + y_1(x) - \delta(x) + A_6 b_o(x)] \qquad [4–69]$$

$$M(x) = \int_0^{\infty} dy \int_0^{H_o} \rho\ u^2(x,y,z)dz$$

$$= \rho H_o \int_0^1 g^2(\zeta)d\zeta[\int_0^{\delta(x)} u^2(x,y)dy + \int_{\delta(x)}^{y_1(x)} u^2(x,y)dy + \int_{\delta(x)}^{\infty} u^2(x,y)dy]$$

$$= \rho H_o D_2 U_o^2\ [D_2\delta(x) + y_1(x) - \delta(x) + A_7 b_o(x)] \qquad [4–70]$$

Considering entrainment and friction, the rates of change of flow rate and momentum are, respectively,

$$\frac{dQ(x)}{dx} = \frac{d}{dx}\{H_0 D_1 U_0 [D_1\delta(x) + y_1(x) - \delta(x) + A_6 b_0(x)]\}$$

$$= H_0 D_1 U_0 [(D_1 - 1)\frac{d\delta(x)}{dx} + \frac{dy_1(x)}{dx} + A_6\frac{db_0(x)}{dx}]$$

$$= \int_0^{H_0} v_e \, dz$$

$$= \alpha_e \, U_0 \, H_0 \, D_1 \qquad [4\text{–}71]$$

$$\frac{dM(x)}{dx} = \frac{d}{dx}\{\rho H_0 D_2 U_0^2 [D_2\delta(x) + y_1(x) - \delta(x) + A_7 b_0(x)]\}$$

$$= \rho D_2 H_0 U_0^2 [(D_2 - 1)\frac{d\delta(x)}{dx} + \frac{dy_1(x)}{dx} + A_7\frac{db_0(x)}{dx}]$$

$$= - (D_{xb} + D_{xw})$$

$$= - \theta \, \rho[H_0/\nu]^{-0.25}\int_0^{\infty} u(x,y)^{1.75}dy - 0.0296\rho H_0 D_2 \, U_0^{1.8} \, [x_0/\nu]^{-0.2}$$

$$= \rho H_0 U_0^{1.75}\{D_{19}[\, D_{20}\delta(x) + y_1(x) + D_{70}b_0(x)] + D_{14} \, U_0^{0.05}x_0^{-0.2}\}$$

$$= \rho H_0 U_0^{1.75} \, H[x_0, \, \delta(x), \, b_0(x), \, y_1(x)] \qquad [4\text{–}72]$$

where $D_{19} = \int_0^1 g(\zeta)^{1.75}d\zeta - 1 = - 0.2$

$D_{20} = - 0.023 \, [H_0^5/\nu]^{-0.25}$

From [4–57], we obtain the rate change of the boundary layer thickness $\delta(x)$ in the flow development region as

$$\frac{d\delta(x)}{dx} = 0.296 \, (\frac{U_0 \, x}{\nu})^{-0.2} \qquad [4\text{–}73]$$

We multiply [4–71] by D_2, and then subtract [4–72] from [4–71], substitute [4–73] into the resulting equation and rearrange to obtain

$$D_{22}\frac{db_0(x)}{dx} = - D_{23}\frac{d\delta(x)}{dx} + D_2 \, \alpha_e - U_0^{-0.25} \, H[x_0, \, \delta(x), \, b_0(x), \, U_0] \qquad [4\text{–}74]$$

where $D_{22} = D_2(A_6 - A_7)$

$D_{23} = D_2[D_1 - D_2]$

Multiply [4–71] by D_2A_7 and multiply [4–72] by A_6, and then subtract [4–72] from [4–71] to obtain

$$- D_{22} \frac{dy_1(x)}{dx} + [D_{22} + D_{18}] \frac{d\delta(x)}{dx}$$

$$= D_2A_7\alpha_e - A_6U_0^{-0.25} H[x_0, \delta(x), b_0(x), U_0] \qquad [4–75]$$

By combing the flow development model with the fully developed flow model, we obtain a complete model for wall jets.

IV.2.2 Comparison of the numerical results with experimental data

Experiments on plane wall jets have been performed by Zebra and Selna (1946), Sigalla (1958), Myers et al. (1961), Schwarz and Cosart (1961), and others. A comprehensive bibliography of these studies has been given by Rajaratnam and Subramanya (1967). These investigations focus on jet geometry without effects of boundaries and friction.

Unfortunately no experimental data for the wall jet could be located. If we use a very small aspect ratio AR_0 and neglect friction on the bottom, we approaches conditions which previous authors have studied. Fig. 4–15 and Fig. 4–16 show a comparisons of model results and experimental data for dilution and growth of the length scale.

Fig. 4–17 shows a comparison of the variation of the velocity scale. The model results does not match the experimental data well. For the flow development region, x_0/b_0 was found to vary from 6.1 to 6.7 (Rajaratnam, 1967) for $Re_0 = U_0b_0/\nu = 10^4$ and 10^5. According to the model results x_0/b_0 is about 9.0 for $Re_0 = 10^4$. The error may come from assumptions such as velocity distributions and local friction coefficient. Recent observations of Myers et al. (1961) and Schwarz and Cosart (1961) have shown that the velocity distribution in the boundary layer is better described by a power law having an exponent of 1/14 rather than 1/7. Sigalla recommended the empirical equation

$$c_f = \frac{\tau_0}{\rho u_m^2/2} \simeq \frac{0.0565}{(u_m\delta/\nu)^{0.25}}$$

$$= \frac{0.0724}{(u_m x/\nu)^{0.2}} \qquad [4–75]$$

A comparison of [4–75] with [4–4] reveals that the empirical c_f values differ by more than a factor of two. Further study of the velocity distributions is therefore necessary.

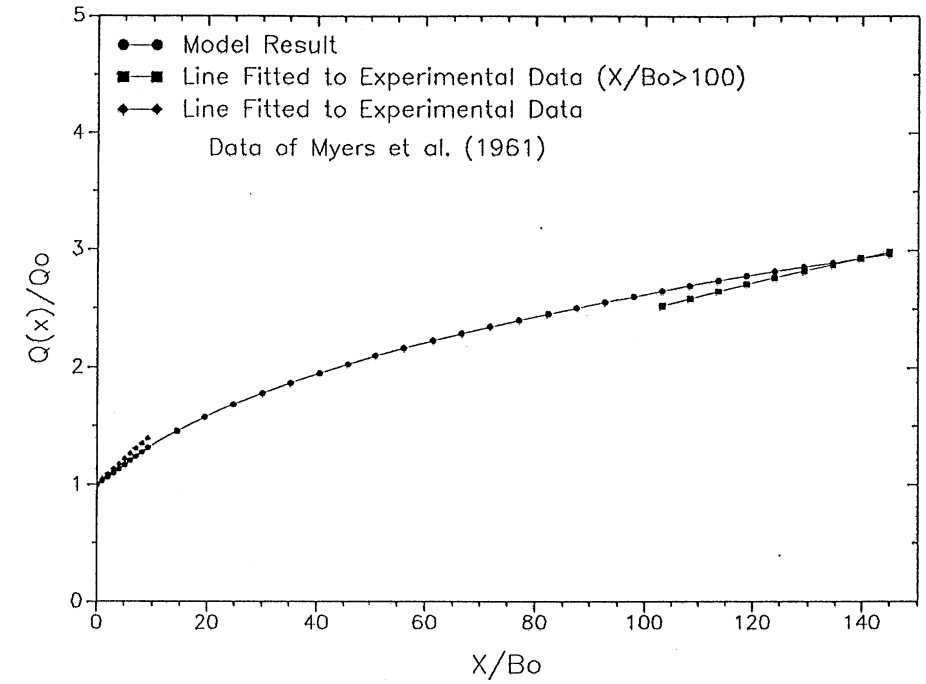

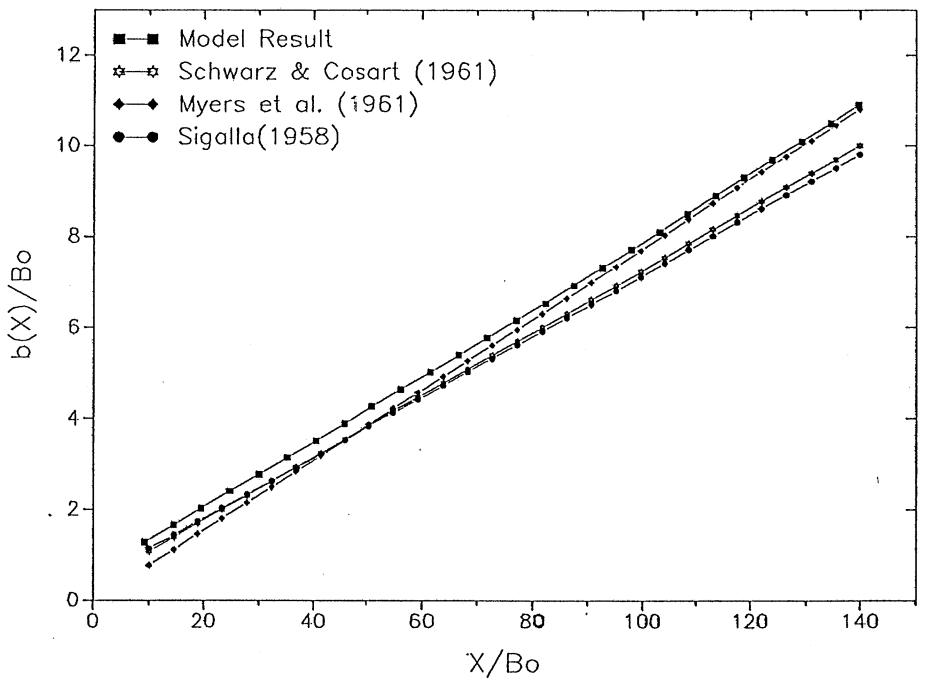

Fig. 4–16 Comparison of numerical model results with experimental data for dilution and growth of the length scale b(x) of wall jets.

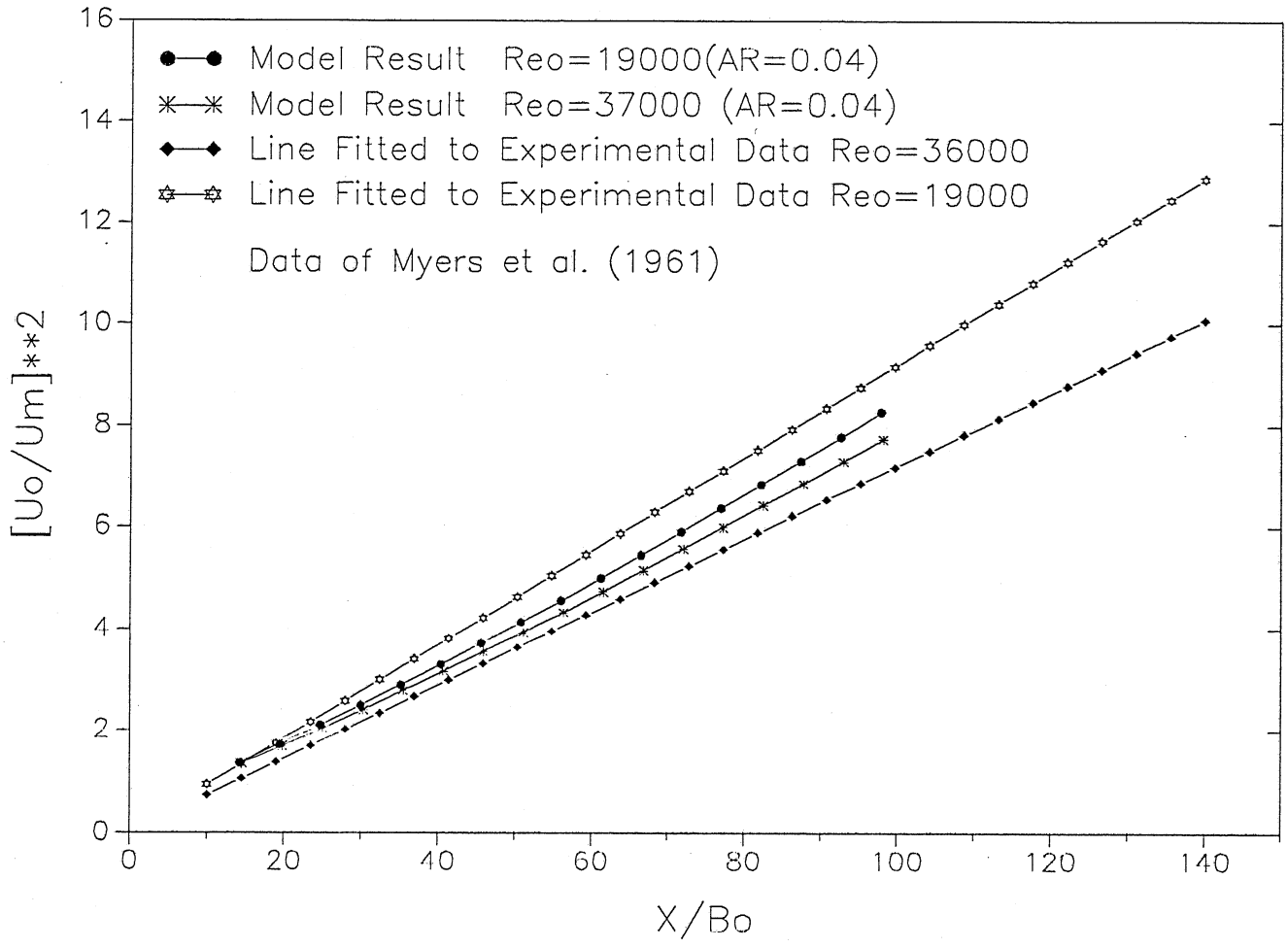

Fig. 4–17 Comparison of numerical model results with experimental data for variation of the velocity scale of wall jets.

Chapter V

APPLICATIONS OF COMPLETE MODEL TO LABORATORY DATA AND FIELD CONDITIONS

An integral model for a discharge from a channel over a horizontal or a sloping bottom into a wide water body has been developed (Chapters II and IV). Viewed from above inflows have jet–like features. Integral jet flow models are therefore used to analyze the pre–plunging flow (Johnson and Stefan, 1988). Applications of the complete integral model to laboratory data and field conditions will be reported in this chapter.

V.1 Densimetric Froude Number F for Jet Flow

The plunging phenomenon is hydrodynamically related to negative buoyancy forces and inertial forces. The location of plunging (x_p) (Fig. 1–1) can be related to a densimetric Froude number (F_p) as introduced by Elder and Wunderlich (1972). The densimetric Froude number (F) at any cross section before plunging is defined as

$$F = U\,(g'\,H)^{-0.5} \qquad [5\text{–}1]$$

where

$$g' = g\,\frac{\rho - \rho_a}{\rho_o} = g\,\frac{\Delta\rho}{\rho_o} \qquad [5\text{–}2]$$

U = mean flow velocity of jet in cross section

H = water depth in cross section

g = acceleration of gravity

ρ = water density

a, o = subscripts referring to ambient & outlet, respectively.

Conservation of mass and buoyancy between the inflow section (subscript o) and any cross section (no subscript) can be expressed as:

$$Q_o + Q_a = Q \qquad [5\text{–}3]$$

$$\Delta\rho_o Q_o = \Delta\rho\, Q \qquad [5\text{–}4]$$

where Q_0 = inflow rate, $\Delta\rho_0 = \rho_0 - \rho_a$, Q_a and ρ_a refer to the flow rate and density of the ambient water entrained by the flow between x = 0 and x. Substituting [5–2] and [5–3] into [5–1], a relationship between densimetric Froude number F_0 of inflow and F at any cross section downstream before plunging is obtained.

For a horizontal channel

$$\frac{F}{F_0} = \frac{U}{U_0} \left(\frac{\Delta\rho}{\Delta\rho_0} \right)^{-0.5} = \frac{U}{U_0} \left(\frac{Q}{Q_0} \right)^{0.5} \qquad [5–5]$$

For a sloping channel

$$\frac{F}{F_0} = \frac{U}{U_0} \left(\frac{\Delta\rho \ H}{\Delta\rho_0 \ H_0} \right)^{-0.5}$$

$$= \frac{U}{U_0} \left(\frac{Q}{Q_0} \right)^{0.5} \left(\frac{H_0 + x \tan\beta}{H_0} \right)^{-0.5} \qquad [5–6]$$

If the flow rate in the jet upstream from plunging is specified as

$$Q = U \ b \ H \qquad [5–7]$$

where b = characteristic width of jet, equation [5–5] becomes

$$F_p = F_0 \left(\frac{b_p}{B_0} \right)^{0.5} \left(\frac{U_p}{U_0} \right)^{1.5} \qquad [5–8]$$

These equations use parameters averaged within the jet cross section for U and $\Delta\rho$. The velocity U is a cross–sectional average across the width of the jet, given as

$$U = \frac{Q}{b \ H} \qquad [5–9]$$

The average velocity U is dependent on definition of width b. For comparison of the model results with experimental data by Johnson and Stefan (1988), width b is defined as

$$b = 4 \ \sigma \qquad [5–10]$$

where σ is the standard deviation of the Gaussian velocity distribution. The Gaussian velocity distribution can be represented by the distribution function

$$u = u_m \ f(\eta) = u_m \exp(- \eta^2) = u_m \exp(- 8 \left[\frac{y}{4\sigma} \right]^2) \qquad [5–11]$$

Substituting [5–11] into [5–9], the average velocity in a cross section in the fully developed flow region is

$$U = u_m \, 2 \int_0^\infty f(\eta) \, d\eta = 0.627 \, u_m \qquad [5\text{–}12]$$

In the flow development region, which includes a potential core and a mixing layer, the mean velocity U can be written according to equations [2–64] and [5–11] as

$$U = \frac{2[y_1(x) + A_6 b_0(x)]}{2\, y_1(x) + 4\, \sigma} \, U_0 \qquad [5\text{–}13]$$

The characteristic width b for average cross–sectional velocity is equal to the width of the potential core [$2y_1(x)$] plus four times the standard deviation of Gaussian velocity distribution of the mixing layer [$4\sigma = 3.397\ b_0(x)$]. At the inflow $y_1(x) = B_0/2$ and $b_0(x) = 0$, $U = U_0$. At the end of the potential core $y_1(x) = 0$, $U = 0.627\ U_0$. This is consistent with equation [5–12] of the fully developed flow region. Substituting [5–12] and [5–13] into [5–5] and [5–6], the densimetric Froude number F can be obtained.

For a free turbulent jet, centerline velocity u_m, width b and dilution are related to distance by the equations (Johnson et. al, 1988)

$$\frac{u_m}{U_0} = C_1 \left(\frac{x}{B_0} \right)^{-0.5} \qquad [5\text{–}14]$$

$$\frac{b}{B_0} = C_2 \frac{x}{B_0} \qquad [5\text{–}15]$$

and

$$\frac{Q}{Q_0} = C_1 \, C_2 \int_0^\infty f(\eta) \, d\eta \left(\frac{x}{B_0} \right)^{0.5} = C_3 \left(\frac{x}{B_0} \right)^{0.5} \qquad [5\text{–}16]$$

where C_1, C_2 and C_3 are experimentally determined coefficients. C_1 and C_3 are dependent on width B_0 of inflow (using $b_0 = 0.5\ B_0$ in Chapter II) and are independent of the definition of jet width b. C_2 is dependent on definition of jet width b and is independent of B_0. Substituting [5–14], [5–15] and [5–16] into [5–8], the relationship between F_p and F_0 (Johnson and Stefan, 1988) is

$$F_0 = \frac{F_p}{C_4} \left(\frac{x_p}{B_0} \right)^{0.25} \qquad [5\text{–}17a]$$

where $C_4 = C_2^{-1} \, C_3^{1.5}$. Using [5–17a] to fit experimental data, Johnson and Stefan obtained the following empirical equation

$$\frac{x_p}{B_0} = 0.52 \, F_0^4 \qquad [5\text{–}17b]$$

V.2 Application of Complete Model to Laboratory Data

Values from 0.5 to 0.92, with an average near 0.6 in field or laboratory observations, have been reported in the literature for densimetric Froude numbers at plunging F_p . Ford and Johnson(1983), Akiyama and Stefan (1984), and Farrell and Stefan (1986) give summaries of past studies and values of F_p. In the complete integral model the distance to plunging x_p is determined by setting $F = F_p$. Dilution Q_p/Q_o up to plunging can be calculated once x_p is known.

V.2.1 Horizontal channel discharge

Fig. 5–1 illustrates the relationships between F and x/B_o for different F_o values starting with F_o. F decreases with x/B_o. Fig. 5–2 shows the dependence of x_p/B_o on F_o if $F_p = 0.6$ or 0.8 or 1.0. The model used does not include friction effects. Comparing the numerical result with the semi–empirical equation [5–17b] by Johnson and Stefan, 1988, one can see that model and data predict that x_p/B_o is proportional to F_o^4, but the numerical model results do not match the experimental data (Johnson and Stefan, 1988). **This is not surprising since the data do include frictional effects and hence give shorter distances to plunging than the model without friction.**

The effect of bottom friction is included in the results of Fig. 5–3. The model used for Fig. 5–3 includes the power law velocity profile and is applied with $F_p = 1.0$. The numerical results which include a ZFE, do not match experimental data as well as these without a ZFE. The reason is that In the laboratory studies (Johnson and Stefan, 1988) the inflow has fully developed turbulent flow velocity distribution and a small aspect ratio AR_o. It is not appropriate to simulate a flow development region from an initially uniform velocity profile for such inflows. The flow development region (ZFE) can be left out of the model for (laboratory) conditions with small AR_o values but must be included for large AR_o values.

Fig. 5–4 and Fig. 5–5 show model results and experimental data for flow rate Q_p/Q_o (dilution) (Johnson and Stefan, 1988). Experimental data are in the non–buoyant free jet before plunging. Model results match the sparse experimental data reasonable well.

Fig. 5–6 shows the sensitivity of x_p/B_o to the choice of F_p at different inflow F_o values. The numerical results are sensitive to the F_p value specified in the integral model. **In summary, we recommend $F_p = 1.0$ in the application of the model. It is important to have bed friction and vertical velocity profiles included in the model. It is not necessary to include a ZFE in the model for laboratory studies with small aspect ratio inflow channels.**

A relationship of dilution Q_p/Q_o versus inflow densimetric Froude number F_o is shown in Fig. 5–7 for large divergence angles ($\delta > 45°$), horizontal bottom ($\beta = 0°$), and small channel aspect ratios $AR_o \leq 2.2$. The

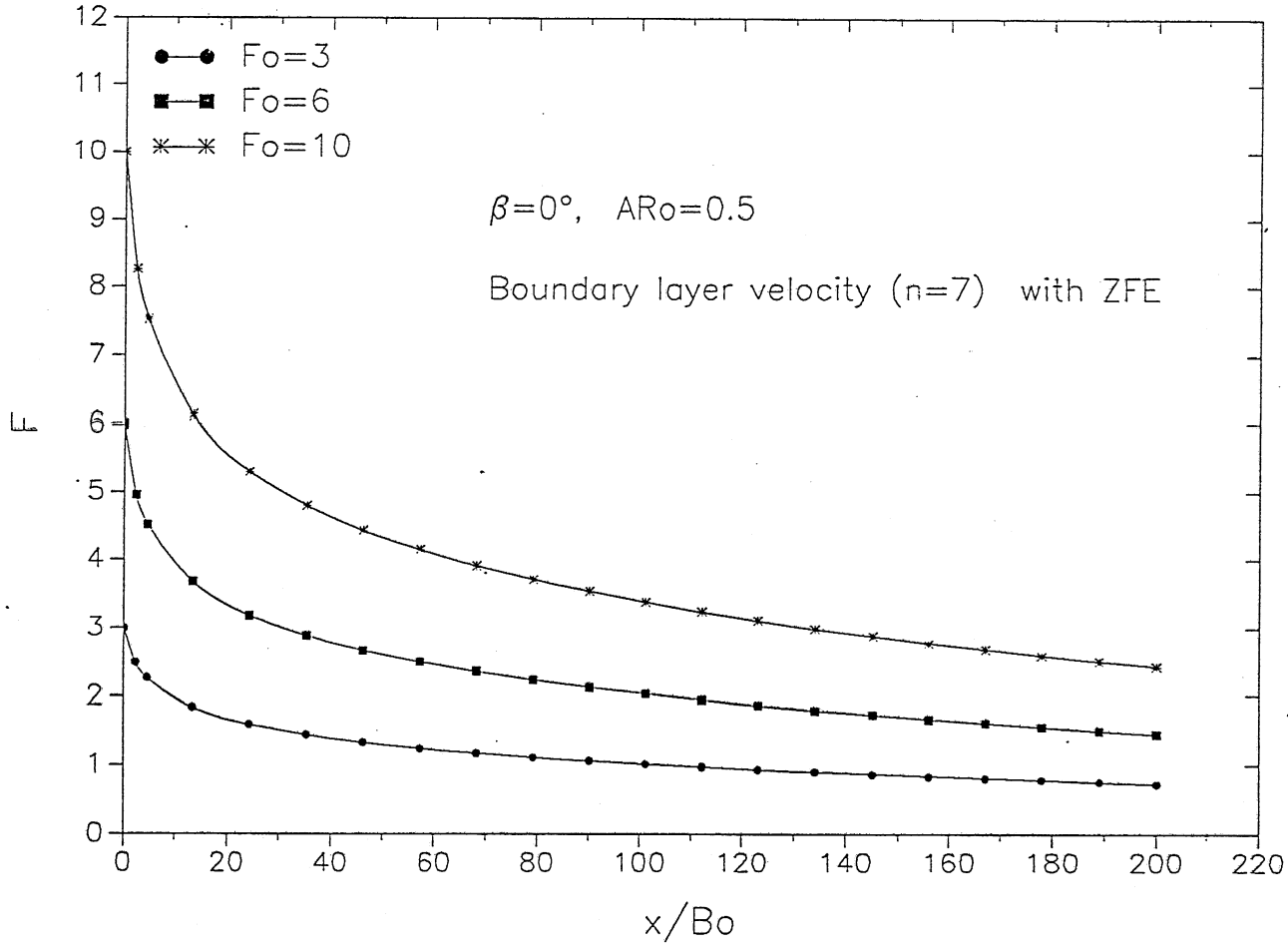

Fig. 5–1 Relationship between F and x/B_o for different F_o at $AR_o = 0.5$.

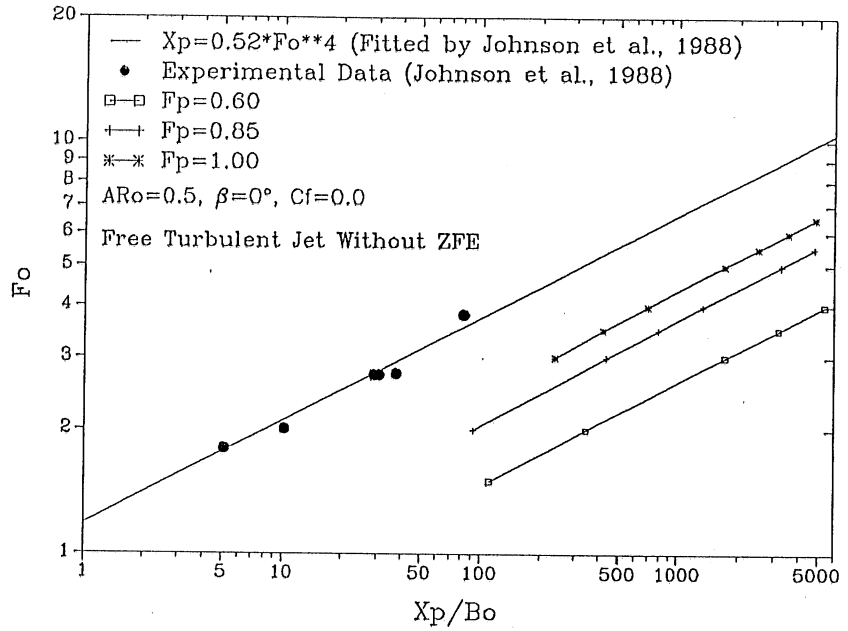

Fig. 5–2 Model results and experimental data for the relationship $x_p(F_0)$. Line through experimental data and model results are for free jet theory (frictionless).

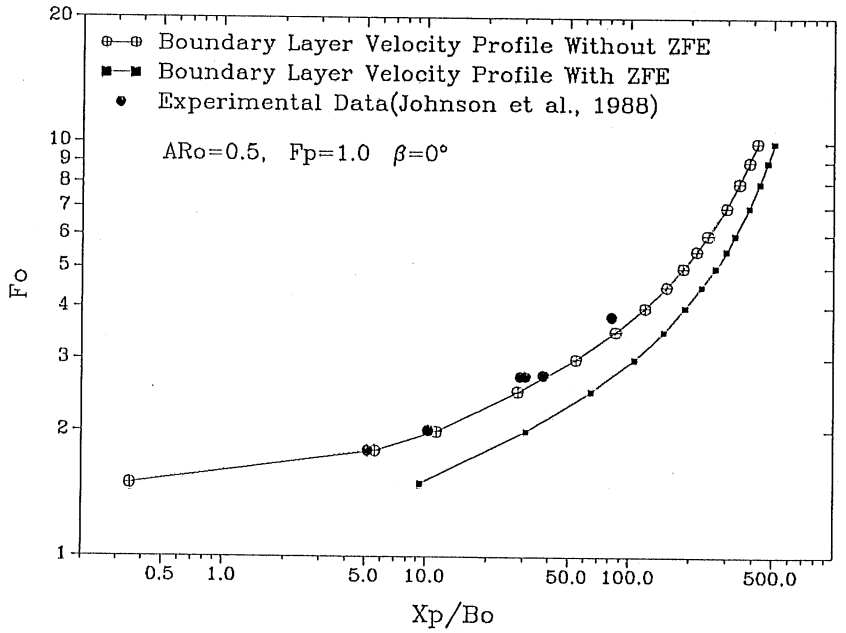

Fig. 5–3 Model results and experimental data for the relationship $x_p(F_0)$. The model includes bottom friction effects.

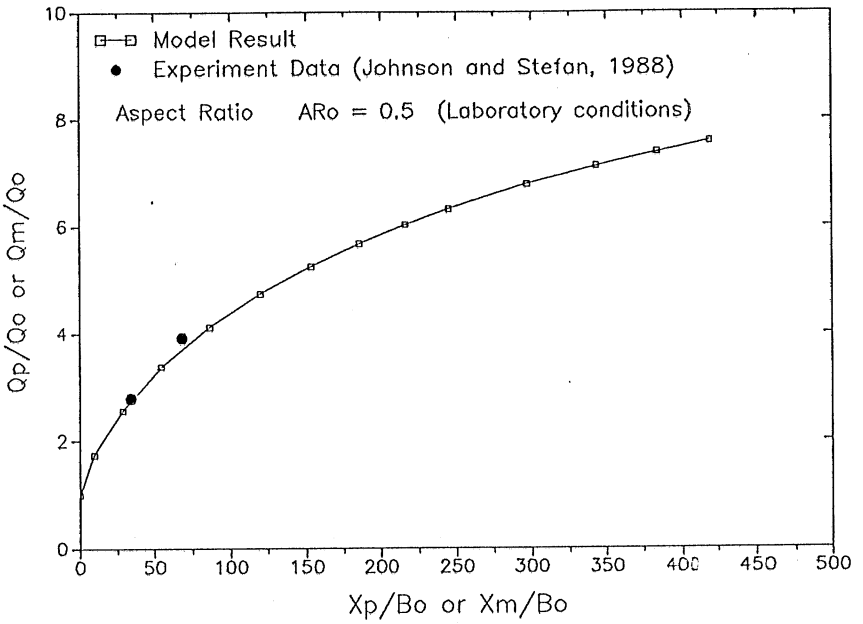

Fig. 5–4 Experimental data and model results for dilution Q_p/Q_o at $\beta = 0°$ and $AR_o = 0.5$.

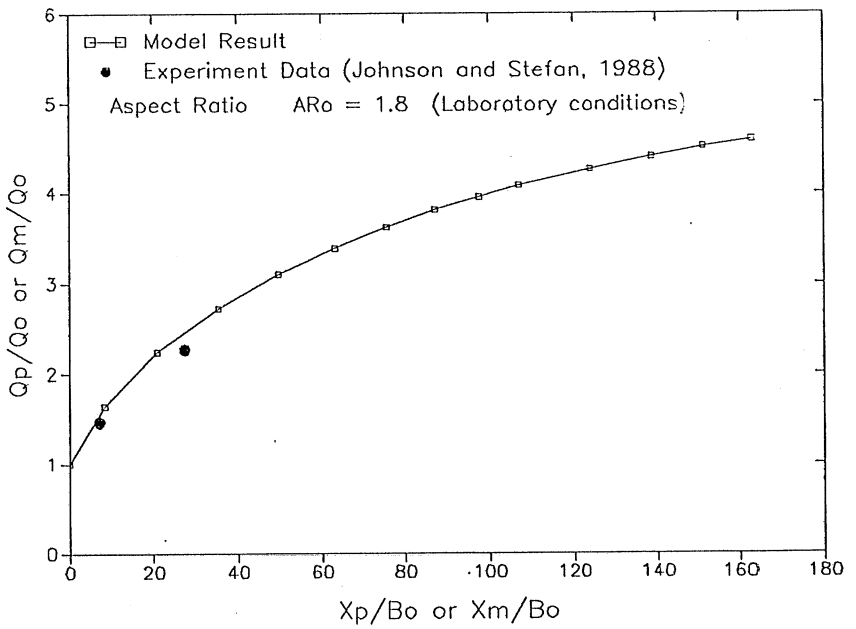

Fig. 5–5 Experimental data and model results for dilution Q_p/Q_o at $\beta = 0°$ and $AR_o = 1.8$.

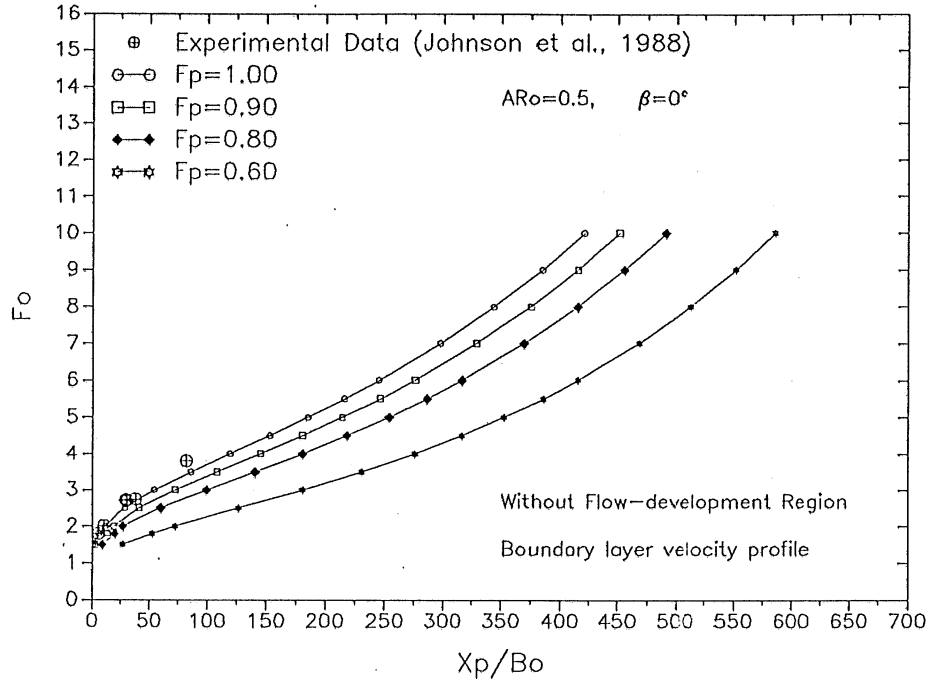

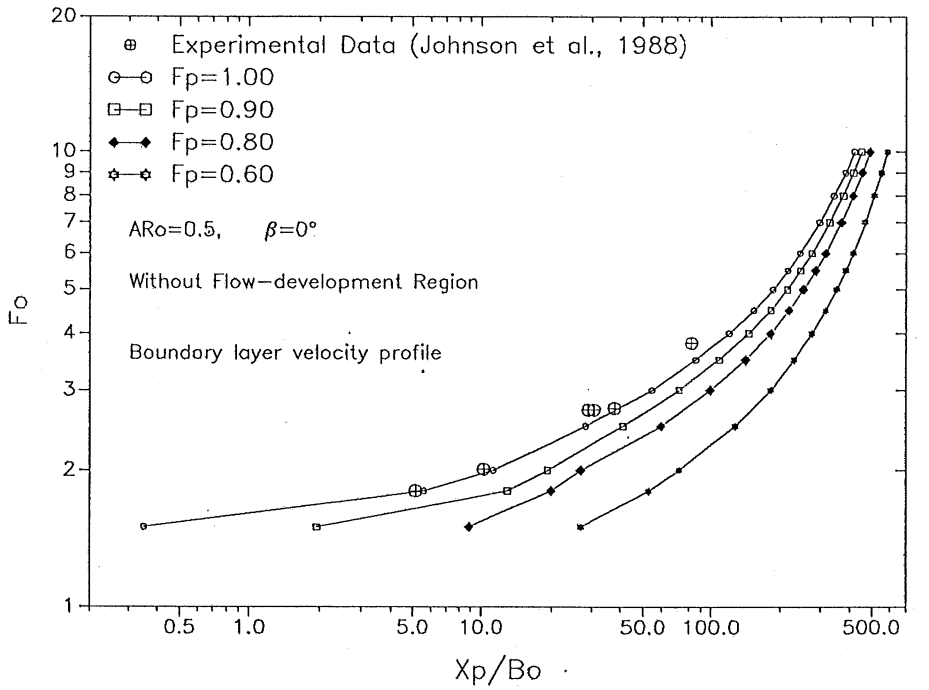

Fig. 5–6 Sensitivity of model results at different F_p in cartesian(top) and log–log(bottom) coordinates. The model includes effects of bottom friction.

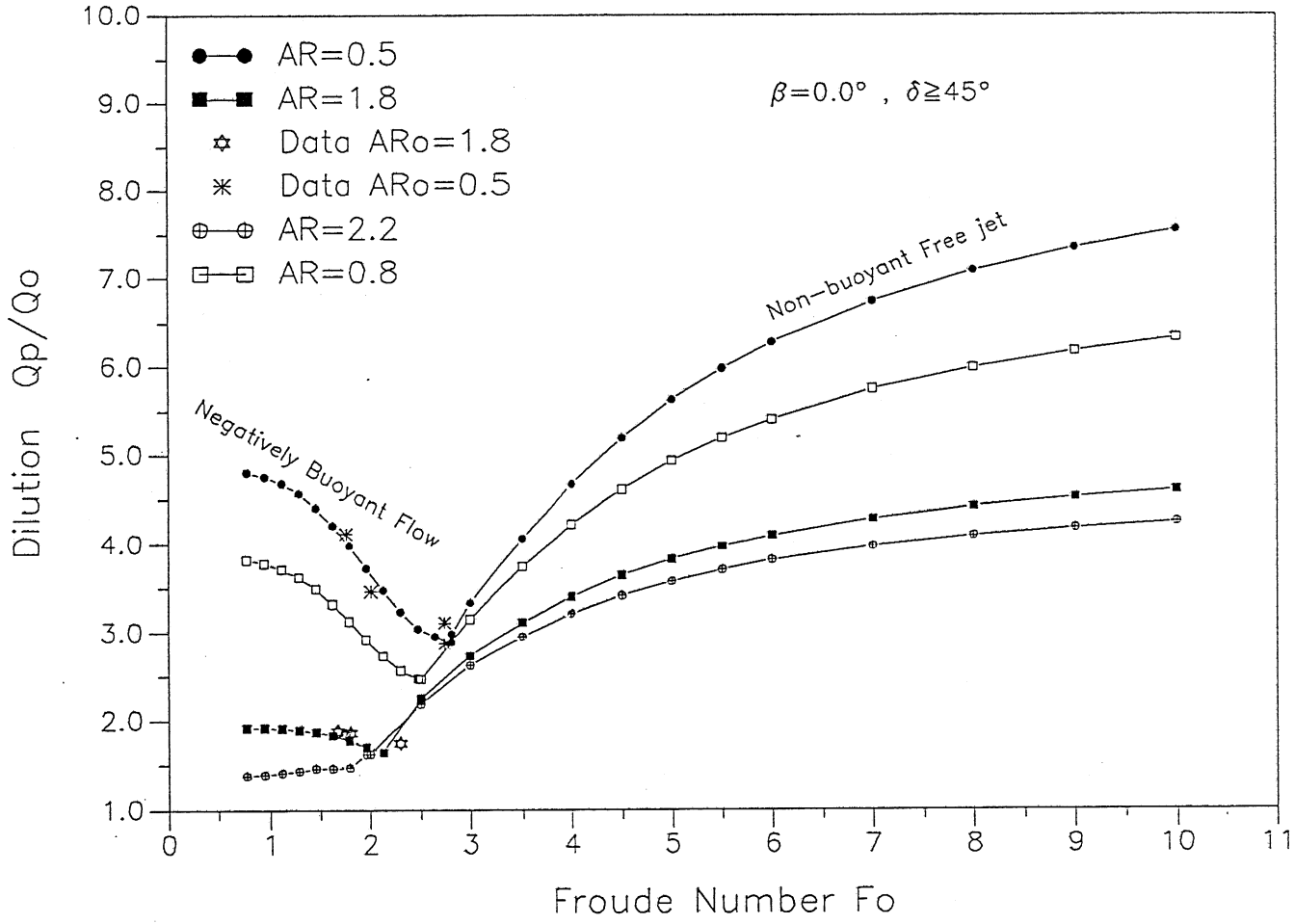

Fig. 5–7 Prediction of dilution under laboratory conditions.

figure provides information to predict dilution before plunging if F_o is given. The right–hand portion of the graph labeled "Non–buoyant Free Jet" is a model simulation result. The left–hand portion labeled "Negatively Buoyant Flow" is from an empirical analysis of laboratory data given in Appendix A.

In Appendix A, Fig. A–18 gives the relationship between Q_p/Q_o and F_o at different aspect ratios AR_o. It extrapolates from the data by use of the same formula for any aspect ratio AR_o if F_o is large (approximately a non–buoyant jet flow). The numerical model developed in the previous section is for non–buoyant jet flow and it shows that **dilution Q_p/Q_o is dependent on inflow channel aspect ratio.** Combing the experimental empirical result of negatively buoyant flow with the numerical model results of non–buoyant flow gives Fig. 5–7. This figure is the currently best estimate of the relationship between Q_p/Q_o and F_o for the constraints stated ($AR_o < 2.2$, $\beta = 0°$, $\delta > 45°$). More general situations will be analyzed later.

V.2.2 Sloping channel discharge

In sloping channels, the water depth varies and affects densimetric Froude number F as shown by equation [5–6]. Fig. 5–8 gives the relationship of F_o versus x_p/B_o (top) and F_o versus $x_p/\sqrt{A_o}$ (bottom) for a bottom slope $\beta = 3°$ and with $F_p = 1.0$. A_o is the cross–sectional area at the outlet. Agreement of the numerical results with a few experimental data (Johnson and Stefan, 1988) is reasonable but not outstanding. Fig. 5–9 shows dilution Q_p/Q_o versus F_o. Dilution increases linearly with F_o when $F_o > 2$. Using $c_f = 0.0055$ (see chapter II) and a power law velocity profile with $n = 7$, the numerical results match well with experimental data.

V.3 Application of complete model to field conditions

V.3.1 Friction coefficient c_f under field conditions

We wish to apply the model to field conditions, with typical Manning coefficients n, water depths H_o, and aspect ratios AR_o. We use English units for field conditions. The mean flow velocity U can be written as

$$U = \frac{1.49}{n} R_h^{2/3} S_o^{1/2} , \qquad [5–18]$$

where R_h = hydraulic radius and S_o = hydraulic slope. We assume that the flow is a normal flow if the slope of the channel is small, then S_o is the slope of channel bottom. We assume the inflow channel is rectangular such that

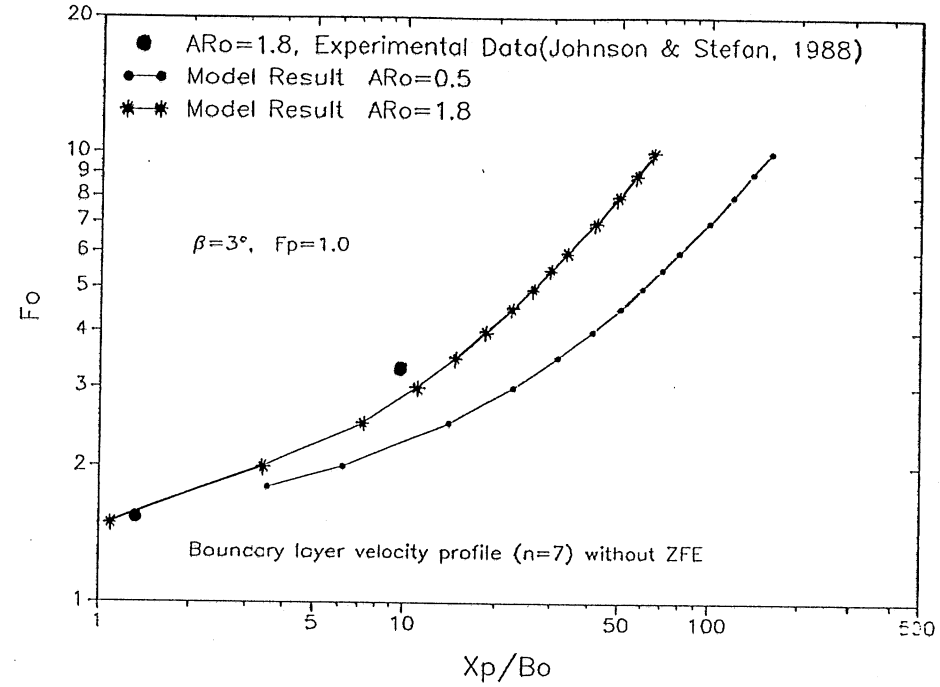

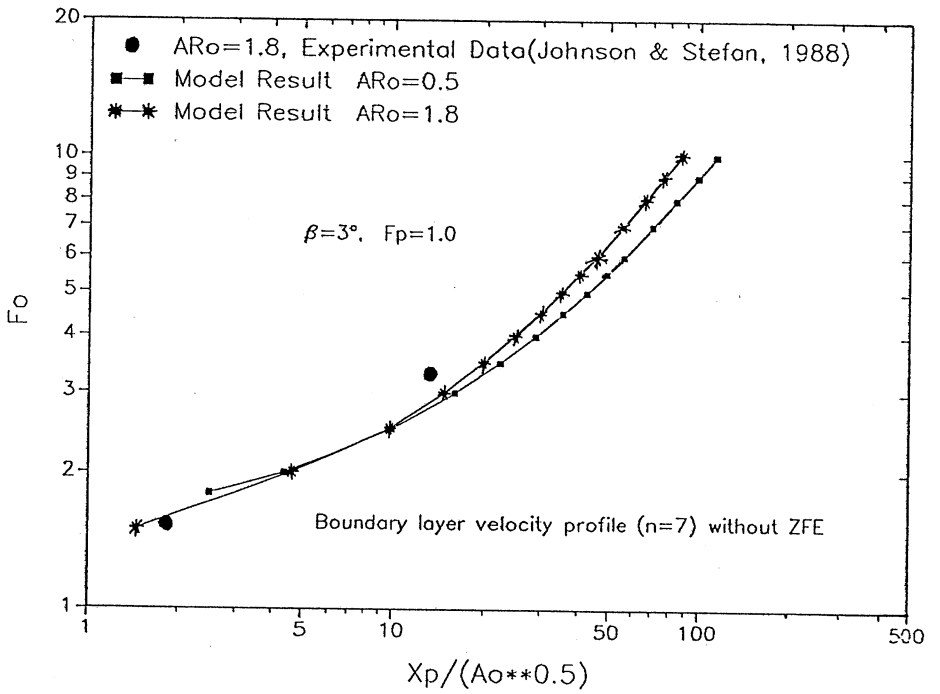

Fig. 5–8 Comparison of experimental plunging point data with model results at $\beta = 3°$ and $F_p = 1.0$. x_p is normalized by B_o (top) or $\sqrt{A_o}$ (bottom)

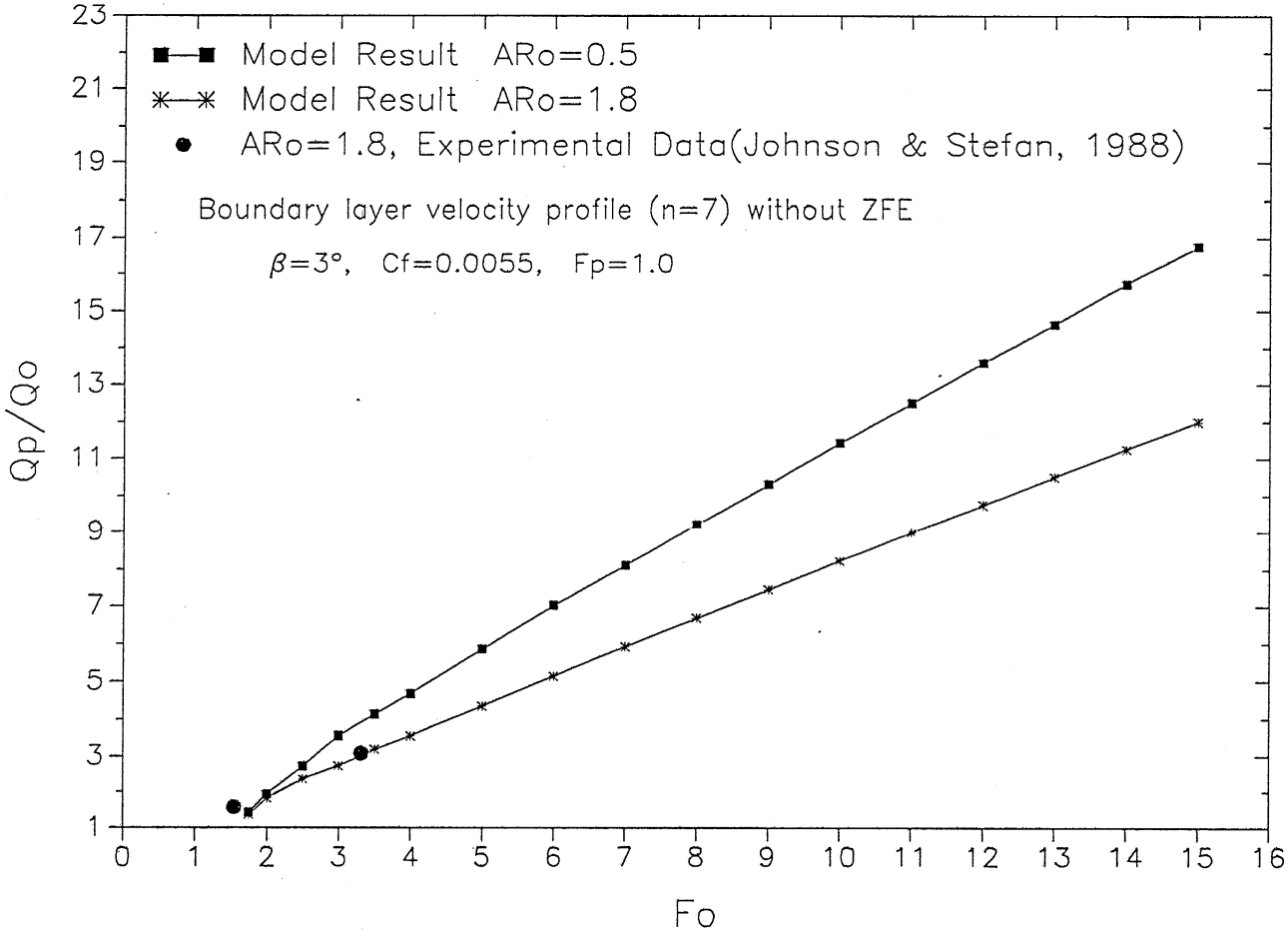

Fig. 5–9 Comparison of experimental data with numerical results of dilution Q_p/Q_o at $\beta = 3°$ [laboratory condition].

$$R_h = \frac{B_o H_o}{B_o + 2H_o} \qquad [5\text{–}19]$$

Assuming $\nu = 10^{-5}$ ft^2/sec, we can obtain a Reynolds number $Re_o = \frac{U_o H_o}{\nu}$, and then determine the exponent n of the vertical velocity profiles. The Chezy coefficient C (Vennard & Street, 1975) is

$$C = \frac{1.49\ R_h^{1/6}}{n} = \sqrt{8g/\lambda} \qquad [5\text{–}20]$$

where λ = non–dimensional coefficient of resistance defined in [4–4a], and g = acceleration of gravity. Then

$$\lambda = \frac{8g}{1.49^2}\ n^2/R_h^{1/3} = 35.3\ n^2/R_h^{1/3} \qquad [5\text{–}21]$$

From equation [4–4a] and definition of the friction coefficient $c_f = \frac{\tau_o}{0.5\rho U_\infty^2}$, one derives the relationship

$$c_f = \frac{\lambda}{4}\ (U/U_\infty)^2 \qquad [5\text{–}22]$$

where $\frac{U}{U_\infty} = \chi$ is dependent on Reynolds number Re_o as shown in Table 4.1.

With reference to Table 5 (Vennard & Street, 1975) for a natural channel, if it is clean and fairly straight, Manning's n = 0.03; a typical range of n values is n = 0.025 to 0.10. We use two typical Manning coefficients n = 0.03 and n = 0.06. For channel slope, we use three typical values: $S_o = \frac{1}{2000} = 0.0005$ (mild slope), $S_o = \frac{1}{1000} = 0.001$, and $S_o = \frac{1}{200} = 0.005$ (very steep slope). We assume a water depth H_o = 3 ft. If aspect ratio AR_o is large, we can use $R_h \approx 3.0$. From equations [5–18], [5–21] and [5–22], we obtain Table 5.1.

For field conditions, Reynolds number Re_o is on the order of 10^5 to 10^6, and the exponent n of the power law velocity profile is 9 or 10. We use an exponent n = 10 for numerical calculations. With reference to Fig 20.18 (Schlichting, 1960) the local friction coefficient c_f is in the *completely rough regime* and c_f is a function of relative roughness only.

Table 5.1 Friction coefficient c_f and Reynolds number Re_0 for field conditions.

n*	S_0	U_0(ft/sec)	Re_0	λ	c_f
0.03	0.0005	2.31	6.9×10^5	0.022	0.004
0.03	0.001	3.27	9.8×10^5	0.022	0.004
0.03	0.005	7.31	2.2×10^6	0.022	0.004
0.06	0.0005	1.16	3.5×10^5	0.088	0.016
0.06	0.001	1.64	4.9×10^5	0.088	0.016
0.06	0.005	3.65	1.1×10^6	0.088	0.0165

where n* is Mannings' n.

V.3.2 Comparison of model prediction with field data

A set of field data has been collected at a wastewater effluent site (Johnson and Stefan, 1988) and those results were compared with model results. A density driven "plunging" flow was observed where the effluent from the Metro Wastewater Treatment Plant in St Paul, MN, is discharged into the impounded Mississippi River. Velocity measurements were taken across the mouth of the discharge channel twice in 1984 by Johnson and Stefan (1988). The geometrical parameters of the inflow channel were: H_0 = 4.2 ft, A_0 = 330 ft^2 = effluent channel cross–section, AR_0 = 19 = effluent channel aspect ratio, x_m = distance to measurement section = 490 ft (2/22/84) or = 470 ft (2/30/84). δ = 22° = channel divergence half–angle, β = 2° = mean slope. The bottom slope β in the receiving bay is actually quite variable. Sections as steep as 5° are present but the average is about 2° over the entire length of the diffuser (Johnson and Stefan, 1988).

Before we discuss the integral model predictions we need to specify all parameters in the numerical model simulation of the field conditions. The inflow Reynolds number $Re_0 = \frac{U_0 H_0}{\nu} = 5.3\times10^5$. With reference to Table 4.1 the exponent of boundary layer velocity profile n = 8.8 is used. In order to specify the local coefficient c_f we use a Manning's coefficient n = 0.03 for natural channel. Using equations [5–19], [5–21] and [5–22], gives

$$\lambda = 35.3\ n^2/R_h^{1/3} = 0.02$$

$$c_f = \frac{\lambda}{4}\ (U/U_\infty)^2 = 0.004$$

Since the flow from the outlet channel separated only from one bank and remained attached to the other, it was analyzed as a half–jet, here called "wall jet" (Johnson and Stefan, 1989). As shown in Fig. 5–10 (bottom), the bank without separation can be considered the line of symmetry of a free jet. To account for the "wall jet" image in the numerical model we need to double the inflow aspect ratio AR_0 but do not need to change other conditions of inflow. Comparisons of integral model predictions with field data are shown in Fig. 5–10 (top).

Since it was difficult to specify slope angle exactly the sensitivity of the model results to β was determined. Fig. 5–10 shows model results with β = 2°, 3° and 4° as well as field data (Johnson and Stefan, 1988). The relationship between $Q(x)/Q_0$ and x/B_0 is sensitive to slope angle β. Numerical model results match the field data in the range of measurement and calculation errors quite well. Fig. 5–11 shows the sensitivity of the model results to densimetric Froude number F_p and slope angle β. The model results are sensitive to F_p. The model result with F_p = 1.0 does not match the field data well. The numerical model results with F_p = 0.7 and β =2° fit reasonably with field data. It is therefore difficult to recommend an appropriate F_p value for field conditions because of the sparsity of field data.

If we leave out the flow development region (ZFE) from the integral jet model, we do not obtain results which match field data well. **Since the aspect ratio AR_0 is relatively large, a flow development region is necessary to model the transition from inflow with nearly uniform velocity profile to a fully developed flow region with Gaussian velocity distribution. This is different from small aspect ratios such as used in the laboratory experiments.**

V.3.3 Application and extrapolation of model to general field conditions

Under field conditions, a *hydraulically smooth regime* is sometimes possible. Some numerical extrapolation results in a *hydraulically smooth regime* are shown in Figs. 5–12 and Fig. 5–13 using a boundary layer velocity profile with n = 7 and a ZFE at β = 0°. Fig. 5–12 shows the relationship of F_0 versus x_p/B_0 at large aspect ratios AR_0. The numerical results are very sensitive to aspect ratio AR_0. The numerical results cannot be reduced to one curve by use of $AR_0^{1/8}$ as proposed originally by Johnson et al. (1988). Fig. 5–13 shows the relationships between dilution Q_p/Q_0, as well as the location of plunging x_p/B_0 on F_0 for large aspect ratios. If aspect ratio AR_0 is large, dilution increases slowly with F_0 and is less than that with small aspect ratio AR_0.

Under most field conditions the local friction coefficient c_f is in the *completely rough regime* (Table 5.1). Fig. 5–14 to Fig. 5–16 show the relationship of dilution Q_p/Q_0 versus inflow densimetric Froude number F_0 at β = 0° and aspect ratios from AR_0 = 5 to AR_0 = 100 as the local friction coefficient c_f is kept constant at either 0.0005 or 0.005 or 0.02. The exponent of the boundary layer velocity profile n = 10. The dilution Q_p/Q_0 increases

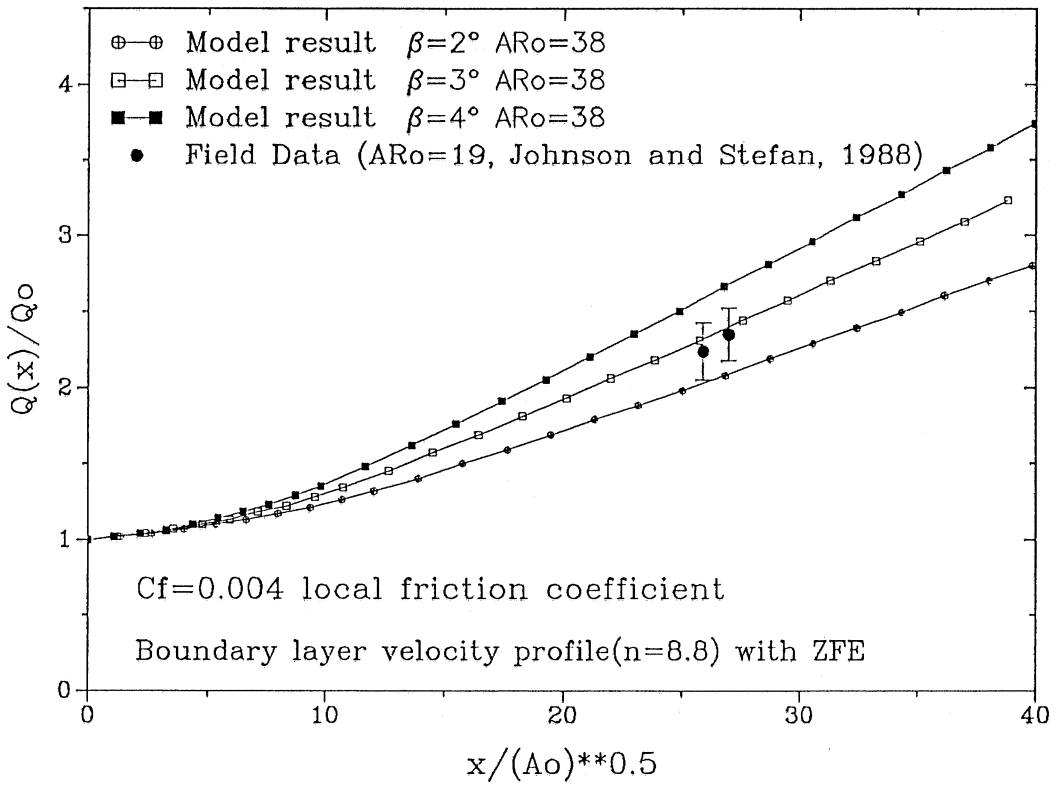

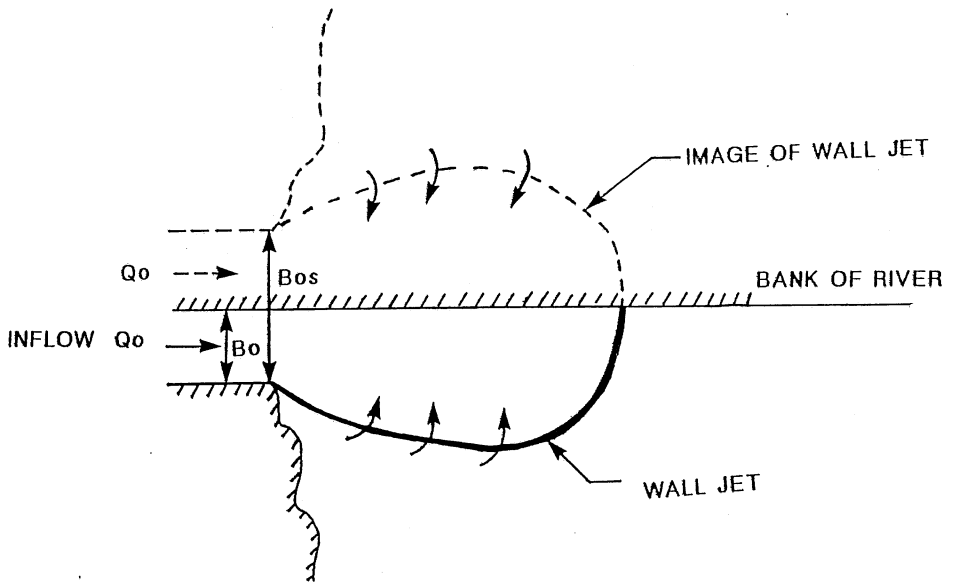

Fig. 5–10 Schematic plan view of wall jet in field condition (bottom) and cumulative effluent flow rates as a function of distance (top).

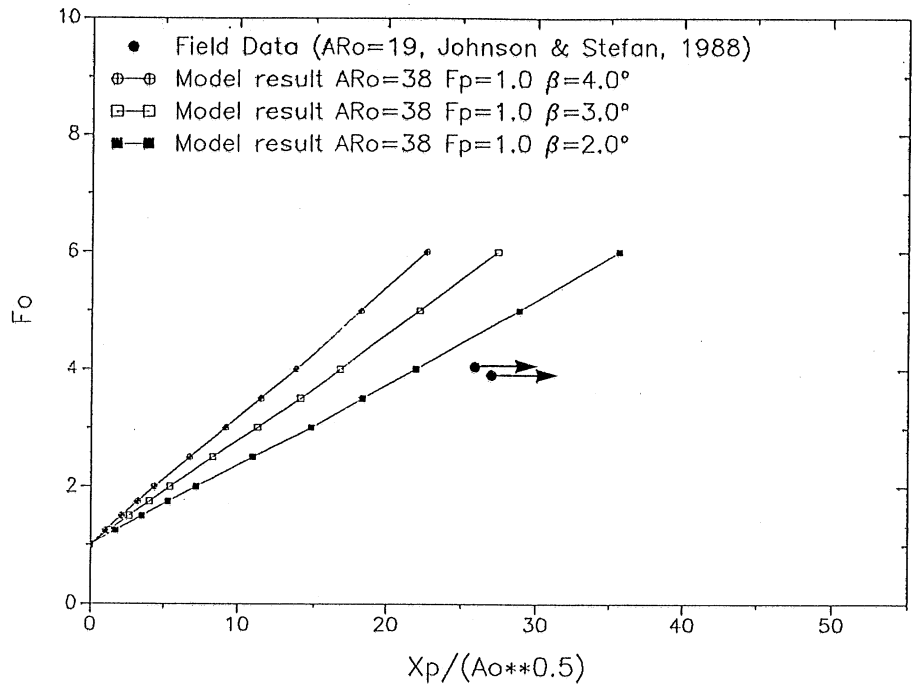

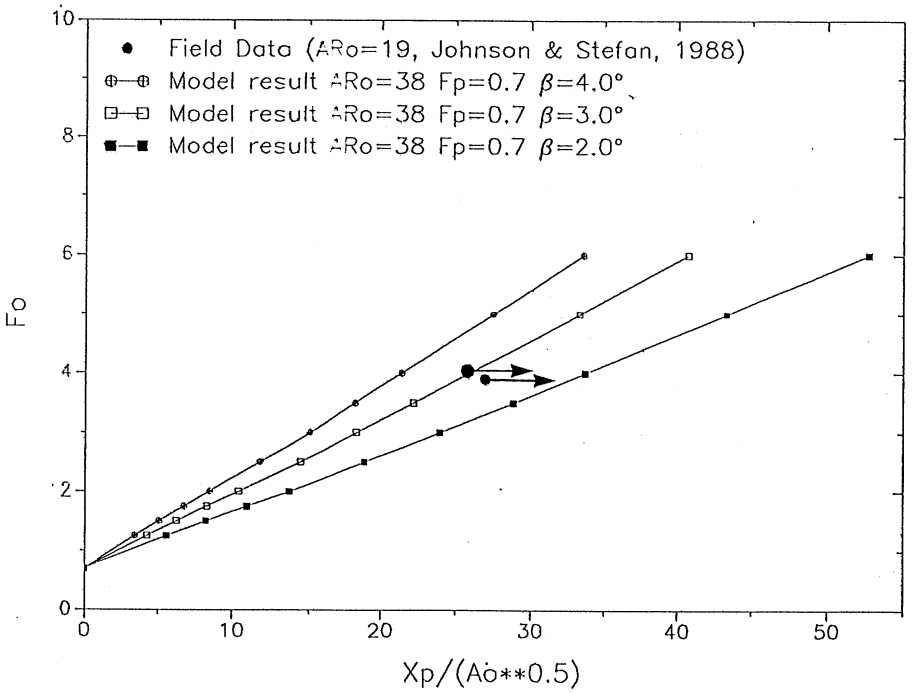

Fig. 5–11 Sensitivity of predicted distance to plunging x_p to densimetric Froude number F_o at plunging F_p and slope angle β.

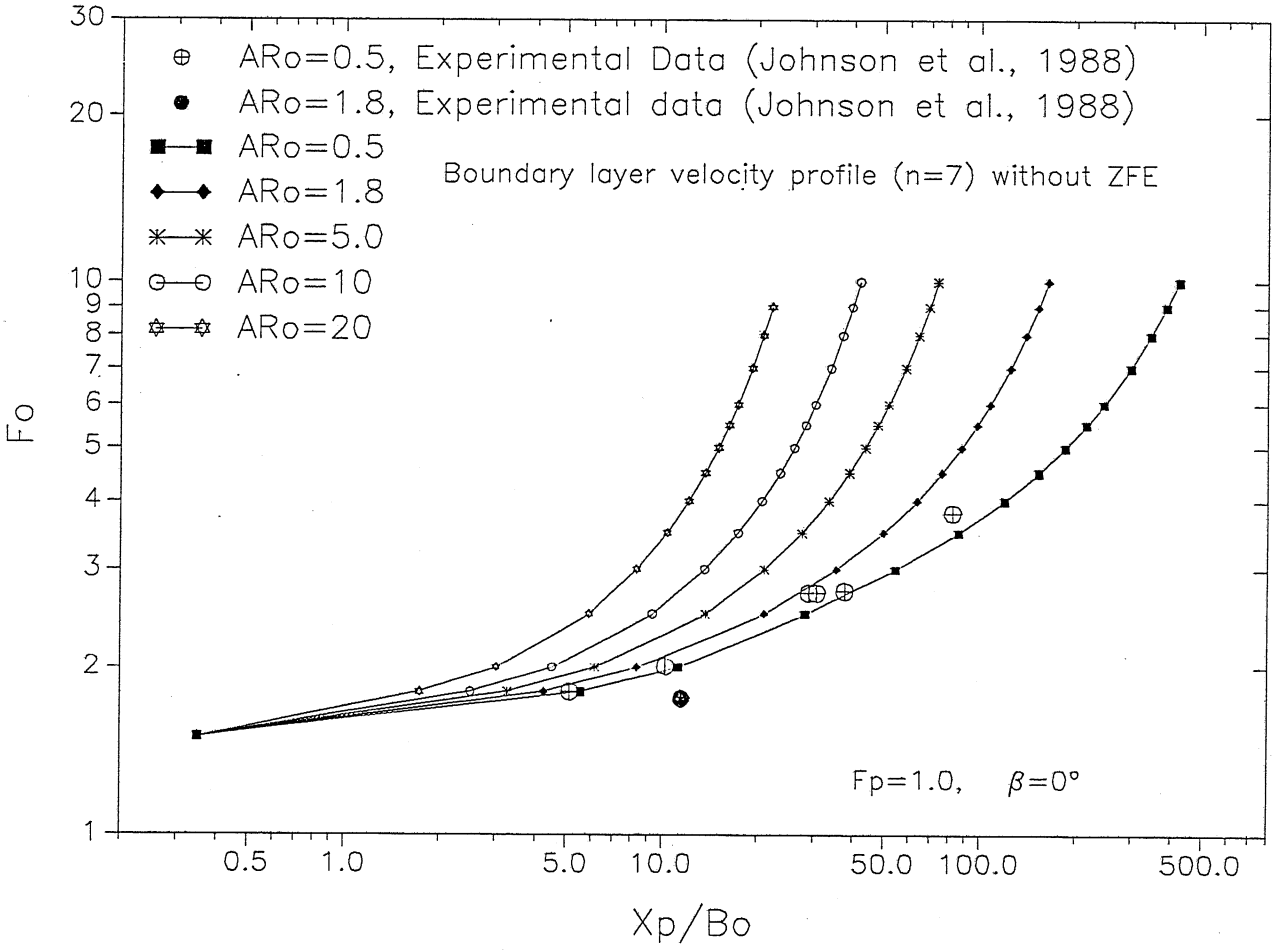

Fig. 5–12 Sensitivity of x_p/B_o to aspect ratio AR_o for smooth bottom.

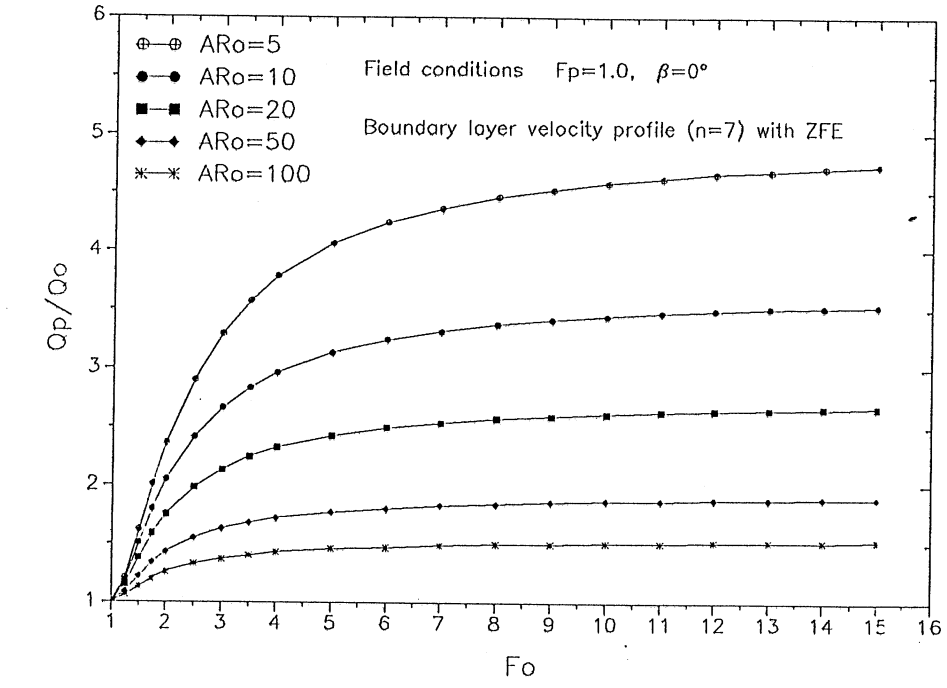

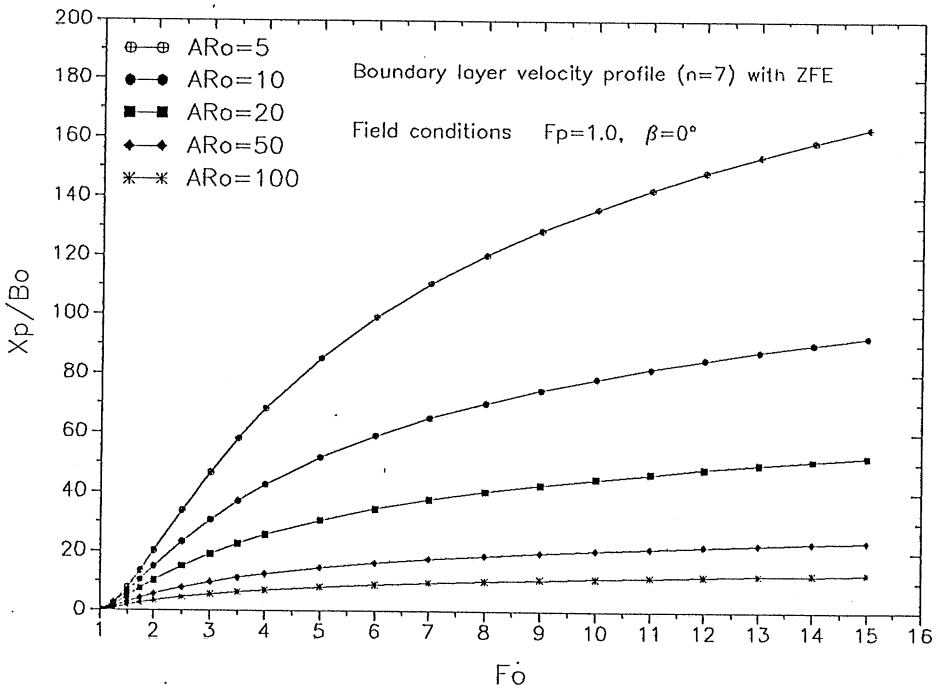

Fig. 5–13 Prediction of dilution (top) and plunging (bottom) for smooth bottom.

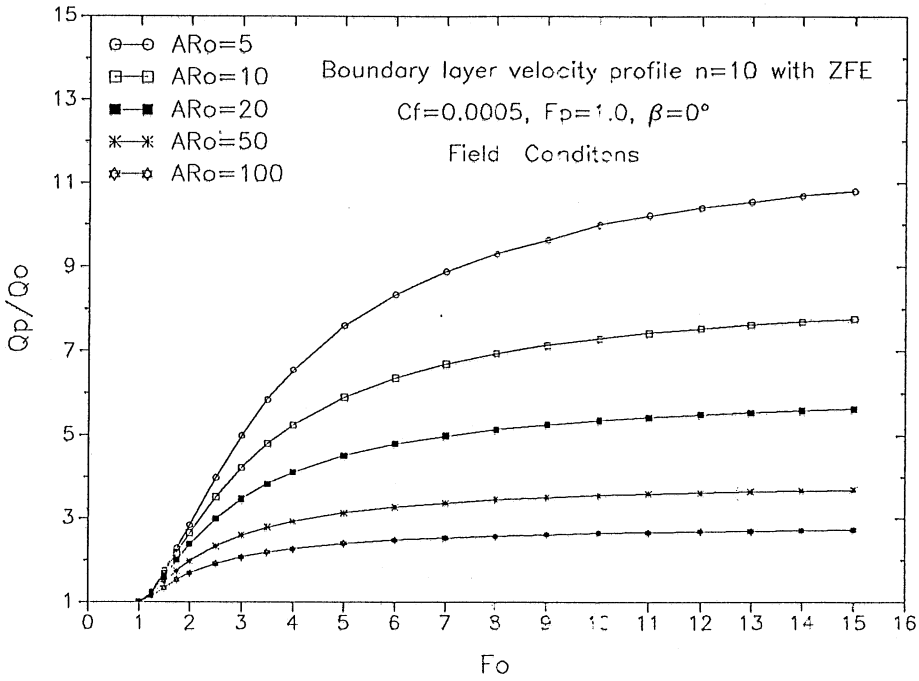

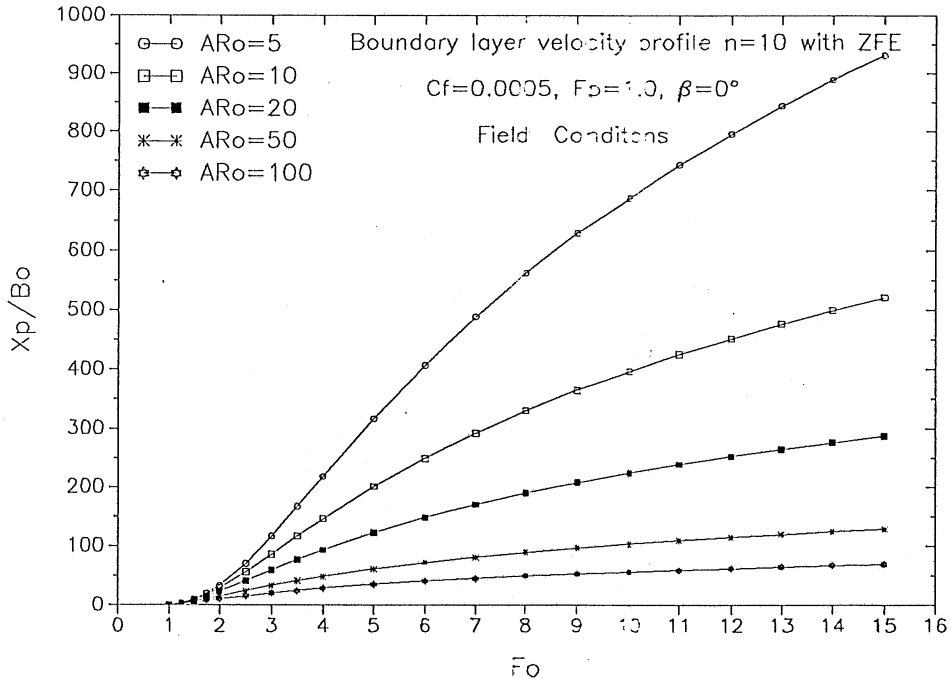

Fig. 5–14 Prediction of dilution (top) and plunging (bottom) at $c_f = 0.0005$.

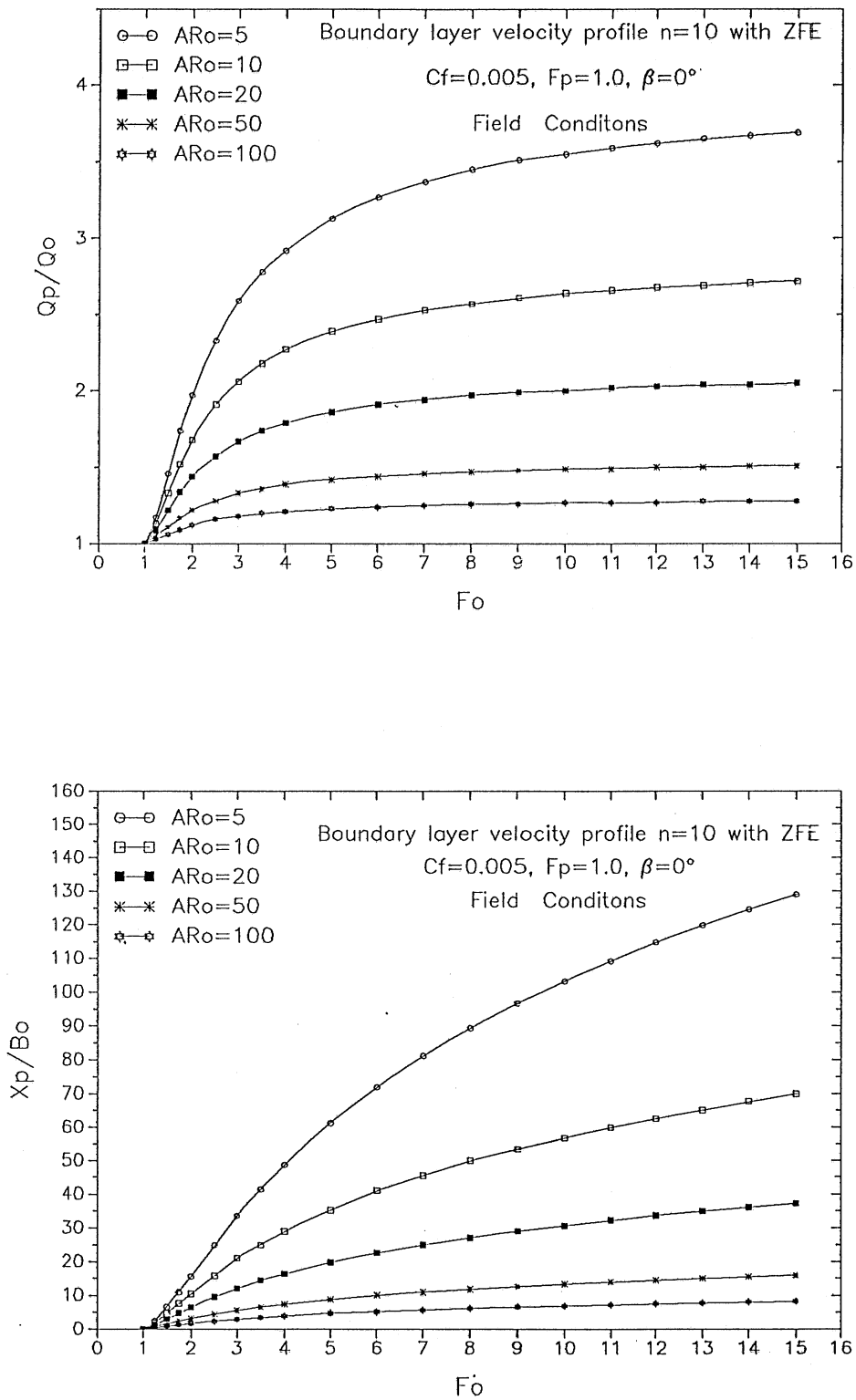

Fig. 5–15 Prediction of dilution (top) and plunging (bottom) at $c_f = 0.005$.

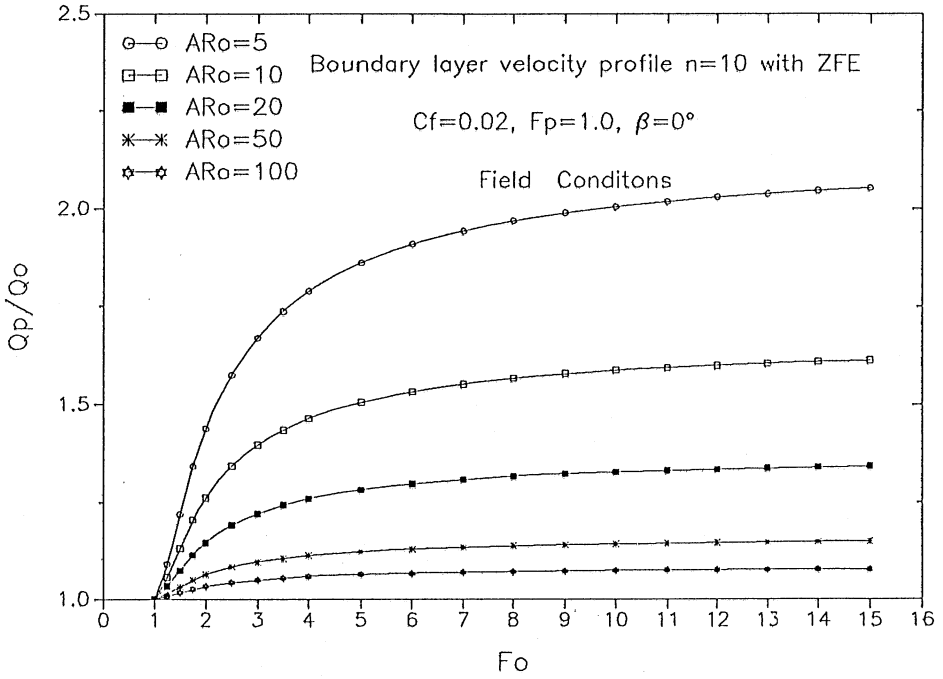

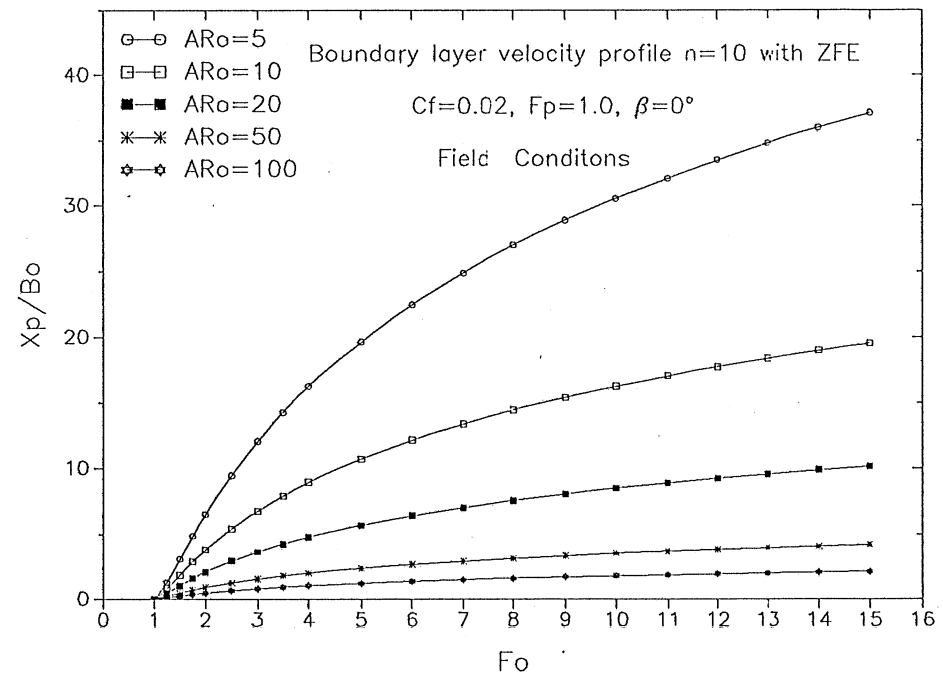

Fig. 5–16 Prediction of dilution (top) and plunging (bottom) at $c_f = 0.02$

very slowly with F_o and becomes almost a constant if aspect ratio AR_o is large and F_o is large. The limit values of dilution before plunging, taken to be approximately the dilution at $F_o = 15$, are shown in Fig. 5–17. The limit values are quite sensitive to the local friction coefficient and aspect ratio AR_o. **It is therefore important to specify carefully the local friction coefficient in the application of the integral model to field conditions.**

Typical bottom slopes are from 0° to 5°. Fig. 5–18 to Fig. 5–22 show predictions of dilution and x_p/B_o versus F_o for different slope angles β from 0.5° to 5° and different aspect ratios AR_o from 5 to 100 with $c_f = 0.005$. The dilution is very sensitive to aspect ratio of inflow. Fig. 5–23 shows the dependence of dilution Q_p/Q_o on slopes very explicitly. For small F_o dilution Q_p/Q_o decreases if β increase. For large F_o dilution Q_p/Q_o increases if β is less than some angle β (i.e. 1.5° for $c_f = 0.005$, $AR_o = 5$), and then decreases if β is less than that angle β. This relationship is more clearly shown in Fig. 5–24.

For discharge over a horizontal bottom Q_p/Q_o increases approximately parabolically with F_o. If slope angle $\beta > 1°$, dilution Q_p/Q_o becomes linearly related to F_o. The reason for this behavior is that if slope angle β increases, dilution $Q(x)/Q_o$ increases, but distance x_p to plunging decreases. The superimposed results are shown in Fig. 5–23.

$Q(x)/Q_o$ and x_p/B_o are also related to the choice of local friction coefficient c_f, entrainment coefficient α_e and aspect ratio AR_o. Fig. 5–25 shows model results of Q_p/Q_o versus F_o when $c_f = 0.005$ and $AR_o = 50$ are chosen. Fig. 5–26 shows explicitly that dilution of plunging Q_p/Q_o is very sensitive to small slope angles β if the friction coefficient c_f is very small. Fig. 5–27 shows that dilution of plunging Q_p/Q_o increases almost monotonically with slope angle β ($0° < \beta < 5°$) if the friction coefficient is very large. Fig. 5–28 shows not surprisingly that dilution is larger if a larger entrainment coefficient α_e is used provided that all other conditions are the same Fig. 5–25 & Fig. 5–28 have same conditions except for α_e=0.004 and α_e=0.005, respectively.

The envelope for maximum dilution for slope angles $0° \leq \beta \leq 5°$ and large aspect ratios $5 \leq AR_o < 100$ at $c_f = 0.005$, which is a typical friction coefficient under field conditions, is shown in Fig. 5–29. These envelope values $(Q_p/Q_o)_{max}$ are sensitive to the inflow aspect ratio AR_o. The relationship between Q_p/Q_o and AR_o in log–log coordinates is **approximately a straight line family with average slope 0.28** for different F_o. For the range $0.0015 < c_f < 0.015$, appropriate for field conditions, the slope does not change significantly. Fig. 5–30 shows $(Q_p/Q_o)_{max} * AR^{0.28}$ versus F_o for three different friction coefficients. For aspect ratios $5 \leq AR_o \leq 100$ the family of lines with same c_f can be reduced to one narrow bound by use of $AR^{0.28}$. Fig. 5–30 is the currently best estimate of maximum dilution for large aspect ratios $AR_o \geq 5$ under field conditions.

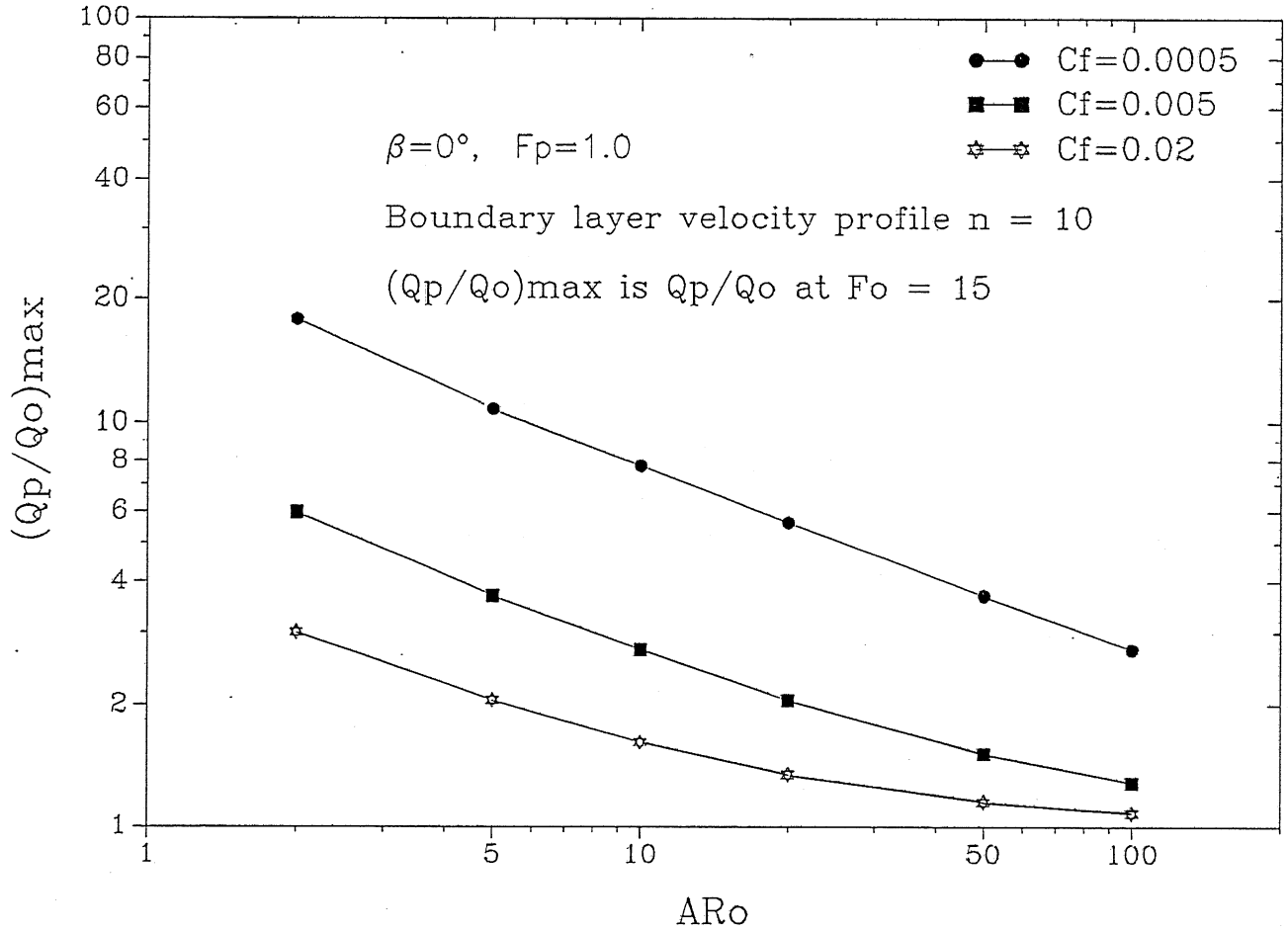

Fig. 5–17 Dilution at $F_o = 15$ for different AR_o and c_f.

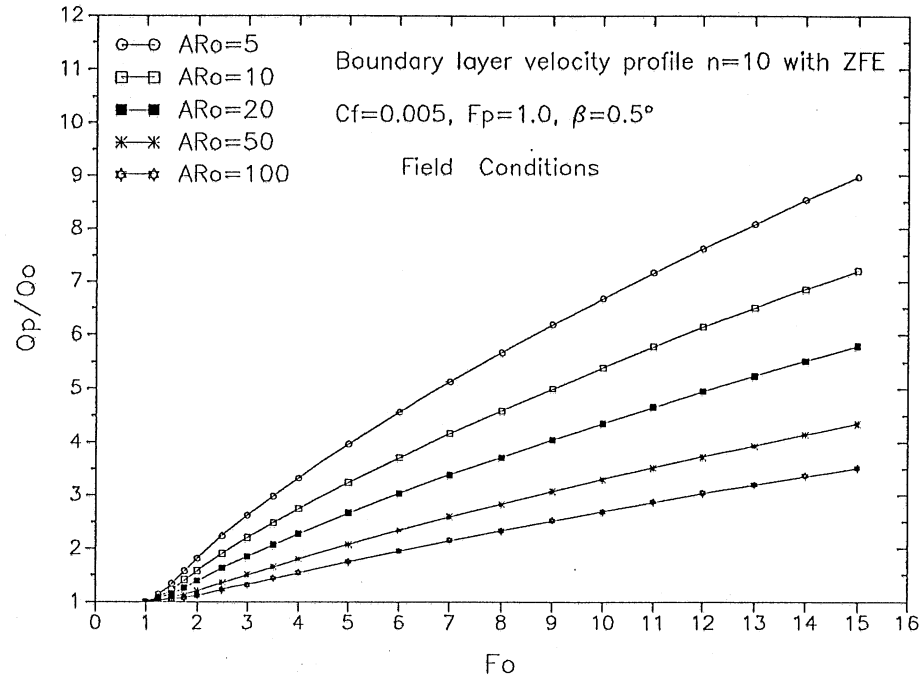

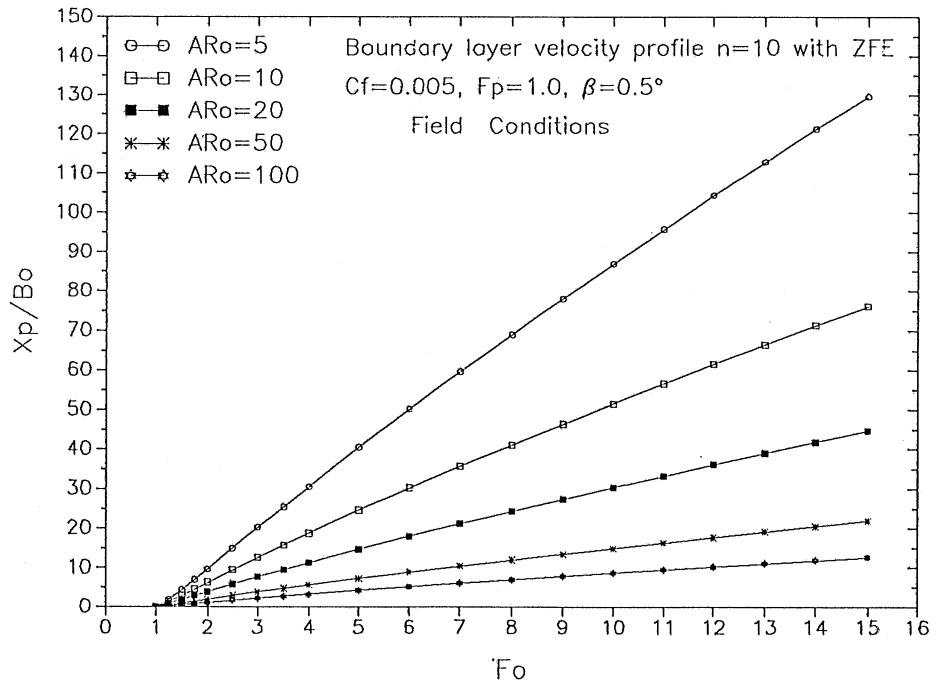

Fig. 5–18 Numerical results of dilution versus F_o at $c_f = 0.005$, $\beta = 0.5°$ for different aspect ratios AR_o.

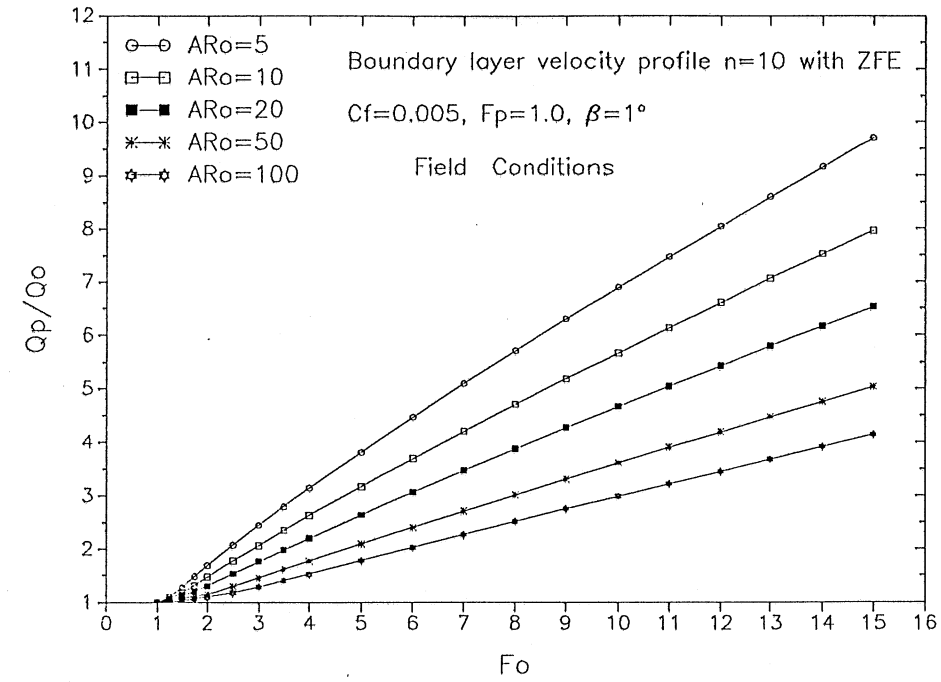

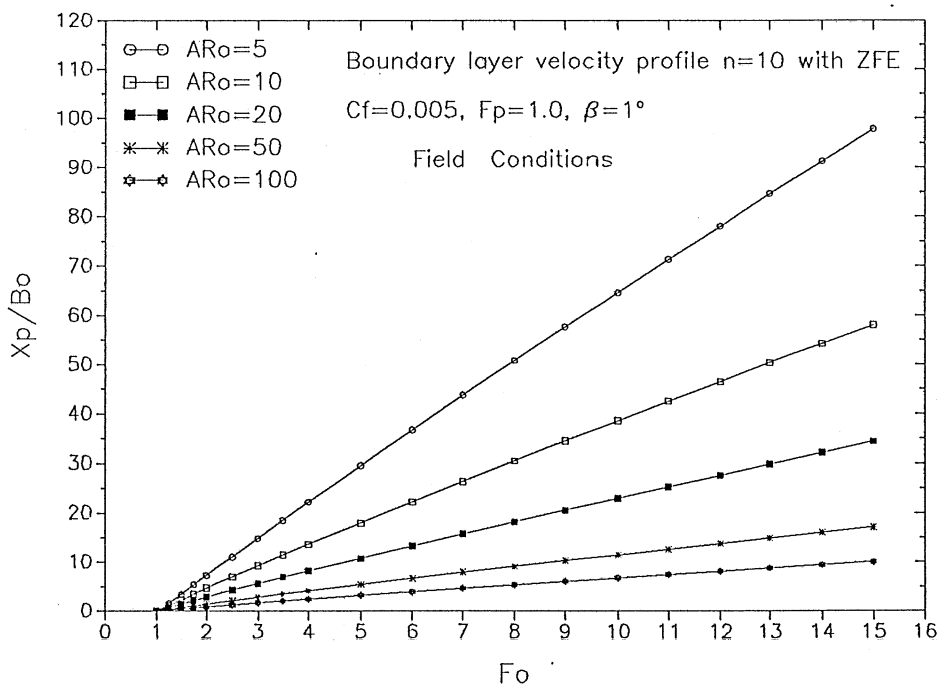

Fig. 5–19 Numerical results of dilution versus F_o at $c_f = 0.005$, $\beta = 1°$ for different aspect ratios AR_o.

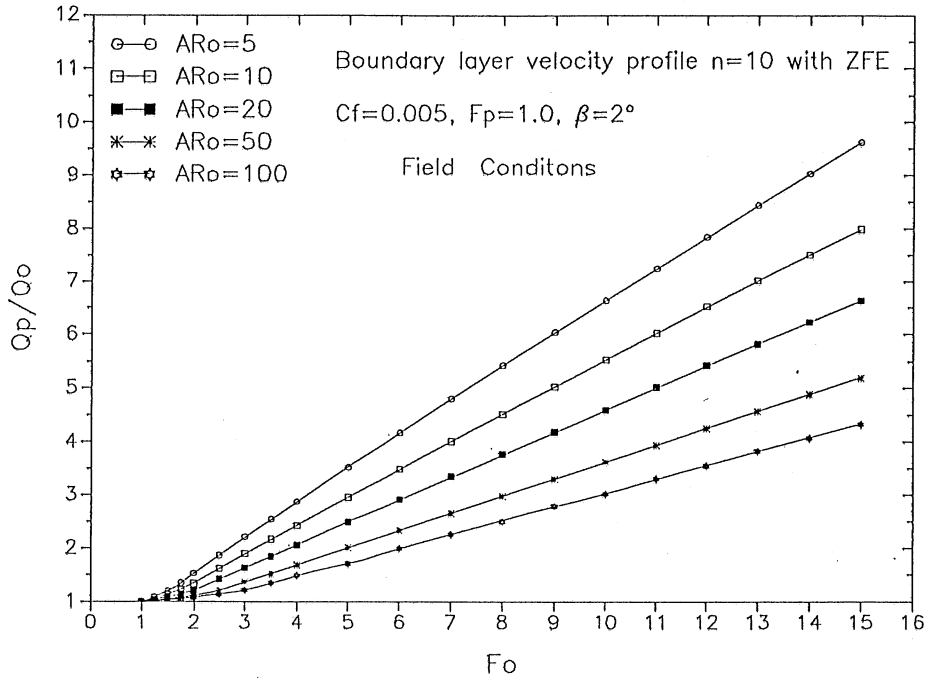

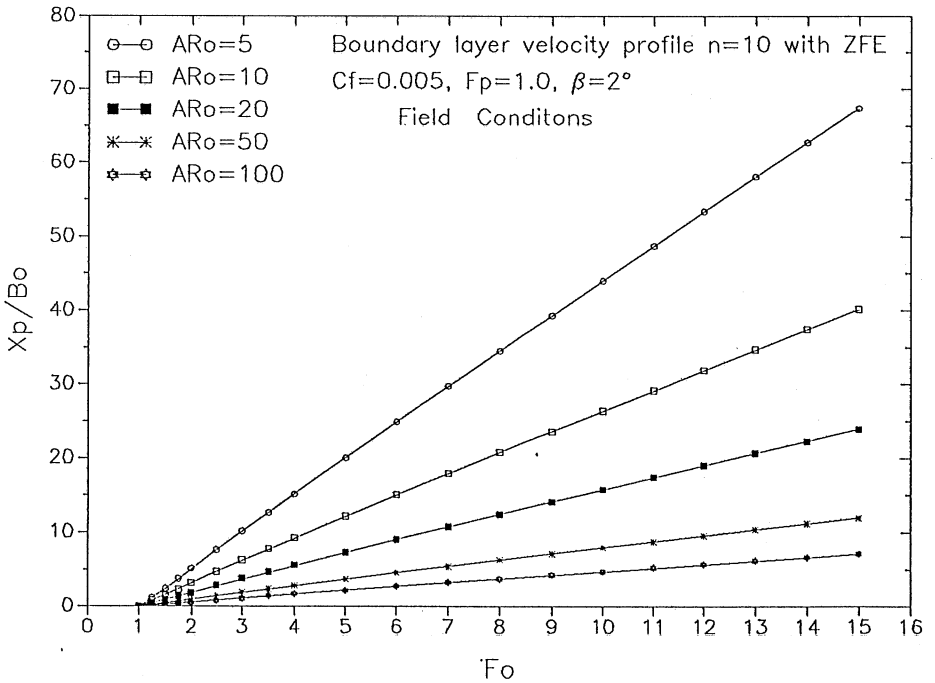

Fig. 5–20 Numerical results of dilution versus F_o at $c_f = 0.005$, $\beta = 2°$ for different aspect ratios AR_o.

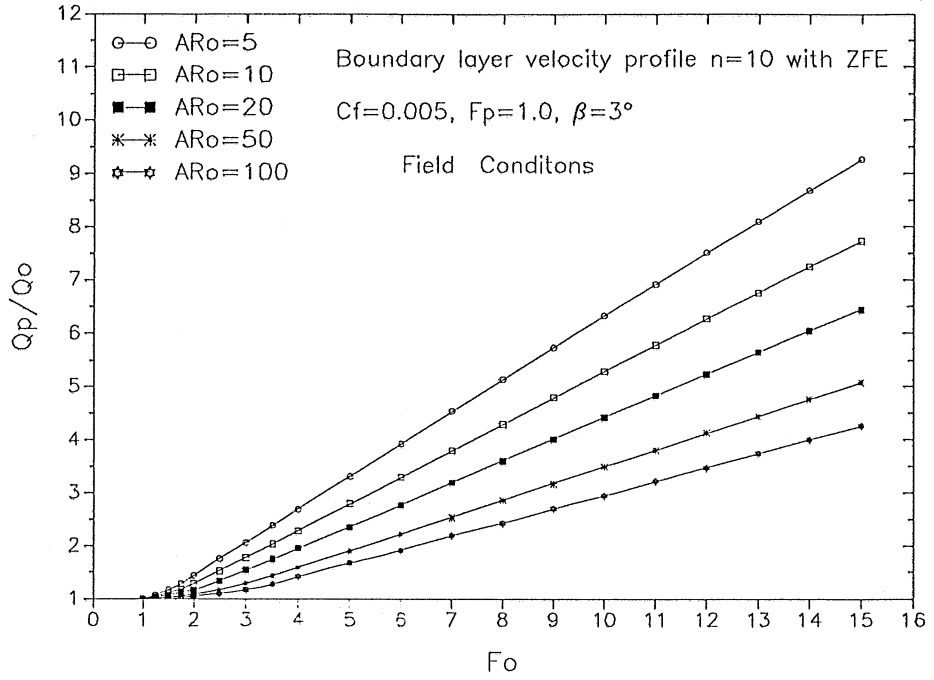

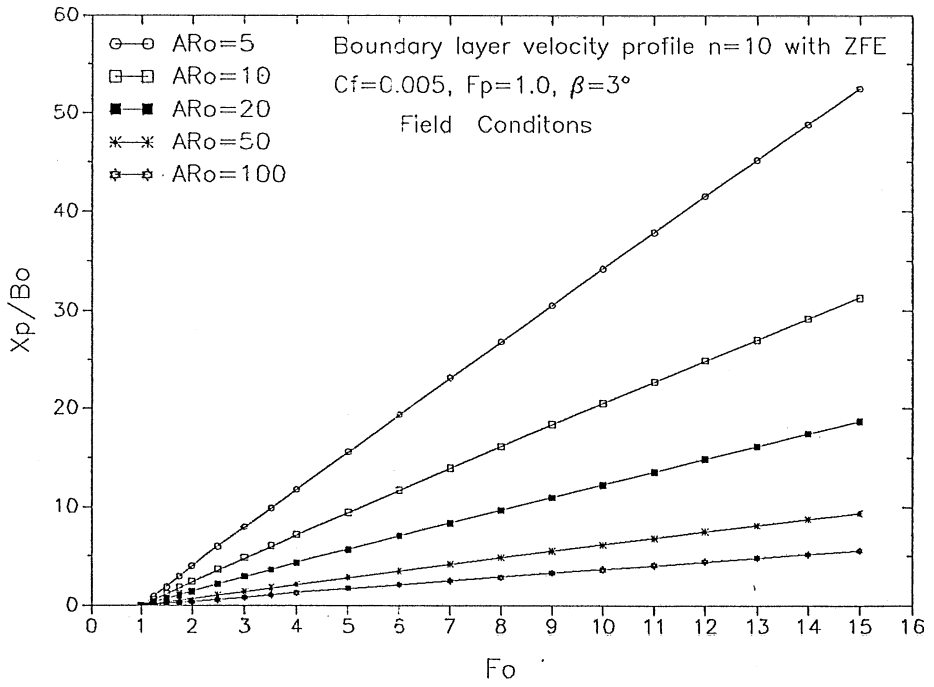

Fig. 5–21 Numerical results of dilution versus F_o at $c_f = 0.005$, $\beta = 3°$ for different aspect ratios AR_o.

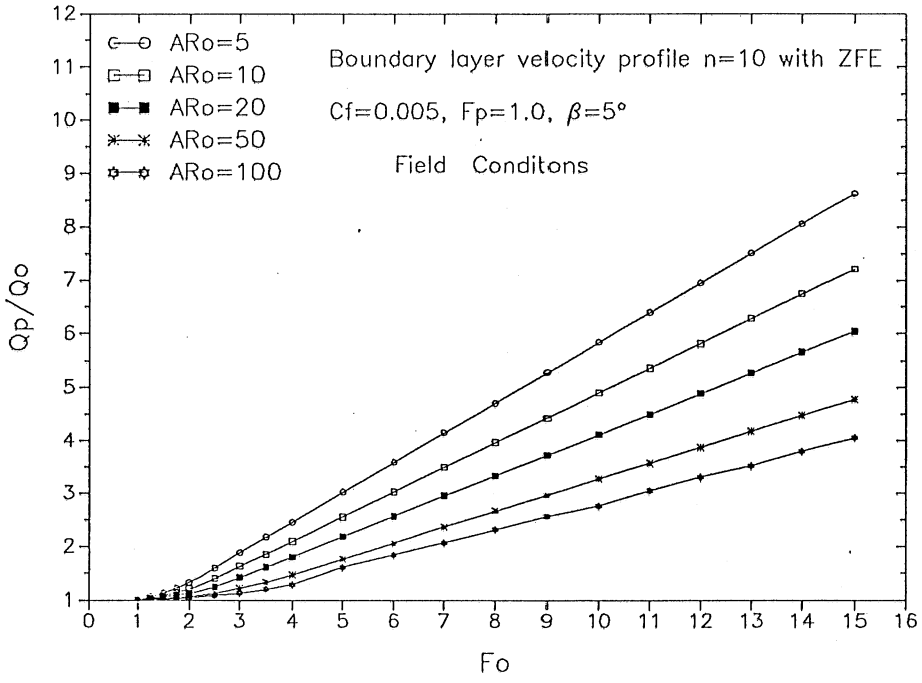

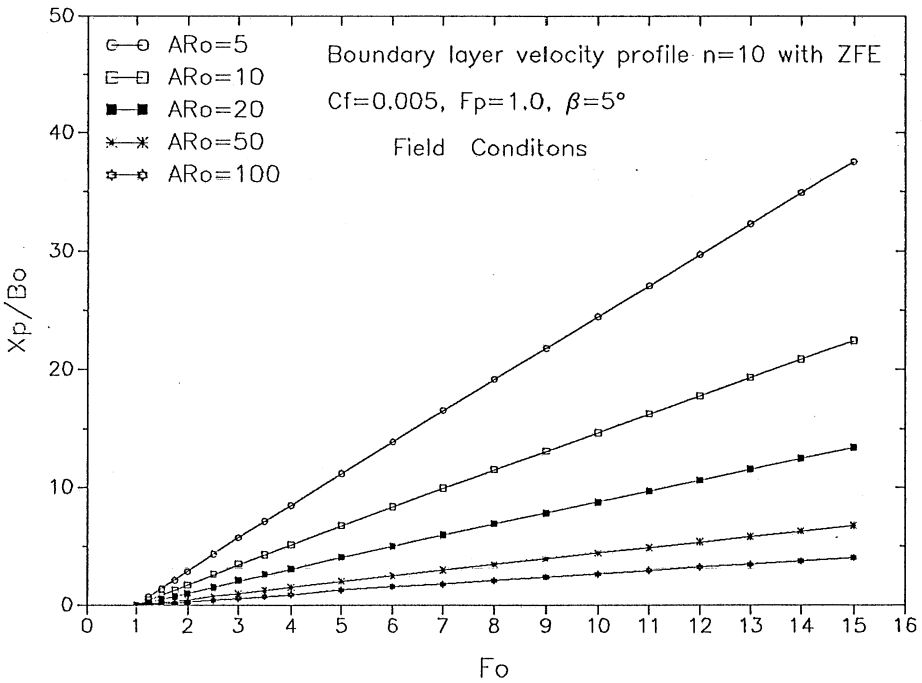

Fig. 5–22 Numerical results of dilution versus F_o at $c_f = 0.005$, $\beta = 5°$ for different aspect ratios AR_o.

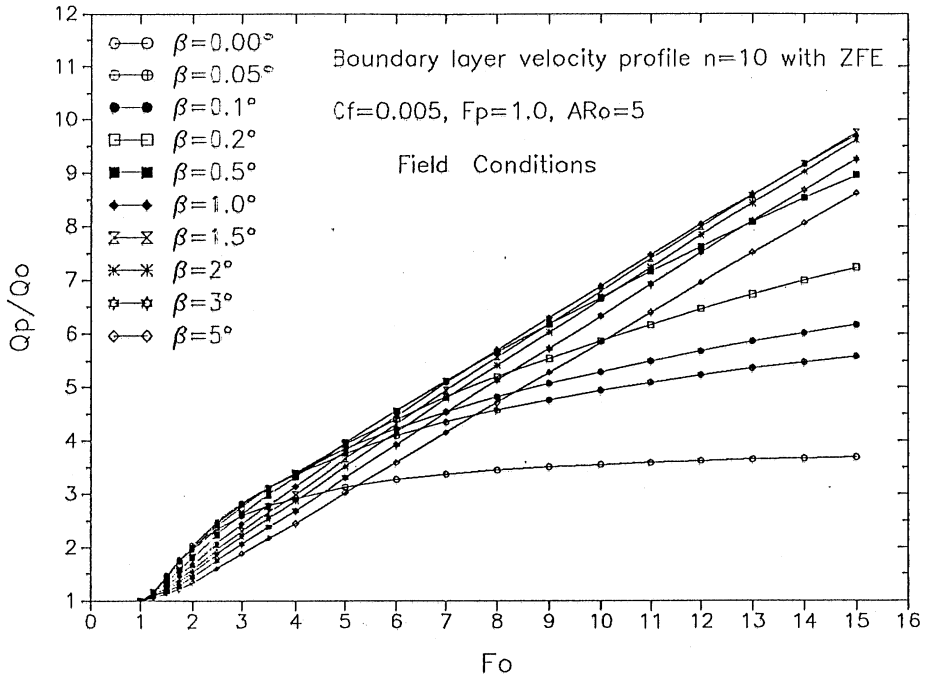

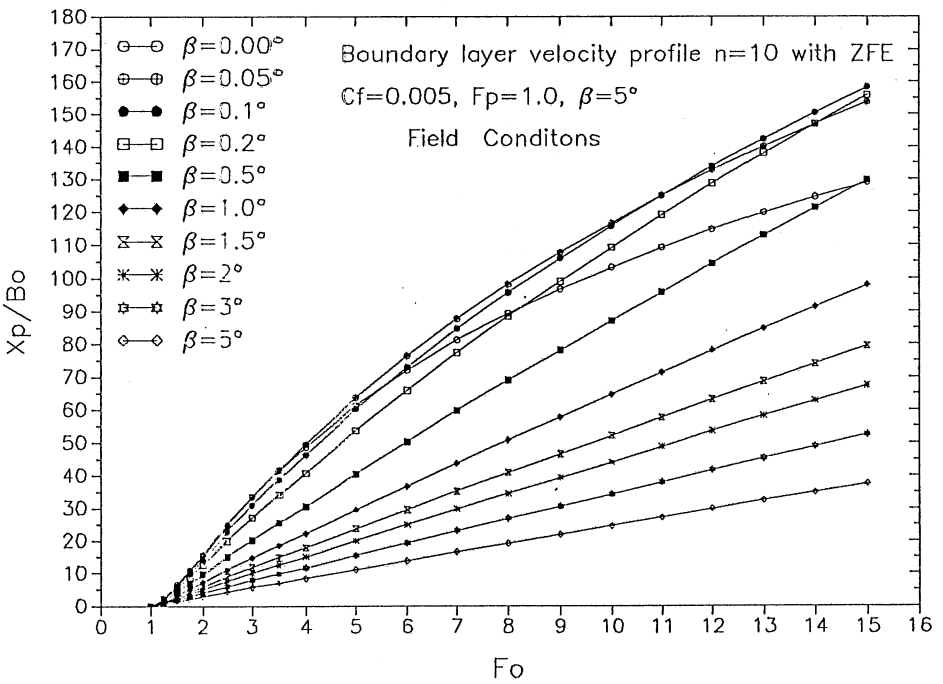

Fig. 5–23 **Predicted relationship between dilution and F_o at $c_f = 0.005$ and $AR_o = 5$ as slope angle β increases from 0° to 5°.**

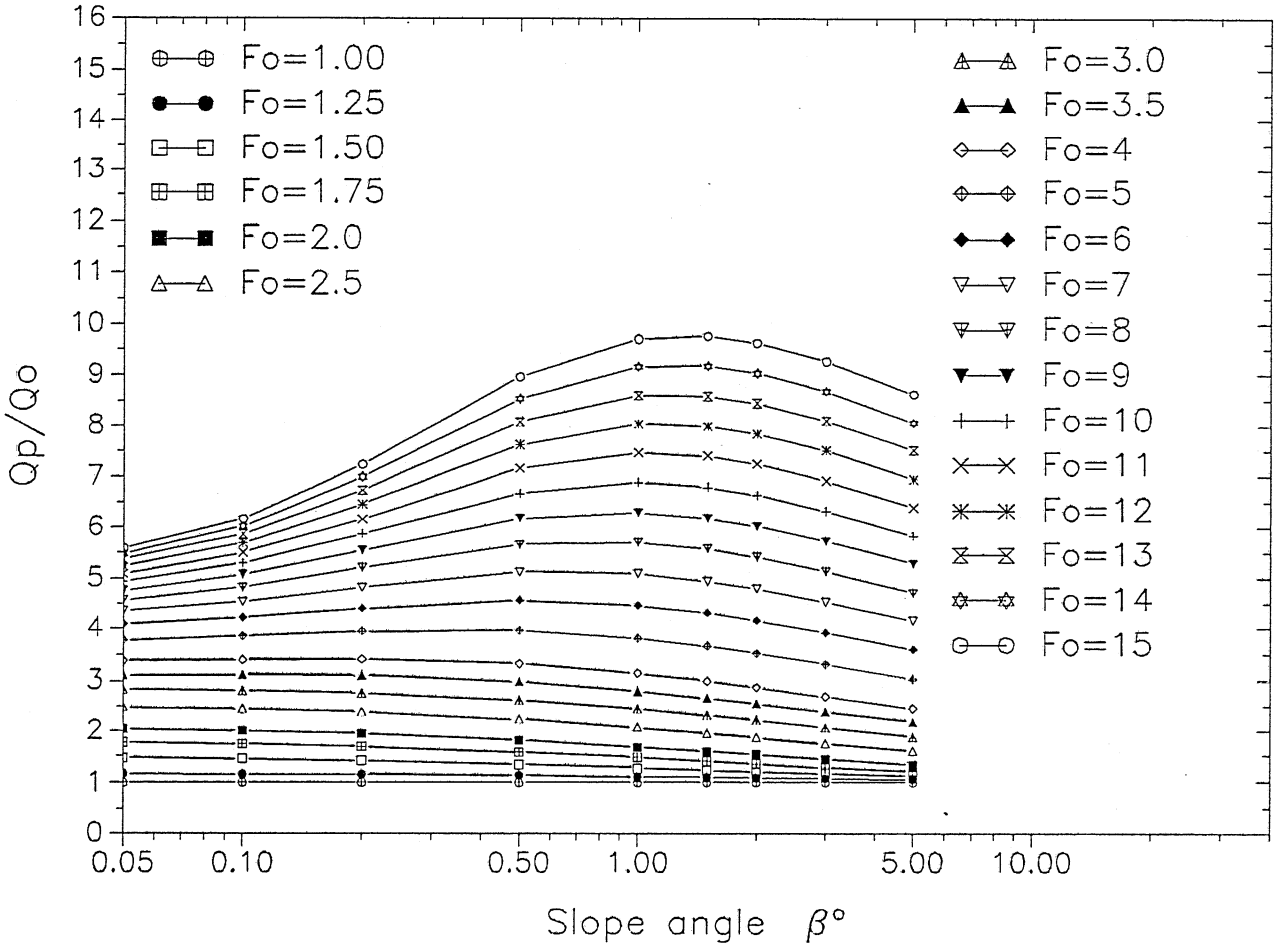

Fig. 5–24 Predicted relationship between dilution and $\beta°$ at $c_f = 0.005$ and $AR_o = 5$ for different densimetric Froude numbers F_o.

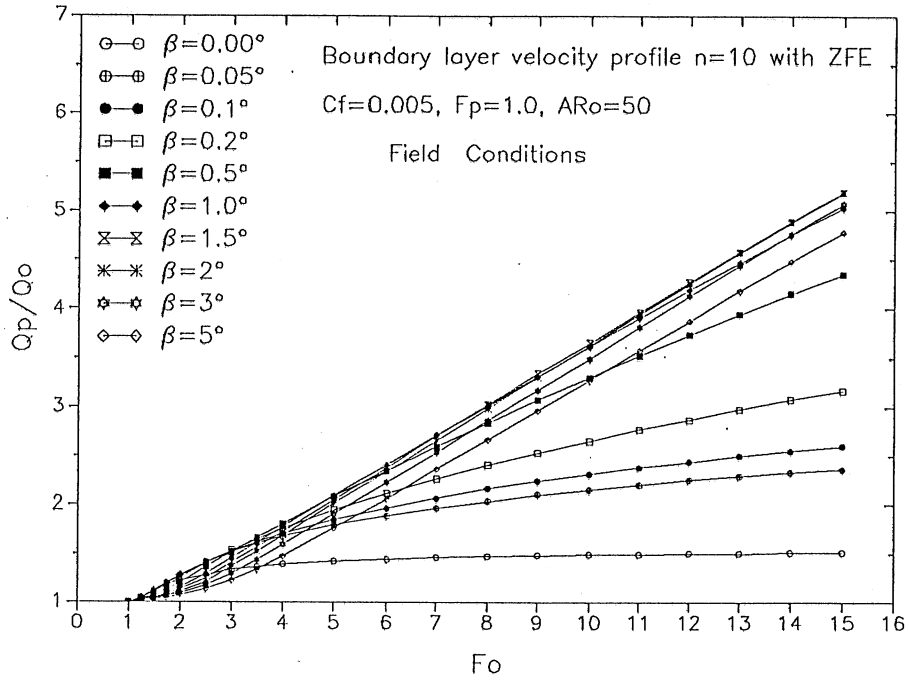

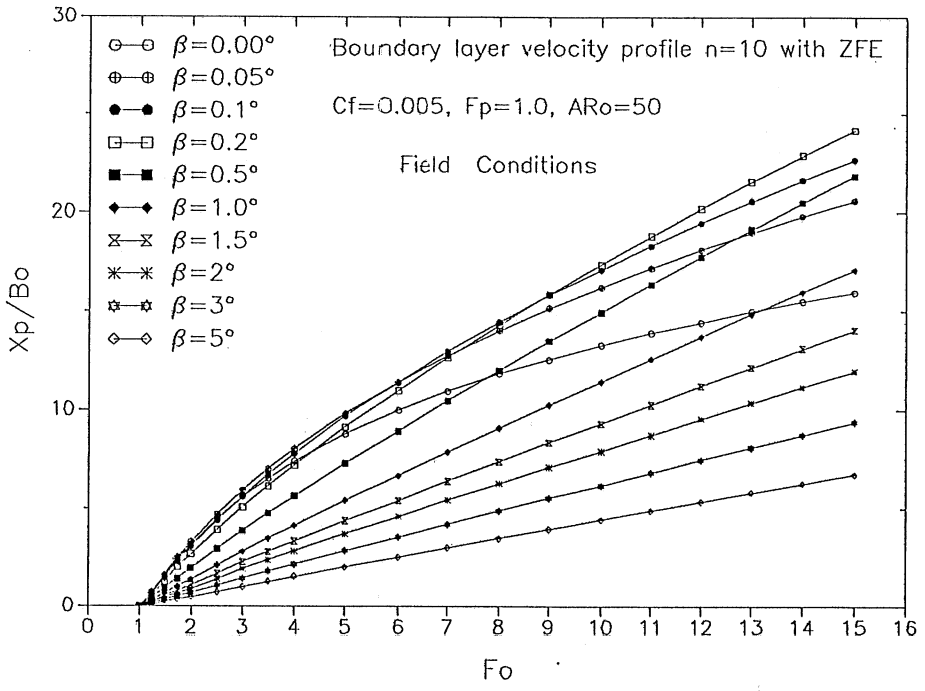

Fig. 5–25 Sensitivity of dilution to F_o and β at $c_f = 0.005$ and $AR_o = 50$.

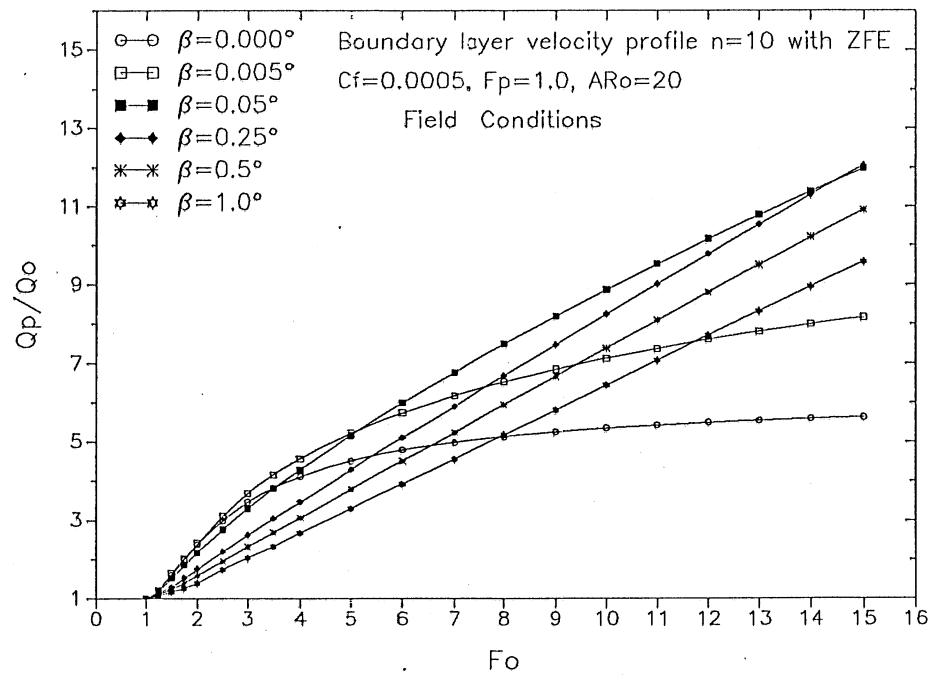

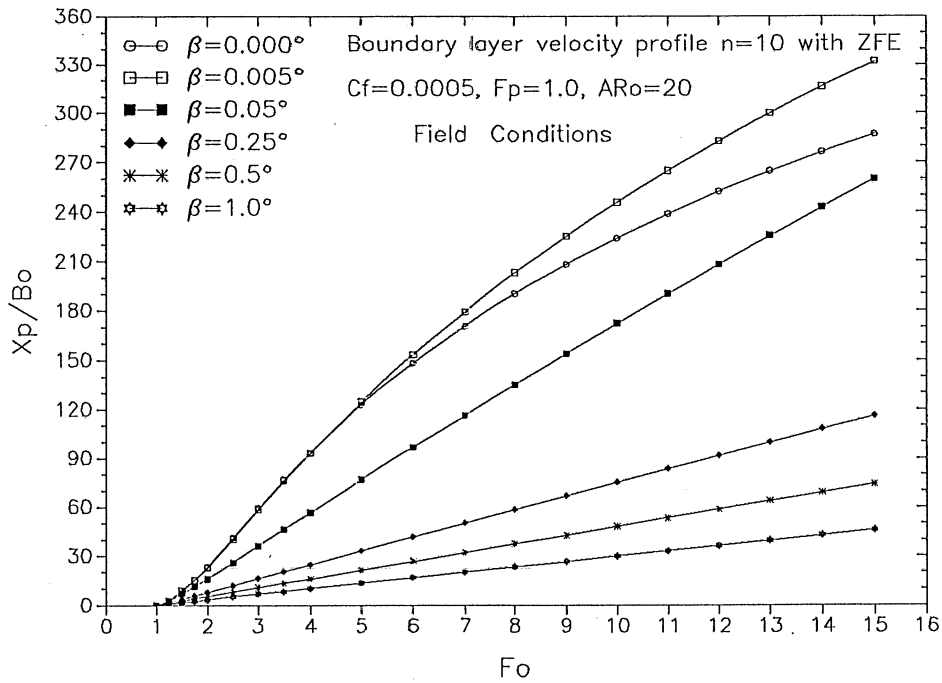

Fig. 5–26 Sensitivity of dilution to F_o and β at $c_f = 0.0005$ and $AR_o = 20$.

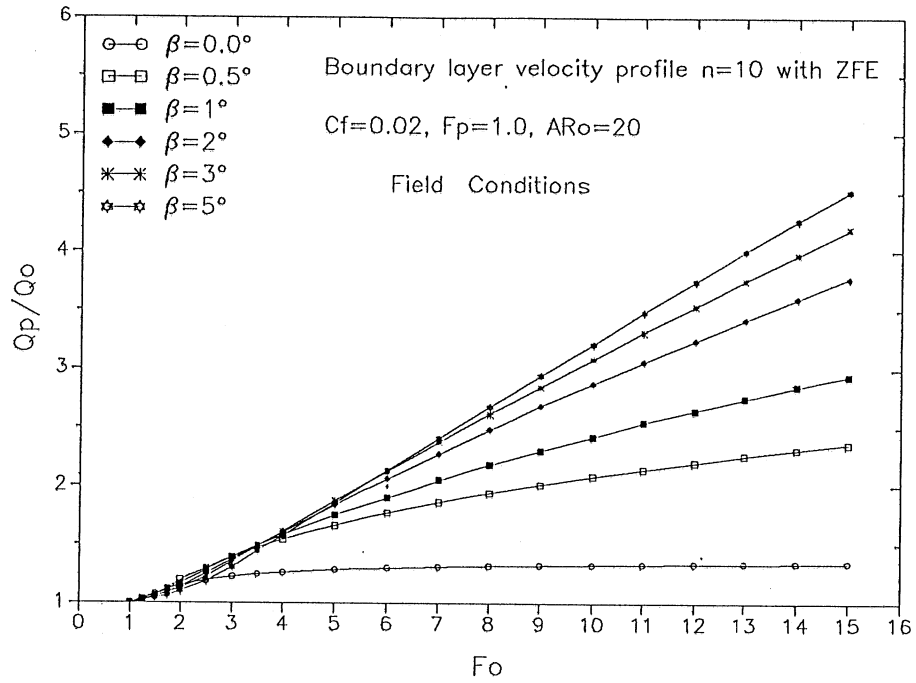

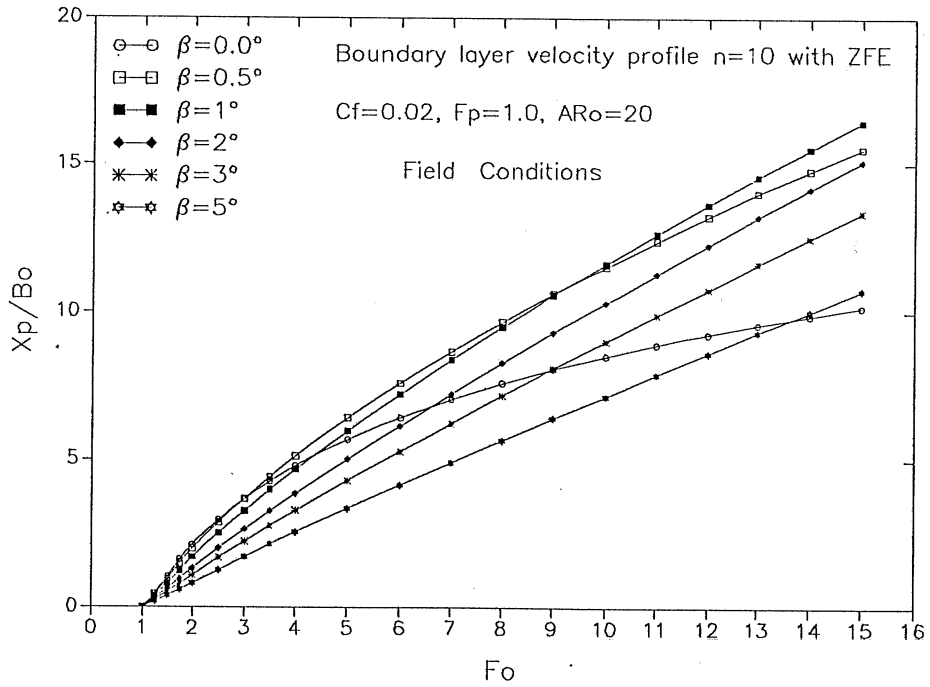

Fig. 5–27 Sensitivity of dilution to F_o and β at $c_f = 0.02$ and $AR_o = 20$.

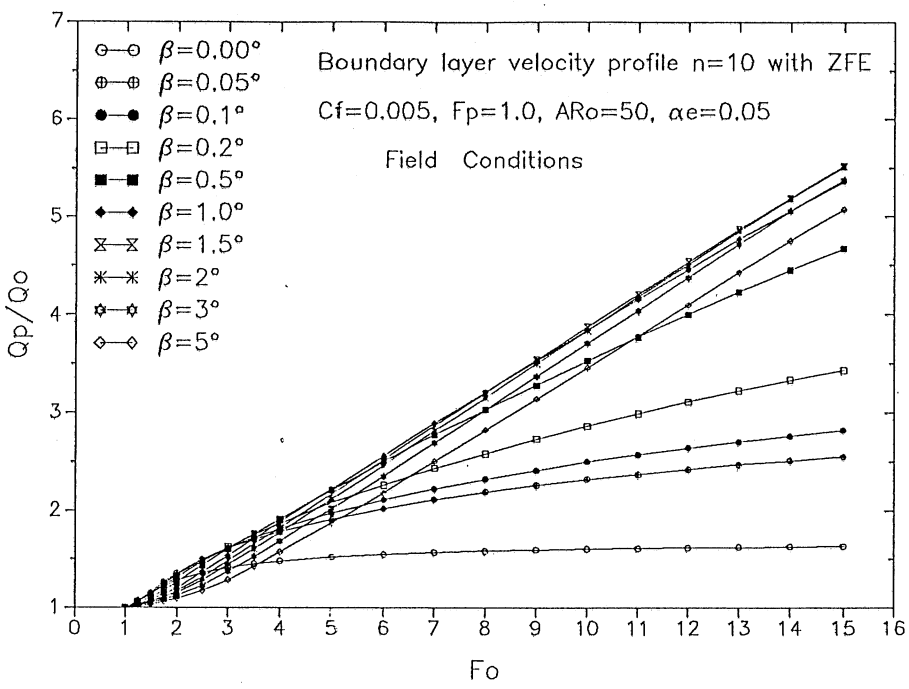

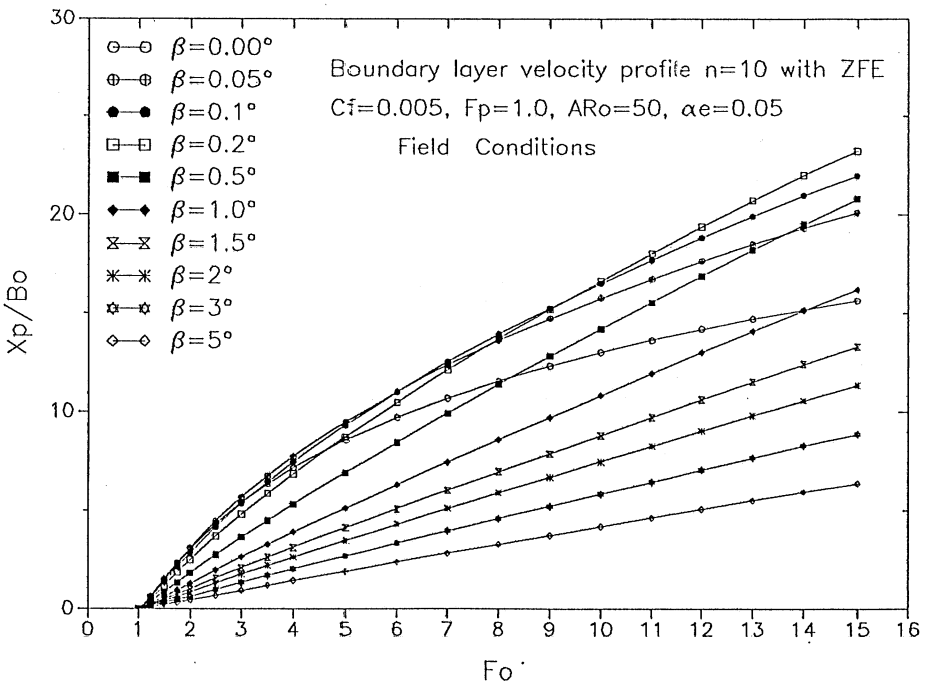

Fig. 5–28 Sensitivity of dilution to F_o and β at $c_f = 0.005$, $AR_o = 50$ and $\alpha_e = 0.005$.

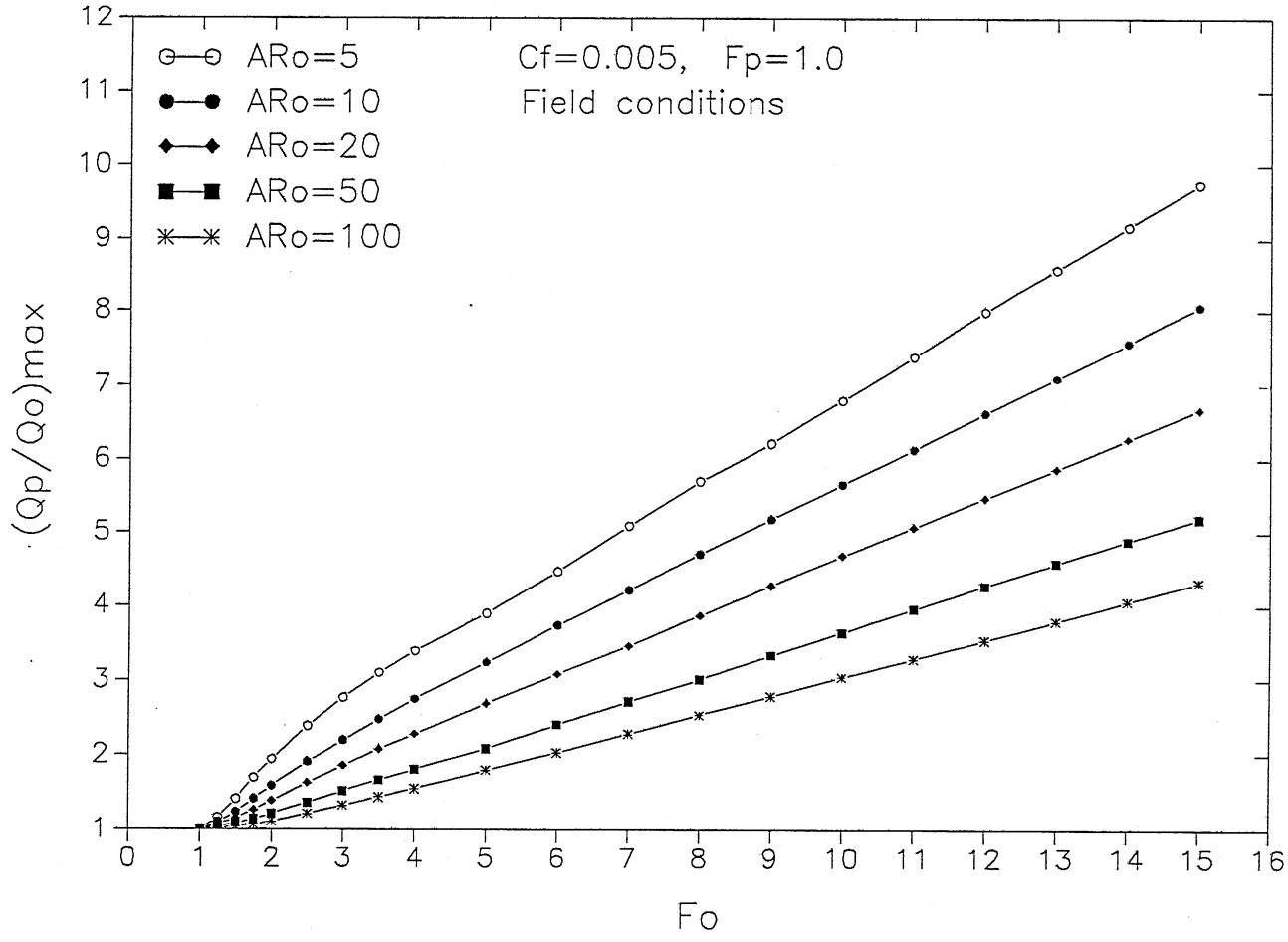

Fig. 5–29 Envelope of maximum dilution $(Q_p/Q_o)_{max}$ for slope angles $0° \leq \beta \leq 5°$ and aspect ratios $5 \leq AR_o \leq 100$ with $c_f = 0.005$.

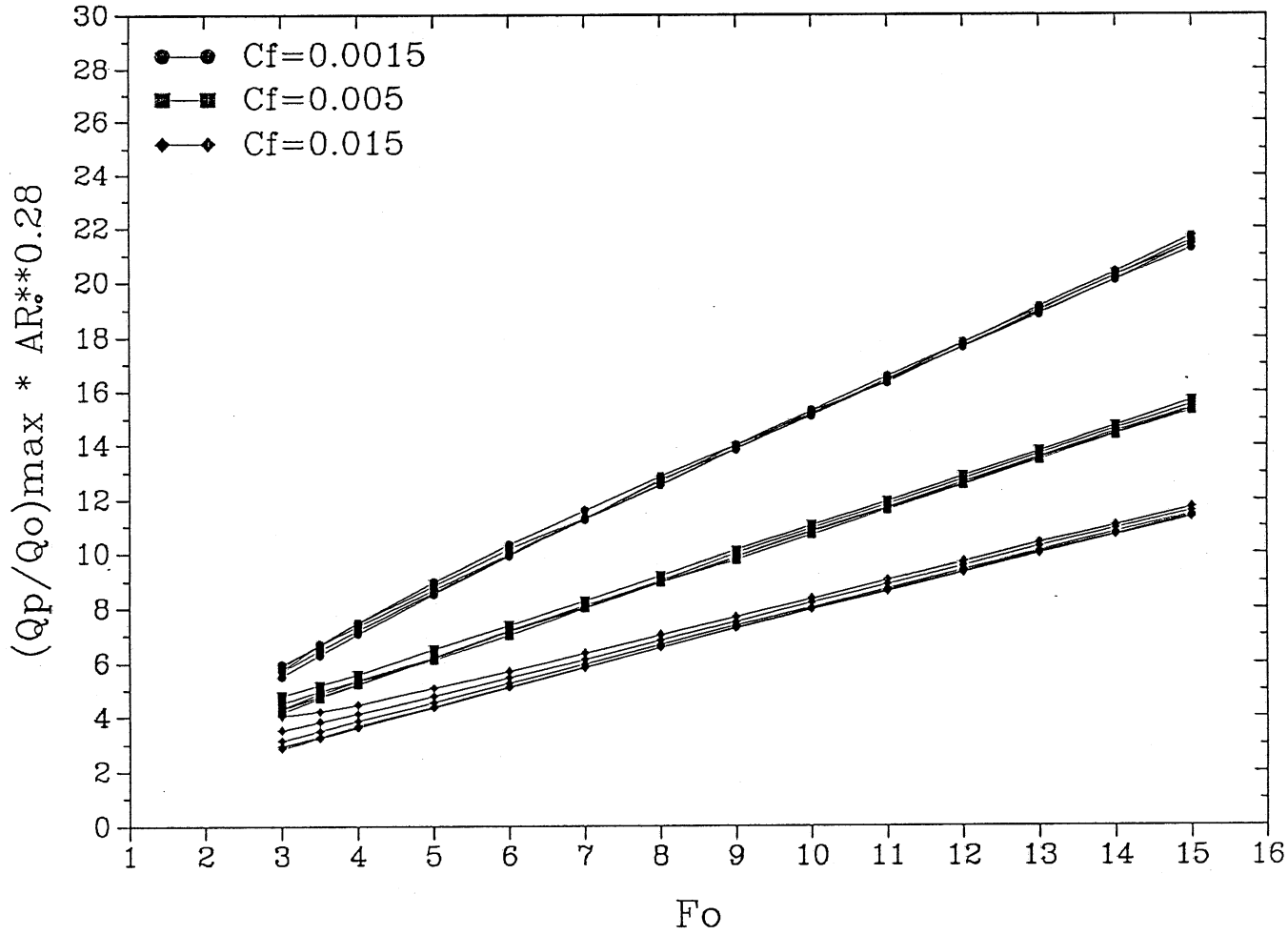

Fig. 5–30 Envelop of maximum dilution $(Q_p/Q_o)_{max}$ (defined at $F_o = 15$) for slope angles $0° \leq \beta \leq 5°$ and aspect ratios $5 \leq AR_o \leq 100$ with three friction coefficient normalized by $AR_o^{0.28}$.

Chapter VI SUMMARY, CONCLUSIONS AND RECOMMENDATIONS

An integral model for a discharge form a channel over a horizontal or a sloping bottom into a wide water body has been developed. The integral forms of the momentum and continuity equations are solved. The model has been developed primarily to determine dilution of plunging inflows for applications in 1–D water quality models of stratified water bodies such as lakes and reservoirs. A relatively simple model for inflow dilution is needed. Effects of finite water depth and side wall effects have been considered.

In summary the integral jet model developed herein includes the following concepts and assumptions:

(1) A similarity hypothesis for velocity profiles. The transverse velocity profiles are assumed Gaussian velocity distributions. The vertical velocity profiles are the n–th power law of boundary layer velocity profiles, where n is dependent on the inflow Reynolds number Re_o.

(2) The entrainment principle. The lateral jet entrainment velocity v_e is proportional to the jet centerline velocity u_m.

(3) Bottom friction effects on momentum. In the *hydraulically smooth regime* the local friction coefficient c_f is dependent on inflow Reynolds number but is independent of relative roughness. In the *completely rough regime* c_f is dependent on relative roughness but is independent of inflow Reynolds number.

(4) For laboratory studies, a friction coefficient $c_f = 0.005$ is specified. It is derived from experimental conditions. For field studies, a friction coefficient from 0.0015 to 0.02 is specified. It is derived from typical Mannings' coefficients.

(5) An entrainment coefficient $\alpha_e = 0.004$, which is less than the entrainment coefficient $\alpha_e = 0.0053$ of free turbulent jets, is specified. It is established by comparing model calculations with laboratory data in a horizontal channel.

(6) For negative buoyant inflows plunging is related to a densimetric Froude number F_p. The value of F_p is dependent on the definition of jet width b which is chosen to be $b = 4\sigma$. Where σ = standard deviation of Gaussian velocity profile.

The integral model has produced the following simulation results:

(1) **It is important to have bed friction and vertical velocity profiles included in the model.**

(2) **It is not necessary to include a zone of flow establishment (ZFE) in the model for laboratory conditions with small channel aspect ratio $AR_o < 2$. It is, however, important to consider a ZFE in the model for field conditions with larger aspect ratio $AR_o > 5$.**

(3) Model results are sensitive to densimetric Froude number at plunging F_p. **We recommend $F_p = 1.0$ in the application of the model.**

(4) Predictions of the model with boundary layer velocity profiles ($n = 7$) and without flow establishment region (ZFE) at $F_p = 1.0$ match the experimental data by Johnson and Stefan, 1988.

(5) The simulation model can be used to predict the dilution before plunging under laboratory and field conditions with large diffuser angle $\delta^\circ \geq 45^\circ$ if the aspect ratio of inflow (AR_o), the sloping angle of the bottom (β°) and inflow densimetric Froude number (F_o) are given. **Predictions of the integral model agree well with laboratory and field data.**

(6) In horizontal channels, dilution Q_p/Q_o is small and increases slowly with F_o if channel aspect ratio AR_o is large as is often the case. On sloping bottoms dilution Q_p/Q_o is large and increases linearly with F_o if slope angle β is large. The transition from horizontal to sloping bottoms and its effect on dilution has been investigated. Model results of Q_p/Q_o are quite sensitive to slope angle β and local friction coefficient c_f.

(7) Fig. 5–7 is the currently best estimate of the relationship between Q_p/Q_o and F_o for discharges from narrow laboratory channels over horizontal bottoms. Fig. 5–30 gives the best estimate of the maximum dilution of discharges from wider channels under field conditions. The relationships between Q_p/Q_o and F_o for several c_f values are reduced to narrow bounds by use of $AR^{0.28}$.

(8) Experiments by Johnson and Stefan, 1988 provided very useful data for small aspect ratio AR_o and $\beta = 0^\circ$ or $\beta = 3^\circ$. Purely empirical equations are developed in Appendix A to predict the dilution before plunging of inflow with strong negative buoyancy. The empirical equations are only for experimental data with small aspect ratios ($AR_o < 2$).

(9) A method described in the Appendix B has been developed to fit finite numbers of experimental measurements to Gaussian distributions.

Even though some useful predictions have been obtained from the integral jet model, recommendations are made for further study of some of the assumptions:

(1) All results are dependent on assumptions of velocity profiles. Plunging flow is a three–dimensional flow and transverse velocity profiles are not exactly Gaussian velocity distributions.

(2) Predictions depend on entrainment coefficient α_e, but α_e was specified from a few experimental data. More experimental data and field data are needed.

(3) Prediction of dilution before plunging is dependent on definition of jet width and the value of densimetric Froude number F_p. Alternative definitions and values deserve further study.

(4) Predictions of dilution by the integral model are sensitive to slope angle β, but it can be difficult to specify slope angle β under field conditions. Alternatives to slope averaging need to be explored.

REFERENCES

Abramovich, G. N., (1963). *The theory of turbulent jets.* English translation published by M.I.T. Press, Massachusetts, 671 pp.

Albertson, M.L., Dai, Y.B., Jensen, R.A. and Rouse, H., (1950). "Diffusion of submerged jets." *Trans. ASCE,* 115:639–967.

Akiyama, J., and Stefan, H. G., (1984). "Plunging flow into a reservoir: Theory." *J. Hydr. Engrg.*, ASCE, 110(4), 484–499.

Akiyama, J., and Stefan, H. G., (1987). "Onset of underflow in slightly diverging channels." *J. Hydr. Engrg.*, ASCE, 113(7), 825–844.

Ellison, T. H., and Turner, J. S., (1959). "Turbulent entrainment in stratified flows." *J. Fluid Mech.*, 6(3), 423–448.

Farrell, G. J. and Stefan, H. G., (1988). "Mathematical modeling of plunging reservoir flows", *J. Hydraulic Research,* Vol. 26, No. 5.

Farrell, G. J. and Stefan, H. G., (1989). "Two–layer analysis of a plunging density current in a diverging horizontal channel", *J. Hydraulic Research,* Vol. 27, No. 1.

Fischer, H. B., et al., (1979). *Mixing in inland and coastal waters.* Academic Press, Inc. Orlando, Fla.

Forthmann, E., (1936). *Turbulent jet expansion.* English translation N.A.C.A. Tm–789. (Original paper in German, 1934. Ing. Archiv., 5.)

Goertler, H., (1942). *Berechnung von Aufgaben der freien Turbulenz auf Grund eines neuen Naherungsansatzes.* Z.A.M.M., 22:244–254.

Hebbert, B., Imberger, J., Loh, I., and Patterson, J., (1979). "Collie River Underflow into the Wellington Reservoir," *Journal of the Hydraulics Division, ASCE,* Vol. 105, No. HY5, Proc. Paper 14593, May, pp. 533–545.

Heskestad, G., (1965). "Hot–wire measurements in a plane turbulent jet." *Trans. ASME., J. Appl. Mech.*, pp. 1–14.

Johnson, T. R., Farrell, G. J., Ellis, C. R., and Stefan, H. G., (1987a). "Negatively buoyant flow in a diverging channel. I: Flow regimes." *J. Hydr. Engrg.*, ASCE, 113(6), 716–730.

Johnson, T. R., Ellis, C. R., Farrell, G. J., and Stefan, H. G., (1987b). "Negatively buoyant flow in a diverging channel. II: 3–D Flow field descriptions" *J. Hydr. Engrg.*, ASCE, 113(6), 731–742.

Johnson, T. R., and Stefan, H. G., (1988). "Experimental Study of Density Induced Plunging Flow into Reservoirs and Coastal Regions." Proj. Rept. No. 245, St. Anthony Falls Hydr. Lab., Univ. of Minnesota, Minneapolis, Minn.

Johnson, T. R., Ellis, C. R., and Stefan, H. G., (1989). "Negatively buoyant flow in diverging channel. IV: Entrainment and dilution." *J. Hydr. Engrg.*, ASCE, 115(4), 437–456.

Myers, G.E., Schauer, J.J. and Eustis, R.H., (1961). The plane turbulent wall jet. I, Jet development and friction factor. Tech. Rep., 1, Department of mechanical Eng., Stanford Univ. (Also published in *Trans. ASME, J. Basic Eng.*, 1963).

Rajaratnam, N. and Subramanya, K., (1967), "An annotated bibliography of wall jets," *Tech. Rep.* Department of Civil Engineering, Univ. of Alberta, Edmonton.

Rajaratnam, N., (1976). *Turbulent jets.* Elservier Scientific Publishing Company, New York, N. Y.

Reichardt, H., (1942). Gesetzmaßigkeiten der freien Turbulenz. VDI–Forschungsheft, 414 (1942), 2. ed. 1951.

Riley M. J. and Stefan H. G., (1987). "Dynamic Lake Water Quality Simulation Model MINLAKE." Proj. Rep. No. 263, St Anthony Falls Hydr. Lab., Univ of Minnesota, Minneapolis, Minn.

Schlichting, H., (1968). *Boundary layer theory.* McGraw–Hill Book Co., Inc., New York. 6th edition, 747pp.

Schwarz, W.H. and Cosart, W.P., (1961). The two–dimensional turbulent wall jet. *J. Fluid Mech.*, 10:481–495.

Sigalla, A., (1958). Measurements of skin friction in a plane turbulent wall jet. *J. R. Areonaut. Soc.*, 62:873–877.

Stefan, H. G., Johnson, T. R., and Farrell, G. J., (1988). "Initiation of Density Currents in Diverging Channels: Comparison of Field and Laboratory Data," *Proceedings of 1988 National Conference HY Div/ASCE, Colorado Springs, Colorado.*

Stefan, H. G., and Johnson, T. R., (1989). "Negatively buoyant flow in diverging channel. III: Onset of underflow." *J. Hydr. Engrg.*, ASCE, 115(4), 423–436.

Tollmien, W., (1926). Berechnung turbulenter Ausbreitungsvorgange. Z.A.M.M., 6:468–478. (English translation, *N.A.C.A. TM* 1085, 1945).

Vennard, J. K., and Street, R. L., (1975). *Elementary fluid mechanics*, 5th edition, John Wiley & Sons Inc. New York.

Wunderlich, W. O., and Elder, R. A., (1973). "Mechanics of Flow Through Man–Made Lakes," *Man–Made Lakes: Their Problems and Environmental Effects*, W. C. Ackermann, G. F. White, and E. B. Worthington, eds., American Geo–physical Union, Washington, D. c., 1973.

Yuan, M., Song, C.C.S. and He J., (1991). "Numerical Analysis of Turbulent Flow in a Two–dimensional Asymmetric Plane–wall Diffuser," June, *ASME, J. Fluids Eng.*

Zerbe, J. and Selna, J., (1946). "An empirical equation for the coefficient of heat transfer to a flat surface from a plane heated air jet directed tangentially to the surface. *NACA, TN,* 1070.

Zijnen, B.G. Van der Hegge, (1958a). "Measurements of the velocity distribution in a turbulent plane jet of air." *Appl. Sci. Res.*, Sect. A, 7:256–276.

PLOTIT User's Guide, September (1987). Scott P. Eisensmith.

APPENDIX A

EMPIRICAL EQUATIONS FOR DILUTION BEFORE PLUNGING

A.1 Introduction

The total dilution of sinking inflows to reservoirs is of particular interest for water quality modeling. Not only is the rate of dilution related to the location of the plunge line (Akiyama and Stefan, 1984), but also the depth to which the underflow will sink in a stratified reservoir, lake, or impoundment (Elder and Wunderlich, 1972). A model of inflow dilution at plunging is therefore needed in one–dimensional unsteady water quality models of stratified reservoirs and lakes.

In the MINLAKE model (Riley et al., 1988) a subroutine PDEPTH is used for computing depth of plunging and initial dilution before plunging (Akiyama, 1987). Total dilution before plunging are kept constant at:

γ=1.15	for mild slope.
γ=2.80	for steep slope.

where γ is the dilution before plunging. Setting the dilution constant is however not enough for natural reservoirs and lakes.

To study the plunge flow on mild slopes and steep slopes with different divergence angles, experiments were conducted in a horizontal diverging channel and a sloping diverging channel (Akiyama, 1984, Johnson and Stefan, 1985). They obtained many useful results about flow regimes, distance to plunging, dilution before plunging etc. Constructing a more effective empirical model for computing the dilution before plunging from these data is possible and will be reported herein.

A.2 Formulation of Inflow Model for Plunging Flow

A.2.1 Flow concepts, governing parameters and flow regimes

(1) Flow concepts: The flow at the head of a reservoir and near effluent sites into lakes is complicated and changes with seasons because the inflow entering a lake or reservoir is not always precisely of the same density as the lake or reservoir. If the density of the inflow is less than the receiving water, the inflow will be a surface flow (overflow). If the density of the inflow is greater than the ambient water, the inflow sinks below the surface at some place, forming a density stratified current (plunging flow). The

plunge phenomenon can be defined as the transitional flow from homogeneous open channel flow to stratified, entraining underflow.

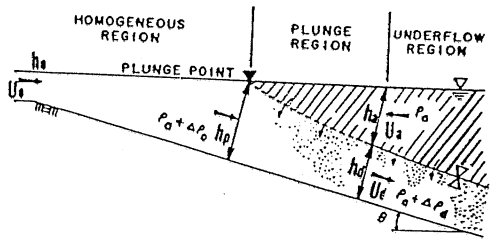

Fig. A–1 Flow parameters of plunging flow (after Akiyama et al., 1984)

The flow field is divided into three fairly distinct regions, called "homogeneous", "plunge" and "underflow", regions as shown in Fig. A–1. The location where the inflow enters below the surface is called as "plunge point" or "plunge line".

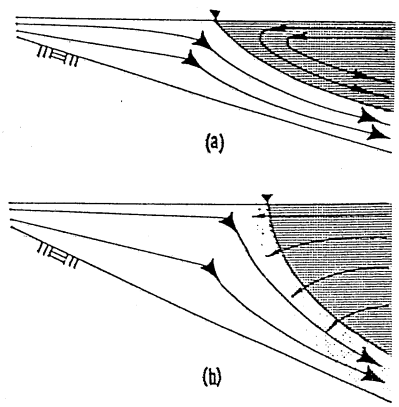

Fig. A–2 Extreme cases of plunging flow:(a)Nonmixing on mild slope (b) Mixing on steep slope. [after Akiyama et al., 1984]

Field and experimental studies of plunging flows have been made by Wunderlich and Elder (973), Herbert (1979), Ellison and Turner (1959), Akiyama and Stefan (1984), Johnson and Stefan (1985), and others. Mixing between inflow and ambient water must be considered in the model of plunging flow. There are two different mixing mechanisms, one occurs in the underflow below the plunge point and consists primarily of entrainment due to the instability of the interface. The other type of mixing is created around the plunge area by turbulent diffusion formed by the abrupt change of flow width and depth. Fig A–2 is a schematic of plunging flows on a mild slope,

which is usually associated with little mixing, and that on a steep slope, which usually mixes significantly more. On a mild slope the underflow remains subcritical and assumes the internally normal underflow depth downstream of the plunge point (Akiyama and Stefan, 1984). On a steep slope the plunging flow will gradually change from subcritical upstream of the plunging flow to supercritical some distance downstream of the plunging due to the acceleration of gravity.

(2) Governing parameters: Physical parameters controlling the plunging phenomenon come from inflow conditions as well as reservoir characteristics. The parameters are the initial inflow rate per width, q_o , the ambient fluid density, ρ_a , the inflow density, $\rho_{in} = \rho_a + \Delta\rho_o$, the acceleration of gravity, g , inflow depth and width, H_o and B_o , the total friction factor, C_f, the bottom slope S (or β angle). Non–dimensional controlling parameters are:

non–dimensional difference of density	$\epsilon_o = (\rho_a - \rho_o) \,/\, \rho_a$
inflow densimetric Froude number	$F_o = [\, q_o^2/(g\ \epsilon_o\ H_o^3)\ ]^{0.5}$
aspect ratio of inflow channel	$AR_o = B_o \,/\, H_o$
diverging angle of channel δ	
bed slope S or β	

The dilution before plunging is defined as $\gamma = Q_d/Q_o$, where Q_d is the mean underflow rate (or downstream flow) just downstream from plunging, and Q_o is the mean flow rate at the inflow. Other symbols are identified in the list of symbols.

We use the non–dimensional difference of density ϵ_o to distinguish between overflow and underflow. $\epsilon_o > 0$ for negatively buoyant flow (underflow), $\epsilon_o < 0$ for overflow. Sometimes if the inflow densimetric Froude number F_o is very large, the distance to plunging is larger than the distance from inflow to outflow and we can consider that the flow is a surface flow.

For negatively buoyant flow and in first approximation it is a mild slope flow when the bed slope S [$S = \tan(\beta)$] is less than 1/150 (Akiyama and Stefan, 1987). It is a steep slope flow when S is larger than 1/150.

(3) Flow regimes: Total dilution before plunging depends most strongly on flow regime (Fig. A–3) and distance to plunging (Johnson and Stefan, 1989 III,IV). The flow regimes are divided into three types: (a) "attached flow", (b) "wall jet", (c) "free jet".

In a mildly diverging ($\delta < 7°$) horizontal channel (Akiyama and Stefan, 1984, Johnson and Stefan, 1985), the inflow remains attached to both walls of the diffuser. Measured entrainment rates have typically been less than 30% of the inflow rate (Fig A–4). As the diffuser angle becomes larger ($10° > \delta > 7°$) separation and stall begin to occur. Entrainment is still small and more or less 30% of the inflow rate because the diffuser walls inhibit the return flow and then reduce entrainment. A more detailed analysis is given by Akiyama and Stefan (1987). As the diffuser angle δ increases, the entrainment γ increases approximately linearly. The linearly fitted function is

$$Q(x)/Q_o = 1.00 + 0.035\ \delta \qquad [A\text{–}1]$$

$$R^2 = 0.826$$

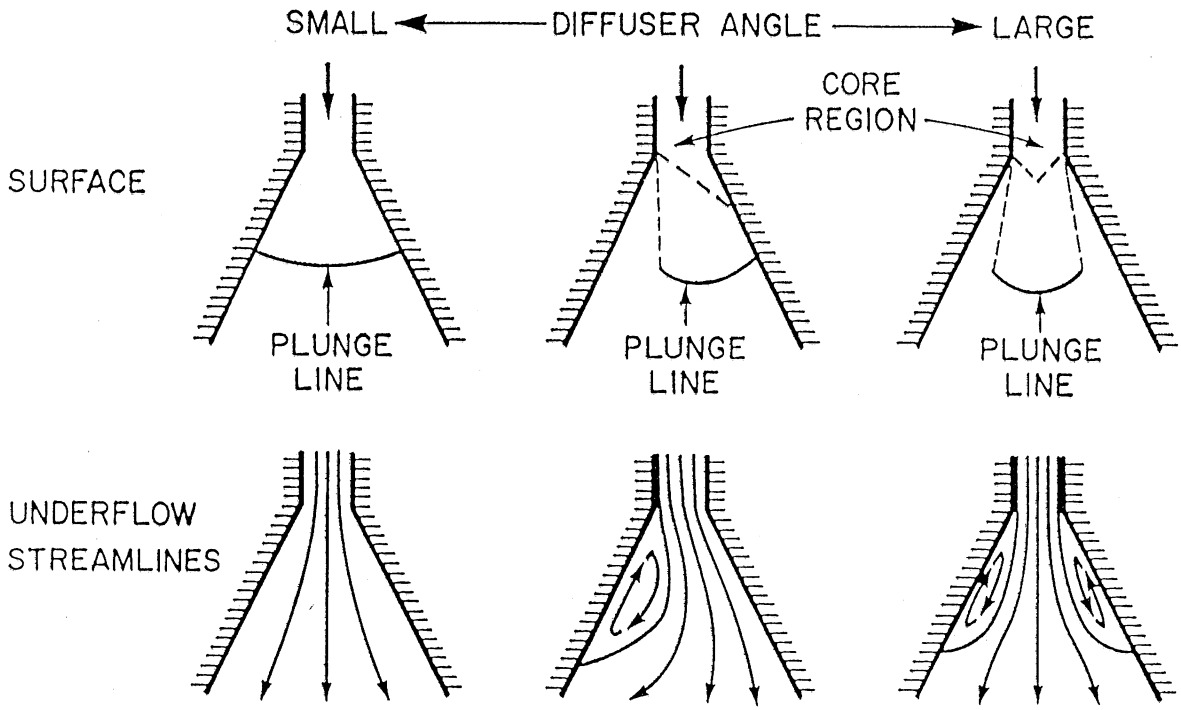

Fig A–3 Flow Regimes: (a) Attached Flow on Left, (b) Wall Jet (One Stalled Region) in Center, (c) Free Jet (Two Stalled Regions) [Johnson and Stefan, 1988].

The three flow regimes should also be found in sloping beach geometries, if the bottom slope does not become so steep that separation from the bottom occurs. Indeed, attached flow was observed in a sloping channel within parallel side walls ($\delta = 0°$). Slightly diverging sloping channels were not investigated. At diffuser half angles of $\delta = 10°$ and bottom slope of $\beta = 3°$ a wall jet was observed (Johnson and Stefan, 1988). The experimental data for $\delta = 0°$, $\beta = 2.7°$ and $\delta = 10°$, $\beta = 3°$ (Johnson and Stefan, 1988) are also shown in Fig A–4 as $\delta < 10°$. The roughly linearly function for steep slope

$$Q(x)/Q_o = 1.23 + 0.016\ \delta \qquad [A\text{–}2]$$

is fitted to the data but is not meaningful because the few data points are available.

The entrainment associated with wall jets and free jets is complicated and changes with slope. This will be discussed in the next section.

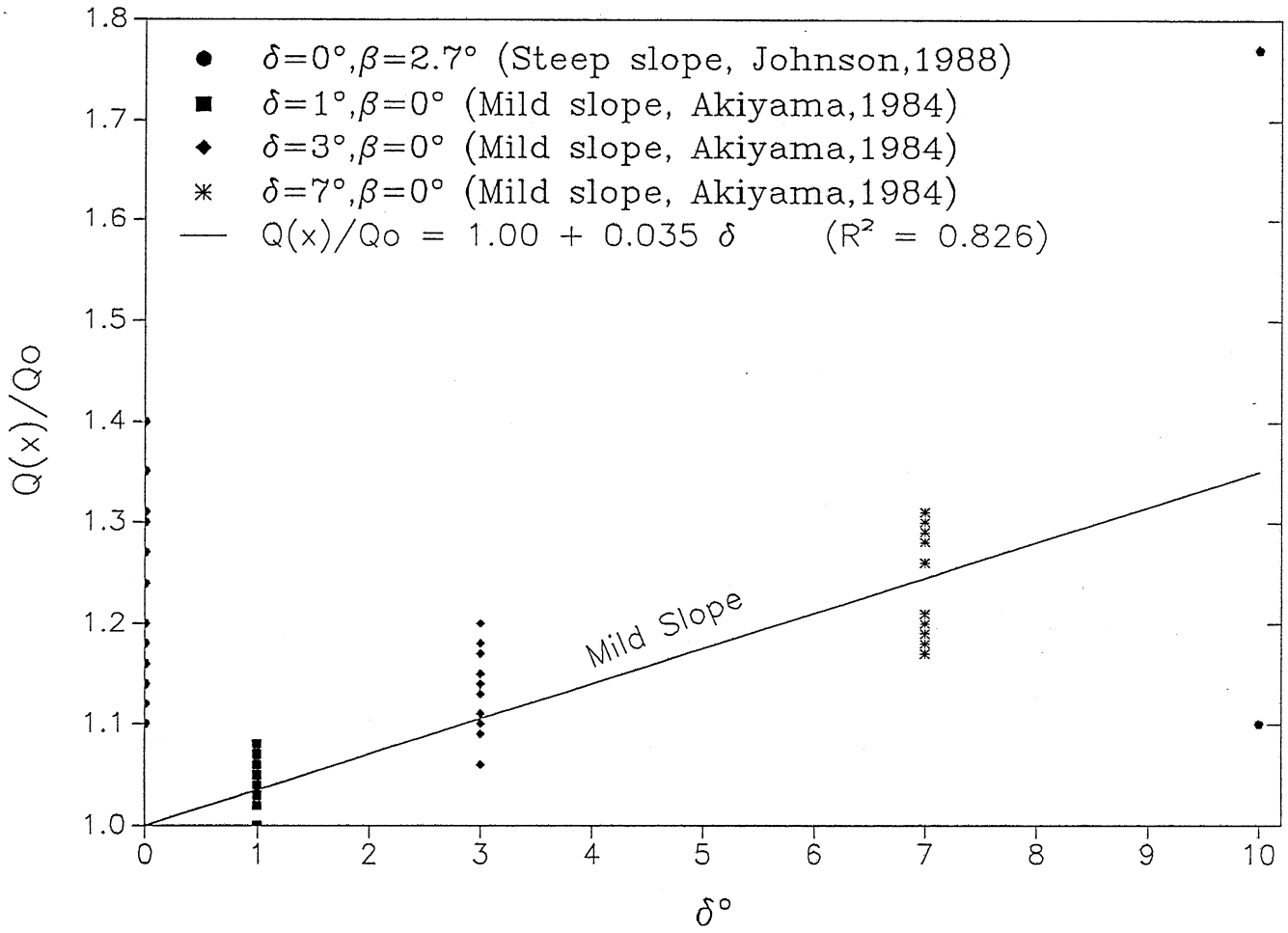

Fig. A–4 Relationship between $Q(x)/Q_o$ and δ ($\delta \leq 10°$ Experimental Data).

A.2.2 Plunging flow on a mild slope

To determine the entrainment up to plunging a two–step procedure is used. First use the inflow densimetric Froude number F_o and aspect ratio AR_o to compute the non–dimensional distance to plunging $x_p/\sqrt{A_o}$, and then find the dilution before plunging (γ) from an experimental (empirical) relationship between dilution and $x_p/\sqrt{A_o}$.

A.2.2.1 Distance to plunging

The governing parameters for plunging flow in a diverging horizontal channel are shown in Fig. A–5. Entrainment is related to distance to plunging (x_p). A more detailed analysis of distance to plunging is given by Johnson and Stefan (1988). The main data are shown in Fig. A–6 and fitted to the relationships

$$x_p \,/\, B_o = 0.52\ F_o^{\,4} \qquad \text{[A–3a]}$$

$$x_p \,/\, \sqrt{A_o} = 0.52\ F_o^{\,2}\ (AR)^{0.5} \qquad \text{[A–3b]}$$

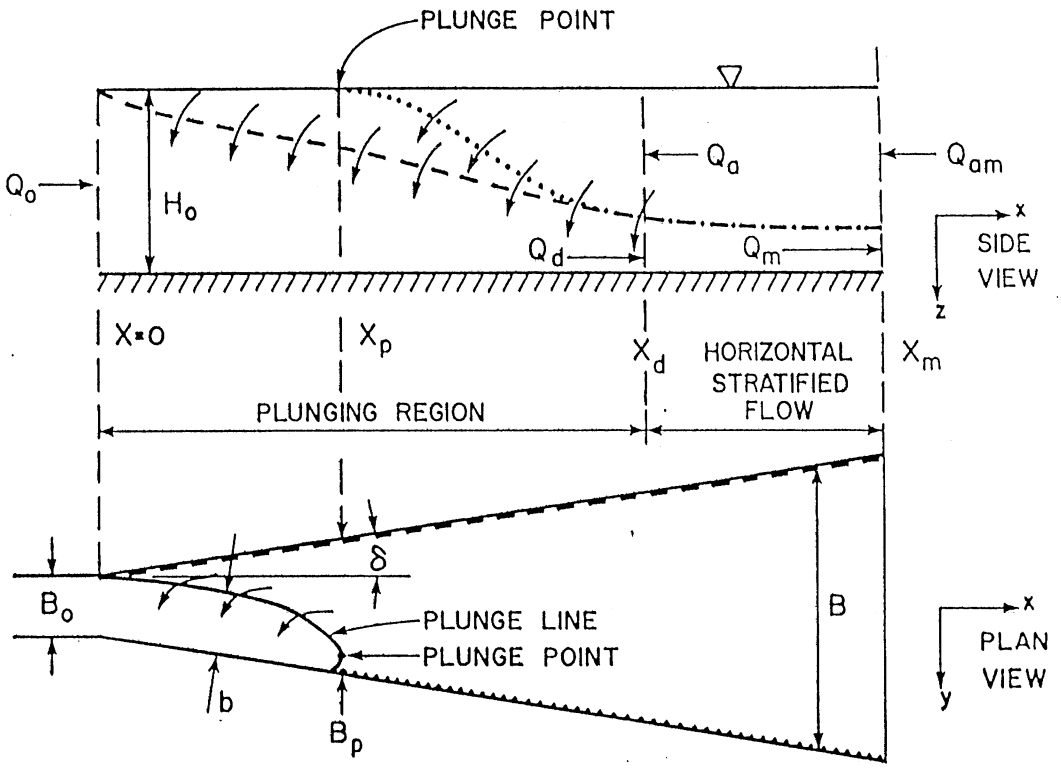

Fig A–5 Schematic of plunging flow in a diverging horizontal channel. A wall jet type flow is shown.[Johnson et al., 1988].

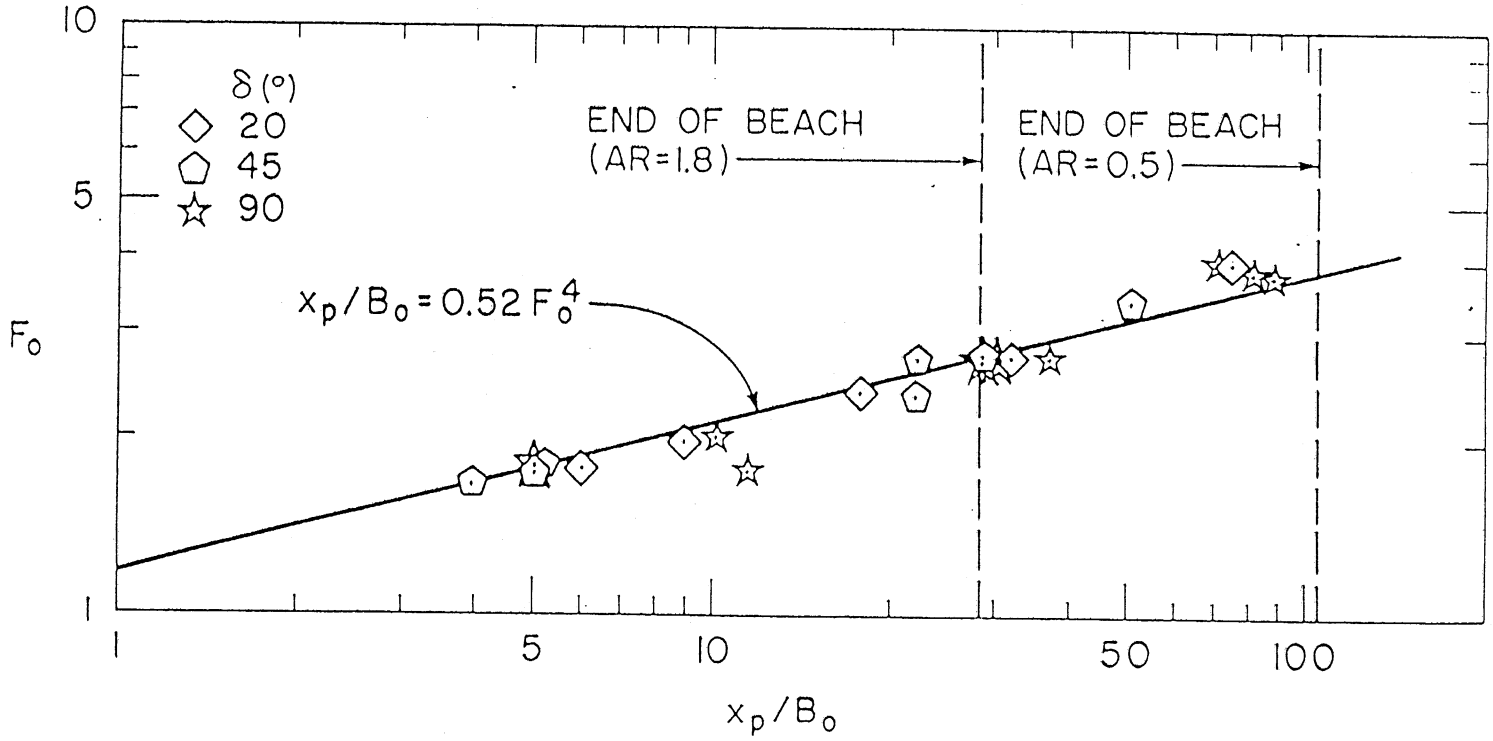

Fig. A–6. Relationship of plunge point location (x_p/B_o) to inflow densimetric Froude number (F_o). Separated flows (wall jets and free jets). (Johnson and Stefan, 1988).

A.2.2.2 Dilution of wall jet and free jet

Fig. 10 to Fig. 13 of Johnson and Stefan (1989 I) and Fig. 4 of Johnson and Stefan (1989 III) can be used to predict flow regimes as a function of the independent variables F_o, δ, and AR_o. According to Fig. 9 to Fig. 12 of Johnson and Stefan (1989 IV) the flow is divided into two regimes. When the half–angle is $90° > \delta \geq 45°$, inflow enters as a free jet. When the diffuser angle is $45° > \delta \geq 10°$, inflow enters as a wall jet. When $45° > \delta \geq 20°$, inflow is a steady wall jet. For $20° > \delta \geq 10°$, inflow can be oscillating and attaching to one wall or another of the diffuser. Data in the range $45° > \delta \geq 10°$ are treated as one regime.

Experiments in the free jet flow regime show that the entrainment is the same when the inflow has the same aspect ratio AR_o and non–dimensional distance to plunging $x_p/\sqrt{A_o}$ regardless of diverging angle δ. For different aspect ratios AR_o linear extrapolation is used herein. Fitting the experimental data by Johnson and Stefan(1989 IV, Fig. 12), one can obtain the empirical equations [A–4] and [A–5] of the entrainment for any non–dimensional distance to plunging $x_p/\sqrt{A_o}$. The form of the equations comes from pattern 20 of the user's manual for PLOTIT (1987).
For $AR_o = 0.5$:

$$(AR_o)^{0.25} Q_d/Q_o = B_1 \; e^{(B_2 \, x)} + B_3 \; e^{(B_4 \, x)} \qquad [A–4]$$

Where $x = x_p/\sqrt{A_o}$

$B_1 = 2.139$

$B_2 = 0.003$

$B_3 = 1.925$

$B_4 = -0.129$

$R^2 = 0.99$

For $AR_o = 1.8$

$$(AR_o)^{0.25} Q_d/Q_o = B_5 \; e^{(B_6 \, x)} + B_7 \; e^{(B_8 \, x)} \qquad [A–5]$$

Where $B_5 = 1.262$

$B_6 = 0.015$

$B_7 = 1.950$

$B_8 = -0.139$

$R^2 = 0.94$

The experimental data and fitted equation are shown in Fig. A–7 & A–8. The experimental data in the wall–jet regime (Fig. 11, Johnson and Stefan, 1989 IV), when $45° > \delta \geq 10°$, show the same entrainment when the divergence angle δ and the non–dimensional distance to plunging are the same (Fig. A–8).

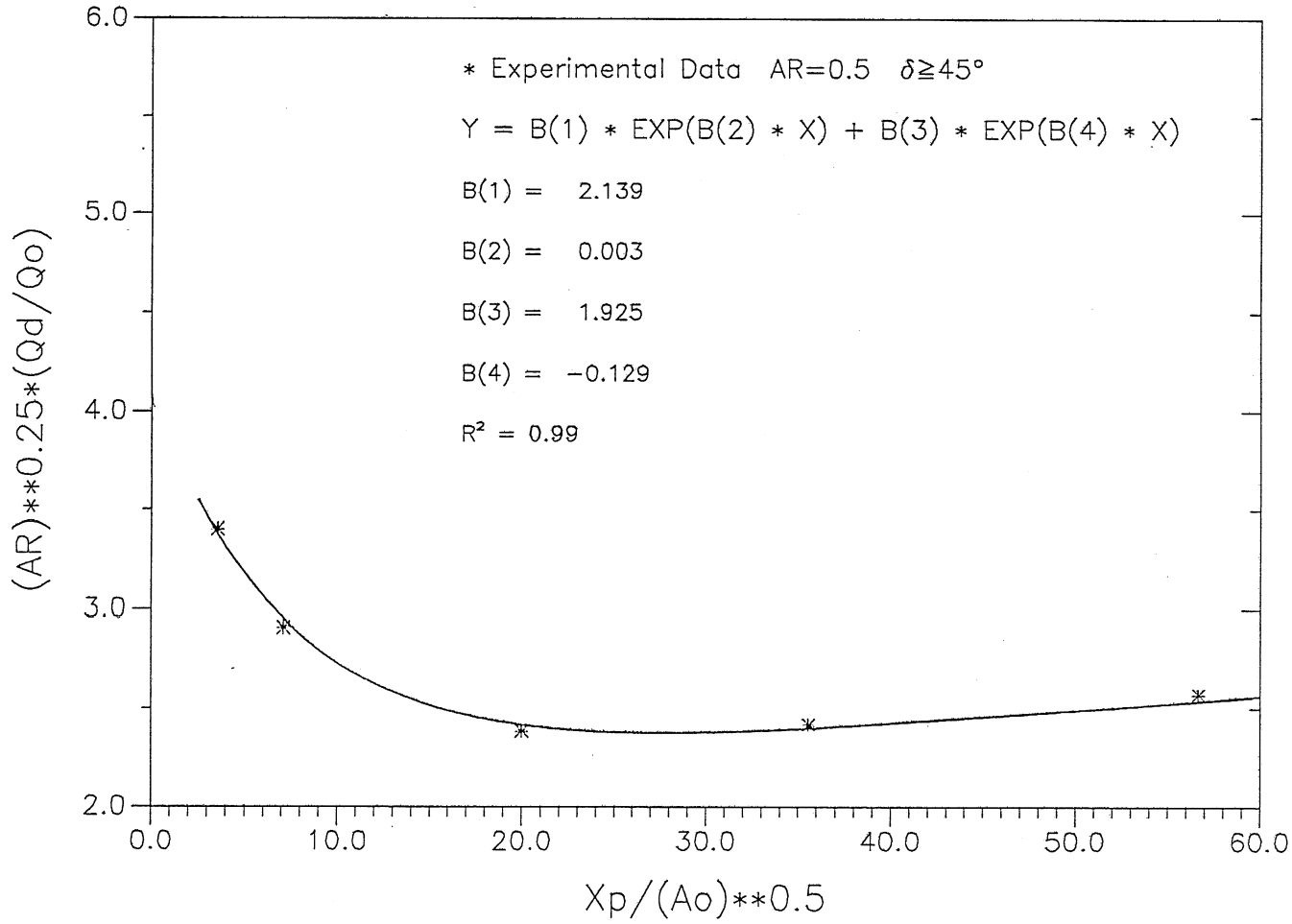

Fig. A–7 Empirical formula and experimental Data at AR=0.5, $\delta \geq 45°$.

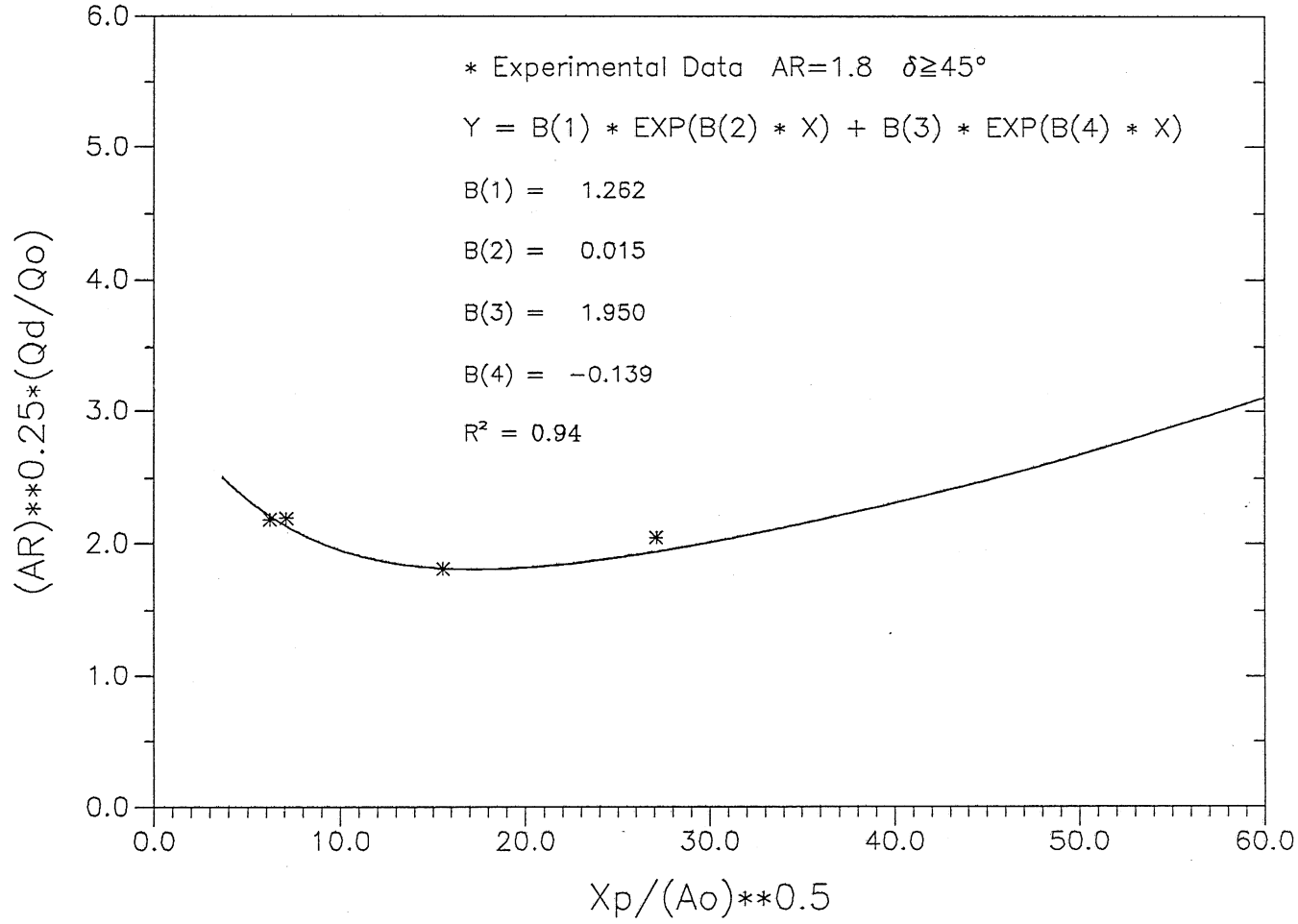

Fig. A–8 Empirical formula and experimental Data at AR=1.8, $\delta \geq 45°$.

For $\delta = 10°$, the empirically fitted formula is: (The form of equation comes from the pattern 20 of PLOTIT user's manual)

$$(AR_o)^{0.25} Q_d/Q_o = B_9\, e^{(B_{10}\, x)} + B_{11}\, e^{(B_{12}\, x)} \qquad [A–6]$$

Where: $B_9 = 1.040$

$B_{10} = 0.012$

$B_{11} = 0.962$

$B_{12} = -0.152$

$R^2 = 0.93$

The empirically fitted formula and experimental data (Johnson and Stefan, 1989 IV) are shown in Fig. A–9. Linear extrapolation between different diverging angles δ for wall jets will be used. Agreement between the linear extrapolation results and experimental data is good (Fig. A–9) when $\delta = 20°$.

A.2.2.3 Non–buoyant flow into strongly diverging channel or with large F_o

For inflows with weak buoyancy effects, such as represented by wide inflow channels and high densimetric Froude numbers, non–buoyant jet theory has been used to compute the entrainment as shown in Fig. 3 & 4 (Johnson and Stefan, 1989 IV). If inflow buoyancy (negative) decrease (F_o or AR_o increase), the plunging moves further downstream (x_p/B_o increase) and experimental entrainment data asymptotically approach the two–dimensional non–buoyant jet results.

Non–buoyant jet flow theory (Albertson et al., 1950, Rajaratnam 1976) relates flow in two–dimensional slot jets to the distance from the orifice by the equation

$$Q/Q_o = C_3\, (x/B_o)^{1/2} \qquad [A–7]$$

Experiments of non–buoyant inflows in a strongly diverging channel were conducted by Johnson et al. (1989, IV). With half angles $\delta = 90°$ and $\delta = 20°$ a free jet and a wall jet formed, respectively. The data obtained in a suddenly expanding open channel with $\delta = 90°$ (free jet regime) follows equation [A–7] with $C_3 \cong 0.5$ (best fit $C_3 = 0.46$) as shown in Fig. A–10. The data obtained in a diverging open channel with $\delta = 20°$ (wall jet regime) is approximated by wall jet theory with $C_3 \cong 0.25$.

A.2.2.4 Transition from negatively buoyant flow to non–buoyant flow

The non–buoyant jet theory equation [A–7] can be used when $F_o > 5$ or $AR_o > 3$ according to Johnson and Stefan (1989). This criterion may, however, be too crude for the transition from negatively buoyant flow to non–buoyant flow.

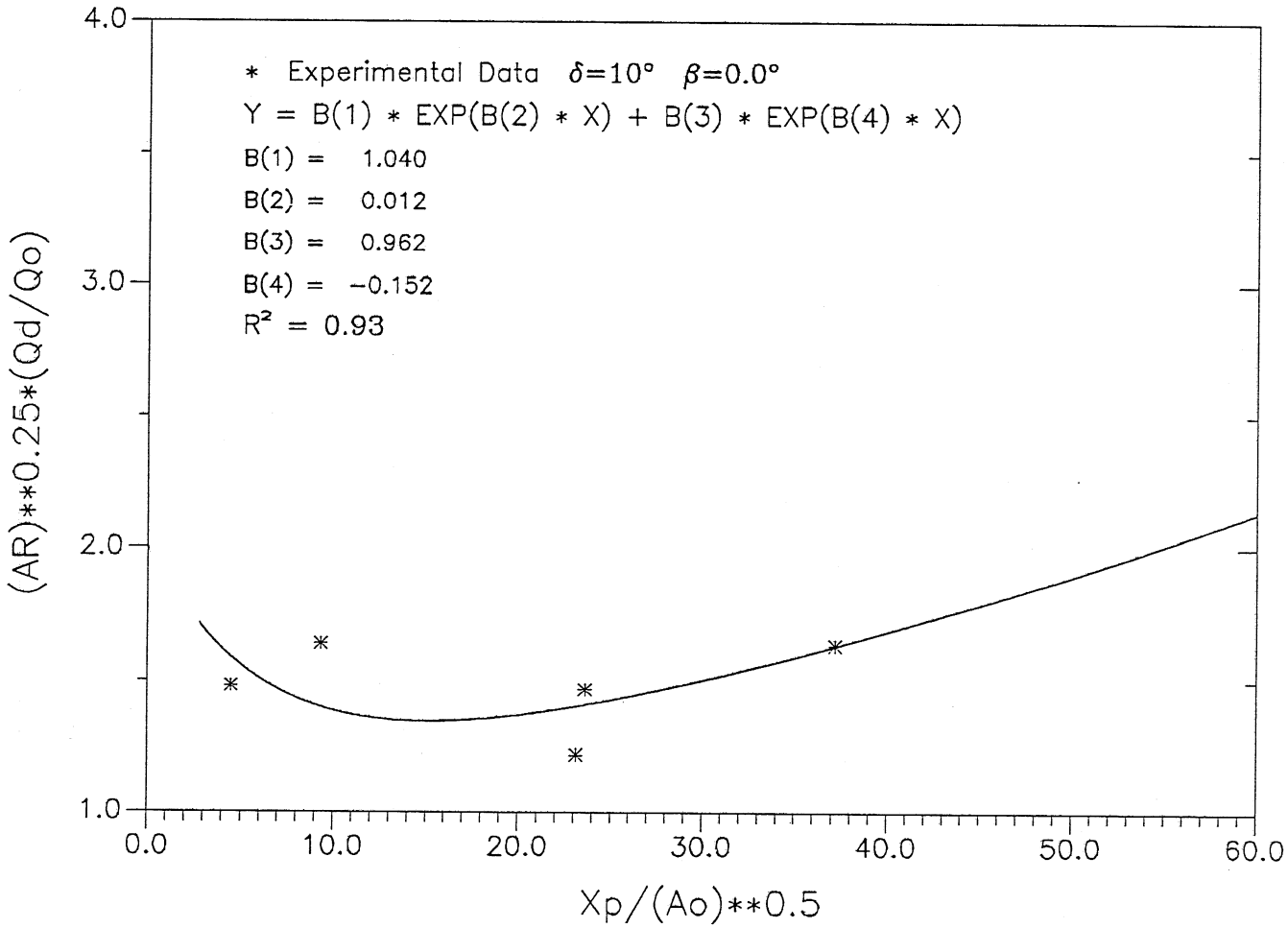

Fig. A–9 Empirical formula and experimental Data at δ=10°, β=0.0°.

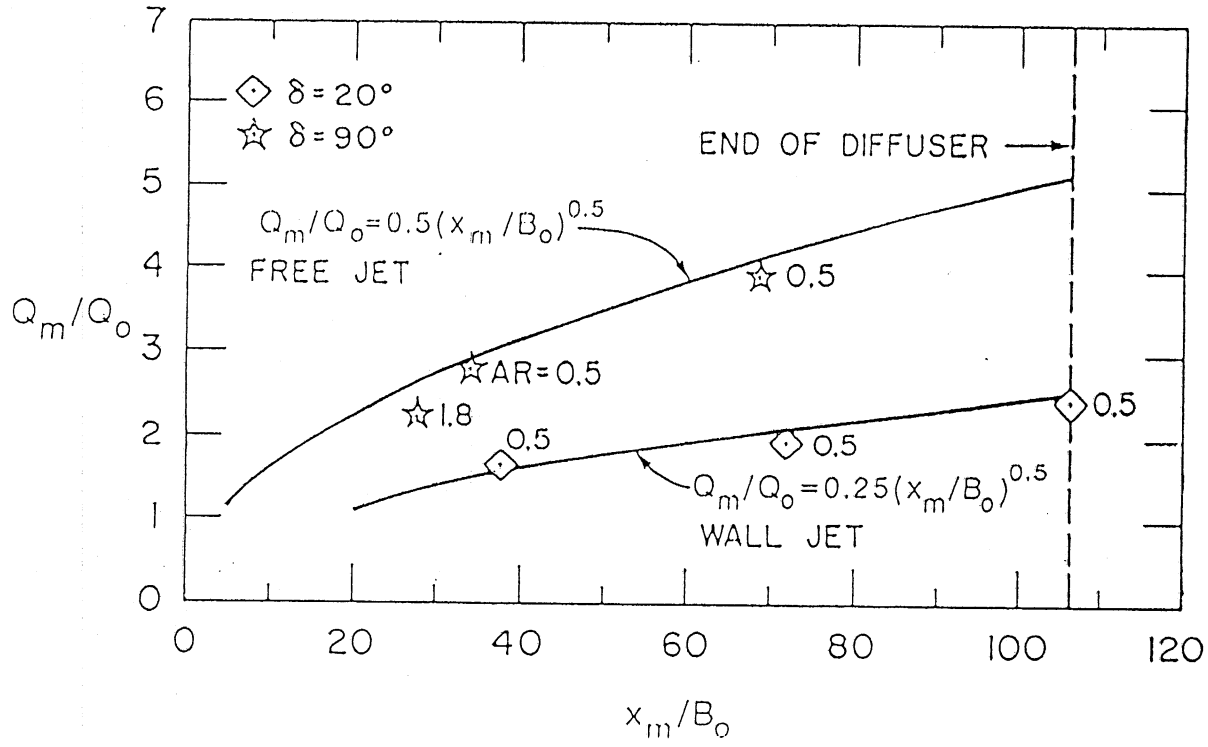

Fig. A–10. Measured cumulative flow rate (Q_m/Q_o) vs. nondimensional distance (x_m/B_o) for nonbuoyant free and wall jets. (Johnson and Stefan, 1988).

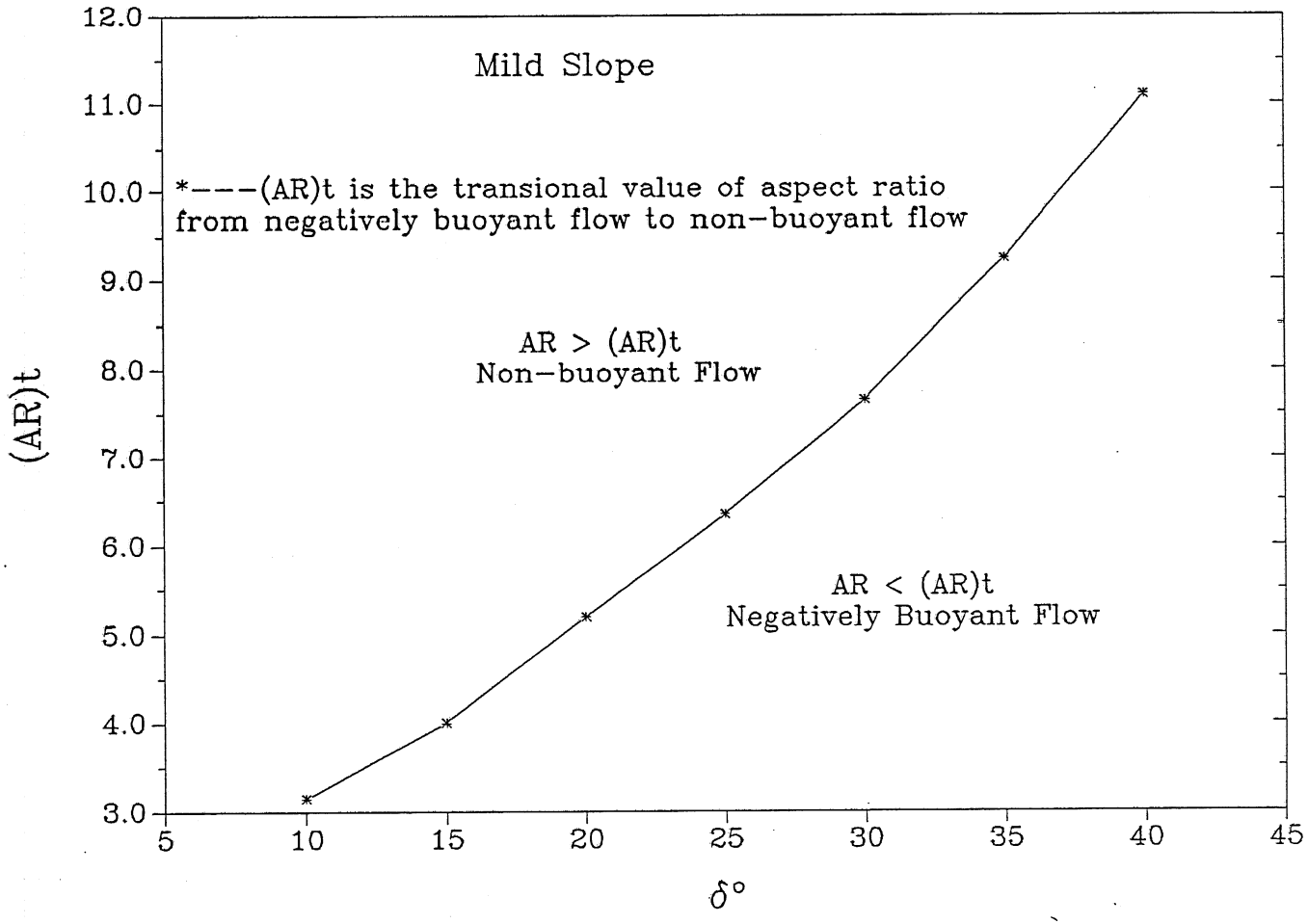

Fig. A–11 Relationship between AR_t and diffuser angle $\delta°$.

The flow ratio Q_d/Q_o (dilution) must be larger than 1.0 for all flows. If aspect ratio AR_o is large, dilution increases slowly from 1.0 as shown in Fig. 2–14. A limiting value of aspect ratio (AR_t) is defined as follows:. If the aspect ratio AR_o is larger than AR_t, the dilution computed from equations [A–4] or [A–5] or [A–6] at specified densimetric Froude number F_o will be less than 1.0 which is unreasonable. AR_t is the transitional value of the aspect ratio where the dilution calculated from equations [A–4] or [A–5] or [A–6] is equal to 1.0. The flow is considered a negatively buoyant flow when $AR_o < AR_t$ and a non–buoyant flow when $AR_o \geq AR_t$. For equation [A–7] of non–buoyant jet flow theory the dilution γ at $x = x_p$ will be less than 1.0 if $F_o \leq 2.3$. So we set dilution $\gamma = 1.0$ if $F_o \leq 2.3$.

Using equations [A–4] or [A–5] or [A–6], AR_t at different divergence angle δ can be calculated by interpolation and extrapolation. The relationship between AR_t and the divergence angle δ is shown as Fig. A–11. The diffuser with a larger divergence angle δ has a larger transitional aspect ratio AR_t. It is physically reasonable that the inflow with a larger aspect ratio AR_o will form a non–buoyant flow when the diffuser has a larger divergence angle δ. The inflow with a small aspect ratio AR_o will form a non–buoyant flow when the diffuser has a smaller divergence angle δ as and will be confined by the wall.

A.2.3 Plunging flow on a steep slope

A negatively buoyant inflow to a lake or reservoir typically encounters a sloping bottom as well as a diverging bank. Experiments were conducted by Johnson (1988) on a sloping beach of $\beta = 3°$ and with diffuser half–angles of $\delta = 0°$, $\delta = 20°$, $\delta = 90°$ and with inflow aspect ratio AR = 1.8. The experimental results are used to calculate the entrainment as follows.

A.2.3.1 Governing parameters and flow regimes

The physically governing parameters for flow in a sloping channel are shown in Fig. A–12. At diffuser half–angles $10° \leq \delta \leq 20°$ and bottom slope of $\beta = 3°$, the inflow is a wall jet. When the half–angle $\delta = 90°$ the inflow enters as a free jet (Johnson and Stefan, 1988). Using linear extrapolation, the entrainment of plunging is calculated for diffuser angles δ for which no measurements were obtained.

The most striking difference between wall jets in a sloping diffuser and a horizontal diffuser is the recirculation region between the wall jet and the opposite diffuser wall shown in Fig. A–13. The entrainment of plunging will be different for different flow regimes. The detailed analysis is given by Johnson and Stefan (1988).

A.2.3.2 Distance to plunging

The determination of the entrainment of a plunging flow requires knowledge of the distance to plunging (x_p). x_p should be calculable from the geometry and inflow densimetric Froude number (F_o). From conservation of mass and buoyancy Johnson (1988) developed an equation relating the inflow densimetric Froude number to the distance to plunging for a sloping and

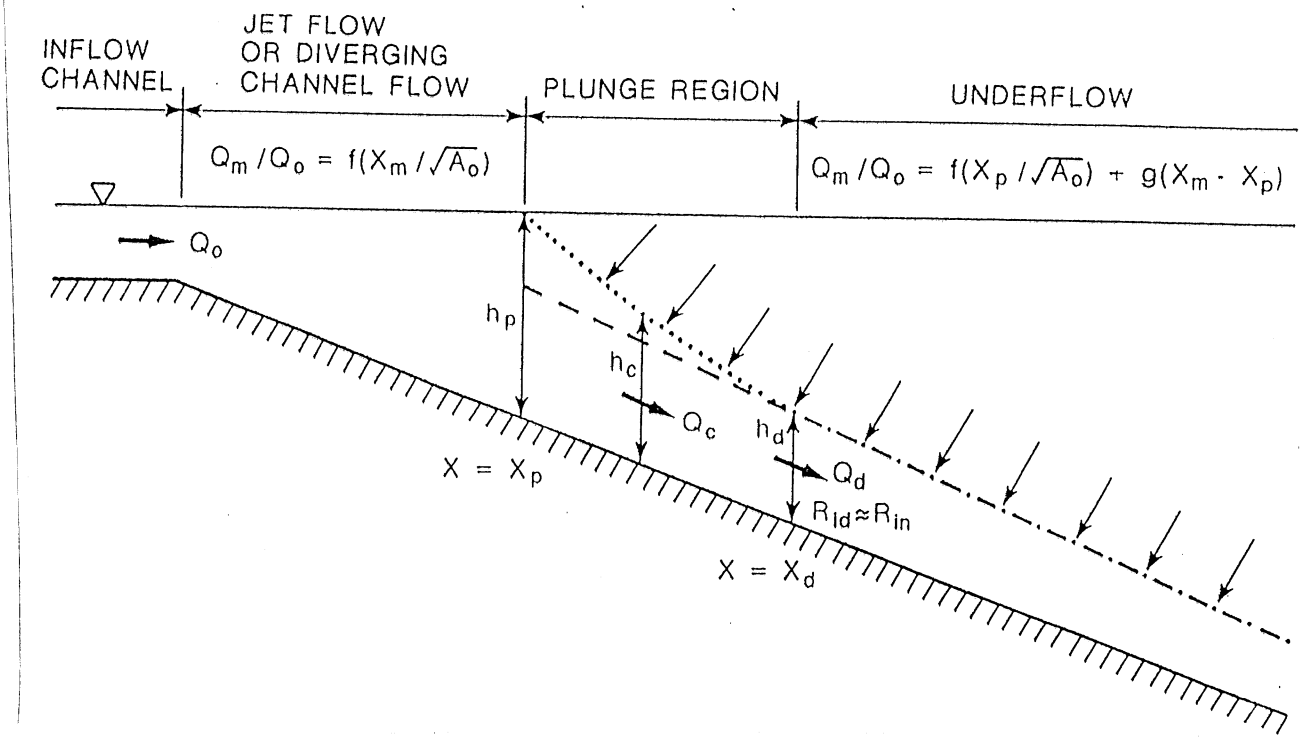

Fig. A–12 Schematic of plunging flow in a diverging and sloping channel (After Johnson et al., 1988]

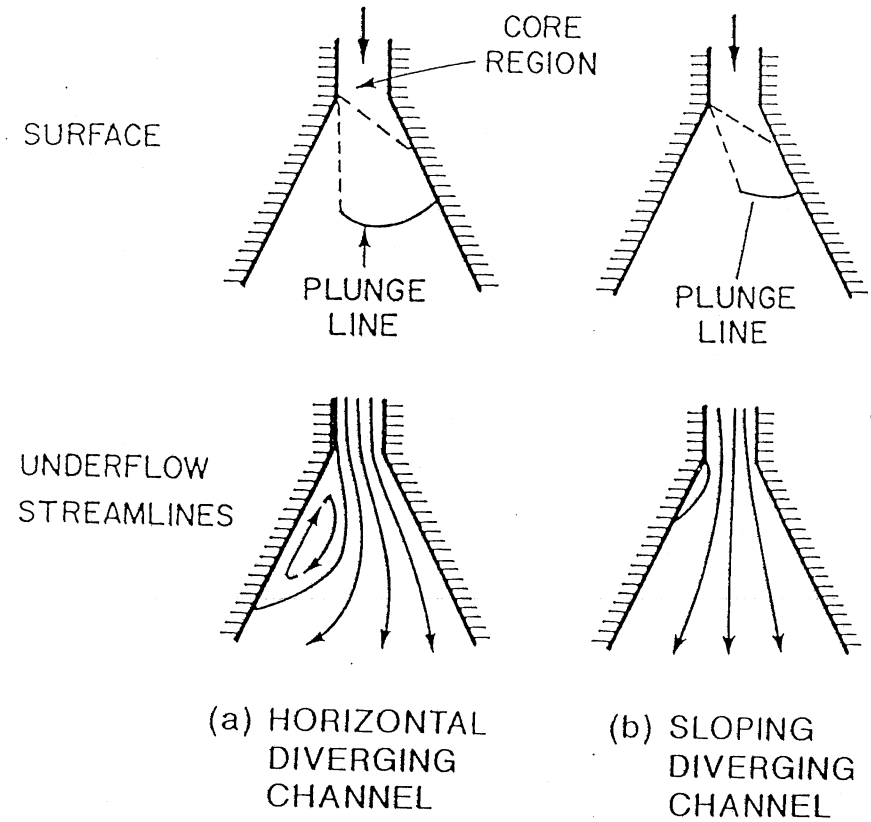

Fig. A–13 Flow patterns of wall jet in horizontal and sloping diffusers.

strongly diverging channel. From the analysis and the experimental data fitted by Johnson a linear relationship between x_p and F_o is obtained. The distance to plunging in the experiments with $\beta = 3°$ and $AR_o = 1.8$ for half angles $\delta = 10°, 20°, 90°$ (Johnson and Stefan, 1988) is

$$x_p/\sqrt{A_o} = 7.35\ (\ F_o - 1.28) \qquad [A–8]$$

If plunging occurs near the channel outlet ($F_o < 1.28$), Eq. [A–6] breaks down. Equation [A–8] is not a general equation. It is for sloping angles $\beta = 3°$ only. Further study of the relationship between x_p and β, AR, δ, C_f (friction coefficient) using the basic turbulent jet theory is needed.

A.2.3.3 Dilution before plunging

Johnson(1988) gave the best fitting line of cumulative flow rate versus distance from inflow channel for different δ and F_o values investigated. All experiments were for bottom slopes $\beta = 3°$.

For $\delta = 10°$, $F_o = 1.48$

$$Q_p/Q_o = 0.976 + 0.006\ \ x_p/\sqrt{A_o} \qquad [A–9]$$

For $\delta = 20°$, $F_o = 1.49$

$$Q_p/Q_o = 0.85 + 0.122\ \ x_p/\sqrt{A_o} \qquad [A–10]$$

For $\delta = 20°$, $F_o = 35.0$

$$Q_p/Q_o = 1.028 + 0.058\ \ x_p/\sqrt{A_o} \qquad [A–11]$$

For $\delta = 90°$, $F_o = 1.54$

$$Q_p/Q_o = 1.133 + 0.237\ \ x_p/\sqrt{A_o} \qquad [A–12]$$

With reference to Fig. IV–25 by Johnson and Stefan (1988), the linear relationships of entrainment before and after plunging lend themselves to combination in one figure: the pre–plunging flow behavior may be much like non–buoyant jet flow and the underflow behavior much like stratified flow. The cumulative flow rate would follow the jet flow line until plunging occurs, then it follows the appropriate stratified flow line for given inflow densimetric Froude number. As in Fig. IV–25, we can get the relationship of the cumulative flow rate versus distance to plunging. For example

For $\delta = 10°$, $F_o = 35.0$

$$Q_p/Q_o = 1.021 + 0.44\ \ x_p/\sqrt{A_o} \qquad [A–13]$$

For $\delta = 20°$, $F_o = 35.0$

$$Q_p/Q_o = 1.33 + 0.13\ \ x_p/\sqrt{A_o} \qquad [A–14]$$

Equation [A–9] to [A–14] are shown in Fig. A–14 to Fig. A–15. Using linear interpolation and extrapolation, the dilution up to the plunging ($x = x_p$) is calculated for different divergence angles δ, densimetric Froude numbers F_o, aspect ratios AR_o and bed slopes β.

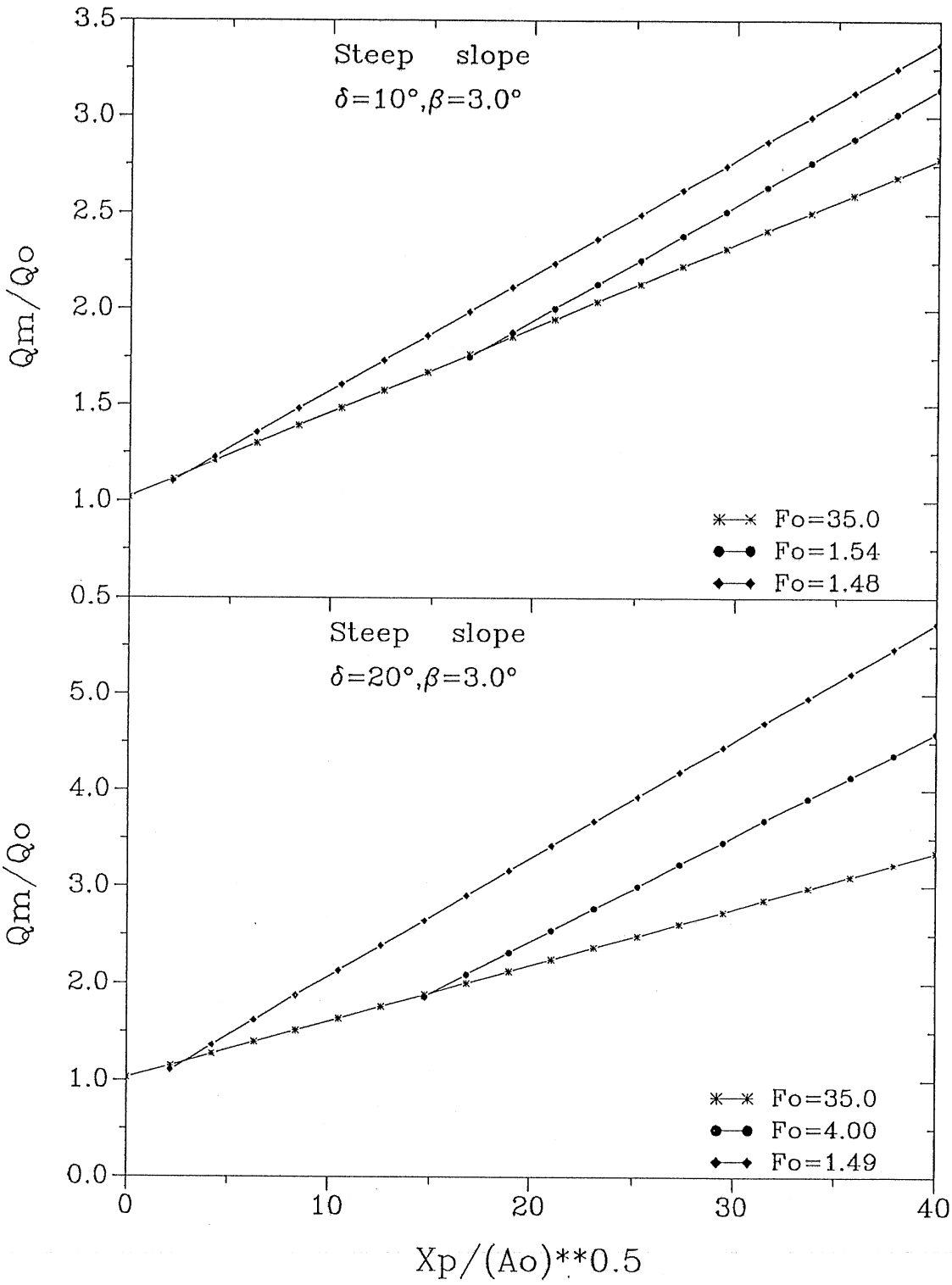

Fig. A–14 Relationship between Q_p/Q_o and F_o for δ=10° and δ=20° as β=3°.

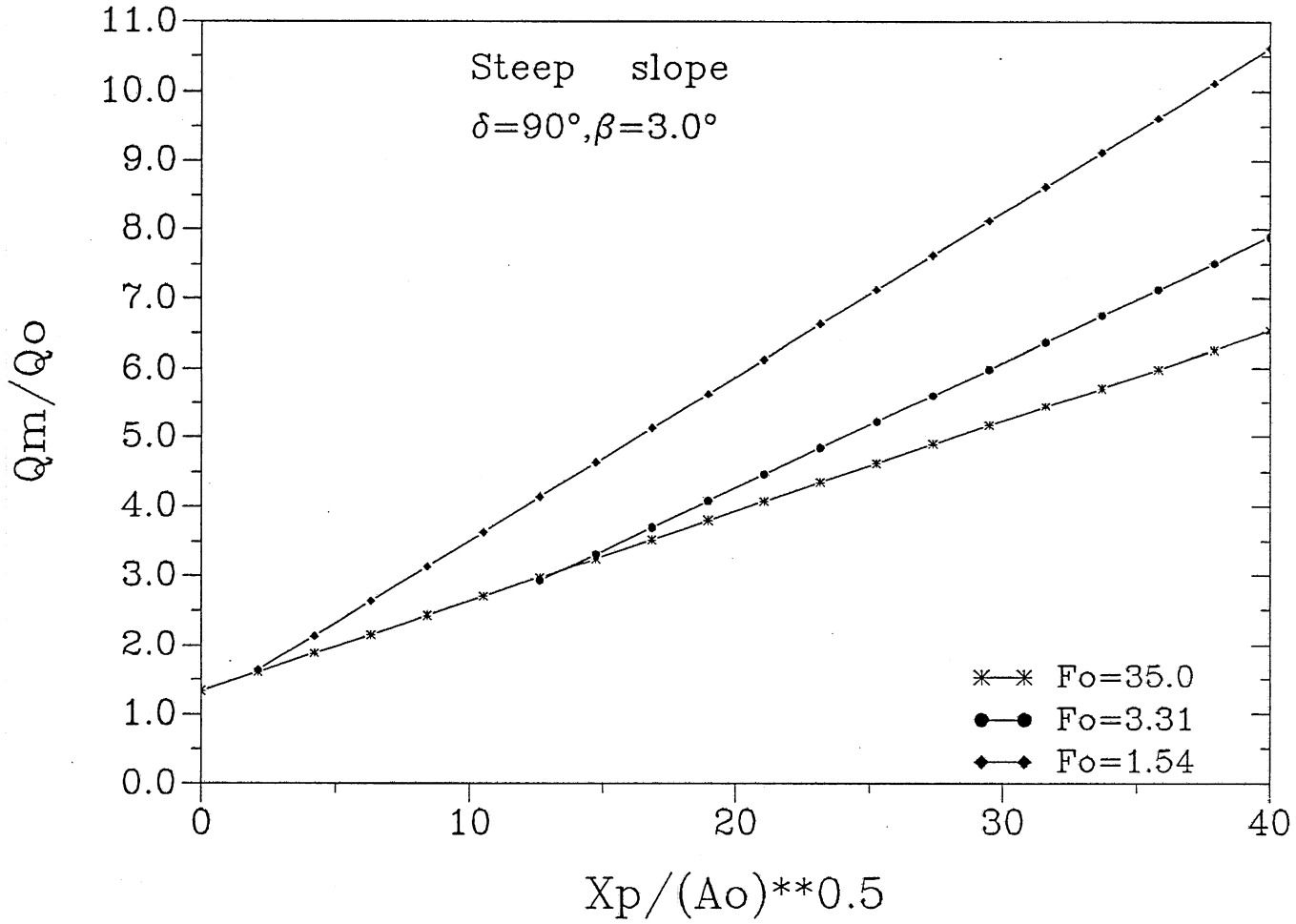

Fig. A–15 Relationship between Q_p/Q_o and F_o for δ=90°, β=3°.

A.3 Application of Inflow Model

Using the inflow model, the relationship between dilution Q_p/Q_o and densimetric Froude number F_o for $\delta = 10°$, $\delta = 20°$ and $\delta \geq 45°$ with different aspect ratios AR_o is shown in Fig. A–16, Fig. A–17 and Fig. A–18 where $\beta = 0°$.

The inflow in Figs. A–16 to A–18 includes three parts: negatively buoyant flow, transitional flow, non–buoyant flow. The densimetric Froude number F_o at which the transition from negatively buoyant flow to non–buoyant flow occurs is different for different aspect ratios AR_o. The densimetric Froude numbers F_o of the transition decreases if the aspect ratio AR increases. Because inflow buoyancy effects decreases as aspect ratio AR_o increases, it is possible for the inflow to change from negatively buoyant flow to non–buoyant flow when the inflow densimetric Froude number F_o is smaller.

The densimetric Froude number F_o at the start and the end of the transition will increase if the divergence angle δ ($\delta < 45°$) increases at the same aspect ratio AR_o. The distance to plunging is the same if AR_o is the same at $\delta < 45°$ (Eqn. [A–3]), so a larger F_o is needed in order to balance the larger stall formed in a larger divergence angle δ. If the inflow is a free jet, the densimetric Froude numbers F_o at the start and the end of the transition do not change for different divergence angles δ because the dilution does not change for different δ; it changes with aspect ratio AR_o.

For a steep slope, Fig. A–19 shows a relationship of dilution Q_p/Q_o versus F_o and experimental data (Johnson and Stefan, 1988) at AR_o =1.8 and $\beta = 3°$. Dilution increases with F_o linearly which is different from the relationship for a mild slope. Agreement of a few experimental data (Johnson and Stefan, 1988) with model results at AR_o =1.8, $\delta = 90°$ and $\beta = 3°$ is poor.

The prediction of dilution from empirical equations needs to be improved before it can used in a water quality model.

A model with a better theoretical foundation has therefore been developed in this report.

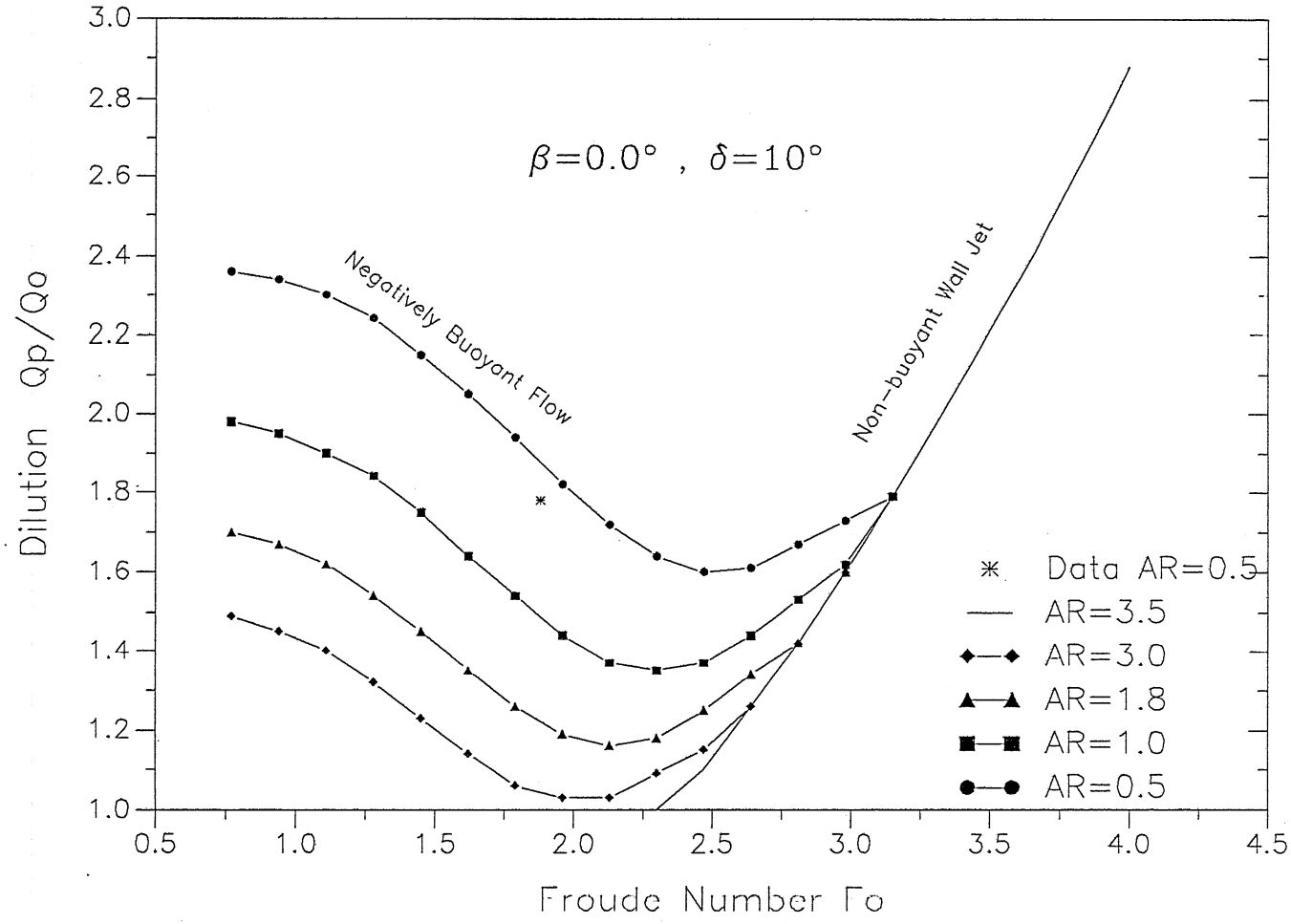

Fig. A–16 Relationship between Q_p/Q_o and F_o for δ=10°, β=0°.

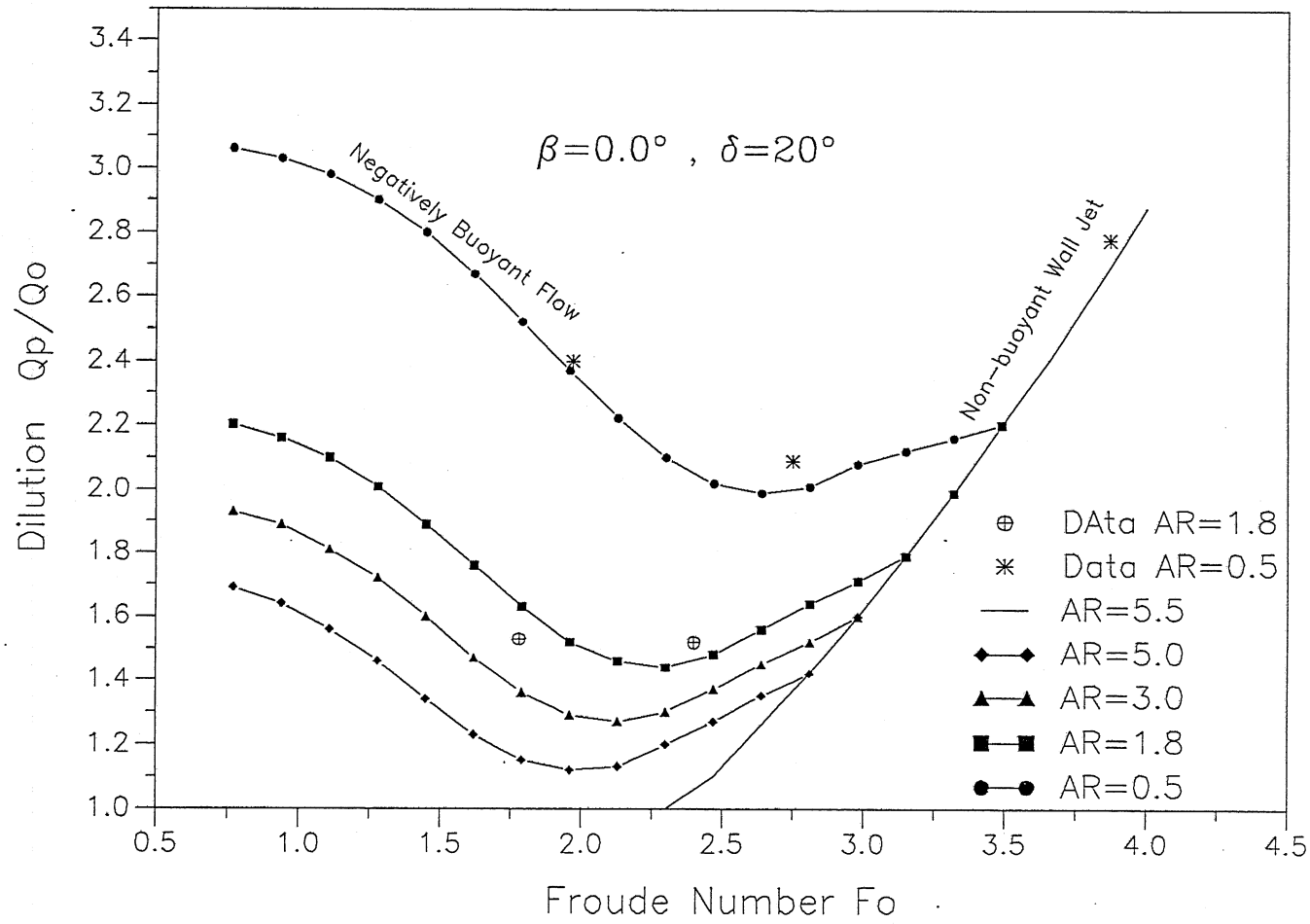

Fig. A–17 Relationship between Q_p/Q_o and F_o for δ=20°, β=0°.

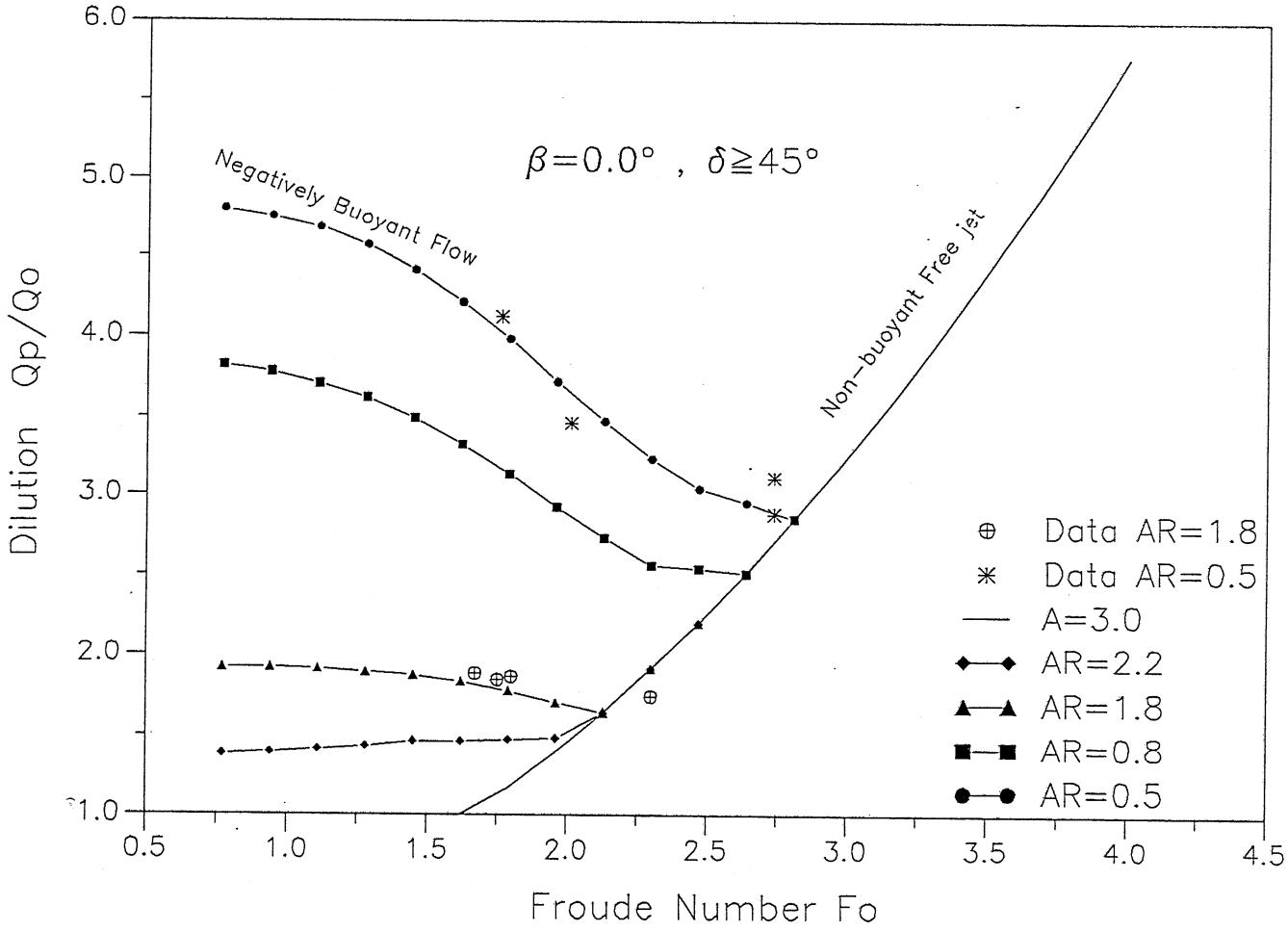

Fig. A–18 Relationship between Q_p/Q_o and F_o for δ=45°, β=0°.

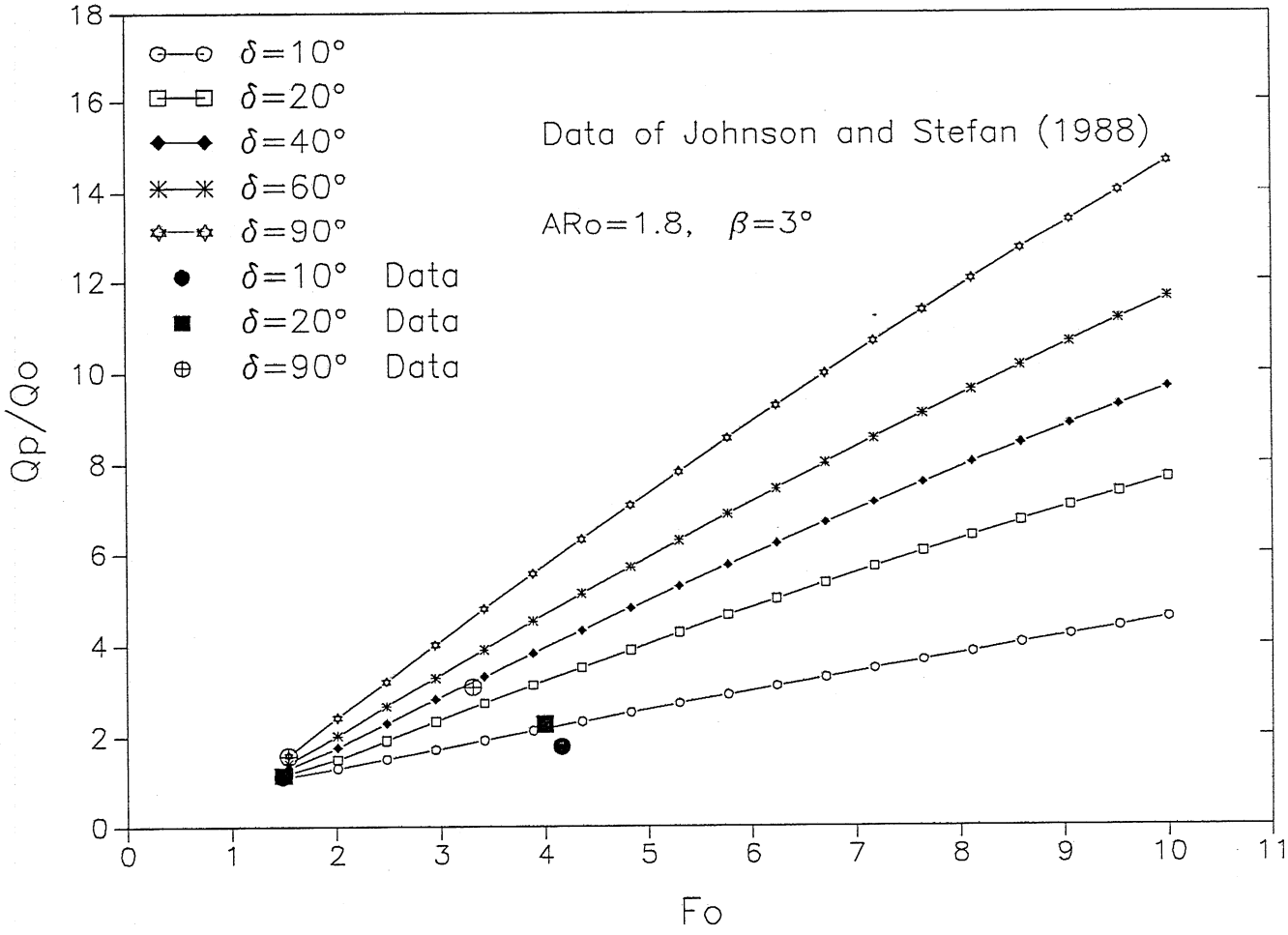

Fig. A–19 Relationship between Q_p/Q_o and F_o for AR_o=1.8, β=3°.

Appendix B

FITTING METHOD ADAPTED TO FINITE DATA SETS

Gaussian distributions are often fitted to the experimental velocity distribution data of jet–like flow (Rajaratnam, 1976). If the experimental measurements are finite numbers, the error of the fitting method is very large as shown in Fig. 3–4 and Fig. 3–5 in chapter III. A fitting method adapted to finite data sets will be reported herein.

B.1 The second moment correction coefficient

Numerical integration uses finite data, and lacks data outside a cut–off point. Using correction coefficient is therefore applied such that

$$m_{2c} = C_{m2}\, m_2 \qquad [B–1]$$

where $m_2 = \frac{M_2}{M_0}$ comes from previous Gauss fitting method. m_{2c} is the corrected second moment. C_{m2} is a correction coefficient of the second moment as given in Eqn. [B–2]

$$C_{m2} = \frac{m_2\ (-\infty \text{ to } +\infty)}{m_2\ (y_n \text{ to } y_p)} \qquad [B–2]$$

Where $$m_2\ (-\infty \text{ to } +\infty) = \frac{\int_{-\infty}^{+\infty} e^{-\eta^2}\, \eta^2 d\eta}{\int_{-\infty}^{+\infty} e^{-\eta^2}\, d\eta} = 0.50$$

$$m_2\ (y_n \text{ to } y_p) = \frac{\int_{y_n}^{y_p} e^{-\eta^2} (\eta - \eta_0)^2\, d\eta}{\int_{y_n}^{y_p} e^{-\eta^2}\, d\eta}$$

y_n is the negative cut–off point on the η axis.

y_p is the positive cut–off point on the η axis.

Numerical integration with a very small calculation step $\Delta\eta$ is used to calculate $m_2\ (y_n \text{ to } y_p)$.

$$\int_{y_n}^{y_p} e^{-\eta^2} d\eta = \sum_{i=1}^{N} e^{-\eta_i^2} \Delta\eta_i \qquad [B-3]$$

$$\int_{y_n}^{y_p} e^{-\eta^2} \eta \, d\eta = \sum_{i=1}^{N} e^{-\eta_i^2} \eta_i \Delta\eta_i \qquad [B-4]$$

$$\int_{y_n}^{y_p} e^{-\eta^2} (\eta-\eta_o)^2 \, d\eta = \sum_{i=1}^{N} e^{-\eta_i^2} (\eta_i-\eta_o)^2 \Delta\eta_i \qquad [B-5]$$

where $$\eta_o = \frac{\int_{y_n}^{y_p} e^{-\eta^2} \eta \, d\eta}{\int_{y_n}^{y_p} e^{-\eta^2} d\eta} \qquad [B-6]$$

As i=2 to N–1 $\quad \Delta\eta_i = (y_p - y_n) / N$

As i=1 and N $\quad \Delta\eta_i = (y_p - y_n) / (2 N)$ [B–7]
N is a large number [i.e. 200]

We will first consider a symmetrical cut–off, that is, $y_p = - y_n$. Non–dimensional velocity at cut–off point is given in Equation [B–8]

$$u/u_{max(\text{cut–off point})} = e^{-(y_p)^2} = e^{-(y_n)^2} \qquad [B-8]$$

The relationship between C_{m2} and the non–dimensional velocity at the cut–off point is shown in Fig. B–1. When the cut–off point is near the centerline (loss more data outside of the cut–off point), C_{m2} increases rapidly. C_{m2} strongly depends on the cut–off point.

Before applying correction coefficients to the Gauss fitting method, we introduce another numerical integration method for calculating moments of velocity distributions. It will be called method 2. The previous numerical integration using Eqn. [3–15] to Eqn. [3–20] is called method 1. Fig. B–2 is a scheme of numerical integration by method 2. The velocity is in the middle of two experimental points (using linear extrapolation). Numerical integration formulas of method 2 are as follows:

$$M_o = \int_{y_n}^{y_p} u(y) \, dy$$

$$= \sum_{i=1}^{N} \frac{u(i)+u(i+1)}{2} \Delta y_i \qquad [B-9]$$

$$M_1 = \int_{y_n}^{y_p} u(y)\ y\ dy$$

$$= \sum_{i=1}^{N} \frac{[u(i)+u(i+1)][y(i+1)+y(i)]}{4.0}\ \Delta y_i \qquad [B-10]$$

$$M_2 = \int_{y_n}^{y_p} u(y)\ (y-y_o)^2\ dy$$

$$= \sum_{i=1}^{N} \frac{u(i)+u(i+1)}{2}\ [\frac{y(i+1)+y(i)}{2} - y_o]^2\ \Delta y_i \qquad [B-11]$$

B.2 Results of the modified fitting method

(a) Effects of different cut–off point with same calculation step $\Delta\eta$

Fig. B–3 shows the relationship between corrected characteristic length B_c defined by equation [B–12] and non–dimensional velocity at cut–off point. B_c by method 1 increases but B_c by method 2 decreases when non–dimensional velocity at cut–off point is increased (cut–off point is near centerline).

$$B_c = m_{2c}\sqrt{2} \qquad [B-12]$$

$$B(\text{exact}) = m_2\sqrt{2} = 1.0 \qquad [B-13]$$

Fig. B–3 shows the error of B_c (%) for different cut–off point. The error of B_c is defined by Eqn. [B–14]. The error of B_c by method 1 is larger than that by method 2.

$$\text{Error of } B_c = \frac{B_c(\text{fitting}) - B(\text{exact})}{B(\text{exact})} * 100\% \qquad [B-14]$$

Figs. B–4, B–5 show four examples of modified Gauss fitting if calculation step size $\Delta\eta$ is small and cut–off point is further from the centerline. The difference between method 1 and method 2 is small. Fitted data are on the curve of Gaussian profile for symmetric and unsymmetric cut–off points.

(b) Effects of different calculation step size $\Delta\eta$

Fig. B–6 shows example with different calculation step size $\Delta\eta$, all examples use symmetrical cut–off. Step size $\Delta\eta$ is defined as:

$$\Delta\eta = \frac{\eta_p - \eta_n}{N} \qquad [B-15]$$

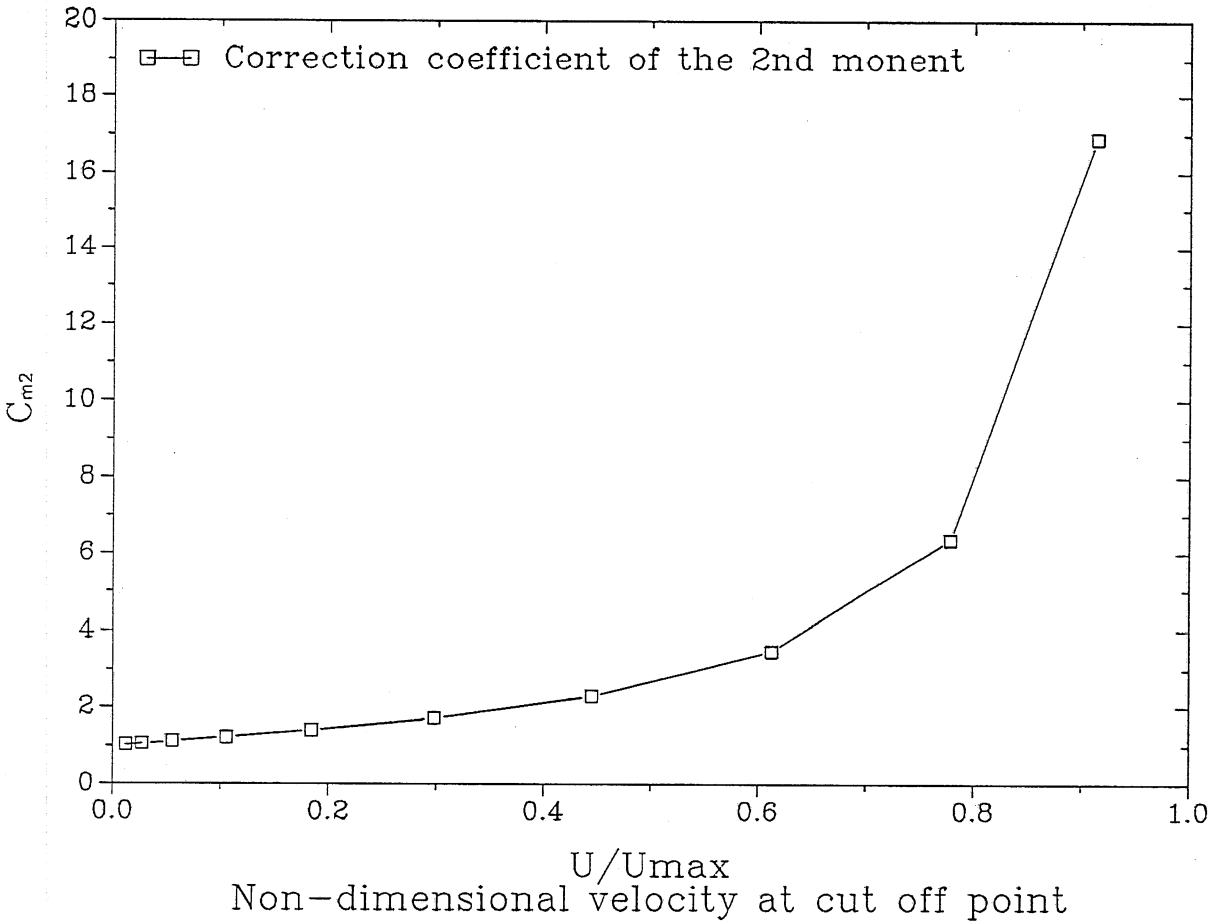

Fig. B–1 The correction coefficient of the second moment versus non–dimensional velocity at cut–off point.

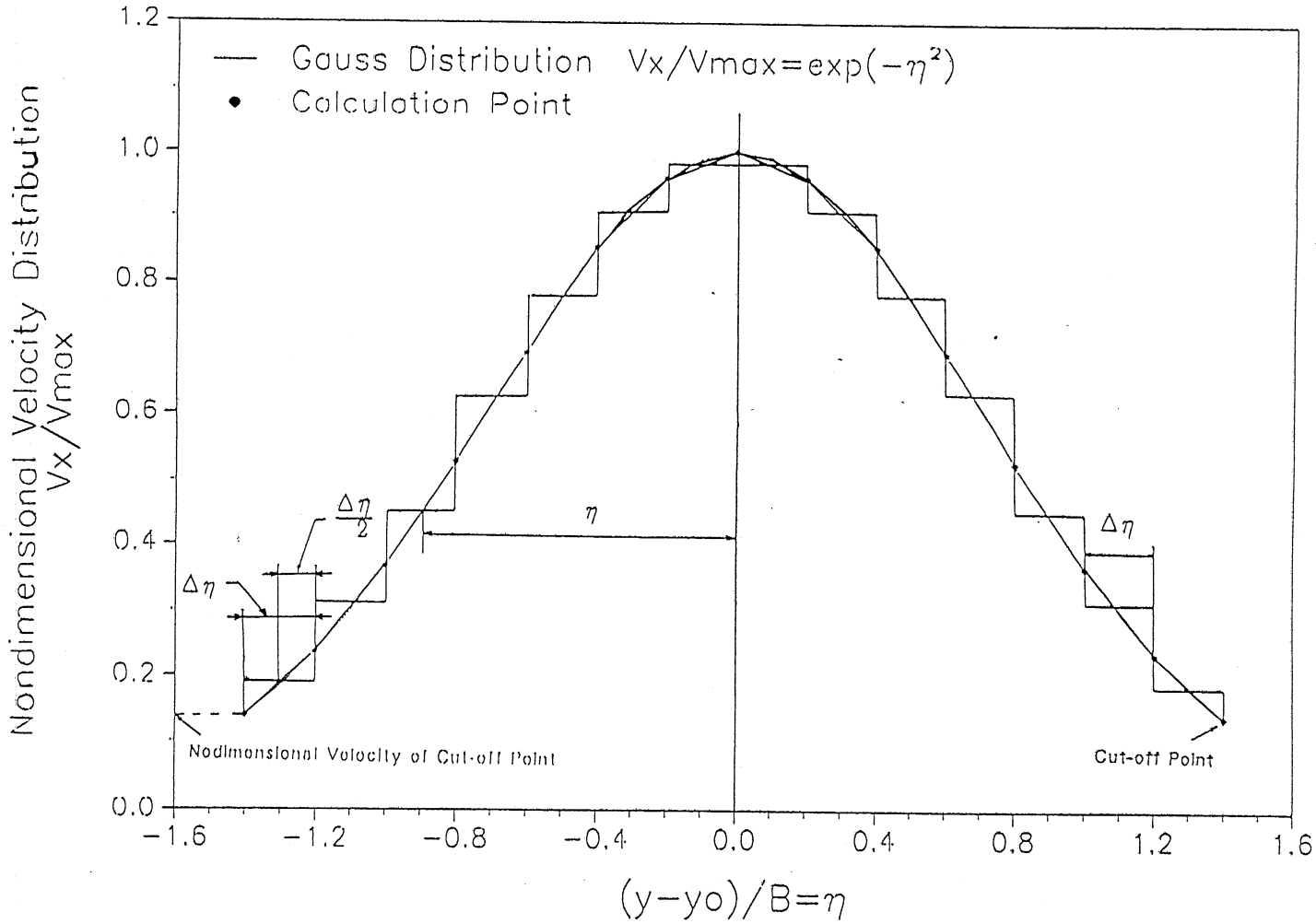

Fig. B–2 An scheme of numerical integration. (Method 2).

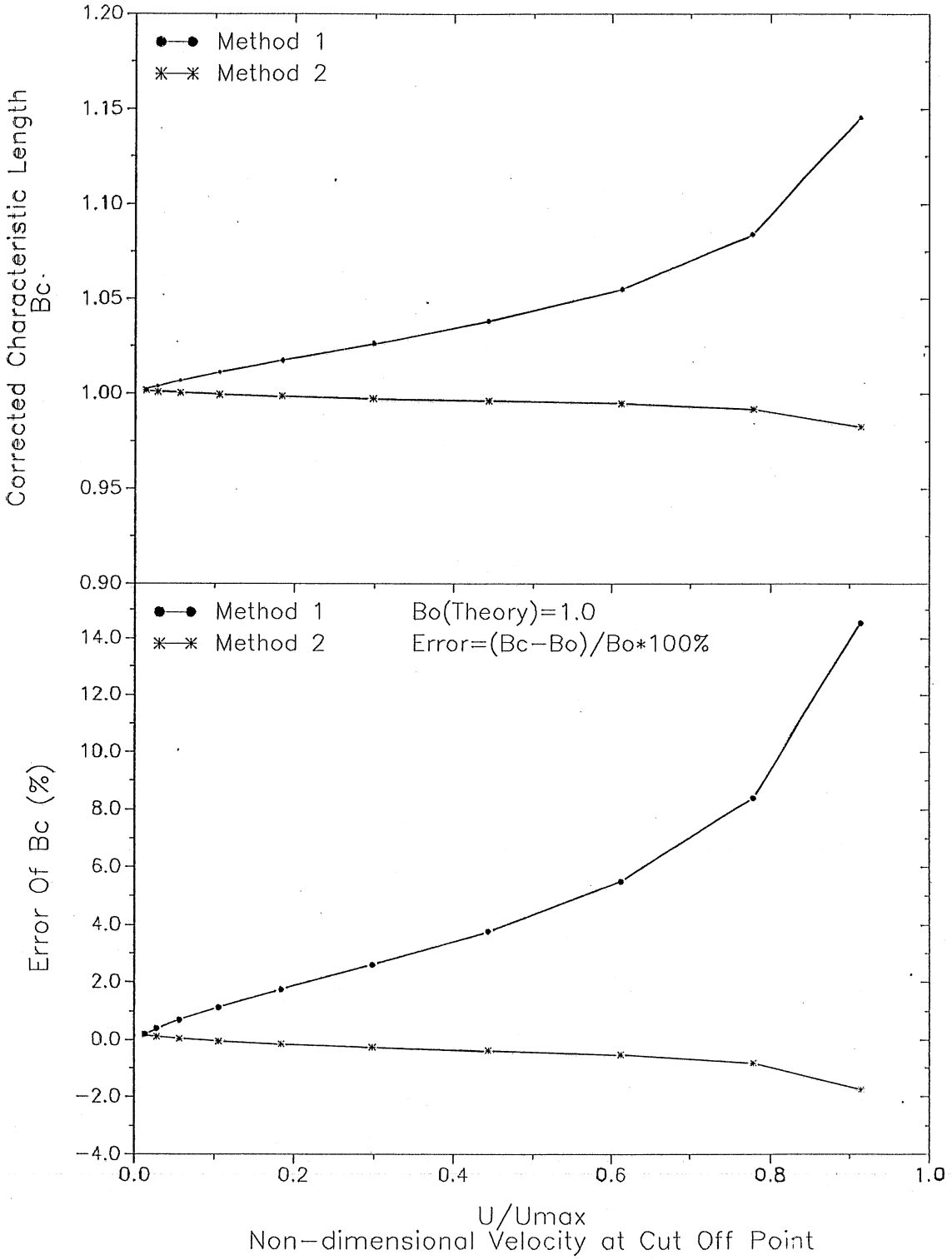

Fig. B–3 **Effects of different cut–off points with same calculation step $\Delta\eta$.**

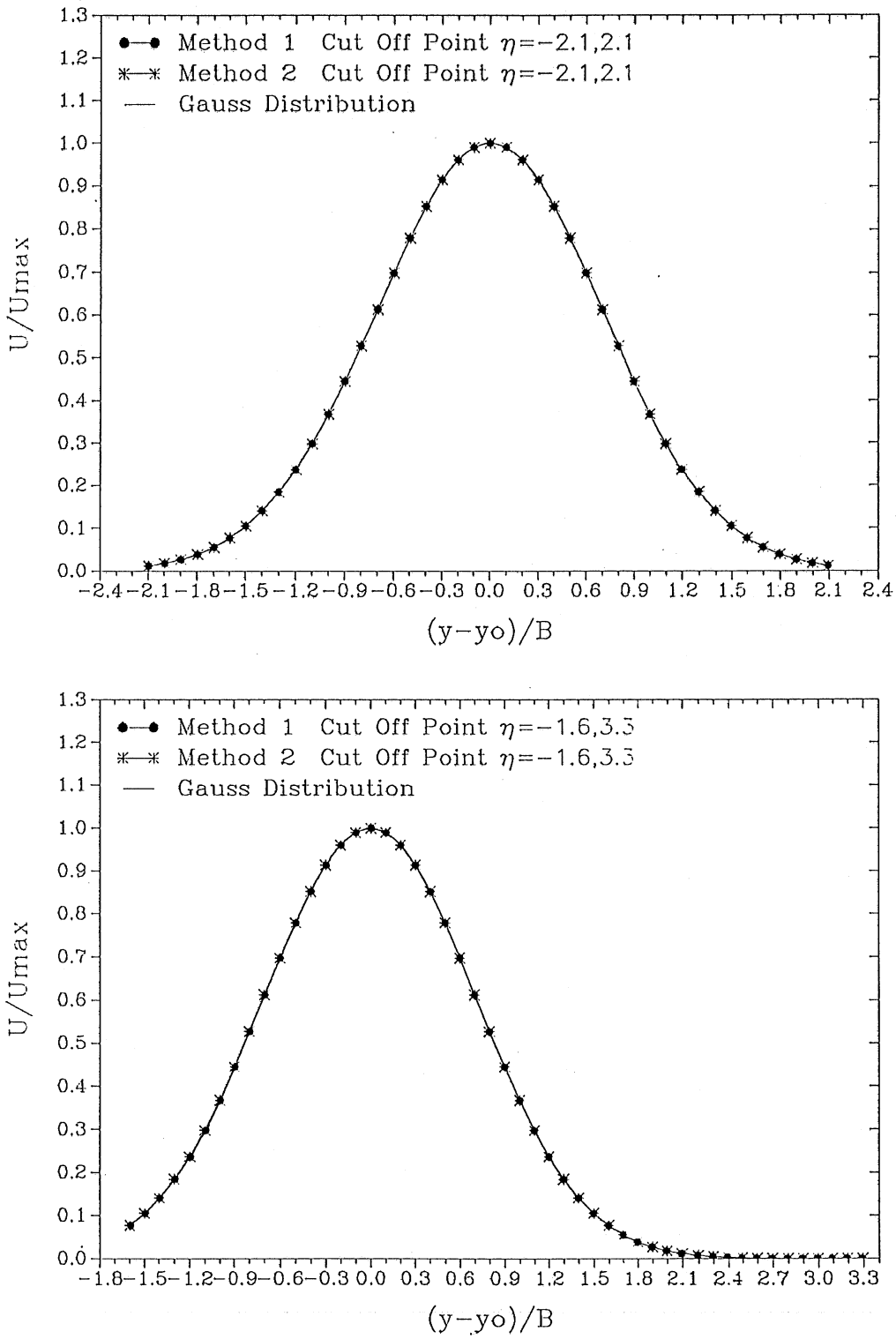

Fig. B–4 Examples of the modified Gauss fitting method with symmetric and unsymmetric cut–off points.

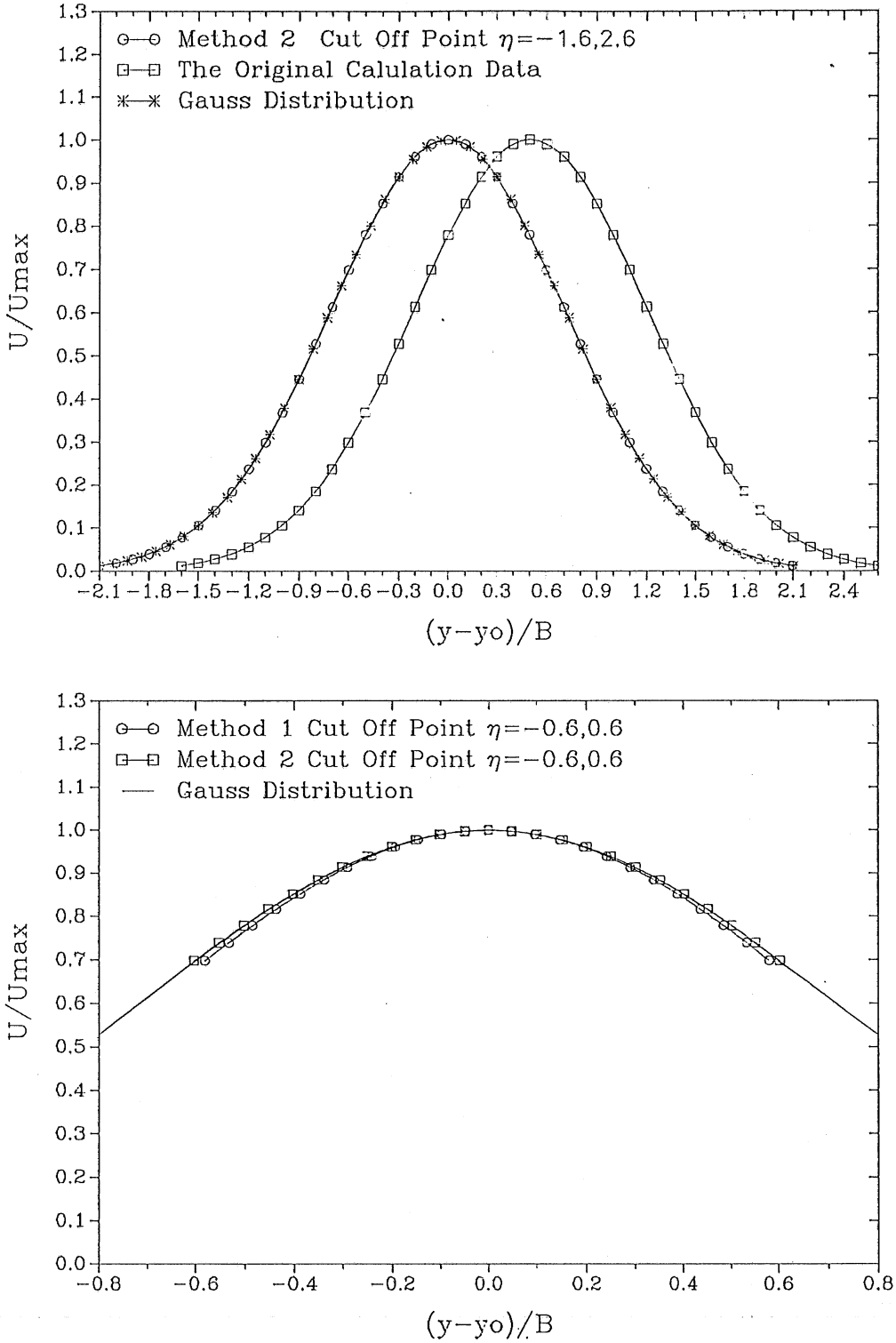

Fig. B–5 Examples of the modified Gauss fitting method.

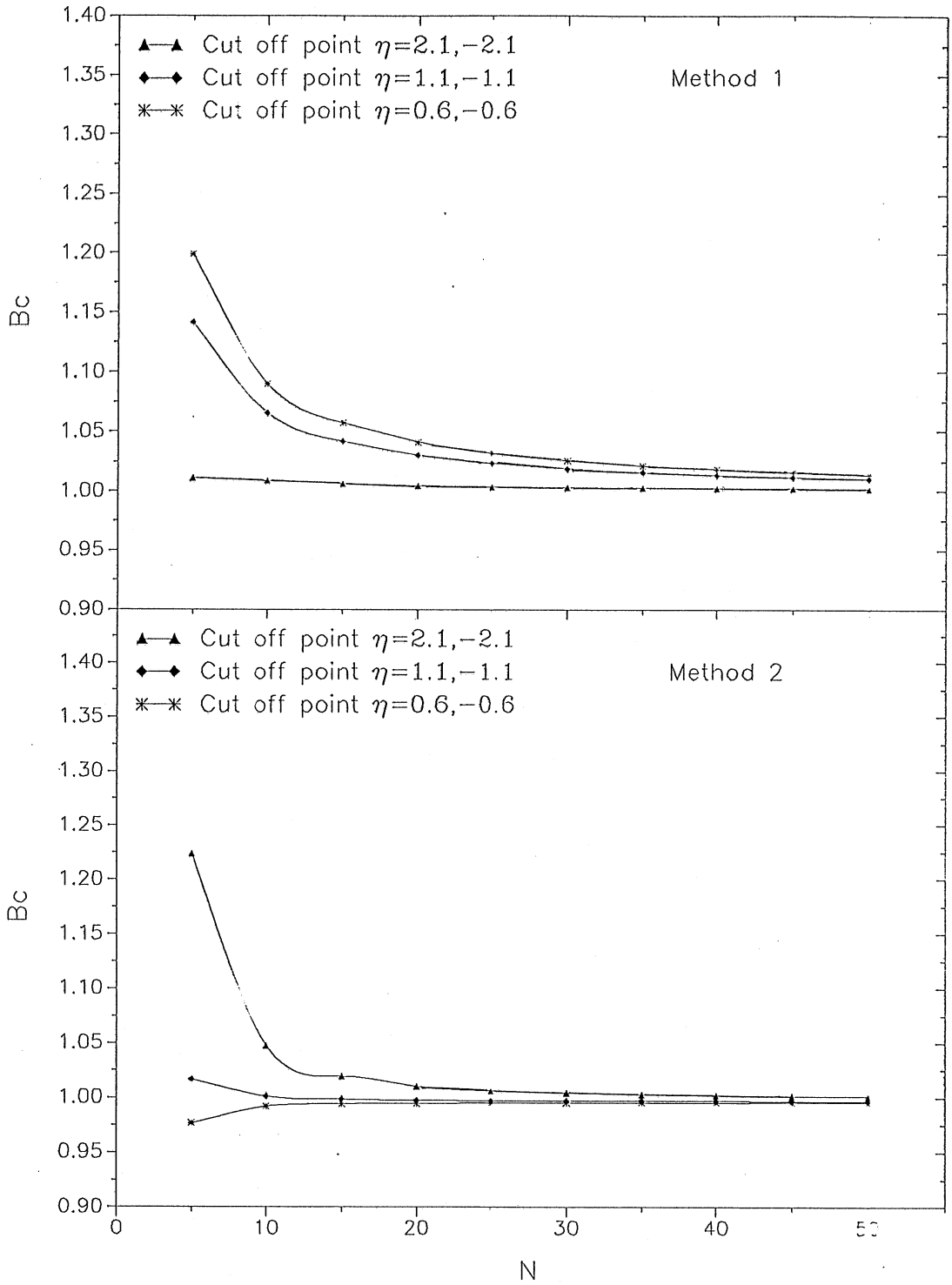

Fig. B–6 Examples of effects of different calculation step $\Delta\eta$.

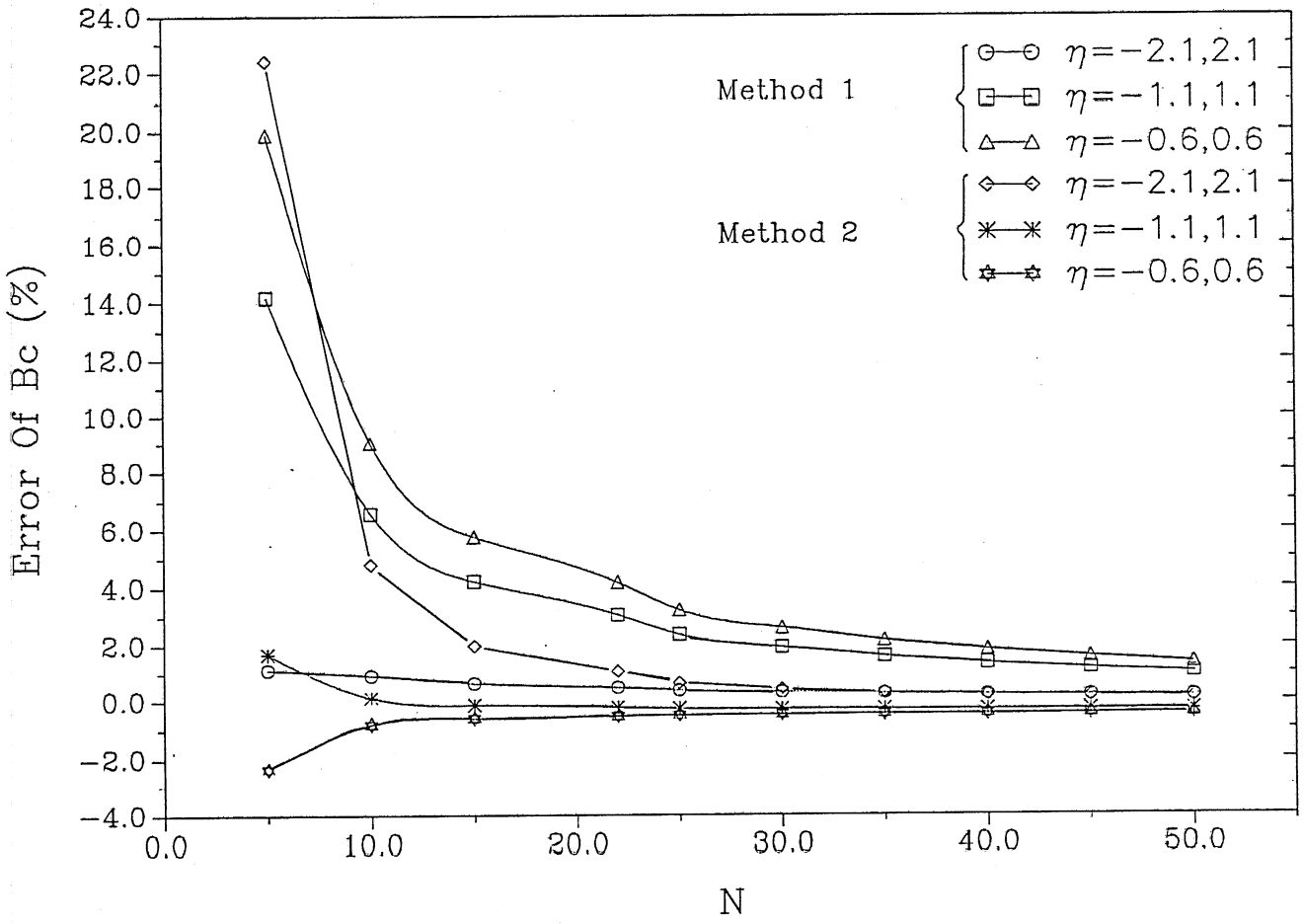

Fig. B–7 Analysis of error of B_c with different calculation step $\Delta\eta$.

Fig. B–7 shows the relationship between B_c and N. Effect of cut–off point is more important than the effect of calculation step $\Delta\eta$.

The relationships between the error of B_c (%) and N is shown in Fig. B–8 for method 1 and method 2. Fig. B–9 (top) shows two examples with larger calculation step size $\Delta\eta$ when cut–off point is near the centerline.

B.3 The first moment correction coefficient

If the cut–off point is unsymmetrical, even though an exact Gauss velocity Profile is used, the first moment of the velocity profile is not zero. That is unreasonable. The correction of the first moment y_o is used to modify first moment m_1 shown by Eqn. [B–16]:

$$m_{1c} = m_1 - y_o \qquad [B–16]$$

where m_{1c} is the corrected first moment.

m_1 comes from the Gauss fitting of experimental data using equation [3–17] and [B–10]).

$$y_o = \int_{y_n}^{y_p} e^{-\eta^2}\ \eta\ d\eta$$

Fig. B–9 (bottom) shown on m_{1c} versus cut–off point. [suppose η(negative) as constant], m_{1c} is very small although cut–off point is very unsymmetrical, m_{1c} is less than zero for method 1, m_{1c} is larger than zero for method 2. the corrective results of method 2 is better than these of method 1 also. Fig. B–8 has used the correction coefficient of first moment.

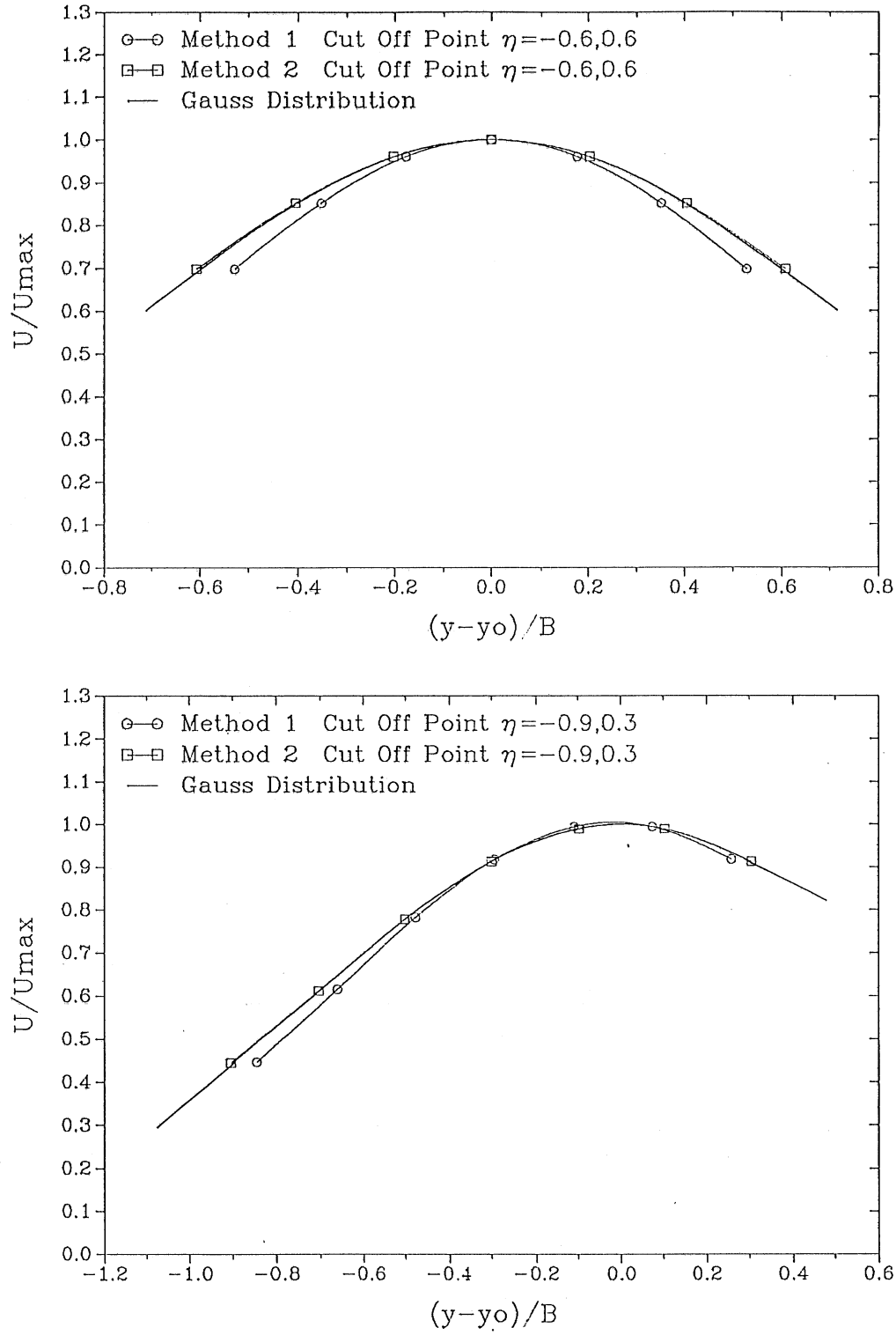

Fig. B–8 Comparison of integration by method 1 and method 2 with a finite number of measurements.

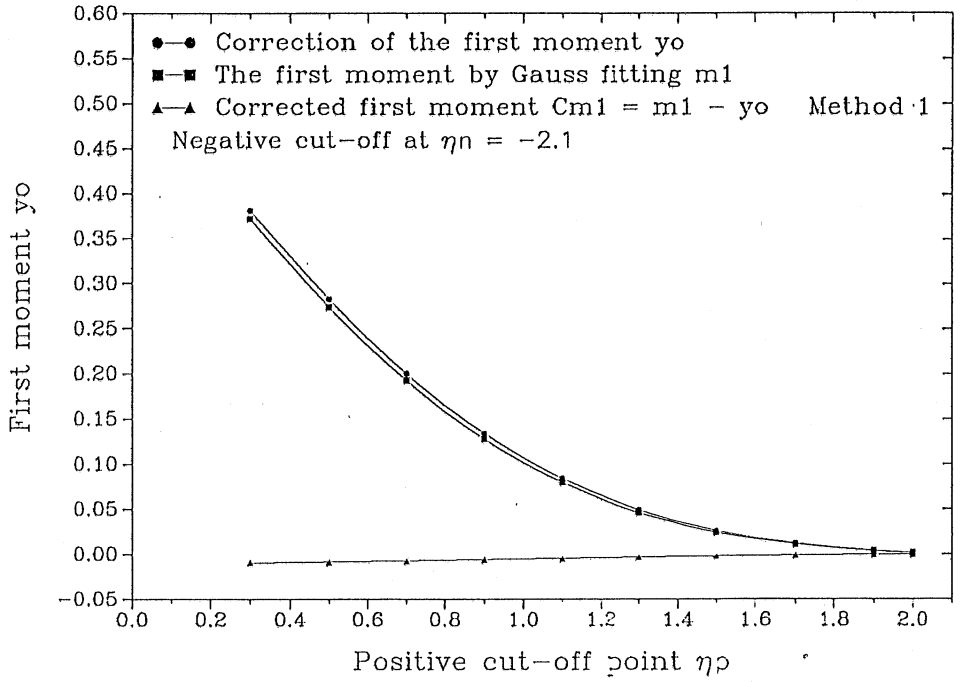

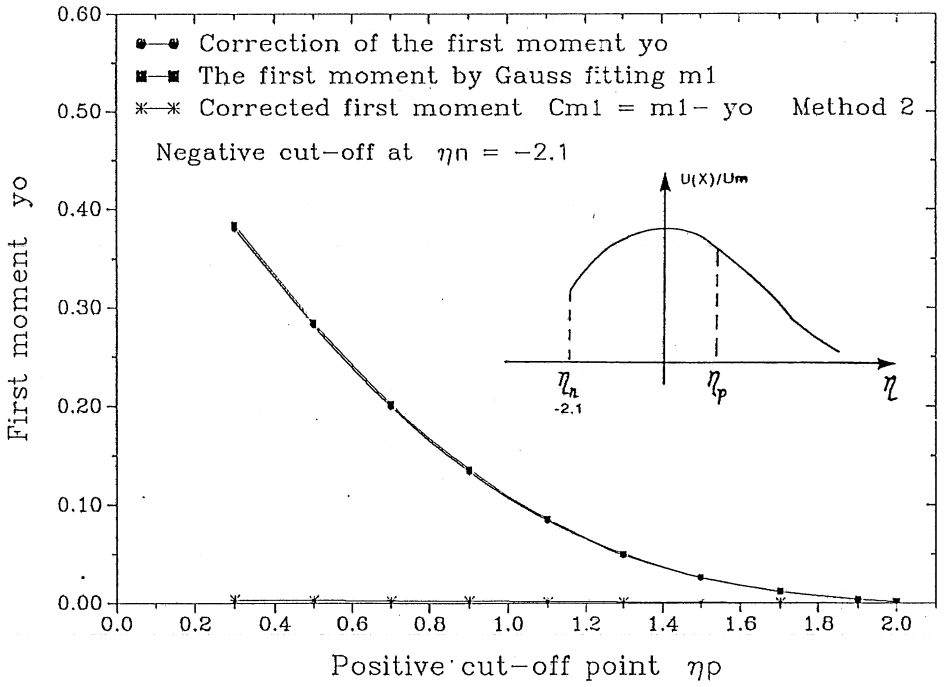

Fig. B–9 Correction coefficient of the first moment.

APPENDIX C

LISTING OF COMPUTER PROGRAMS AND NOTES

File name: PHOR.FOR

Function: Computes dilution before plunging and distance to plunging of channel discharge **over horizontal bottom.**

Equations: [4–20c] and [4–20d] for fully developed region.
[4–34] and [4–35] for flow development region.

Input file: PHOR.DAT

Function: Specifies inflow conditions.

Variables:
U_0 = inflow velocity.
CF = local friction coefficient c_f.
B_0 = width of inflow channel.
H_0 = depth of inflow channel.
Fo = inflow densimetric Froude number F_0.
SN = exponent n of vertical velocity profiles.

Output file: PHOR.PRN

Function: Prints inflow conditions, jet dimensions, dilution before plunging and distance to plunging.

Variables:
XB0 = dimensionless length x/B_0
UC4 = jet centerline velocity $u_m(x)/U_0$
B4 = dimensionless jet width $b(x)/B_0$
YX = width of potential core in ZFE
FP = densimetric Froude number F
XPBO = distance to plunging x_p/B_0
QPQO = dilution before plunging Q_p/Q_0
XPAO = distance to plunging $x_p/\sqrt{A_0}$

```
C***** BETA ANGLE = 0.0 (HORIZONTAL CHANNEL)******
C***** PHOR.FOR*****CONSIDER DEVELOPING REGION****
C*****
      DIMENSION X(86),UC4(86),B4(86),Q4(86),XB0(86)
      DIMENSION BX(20),YX(20),FP(86)
      F(XD,YD)=-(A1*YD+A2*YD**3/EXP(-A1*XD))
      FU(XO,YO)=(A1*FITE4*YO+A1*XO+AE1)/A6
      GU(XO,YO)=(A1*YO+A1*FITE4*XO+A8*AE1)/A7
      OPEN(5,FILE='PHOR.DAT')
      OPEN(6,FILE='PHOR.PRN')
      DATA  C1,C2,FITE1,FITE2/1.4142,0.6642,0.53229,0.37639/
      DATA  AE,AE1,FPC/0.04,0.035,1.0/
      READ(5,*) U0,CF,B0,H0,F0,SN
C*****
C***** COMPUTE CONSTANTS OF DIFFERENTIAL EQUATION
C*****
      M=86
      FITE3=1.06458
      FITE4=0.75277
      AR=B0/H0
C*****
C*****  SN = EXPONENT OF BOUNDARY LAYER VELOCITY PROFILE
C*****
      IF(SN.EQ.1.0) THEN
      D2=1.0
      ELSE
      D2=SN/(SN+2.0)
      ENDIF
      A1=CF/(2.0*D2*H0)
      A2=2.0*AE/(B0*C1)
      A3=2.0*FITE1
      A6=(FITE3-FITE4)
      A7=FITE4/FITE3-1.0
      A8=FITE4/FITE3
C*****
C***** INTIAL CONDITION OF DIFFERENTIALL EQUATION
C*****
      UC4(1)=1.0
      B4(1)=1.0
      Q4(1)=1.0
      BX(1)=0.0
      YX(1)=B0/2.0
C****
C**** COMPUTE ZFE KX=1
C****
      KX=1
      FF=1.0
C****
C**** SET TOTAL COMPUTATION LENGTH XU
C**** XU MAY BE REALTIVE TO AR OR CF
C**** THE FOLLOWING EQUATION OF XU IS EMPIRICAL
C****
```

```
C*****
      IF(YX(I).LT.0.0.AND.KX.EQ.1) THEN
      CFA=YX(I-1)/(YX(I-1)+ABS(YX(I)))
      X0=(X(I-1)+AX*CFA)/B0
C*****
C***** FINSH COMPUTATION ZFE IF KX=2
C*****
      KX=2
      GOTO 366
      ENDIF
      IF(I.EQ.20.AND.YX(I).GT.0.0) THEN
      FF=2.0*FF
      KX=1
      GOTO 366
      ENDIF
      B4(I)=2.0*(YX(I)+BX(I))/B0
      Q4(I)=2.0*YX(I)/B0+2.0*BX(I)*FITE3/B0
100   CONTINUE
C*****
C*****    OUTPUT PARAMETERS OF COMPUTATION
C*****
      BET=0.0
      WRITE(6,10) BET,B0,H0,AR,CF,AE1,AE,X0,C1,C2,FITE1,FITE2
 10   FORMAT(5X,'BET=',F5.2,2X,'(DEGREE)'//5X,'B0=',F7.2,17X,'H0=',F7.2
     1        //5X,'AR=',F7.2, 17X,'CF=',F7.5//5X,'Aeo=',F6.5,
     2        '(Developing)',5X,'Ae=',F7.5,'(Developed)'//
     3        5X,'Xo=',F9.4,3X,'(LENGTH OF ZFE WITH Cf)'
     4        //5X,'C1=',F7.5,17X,'C2=',F7.5
     5        //5X,'FITE1=',F7.5,14X,'FITE2=',F7.5//)
      WRITE(6,20)
 20   FORMAT(4X,'X/B0',9X,'Um/U0',12X,'b/B0'/)
C*****
C***** OUTPUT WIDTH & CENTRAL VELOCITY OF JET
C*****
      DO 30 I=1,M
      WRITE(6,41) XB0(I),UC4(I),B4(I)
41    FORMAT(5x,F7.2,5x,F7.4,7x,F9.3)
30    CONTINUE
C****
C****     DETERIMINE Xp/Bo AND Qp/Qo
C*****    COMPUTE Fp FOR FREE TURBULENT JET
C*****
466   DO 566 I=1,M
      IF(I.GT.10) THEN
      FP(I)=0.626657*F0*UC4(I)*Q4(I)**0.5
      ELSE
      FT=2.0*(YX(I)+FITE3*BX(I))/(2.0*YX(I)+3.397*BX(I))
      FP(I)=FT*F0*UC4(I)*Q4(I)**0.5
      ENDIF
566   CONTINUE
      DO 666 I=1,M
      IF(FP(I).LE.FPC) GOTO 166
666   CONTINUE
```

```
      XU=B0/(CF*H0)
 366  DO 100 I=1,M
      IF(I.EQ.1) GOTO 15
      IF(KX.EQ.1) THEN
      AX=FF*B0/FLOAT(20)
      ELSE
      IF(I.LE.10) AX=X0*B0/9.0
      IF(I.GT.10) AX=(XU-X0*B0)/(FLOAT(M)-10.0)
      ENDIF
      X(I)=X(I-1)+AX
      XB0(I)=X(I)/B0
 15   X(1)=0.0
      IF(I.EQ.1) GOTO 100
C*****
C*****  AS KX=1  COMPUTE ZFE ONLY
C*****
      IF(KX.EQ.1) GOTO 200
C*****
C*****  AS KX=2 COMPUTE ZFE FOR 10 STEP SIZE
C*****
      IF(I.LE.10) GOTO 200
C*****
C***** HAVE ENTRAINMENT IN FREE JETS(DEVELOPED)
C*****
160   YN=UC4(I-1)
      XN=X(I-1)
      UK1=AX*F(XN,YN)
      UK2=AX*F(XN+AX/2.0,YN+UK1/2.0)
      UK3=AX*F(XN+AX/2.0,YN+UK2/2.0)
      UK4=AX*F(XN+AX,YN+UK3)
      UC4(I)=UC4(I-1)+(UK1+2.0*UK2+2.0*UK3+UK4)/6.0
      B4(I)=EXP(-A1*X(I))/(UC4(I)**2*2.0*FITE2)
      Q4(I)=A3*UC4(I)*B4(I)
      GOTO 100
C*****
C***** DEVELOPING REGION WITH FRICTION
C*****
200   UC4(I)=1.0
      YO=YX(I-1)
      XO=BX(I-1)
      YK1=AX*FU(YO,XO)
      QK1=AX*GU(XO,YO)
      YK2=AX*FU(YO+QK1/2.0,XO+YK1/2.0)
      QK2=AX*GU(XO+YK2/2.0,YO+QK1/2.0)
      YK3=AX*FU(YO+QK2/2.0,XO+YK2/2.0)
      QK3=AX*GU(XO+YK3/2.0,YO+QK2/2.0)
      YK4=AX*FU(YO+QK3,XO+YK3)
      QK4=AX*GU(XO+YK3,YO+QK3)
      BX(I)=BX(I-1)+(YK1+2.0*YK2+2.0*YK3+YK4)/6.0
      YX(I)=YX(I-1)+(QK1+2.0*QK2+2.0*QK3+QK4)/6.0
C*****
C***** DETERMINE LENGTH Xo 0F ZFE
```

```
C****
C****   IF ALL FP(I) IS GREATER THAN FPC
C****   WE SHOULD INCREASE XU
C****
      XU=XU*2.0
      KX=2
      GOTO 366
166   IF(I.EQ.1) THEN
      XPB0=XB0(I)
      QPQ0=Q4(I)
      ELSE
      FA=(FP(I-1)-FPC)/(FP(I-1)-FP(I))
      XA=FA*(XB0(I)-XB0(I-1))
      XPB0=XB0(I-1)+XA
      QPQ0=Q4(I-1)+FA*(Q4(I)-Q4(I-1))
      ENDIF
      A0=B0*H0
      XPA0=XPB0*B0/(A0**0.5)
C****
C****   OUTPUT Q(x)/Qo   , F  WITH X/Bo
C****
      WRITE(6,50)
 50   FORMAT(5X//7X,'X/B0',9X,'Q(X)/Q0',9X,'Fp',5X//)
      DO 45 K=1,M
      WRITE(6,61) XB0(K),Q4(K),FP(K)
 61   FORMAT(5X,F7.2,6X,2(F7.3,6X))
 45   CONTINUE
C****
C***   OUTPUT DEVELOPMENT REGION -----  ZFE
C****
      WRITE(6,83)
 83   FORMAT(5X//5X,'Developing  Region'//5X,'Distance X(I)',
     1    10X,'Y(I)  Half_width of center region'/25X
     2    ,'Have frication'//)
      WRITE(6,85) (XB0(K),YX(K),K=1,10)
 85   FORMAT(5X,F7.3,15X,F10.4)
 66   WRITE(6,68) F0,XPB0,QPQ0,XPA0
 68   FORMAT(5X//5X,'RESULTS OF PLUNGING FLOW:'//5X,4(F9.3,3X))
      WRITE(6,80)
 80   FORMAT(5X//5X,'RUN******* PHOR.EXE*******')
      STOP
      END
```

File name: PSLOP.FOR

Function: Computes dilution before plunging and distance to plunging of channel discharge **over sloping bottom.**

Equations: [4–44a] and [4–44b] for fully developed region.
[4–53a] and [4–53b] for flow development region.

Input file: PSLOP.DAT

Function: Specifies inflow conditions.

Variables:
BET = slop angle β
U_0 = inflow velocity.
CF = local friction coefficient c_f.
B_0 = width of inflow channel.
H_0 = depth of inflow channel.
Fo = inflow densimetric Froude number F_0.
SN = exponent n of vertical velocity profiles.

Output file: PSLOP.PRN

Function: Prints inflow conditions, jet dimensions, dilution before plunging and distance to plunging.

Variables:
XB0 = dimensionless length x/B_0
UC4 = jet centerline velocity $u_m(x)/U_0$
B4 = dimensionless jet width $b(x)/B_0$
YX = width of potential core in ZFE
FP = densimetric Froude number F
XPBO = distance to plunging x_p/B_0
QPQO = dilution before plunging Q_p/Q_0
XPAO = distance to plunging $x_p/\sqrt{A_0}$

```
C*****
C*****  PSLOP.FOR****BET IS NOT ZERO****STEEP SLOPE***
C*****
      DIMENSION X(86),UC4(86),B4(86),Q4(86),XB0(90)
      DIMENSION BX(20),YX(20),FP(86)
      FU(XO,YO)=A2*YO**3*(1.0+XO*A4)**A3
      F(XO,YO)=-YO*CF/(2.0*D2*(H0+XO*A1))-FU(XO,YO)
      H(XN)=H0+XN*A1
      BF2(XN,BZ,YZ)=C4+C5*YZ/H(XN)+BZ*C6/H(XN)
      YF2(XN,BZ,YZ)=C7-C8*YZ/H(XN)-BZ/H(XN)*C9
      DATA C1,C2,FITE1,FITE2/1.4142,0.6642,0.53229,0.37639/
      DATA AE,AE1,FPC/0.04,0.035,1.0/
      OPEN(5,FILE='PSLOP.DAT')
      OPEN(6,FILE='PSLOP.PRN')
      READ(5,*) BET,U0,CF,B0,H0,F0,SN
      M=86
      BETW=BET
      BET=3.14159*BET/180.0
      FITE3=2.0*FITE1
      FITE4=2.0*FITE2
      IF(SN.EQ.1.0) THEN
      D1=1.0
      D2=1.0
      ELSE
      D1=SN/(SN+1.0)
      D2=SN/(SN+2.0)
      ENDIF
      A1=TAN(BET)
      A2=2.0*AE/(C1*B0)
      A3=(CF+2.0*A1)/(2.0*A1)
      A4=TAN(BET)/H0
      A7=1.0/(2.0*FITE2)
      A8=2.0*FITE1/H0
      C3=FITE3-FITE4
      C4=AE1/C3
      C5=CF/(2.0*C3)
      C6=C5*FITE4-A1
      C7=-AE1*FITE4/C3
      C8=A1+C5*FITE3
      C9=CF*FITE3*FITE4/(2.0*C3)
C*****
C*****  INTINAL CONDITION  OF DE
C*****
      UC4(1)=1.0
      B4(1)=1.0
      Q4(1)=1.0
      BX(1)=0.0
      YX(1)=B0/2.0
C*****
C*****  COMPUTE ZFE IF KX=1
C*****
      KX=1
```

```
      FF=1.0
C****
C****  XU IS PROPROTIONAL TO Cf AND WIDTH Bo
C****  XU IS VERY LARGE, MAKE  A LITTLE BIT OF EORROR
C****  THE FOLLOWING EQUATION OF XU IS EMPIRICAL
C****
      XU=B0/(CF*10)
366   DO 100 I=1,M
      IF(I.EQ.1) GOTO 15
      IF(KX.EQ.1) THEN
      AX=FF*B0/FLOAT(20)
      ELSE
      IF(I.LE.10) AX=X0*B0/9.0
      IF(I.GT.10) AX=(XU-X0*B0)/(FLOAT(M)-10.0)
      ENDIF
      X(I)=X(I-1)+AX
      XB0(I)=X(I)/B0
 15   X(1)=0.0
      IF(I.EQ.1) GOTO 100
C****
C****   KX=1 COMPUT ZFE ONLY
C****
      IF(KX.EQ.1) GOTO 200
C****
C**** IF KX=2 COMPUTE ZFE FOR 10 STEP SIZE
C****
      IF(I.LE.10) GOTO 200
C****
C**** WITH ENTRAINMENT Ae,  WITH FRICTION Cf
C****
      YN=UC4(I-1)
      XN=X(I-1)
      UK1=AX*F(XN,YN)
      UK2=AX*F(XN+AX/2.0,YN+UK1/2.0)
      UK3=AX*F(XN+AX/2.0,YN+UK2/2.0)
      UK4=AX*F(XN+AX,YN+UK3)
      UC4(I)=UC4(I-1)+(UK1+2.0*UK2+2.0*UK3+UK4)/6.0
      B4(I)=A7/(UC4(I)**2*(1.0+X(I)*A4)**A3)
      Q4(I)=A8*UC4(I)*B4(I)*(H0+X(I)*A1)
      GOTO 100
C****
C****  ZFE WITH  FRICTION Cf
C****
200   XN=X(I-1)
      YZ=YX(I-1)
      BZ=BX(I-1)
      BK1=AX*BF2(XN,BZ,YZ)
      YK1=AX*YF2(XN,BZ,YZ)
      BK2=AX*BF2(XN+AX/2.0,BZ+BK1/2.0,YZ+YK1/2.0)
      YK2=AX*YF2(XN+AX/2.0,BZ+BK2/2.0,YZ+YK1/2.0)
      BK3=AX*BF2(XN+AX/2.0,BZ+BK2/2.0,YZ+YK2/2.0)
      YK3=AX*YF2(XN+AX/2.0,BZ+BK2/2.0,YZ+YK2/2.0)
```

```
      BK4=AX*BF2(XN+AX,BZ+BK3,YZ+YK3)
      YK4=AX*YF2(XN+AX,BZ+BK3,YZ+YK3)
      BX(I)=BX(I-1)+(BK1+2.0*(BK2+BK3)+BK4)/6.0
      YX(I)=YX(I-1)+(YK1+2.0*(YK2+YK3)+YK4)/6.0
C*****
C*****  DETERMINE LENGTH OF ZFE
C*****
      IF(YX(I).LT.0.0.AND.KX.EQ.1) THEN
      CFA=YX(I-1)/(YX(I-1)+ABS(YX(I)))
      X0=(X(I-1)+AX*CFA)/B0
C*****
C***** FINSH COMPUTATION OF ZFE IF KX=2
C****
      KX=2
      GOTO 366
      ENDIF
      IF(I.EQ.20.AND.YX(I).GT.0.0) THEN
      FF=2.0*FF
      KX=1
      GOTO 366
      ENDIF
      B4(I)=2.0*(YX(I)+BX(I))/B0
      UC4(I)=1.0
      Q4(I)=2.0*H(X(I))*(YX(I)+BX(I)*FITE3)/(B0*H0)
 100  CONTINUE
C*****
C*****  OUTPUT PARAMETERS OF COMPUTATIONS
C*****
      WRITE(6,10) BETW,B0,H0,C1,C2,CF,AE,AE1,X0,FITE1,FITE2
  10  FORMAT(5X,'BET=',F5.2,2X,'(DEGREE)'//5X,'B0=',F7.2,13X,'H0=',
     1        F7.5//5X,'C1=',F7.5,13X,'C2=',F7.5//
     2        5X,'CF=',F7.5,13X,'AE=',F7.5,//5X,'Ae=',F7.5,13X,
     3        'Xo=',F7.4//5X,'FITE1=',F7.5,10X,'FITE2=',F7.5//)
      WRITE(6,20)
 20   FORMAT(4X,'X/B0',6X,'Um/U0',9X,'b/B0'//)
C*****
C*****  OUTPUT WIDTH & CENTER VELOCITY OF JET
C*****
      DO 30 I=1,M
      WRITE(6,40) XB0(I),UC4(I),B4(I)
 40   FORMAT(5X,F7.2,3X,F9.3,5X,F9.3,3X)
 30   CONTINUE
C*****
C*****  COMPUTE DESIMETRIC FROUDE NUMBER F AND Xp
C*****
      DO 566 I=1,M
      HPHO=SQRT(1.0+A1*XB0(I)*B0/H0)
      IF(I.GT.10) THEN
      FP(I)=0.626657/HPHO*F0*UC4(I)*Q4(I)**0.5
      ELSE
      FT=2.0*(YX(I)+FITE3*BX(I))/(2.0*YX(I)+3.397*BX(I))
      FP(I)=FT/HPHO*F0*UC4(I)*Q4(I)**0.5
```

```
      ENDIF
566   CONTINUE
      DO 666 I=1,M
      IF(FP(I).LE.FPC) GOTO 166
666   CONTINUE
C*****
C***** IF ALL FP(I) IS GREATER THAN FPC
C***** WE SHOULD INCREASE TOTAL LENGTH XU
C*****
      XU=2.0*XU
      KX=2
      GOTO 366
166   IF(I.EQ.1) THEN
      XPB0=0.0
      QPQ0=Q4(I)
      GOTO 64
      ELSE
      GOTO 69
      ENDIF
69    FA=(FP(I-1)-FPC)/(FP(I-1)-FP(I))
      XA=FA*(XB0(I)-XB0(I-1))
      XPB0=XB0(I-1)+XA
      QPQ0=Q4(I-1)+FA*(Q4(I)-Q4(I-1))
64    A0=B0*H0
      AR=B0/H0
      XPA0=XPB0*B0/A0**0.5
      WRITE(6,50)
 50   FORMAT(5X//4X,'X/B0',7X,'Q(X)/Q0',9X,'F',5X//)
C*****
C*****  OUTPUT X/B0,Q(x)/Qo,F
C*****
      DO 45 I=1,M
      WRITE(6,60)  XB0(I),Q4(I),FP(I)
60    FORMAT(5X,F7.2,6X,2(F7.3,6X),5X)
45    CONTINUE
C*****
C*****   OUTPUT DEVELOPEMENT REGION ----  ZFE
C*****
      WRITE(6,70)
70    FORMAT(5X//5X,'Developing Region'//5X,'Distance  X(I)',
     1    7X,'YX(I)'//)
      WRITE(6,75)  (XB0(I),YX(I),I=1,10)
75    FORMAT(5X,F9.4,10X,F10.5)
      WRITE(6,68) F0,XPB0,QPQ0,XPA0
68    FORMAT(5X//5X,'RESULTS OF PLUNGING FLOW:'//5X,4(F9.2,3X))
      WRITE(6,80)
80    FORMAT(5X//5X,'RUN*******RUNGE2.EXE******')
      STOP
      END
```

File name: DATA.FOR

Function: Analyzes finite experimental data using modified Gaussian fitting method.

Equations: From [B–1] to [B–11]

Input File: DATA.FOR

Function: Specifies experimental data.

Variables:
VMAX = maximum velocity of experimental data
VN = velocity at negative cut–off point
VP = velocity at positive cut–off point.
N = number of experimental data
X = measurement cross section coordinate x
Y = measurement point coordinate y
VX = measurement velocity at (x,y)

Output file: DATA.PRN

Function: Prints experimental data and fitted results

Variables:
VXVMAX = dimensionless velocity $u/u_m(x)$
YB = dimensionless coordinates y/B
TM1 = correction coefficient of the first moment
CT2 = correction coefficient of the second moment
CM2 = corrected second moment
A2 = jet width B_c
VAMX = centerline velocity $u_m(x)$

```
C***** DATA.FOR
C***** Analysis Of Experiment Data
C*****
      DIMENSION Y(5),VX(5),VXVMAX(5),YB(5)
      OPEN(UNIT=5,FILE="DATA.DAT")
      OPEN(UNIT=6,FILE="DATA.PRN")
      READ(5,*) VMAX,VN,VP,N,X,Y,VX
C*****
C*****Compute the corrective-coefficient for moment
C*****
      VNN=VN/VMAX
      VPN=VP/VMAX
      YPV=SQRT(-ALOG(VPN))
      YNV=-SQRT(-ALOG(VNN))
      T0=0.0
      T1=0.0
      T2=0.0
      AYX=(YPV-YNV)/199
      AYY=AYX/2.0
      YX=YNV
      YVX=EXP(-YX**2)
      DO 1 I=1,200
      AA=AYX
      IF(I.EQ.1.AND.I.EQ.200) AA=AYY
      T0=T0+YVX*AA
      T1=T1+YVX*YX*AA
      T2=T2+YVX*YX**2*AA
      YX=YX+AYX
      YVX=EXP(-YX**2)
  1   CONTINUE
      PI=3.1415927
      CT0=SQRT(PI)/T0
      T1=T1/T0
      WRITE(*,*) T1
      T2=T2/T0
      CT2=0.5/T2
C*****
C***** Compute the moment from experiment data
C*****
      AY=Y(2)-Y(1)
      AYH=AY/2.0
      TM0=0.0
      TM1=0.0
      DO 20 I=1,N-1
      AA=AY
      IF(I.EQ.1.AND.I.EQ.N) AA=AYH
      YM=(Y(I)+Y(I+1))/2.0
      VXM=(VX(I)+VX(I+1))/2.0
      TM0=TM0+VXM*AA
      TM1=TM1+VXM*YM*AA
 20   CONTINUE
      CM0=TM0*CT0
```

```
      TM1=TM1/TM0-T1
      WRITE(*,*) TM1
      TM2=0.0
      TM3=0.0
      DO 30 I=1,N-1
      AA=AY
      IF(I.EQ.1.AND.I.EQ.N) AA=AYH
      YM=(Y(I)+Y(I+1))/2.0
      VXM=(VX(I)+VX(I+1))/2.0
      TM3=TM3+VXM*(YM-TM1)**3*AA
      TM2=TM2+VXM*(YM-TM1)**2*AA
30    CONTINUE
      TM2=TM2/TM0
      TM3=TM3/TM0
      CM2=TM2*CT2
      A2=SQRT(2*CM2)
      VM=VX(1)
      DO 60 I=2,N
      VM=AMAX1(VX(I),VM)
      IF(VX(I).EQ.VM) J=I
60    CONTINUE
      VMAX=VM/EXP(-((Y(J)-TM1)/A2)**2)
      DO 70 I=1,N
      VXVMAX(I)=VX(I)/VMAX
      YB(I)=(Y(I)-TM1)/(A2)
70    CONTINUE
      WRITE(6,40) X
      WRITE(6,41) (Y(I),I=1,N)
      WRITE(6,42) (VX(I),I=1,N)
      WRITE(6,45)
      WRITE(6,43) (YB(I),I=1,N)
      WRITE(6,44) (VXVMAX(I),I=1,N)
40    FORMAT(5X/5X,'Distance  X=',F4.1
     1       ,10X,'Method 2'//
     2       5X,'Input Data--------')
41    FORMAT(5X/5X,'     Y(ft)',6F9.4)
42    FORMAT(5X/5X,'VX(ft/sec)',6F9.4)
45    FORMAT(5X//5X,'Output Result--------')
43    FORMAT(5X/5X,'       y/B',6F9.4)
44    FORMAT(5X/5X,'   Vx/Vmax',6F9.4)
      WRITE(6,50) TM1,CT2,CM2,A2,VMAX
50    FORMAT(5X/5X,'COEm1=',F9.4,4X,'COEm2=',F9.4//
     2       5X,'M2c=',F9.4,4X,'Bc=',F9.4//5X,'Vmax=',F9.4)
      STOP
      END
```